OPERATIONAL PARAMETRIC STUDY OF A PROTOTYPE TESLA PUMP

by

Laura J. Dodsworth

Submitted in partial fulfilment of the requirements
for the degree of Master of Applied Science

at

Dalhousie University
Halifax, Nova Scotia
April 2016

Table of Contents

List of Figures

List of Tables

Abstract

A parametric study of a prototype Tesla pump was performed for various disk pack spacings and rotational speeds. The 15 thou spacing was the most effective disk pack spacing. A 40/60 weight percent mixture of propylene glycol and water was used to show the effect viscosity has on the Tesla pump performance. The boundary layer thickness was found to increase for the viscous working fluid and the performance between the various disk pack spacings were clearer than that for the water testing. A CFD simulation of a Tesla pump was attempted to determine if the results are similar to the experimentally obtained results. The boundary layers that form between the disks have been shown to combine and develop similarly to fully developed flow between plates. The effects of vibration on the operation of the prototype Tesla pump were also tested, and no effect was found for two vibrational frequencies.

List of Abbreviations and Symbols Used

A	Amperage (Amps)
b	Disk Radius (m)
B	Magnetic Field Strength
D	Diameter (m)
d	Gap spacing (m)
eps	Error Propagation
E	Signal Voltage (Volts)
g	Gravity (9.81 m/s^2)
H	Net Pump Head (m)
L	Distance Between Electrodes (m)
$\dot{m}$	Mass Flow Rate (kg/s)
n	Rotations Per Minute (RPM)
P	Power (W)
P	Pressure (Pa or psi)
Q	Flow Rate (L/min or m^3/s)
r	Local Radius (m)
T	Torque (N·m)
u	Velocity (m/s)
U	Velocity (m/s)
V	Voltage (Volts)
w	Weight Fraction
x	Given Point Along the Plate (m), starting at x=0

Greek Symbols

ρ	Density (kg/m^3)
δ	Boundary Layer Thickness
γ	Specific Weight

τ	Shear Stress (Pa)
η	Efficiency
ω	Rotational Speed (rad/sec)
μ	Dynamic Viscosity (cP or Pa·s)
ν	Kinematic Viscosity (m^2/s)

Dimensionless Number and Coefficient

Br	Blockage Ratio
C_f	Local Friction Coefficient
C_H	Head Coefficient
C_Q	Capacity Coefficient
C_P	Power Coefficient
N_d	Dimensionless diameter/gap ratio according to Darby et al.
N_h	Dimensionless Pump Head according to Darby et al.
N_Q	Dimensionless Capacity Coefficient according to Darby et al.
N_s	Specific Speed
Re	Reynolds number

Subscript

elec	Electrical
hy	Hydraulic
mech	Mechanical
M	Motor or Electric
r	Radial location
shaft	Shaft
tot	Total
x	Point along x-axis
z	Axial location

∞	Free Stream or Bulk Flow
θ	Angular measure
ϕ	Tangential location
$*$	Dimensionless value

Superscript

$-$	Average value

Abbreviations

bhp	Breaking Horsepower (W)
CFD	Computational Fluid Dynamics
DAQ	Data Acquisition
PGM	Propylene Glycol water Mixture
RPM	Rotations Per Minute
thou	Thousandths of an Inch

Acknowledgements

I would first like to thank my thesis advisor Dr. Dominic Groulx of the Mechanical Engineering department at Dalhousie University. The door to Dr. Groulx's office was always open whenever I ran into a trouble spot or had a question about my research or writing. He consistently allowed this paper to be my own work, but steered me in the right the direction whenever he thought I needed it. A thanks to my committee members for their input and time: Dr. Clifton Johnston and Dr. Jan Haelssig.

I would also like to thank the fellow students in the lab group LAMTE who have helped me along the way, including Martha who provided help with experiments. This project could not have been completed without their help and support. I would additionally like to thank Raytheon and John Jacobs for providing funding for this project.

Finally, I would like to thank my friends and family for their continued support and understanding while working on this project. In specific, I would like to thank Jordan Gilbert and the Dodsworth's: my mom, dad, and sister for their support. I could not have done it without you guys.

Chapter 1 Introduction

Tesla type turbomachinery or disk type turbomachinery was first invented by Nikolas Tesla in 1913, US Patient #1,061,142. In its early stage of development, it had never been seriously considered useful in comparison to conventional turbomachinery. It was therefore regarded as only a conceptual design due to issues in efficiency when compared to bladed turbomachinery (Engin et al., 2009). This type of turbomachinery can be implemented as a turbine, compressor, or pump. A lot of the available literature on such devices deals with the performance issues of a Tesla turbine, with a handful of design and CFD studies of Tesla pumps. There was significant interest in the 1950's in the flow between rotating disks, helping to develop further understanding of how a Tesla pump operates. Understanding the fluid mechanics of the flow between rotating disks and improving the efficiency of Tesla turbomachinery is still studied today.

The main objective of this overall research project was to design a pump for Raytheon with the purpose of cooling electronics in a military environment. The pump was to be compact, rugged and reliable. One of the main design requirements was that the pump had to operate under intense vibration (up to 6 g's), and since a Tesla pump has a lower sensitivity to vibration induced cavitation, it was selected as suitable for this application. This is unlike conventional centrifugal pumps where cavitation can be induced by the application of vibration. Tesla pumps have also been known to work well with viscous fluids which would be advantageous for a cooling application since fluid viscosity tend to increase as the temperature decreases. The prototype pump was previously designed and shown to meet the majority of the design requirements provided by Raytheon. Therefore, the present study looks at how a prototype Tesla pump operates under several operational conditions, focusing on identifying ideal pump configurations. Another aspect of this study includes building a working model of the pump to perform CFD studies, comparing the numerical results to experimental results. The end goal is to further understand how this particular type of pump works and suggest any necessary improvements using the knowledge gained from this study.

1.1 Literature Review

The Tesla pump has a relatively simple design compared to a bladed pump. This type of pump's impeller consists of rigid disks, differing from that of conventional centrifugal pumps which uses blades. The main issue with Tesla turbomachinery is that the efficiency is significantly less than that of conventional pumps of similar size. There are however applications where the working principles of a Tesla pump are advantageous. There is literature available that discusses the performance issues of Tesla type turbomachinery, with a few even focusing on the Tesla pump. The following sections include an explanation of how a Tesla pump works, a brief history and summary of Tesla pump and Tesla turbine studies, and a summary of flow studies relating to spinning disks.

1.1.1 How a Tesla Pump Works?

A traditional centrifugal pump uses rotating blades, called impeller or rotor blades, found inside a snail shaped casing, called a scroll or volute. Due to the use of a bladed impeller, lift forces are used to transfer energy to or from the working fluid (Harikishan & Shyam, 2013). These rotating blades transfer tangential and radial momentum, and additional radial velocity due to centrifugal forces, to the working fluid. For a centrifugal pump, the fluid enters axially through the hollow middle of the pump and then encounters the rotating blades (Cengel & Cimbala, 2010). The fluid then exits radially out of the pump, through the volute. Figure 1.1 details the flow path.
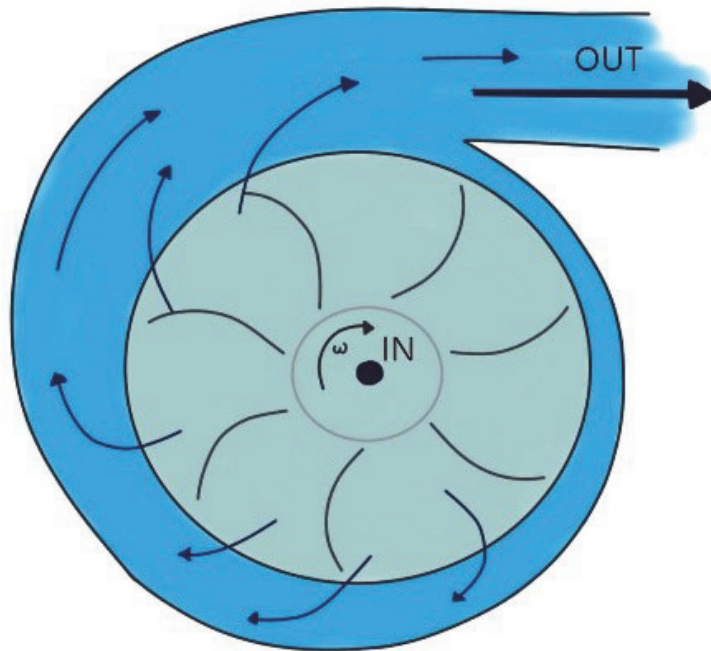
Figure 1.1 View of the flow path for a centrifugal pump (front view).

Tesla turbomachinery, whether used as a pump or turbine, utilizes similar operational principles. It works by utilizing the shear forces produced either by the fluid flowing between the narrow disks (turbine) or by the disks rotating (pump). The working principle of Tesla turbomachinery is therefore based on the friction between the wall of the disk and the fluid, due to its viscosity, through the no-slip condition at the wall. For a pump, this results in the fluid being dragged along by the wall of the rotating disks causing the fluid to accelerate until it reaches the velocity of the disks (Hoya & Guha, 2009). The main operational principle can also be looked at as viscous drag or shear forces of the fluid; this view occasionally leads to the Tesla pump being called a shear-force pump (Rossetti et al., 2010).

For a Tesla Pump, the impeller consists of smooth, flat, parallel disks, arranged on a drive shaft as per Fig. 1.2. The fluid enters the core of the pump, through the center, is pushed outwards though the space between the disks due to their rotation, and then exits the pump. The end result is an increase in pressure across the pump's inlet and outlet (Rice, 1963).
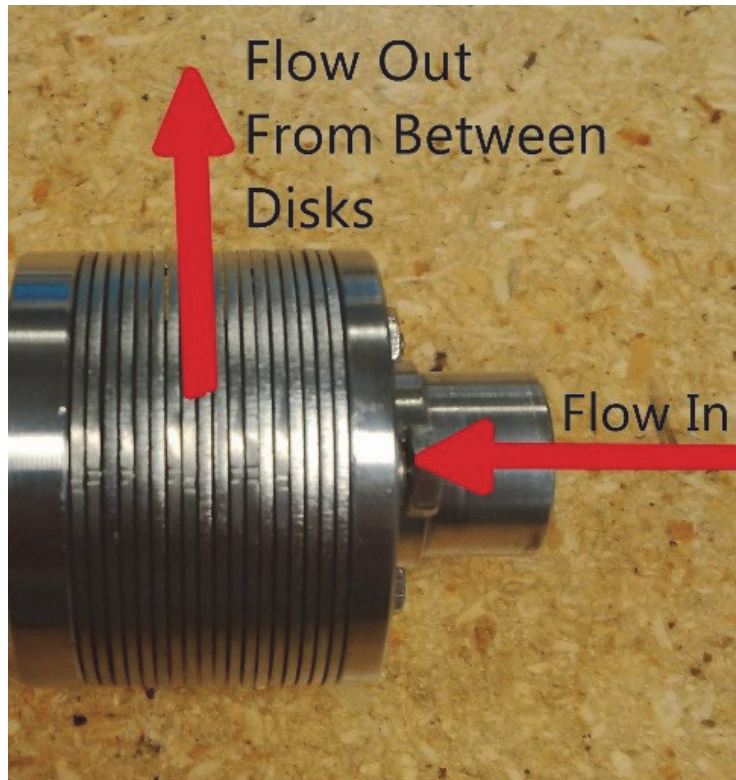
Figure 1.2. Photograph showing the flow through the disk pack assembly.

There are specific applications where the Tesla pump is best utilized in comparison to that of conventional bladed pumps. Some applications for a Tesla pump involve working well with fluids more viscous than water, 'exotic fluids' such as non-Newtonian fluids, two phase (gas-liquid) mixtures, and highly loaded slurries and suspensions (Darby et al., 1987). Essentially, they are a good option in situations where conventional pumps are considered inadequate (Rice, 1963): for example when a conventional pump would be inefficient or dangerous to utilize.

Another important factor that makes Tesla pumps advantageous in certain applications, as mentioned by Darby et al. (1987), is that the pump has a lower sensitivity to cavitation compared to centrifugal pumps. A conventional blade can lead to low pressure points in the fluid when it rotates, which causes vaporization and therefore bubbles, which burst when the pressure then increases again. Since Tesla pumps use cylindrical disks rather than the conventional blades, there is a reduction in low pressure points within the pump, and therefore less cavitation (Darby et al., 1987). Also, there is the fact that the flow is well

4

bounded between the disks, and is mostly entrained in the boundary layer (Hasinger & Kehrt, 1963). The avoidance of cavitation increases the lifetime of the pump and allows for more stable operations compared to convenctional pumps (Darby et al., 1987). Furthermore, in a conventional pump, under conditions where the lift forces are most efficient, if there are any disturbances in the flow, such as separation; cavitation will become even more significant. These flow disturbances would cause operational issues, such as noise, and damage to the blades (Harikishan & Shyam, 2013).

The stable operational conditions of a Tesla pump allows for applications using potentially volatile working fluids, such as combustible fluids. Another problem with the design of conventional centrifugal pumps is the generation of pressure pulses that occur during normal operation. These can affect the pump's mechanical integrity and therefore its life expectancy. This can result in vibrations, causing further problems for the pump's integrity, or causing excessive operational noise. The design process for centrifugal pumps would therefore include testing for instabilities in the flow due to potential damage and vibration (Amaral-Teixeira & Spence, 2009). A Tesla pump tends not to have the same issues, due to the fact the blades are of a very simple design (Darby et al., 1987). Due to the simplicity of the impeller of Tesla pumps, they are also inexpensive to build compared to a conventional pump, and could be manufactured in a modest machine shop (Rice, 1963).

There are a range of suggested industrial applications for a Tesla pump. As mentioned previously, its ability to operate with unusual fluids is beneficial, when conventional pumps would be unsuitable. It was suggested Tesla Pumps could be used in "missile and space-age systems", such as for liquid rocket fuel (Hasinger & Kehrt, 1963; Miller & Fink, 1999; Rice, 1963). Other applications would include ventricular assistance devices (blood pump), or artificial hearts. The disc type impeller has shown that it does not damage blood cells compared to other alternatives. Therefore, it would be ideal as a blood pump for artificial hearts (Rossetti et al., 2010). Another fact supporting the use of Tesla pumps in the biomedical field is that these pumps are advantageous for very small volumetric pumping applications (Engin et al., 2009; Rice, 1963).

Furthermore, Rice suggests that as the Tesla pump decreases in size, its efficiency is expected to remain constant, unlike conventional pumps where efficiency decreases with size (Rice, 1963). Multiple disk fans are similar to a pump as they still move a fluid such as air. One suggested application for a disk fan is moving hot gases above 800^0C, where the gas becomes denser, or more viscous. Industrial processes which require hot gases to increase quality, energy consumption, and possibly reduce gas emissions such as the ceramic industry, and some metallurgical and chemical processes would be good candidates (Engin et al., 2009).

1.1.2 Brief History of Rotating Flow Studies

Understanding the fluid dynamics of flow caused by rotating disks is important in understanding how different design parameters affect the performance of a Tesla pump. When the idea of multiple disk turbomachinery was originally introduced in 1913, where there was a sudden interest in understanding how it works. Von Karman was one of the first to attempt the problem of steady flow of an incompressible viscous fluid caused by an infinite rotating disk by solving the Navier-Stokes equations to obtain an exact solution (Rogers & Lance, 1959). Cochran later brought up an issue regarding Von Karman's numerical solution and presented his improved solution to the non-linear governing equations (Cochran, 1934). The improvement produced more accurate values and the trend of constant improvement to the solution carried on. Rogers and Lance looked at the flow in the presence of a rotating disk, and focused on finding cases where realistic exact solutions existed (Rogers & Lance, 1959). Brenton also looked at the problem, by obtaining steady state solutions from time dependent initial value problems or at least identified where this was possible given the computational limitations at the time (Benton, 1966). This later went on to more detailed analysis, such as by Humphrey et al. (1995), which included the enclosure (casing), comparison to experimental data, and tackling unsteady state analysis. The type of flow was qualified and divided into different regions, and this qualification is shown section 1.1.5 (Humphrey et al., 1995). Computational Fluid Dynamics (CFD) work eventually started to emerge further allowing for better classification of the flow. This constant improvement of knowledge helps with the understanding of how the flow between rotating disks, such as inside a Tesla pump, works.

1.1.3 Tesla Pump Studies

The majority of the research regarding Tesla pumps involves predicting and analyzing the performance of the pump. This includes efficiency, flow rate, power delivered, and head. The main geometric parameters used in performance analysis include the disk/impeller diameter, spacing, and number of disks. Typically, the flow rate, pressure difference across the pump (head), the provided power and/or disk velocity is measured and converted into dimensionless parameters, such as efficiency, flow and head coefficients, for analysis. The results from experimental and theoretical studies provide insight into specific aspects of a design's performance, such that any improvements to the pump can be quantified and performed accordingly.

Hasinger and Kehrt, proposed a pump design by utilizing dimensionless theoretical data and validated it with experimental data. They assumed laminar flow conditions and included some analysis on basic flow losses, efficiencies, cavitation characteristics and specific speed (N_S). Specific speed is defined later in Chapter 2. The rotor design presented and tested in this study is shown in Fig. 1.3. This rotor design is different than a typical Tesla pump, which induces mixed flow within the pump. This was done to obtain high flow rates but low inlet velocities, which would prevent cavitation at the inlet. Some of the more significant findings from this study are as follows. They state that with larger rotors, turbulent flow may occur, however this is more likely to happen for a rotor that is at least a foot in diameter, with water as the working fluid. It was noted that a Tesla pump should be able to obtain rotor efficiencies up to 60% assuming laminar flow, however achieved experimental rotor efficiency was measured to be 54%. One of the main suspected problems is the tendency of the shear forces from the rotor to trap gas, which was reported to cause huge drops in pump performance experimentally. Any gas bubbles entrained in the pump fluid could become trapped in the rotor and would obstruct the flow. This entrapment was due to the combined action of fluid drag forces and centripetal forces. The drag forces would draw the bubbles into the disk pack, and then the centripetal forces would prevent the bubbles from leaving. Therefore, the avoidance of air bubbles in the working fluid and therefore in the disk pack was found to be important to the pump efficiency. Another problem was suspected to be due to the suction speed being highly influenced by

7

the radius ratio (outside vs. inside) and specific speed; this causing high inlet velocities which could induce cavitation. Therefore, higher specific speed geometries are recommended to help prevent these adverse inlet conditions. They suggested that the highest efficiencies are expected around specific speeds of 50, with specific suction speeds in close to a 1000 without cavitation (Hasinger & Kehrt, 1963).
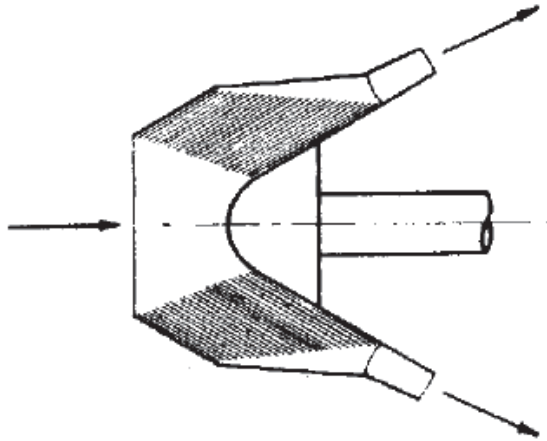
Figure 1.3. Mixed-flow Tesla Pump design. Reproduced from (Hasinger & Kehrt, 1963), with the permission of ASME Publishing.

Rice looked at multiple disk pumps, blowers, and compressors, *i.e.* Tesla turbomachinery. This paper includes several tests of each type of turbomachinery, with focus on pumps and compressors. The flow was found to be unstable over some ranges tested, and this instability is believed to be due to flow separation. These ranges are identified as a set of dimensionless variables and values, for given points on a disk, flow rates and friction factors. This resulted in cavitation within the rotor likely induced at the inlet. A dimensionless 'first approximation' analysis of the flow between a pair of rotating disks is shown in this paper, however it is important to note it does not include frictional losses. The purpose of this analysis was to establish the upper/lower limits of performance that could be achieved. It was suggested that the volumetric flow rate parameter could be used to find the necessary number of disks for an actual pump. In the end, the analysis showed that the efficiency and pump head decrease with increasing volumetric flow rate, which is

similar to other studies (Rice, 1963). This trend is shown and discussed later in Figs. 1.4 and 1.5.

Darby et al. also developed a set of dimensionless relationships to analyze the pump operation and performance. The focus of this study was on the turbulent and transitional stages of flow in a Tesla Pump. This is one of the first studies to mention the pumps greater flow stability, *i.e.*, low sensitivity to cavitation. It is important to note that the disks in the experimental pump were 356 mm (14 in) in diameter, 3.78 mm (0.149 in) thick, and spaced 3.46 mm (0.136 in) apart. The dimensions of Darby's pump study are larger than this present prototype study, however due to the use of non-dimensional analysis they can be compared. They showed that the dimensionless pump power can be related to the flow rate, gap spacing, rotational Reynolds number and the relative roughness of the disk surface (Darby et al., 1987). Figure 1.4 shows the head vs capacity coefficients for various rotational speeds and disk pack spacings from Darby et al. pump. Typically, as the flow rate increases the pump head will decrease, and in Fig. 1.4, as the spacing decreases the flow rate and pump head decreases. Figure 1.5 shows the efficiency for the different spacings, with a corresponding table with the spacing, number of disks and specific speed. Where N_d is the dimensionless diameter (d/D), N_h is the dimensionless pump head, and N_Q is the dimensionless capacity coefficient.

Darby et al. also mentioned that this type of pump has a tendency to trap gas bubbles, which they stated occurs more frequently at low flow rates. Other findings are that the impeller efficiency varied from 45-80%, which decreased as the flow rate increased. It was expected since the residence time within the gap would decrease as the flow rate increased. A dependence upon the rotational Reynolds number and pump speed was observed, especially since the rotational Reynolds number calculation relies on the pump's rotational speed (Darby et al., 1987).
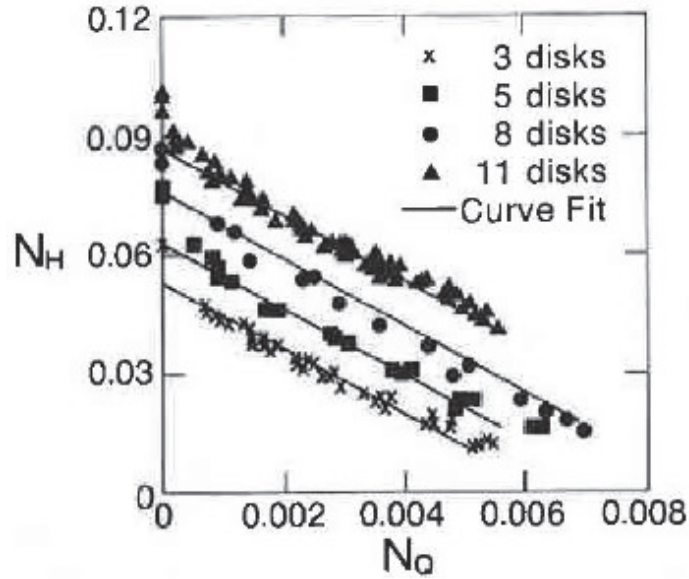
Figure 1.4. Dimensionless pump head vs. flow coefficient for various disk pack spacings, 300 to 2750 RPM. Reproduced from (Darby et al., 1987), with the permission of ASME Publishing.

No. Disks	No. Gaps	Gap Width, in.(mm)	N_d
11	10	0.136(3.45)	0.00971
8	7	0.330(8.38)	0.0236
5	4	0.689(17.5)	0.0492
3	2	1.527(38.8)	0.1090
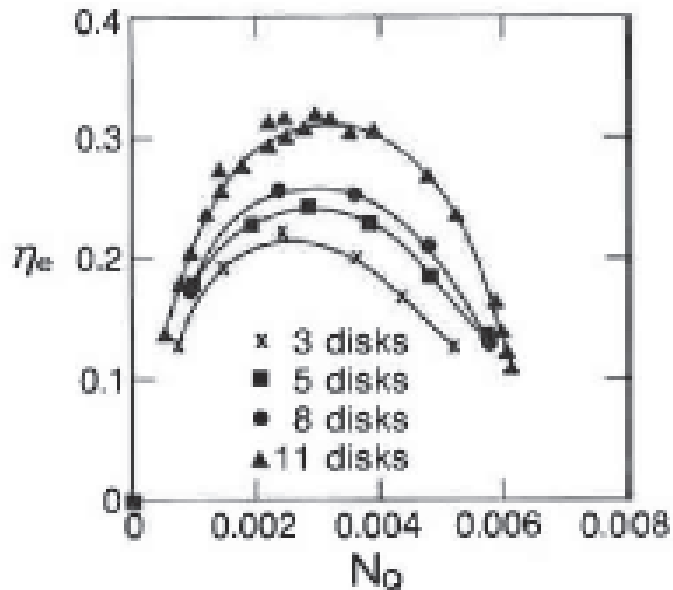
Figure 1.5. Efficiency vs. dimensionless flow coefficient for several different disk pack spacings and number of disk, for 2600 RPM. Reproduced from (Darby et al., 1987), with the permission of ASME Publishing.

The loss mechanisms in shear-force pumps (or Tesla pumps) are discussed in Okamoto et al. They used an experimental analysis, combined with CFD flow analysis, to discuss the main loss mechanisms in Tesla pumps. Three different disk sizes were analyzed where the rotational speeds were chosen to achieve similar disk peripheral speed for each size. One of the main conclusions of the study was that the rotor performance was not affected by downscaling. This was due to the pumps main working principal; viscous forces and frictional losses. In the independent study of the rotor, it was found that the lower the flow coefficient, the higher the efficiency; however there was discrepancy from the experimental results. Therefore, the flow fields were looked at for this case and it was found that re-circulation and reversed flow occur due to the volute design. Recirculation was found to occur mainly at the outlet of the disks, which supports the idea of carefully designing the volute to minimize the occurrence. The flow reversal, which would cause large losses in efficiency, would not have been predicted by the numerical rotor analysis and was the main reason the analytical and experimental results varied (Yamaguchi et al., 2014).

Of the four Tesla pump studies presented, each is slightly different but all contained several re-occurring themes. One such theme being that, as rotational speed increases, the pump head and flow rate would increase (Darby et al., 1987; Hasinger & Kehrt, 1963; Rice, 1963). There are many possible combinations of geometric parameters, with the disk radius ratio, speed and gap size clearly being determining factors of performance (Darby et al., 1987; Hasinger & Kehrt, 1963). The smaller the size of the disk pack the better, since this type of pump is recommended for small volumetric pumping applications. Cavitation occurs mainly due to volute designs which induce high inlet velocities (Darby et al., 1987; Hasinger & Kehrt, 1963; Rice, 1963). Experimentally, air was found to become trapped in the pump under low flow rates, which greatly affected pump performance. Overall efficiencies tend to be higher theoretically than what was found experimentally. This appeared to be the case due to complexities in accounting for losses, flow reversal and cavitation in the theoretical considerations (Darby et al., 1987; Hasinger & Kehrt, 1963; Rice, 1963; Yamaguchi et al., 2014). The maximum efficiency obtained experimentally was 45% (rotor only), and theoretically varied from 45% all the way up to 80%, depending

on the study. Therefore, the geometric design of the disk pack and the design of the casing, mainly being the inlet and outlet areas, are important factors to consider in designing an effective Tesla pump.

1.1.4 Turbine Studies

Tesla turbines operate in a similar manner to that of their pump counterparts; the only real difference is the working fluid that is used to produce power. These turbines have factors, such as disk spacing, thickness, diameter, and chamber/inlet design similar to that of a Tesla pump, which affect its performance. The testing and analysis of these turbines and the causes of loses in efficiency provide useful insight into the design and testing of a Tesla pump. It has been predicted that the rotor efficiency can be somewhere between 85 and 95% (Guha & Smiley, 2010). The total efficiency of these turbines has been shown to be between 14.6 and 35.5 %, which is less than that of conventional turbines. The majority of the studies presented here focus on improving the design of the turbine to obtain better efficiencies such as the inlet and outlet design of the volute. Since Tesla turbines are similar in design and operation to Tesla pumps, the results of these studies can be applied to improve the design a Tesla pump.

It has been determined that the main source of losses in efficiency in Tesla turbines is due to the design of the inlet, which is also an issue with Tesla pumps. Some of the issues with the inlets are 90° bends and elbows which would cause sudden changes in the area. In the study done by Guha and Smiley, who looked at improving the design of an inlet nozzle, using a nozzle with a plenum chamber integrated in the inlet improved the overall performance of the turbine. The plenum chamber produced smaller pressure losses inside the turbine, since the new inlet design allowed for a more uniform jet. A more uniform jet meant that all of the passages between the disks would receive uniform flow conditions. This increases the flow cross-sectional area and helps to reduce losses. The change in the losses of pressure went from 13-14% to less than 1%, after the new nozzle was implemented (Guha & Smiley, 2010). It was clear that the inlet design affects the performance of this type of turbomachinery.

Unlike the flow between two rotating disks in a pump, the flow in the Tesla disc turbine is not generated by the rotation of disks. It is generated from the working fluid entering the gaps between the discs surfaces and generating torque, due to the friction between fluid and disk surfaces. There has been some controversy into what type and which forces affects the flow occurring between the rotating disks inside a Tesla turbine. However, Guha and Sengupta tried to provide some insight in their papers. They provided a theoretical representation of the 3D flow field in the gap and looked at the roles of inertial, centrifugal, Coriolis and viscous forces. The flow pattern is usually a spiral pattern, with flow reversal creating deviation from this pattern. The net torque function is dependent on the viscous drag; this suggests that a desired power output could be achieved by altering the shear stress and controlling losses. By changing parameters such as the surface roughness and designing the turbine in such a way to optimize power output, its efficiency could be increased (Guha & Sengupta, 2013a). Their latest paper looks at how the geometric parameters affect operational parameters, such as the tangential speed ratio, radial pressure drop, angle of the inlet nozzle and exit position. This study looked at the effects of different operational parameters and there corresponding fluid flow path. The findings for small disk gap spacing, the predictions of each model agreed well between the theoretical and CFD models. It was also found that the pressure does not vary perpendicularly to the disk as per the assumption $dP/dz = 0$ in the analytical method. All of the findings agreed with the corresponding assumptions provided for the mathematical theory (Guha & Sengupta, 2013b).

1.1.5 Fluid Flow Studies

It has not been clear as to what type of flow occurs between co-rotating shrouded disks, such as that would be found between the disks in a Tesla pump. There have been several arguments made regarding what type of flow is present between rotating disks. One argument was that when the disks are co-rotating, the type of flow between the disks is of the Batchelor type, therefore having two separate boundary layers and a core flow which consists of two opposing rotating parts. Others have argued that the core remains at rest, which would be deemed as a Stewartson flow. However, it has been shown experimentally that it tends to be a combination of Batchelor and Stewartson flow type. Typically, being

stationary (Stewartson) in the center, and Batchelor type closer to the disk, as shown in Fig. 1.6 (Gauthier et al., 2002).
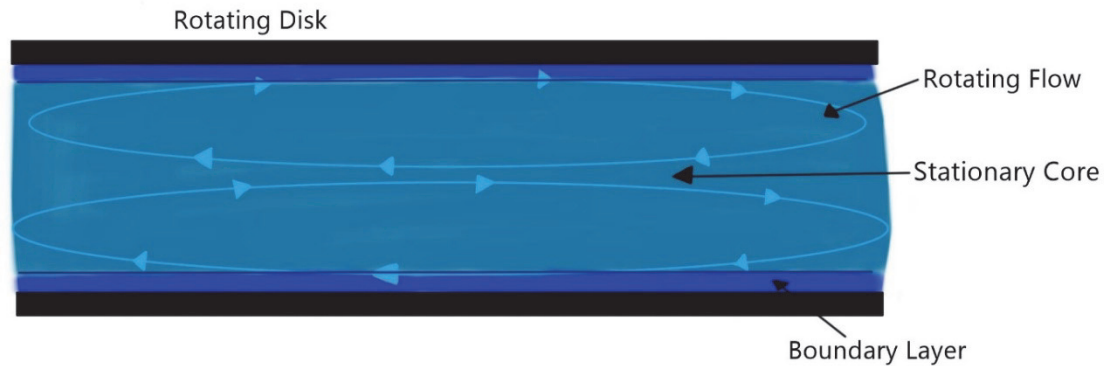
Figure 1.6. Cross section of the fluid flow between two rotating disks.

The flow between two co-rotating disks can be divided into five regions. The regions are used to help provide a theoretical mathematical framework for analysis and some have been proven to be true experimentally. These regions are shown in Fig. 1.7 and are described as such (Greif et al., 1990):

Region I: Called the shroud shear layer. It is the flow that is in close proximity to the shroud. It is usually assumed it is strongly sheared such that it would satisfy the non-slip zero velocity condition at the curved wall.

Region II: Is composed of two counter rotating areas, with a stationary core, and is called the core region.

Region III: Essential for the transition between region II and IV flows, and is called the detached shear layer.

Region IV: The area near the hub, where the rotating solid body is moving at the same velocity as the disk (except at high Reynolds number of order 10^5).

Region V: The boundary layer that occurs on either side of each disk, and is called the Ekman layer. This region of the flow is directed outward in the radial direction and is driven by the imbalance between the inward directed pressure force and the outward centrifugal

force. The outward centrifugal force would be the dominating force for a pump configuration.
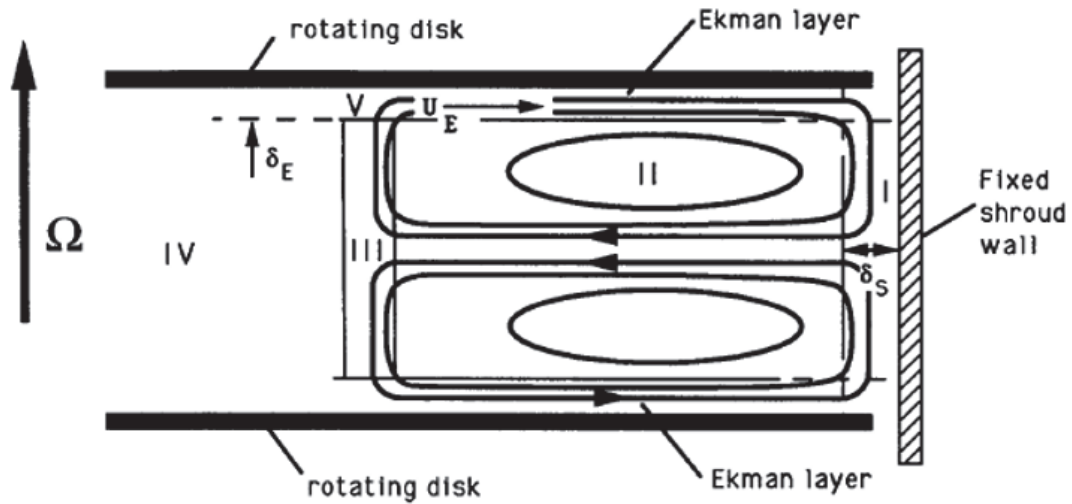
Figure 1.7. Simplified Regions of flow between two shrouded disks. Reproduced from (Greif et al., 1990), with the permission of AIP Publishing.

Studies focusing on the instabilities in the flow caused by rotating disks generally deal with identifying and characterizing the flow. From this, two main types of instabilities caused by co-rotating disks are identified, Type I and Type II. Type I is the instability caused by the cross-flow, such as that found over a swept wing. Type II is due to the combination of the Coriolis and viscous forces. Generally, these instabilities create circular or spiral rolls in the flow, and as the Reynolds number increases become more complex (Furukawa & Watanabe, 2009).

There have been many studies where instabilities are characterized for various geometric variations. A few of those studies are from Gauther et al. (2002), Furukawa & Watanabe (2009) and Huang & Hsieh (2011). Gauther et al. (2002) looked at the instabilities due to two rotating disks and performed experiments to visualize the flow instabilities. Furukawa & Wanatabe focused on the instabilities due to a shrouded disk, varying the gap between the disk and the shroud. Huang and Hsieh have performed experiments to visualize and characterize the flow between two shrouded co-rotating disks. They found five different flow modes from the flow between rotating disks, all of which were polygonal shapes.

1.2 Research Objectives

An undergraduate design group designed and built the prototype tesla pump that was used in this study. The basic design requirements for the pump were that it is to be compact, rugged and reliable to be used in a military environment and be able to continue pumping operation under large amount of vibrations. The pump is ultimately to be used to cool electronics. The design group chose a Tesla pump after comparing it to other types of pumps, due to the fact of its known low sensitivity to cavitation and vibration performance compared to a conventional pump. It was also beneficial that it operates using disks rather than blades, which are more rugged and reliable.

Preliminary testing with the prototype was done by this undergraduate design team. It was found that more testing and analysis was necessary, mainly due to amount of possible configurations for the pump. Testing was performed to see how well the pump operates in several environmental (hot and cold) conditions, including under vibration. The results of the environmental testing were that the prototype could withstand each condition, as long as materials selection for the pump was made accordingly. No conclusions were made regarding the effectiveness of the different configurations and the pump in general. This study is a continuation of their work, utilizing the design they developed.

In this study, to understand how the Tesla pump works and characterize the prototype pump's operation, various possible pump configurations for specific operational conditions needs to be considered. The following objectives for this Tesla pump study are:

- Further the current understanding of the effects of certain operating parameters, such as disk pack spacing and rotational speed experimentally; including a study of the impact of viscosity, where both water and a mixture of propylene glycol (PG)/water are used. The glycol/water mixture was used since it is readily available and typically used as a heat transfer fluid.

- Create a CFD model of the pump with the purpose of creating a working simulation that compares reasonably well with current experimental data. This model could

be used in the future to look at the impact of casing geometry or any other design changes for example.

- Experimentally study the effects of vibration on the pump's function, to confirm that cavitation is not induced due to vibration.

1.3 Organization

The layout of this thesis is as follows. Chapter 2 includes a background in turbomachinery theory, then looking at boundary layer theory focusing on the theory behind the fluid flow caused by spinning disks, and general flow between disks. Chapter 3 provides design details of the prototype pump, along with experimental methodology. Chapter 4 presents the experimental results and discussion, and Chapter 5 presents the analysis of the results of the CFD studies. This followed by a conclusion and future recommendations in Chapter 6.

Chapter 2 Background Theory

This chapter presents the theory related to Tesla pumps. This includes a review of relevant turbomachinery theory followed by boundary layer theory and flow between spinning disks. In the turbomachinery theory section (2.1), the power, efficiency and dimensionless coefficients are presented. Since Tesla pumps operate utilizing viscous or frictional forces within the boundary layer, basic theory is presented in section 2.2. Section 2.3 presents rotating flow boundary layer theory. Finally, section 2.4 presents a short discussion on the fully develop flow between spinning disks.

2.1 Turbomachinery Review

2.1.1 Pump Power and Efficiency

A pump transfers electrical to hydraulic power, through an intermediate mechanical means. The power delivered to the fluid can be quantified using two variables; net pump head (H) and flow rate (Q). The net pump head is the change in Bernoulli head between the inlet and outlet, however since the diameter (hence flow velocities) and elevation of the inlet/outlet are the same, Eq. (2.1) can be used. The pump head is related to the pressure difference across the pump ($P_2 - P_1$) and the fluid properties such as density (ρ) or specific weight (γ).

$$H = \frac{P_2 - P_1}{\rho g} = \frac{P_2 - P_1}{\gamma} \tag{2.1}$$

The flow rate is simply measured experimentally using a flow meter as will be discussed in Chapter 3.

Hydraulic power (P_{hy}) is an important factor to consider when designing a pump. It depends on the flow rate, head and density of the fluid, as shown in Eq. (2.2). Essentially, the net head is proportional to the useful power actually delivered to the fluid. A pump could be designed to achieve certain values of head and flow rate, depending on what is required of the pump (Cengel & Cimbala, 2010). The pump is ultimately provided power

through the electric motor (P_M), which is simply the electrical power as shown in Eq. (2.3), where A is the amperage drawn, and V the voltage used by the motor.

$$P_{hy}(kW) = \frac{Q\rho g H}{3.6 \times 10^6} \qquad (2.2)$$

$$P_M = AV \qquad (2.3)$$

Pump efficiency is another important factor in pump design. The total pump electrical to hydraulic efficiency (η_{tot}) is shown in Eq. (2.4) and is the quotient of the hydraulic power to electrical power.

$$\eta_{tot} = \frac{P_{out}}{P_{in}} = \frac{P_{hy}}{P_M} \qquad (2.4)$$

The mechanical to hydraulic efficiency or the mechanical efficiency (η_{mech}), is shown in Eq. (2.5). The mechanical efficiency is the quotient of the hydraulic power to the shaft or breaking horsepower (bhp). The breaking horse power (bhp) is the external mechanical power supplied to the pump, supplied through a shaft, or as in this study, through a magnetic coupling. The breaking horsepower or shaft power is the product of torque (T_s) and rotational speed (ω), as shown in Eq. (2.6).

$$\eta_{mech} = \frac{P_{hy}}{P_{shaft}} = \frac{P_{hy}}{bhp} \qquad (2.5)$$

$$P_{shaft} = bhp = T_s\omega \qquad (2.6)$$

One more type of efficiency is the electrical to mechanical efficiency, which is shown in Eq. (2.7), and is often provided as the electric motor efficiency:

$$\eta_{elec} = \frac{P_{shaft}}{P_M} \qquad (2.7)$$

2.1.2 Dimensionless Pump Parameters

To effectively compare one pump to another, dimensional analysis is usually performed using relevant variables. It produces the following dimensionless pump parameters: the Head coefficient (C_H) – Eq. (2.8), the Capacity coefficient (C_Q) – Eq. (2.9), and the Power coefficient (C_P) – Eq. (2.7). These are commonly referred to as the pump scaling laws. The typical variables used are the volumetric flow rate (Q), head (H), density (ρ), gravity

(g), the rotational speed (ω), breaking horsepower (bhp), and the diameter of the impeller (D) (Cengel & Cimbala, 2010).

$$C_H = \frac{gH}{\omega^2 D^2} \tag{2.8}$$

$$C_Q = \frac{Q}{\omega D^3} \tag{2.9}$$

$$C_P = \frac{T_s \omega}{\rho \omega^2 D^5} = \frac{bhb}{\rho \omega^2 D^5} \tag{2.10}$$

The pump efficiency can be related to all three of these dimensionless parameters as shown in Eq. (2.11):

$$\eta_{mech} = \frac{C_H C_Q}{C_P} \tag{2.11}$$

Equation (2.12) presents the specific speed (N_S), a unitless dimensionless parameter, which relates speed to different types and sizes of pumps. Rotations per minute (n) are used in this calculation, along with head (H) and flow rate (Q). It can also be calculated using the dimensionless head and capacity coefficients and does not take into account the size of the pump. This is beneficial when trying to compare pumps (Crowe et al., 2005).

$$N_S = \frac{C_Q^{\frac{1}{2}}}{C_H^{\frac{3}{4}}} = \frac{nQ^{\frac{1}{2}}}{g^{\frac{3}{4}} H^{\frac{3}{4}}} \tag{2.12}$$

2.1.3 Cavitation

Cavitation is the formation of vapour bubbles in a liquid as a result of the local pressure dropping below the vapour pressure of that liquid. Within a pump or turbine, if the pressure drops below the vapour pressure at any point in the device, unplanned vaporization may occur forming cavitation bubbles. When the cavitation bubbles form and are swept away from the low pressure region, they burst, generating destructive, high pressure waves. In a pump or turbine, cavitation can cause drops in performance, annoying vibrations, noise, or even damage or erosion of the impeller blades. Cavitation is generally avoided in turbomachinery design and operation, however has been shown to be induced due to vibration (Cengel & Cimbala, 2010).

2.2 Basic Boundary Layer Theory

Originally, the concept of boundary layer theory was proposed by Prandtl in 1904. This theory implies that external flows at relatively high Reynold (Re) numbers can be treated as two different flow regions. One of these regions is the boundary layer which tends to be significantly smaller than the bulk flow region where the fluid is moving at a free-stream velocity (U_∞) and can be considered inviscid. The boundary layer is described as the region bounded by a surface and away from it where the fluid velocity is less than 99% of the bulk fluid velocity and where viscous effects are important (Crowe et al., 2005). Figure 2.1 shows the boundary layer evolution over a flat plate for a range of Reynolds numbers.
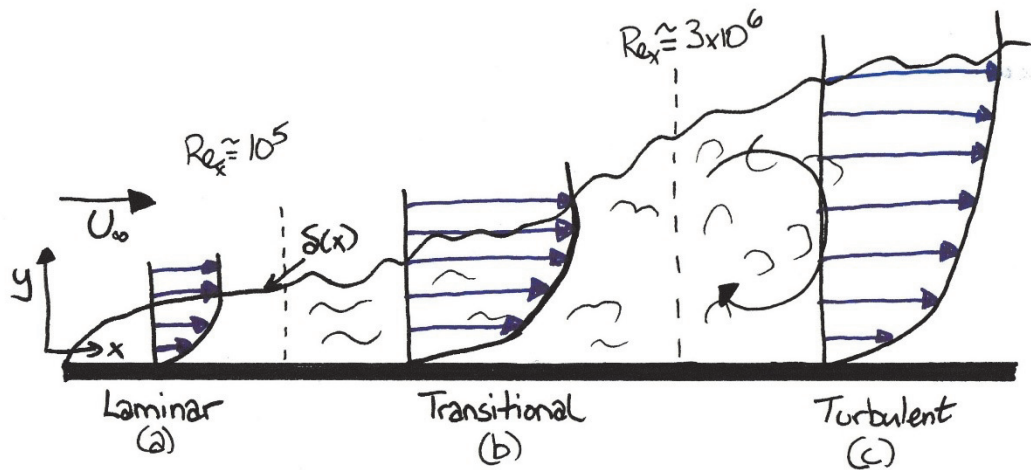
Figure 2.1. Boundary Layer over a flat plate for a range of Reynolds numbers.

As shown in Fig. 2.1, the flow within a boundary layer can be either laminar or turbulent, characterization of the boundary layer therefore depends on the respective flow type (Schlichting & Gersten, 2000). For the flow over a flat plate, the Reynolds number is given by Eq. (2.13), where ν is the kinematic viscosity, U_∞ is the free-stream velocity, and x is the location on the plate starting at $x = 0$ at the leading edge of the plate.

$$Re_x = \frac{U_\infty x}{\nu} \tag{2.13}$$

In general, the higher the Reynolds number, the thicker the boundary layer. As show in Fig. 2.1, the critical Reynolds number for flow over a flat place is equal to 10^5, and represents where the flow goes from laminar (a) to transitional (b). The flow is considered

to be fully turbulent (c) above 3×10^6 which corresponds to the transitional Reynolds number. One of the factors that may affect flow transitions is surface roughness which can induce turbulent flow earlier than at the critical Reynolds number. Flow unsteadiness, disturbances, vibration, acoustic noise and curvature in the wall of the body are also shown to affect the boundary layer. Due to these factors, in real life applications, the engineering critical Reynolds number is generally used. The engineering critical Reynolds number is approximately 5×10^5 and the transitional stage (b), between laminar to turbulent is generally ignored (Cengel & Cimbala, 2010).

The simplest estimation or application of the boundary layer theory is that of laminar flow over an infinite flat plate, with length x and bulk flow velocity U_∞. In that case, the two dimensional incompressible Navier-Stokes equations are simplified to obtain the boundary layer conditions. (Schlichting & Gersten, 2000). Equations (2.14), (2.15) and (2.16) are the 2-D continuity equation and Navier-Stokes equations, respectively:

$$\frac{\partial u}{\partial x} + \frac{\partial v}{\partial y} = 0 \tag{2.14}$$

$$\left(u\frac{\partial u}{\partial x} + v\frac{\partial u}{\partial y}\right) = -\frac{1}{\rho}\frac{\partial P}{\partial x} + \nu\left(\frac{\partial^2 u}{\partial x^2} + \frac{\partial^2 u}{\partial y^2}\right) \tag{2.15}$$

$$\left(u\frac{\partial v}{\partial x} + v\frac{\partial v}{\partial y}\right) = -\frac{1}{\rho}\frac{\partial P}{\partial y} + \mu\left(\frac{\partial^2 v}{\partial x^2} + \frac{\partial^2 v}{\partial y^2}\right) \tag{2.16}$$

The equations can be non-dimensionalized and simplified to Eqs. (2.17) and (2.18) as shown in any undergraduate level Fluid Mechanics' textbook. Note that the y-momentum analysis shows that the pressure difference across the boundary layer remains nearly constant compared to that in the x-direction. Therefore, due to the simplification of the y-momentum equation and the differential pressure term being negligibly small, the analysis leaves only the continuity and the x-momentum equation.

$$\frac{\partial u}{\partial x} + \frac{\partial v}{\partial y} = 0 \tag{2.17}$$

$$u\frac{\partial u}{\partial x} + v\frac{\partial u}{\partial y} = -\frac{1}{\rho}\frac{dP}{dx} + \nu\frac{\partial^2 u}{\partial y^2} \tag{2.18}$$

This system of equations is solved through a similarity solution, ultimately leading to Eq. (2.19). Other less accurate solutions can be used to characterize the boundary layer, including the displacement and momentum thickness methods. Equations (2.19) and

(2.13), the laminar boundary layer thickness relationship and Reynolds number for a flat plate, show that the thickness grows as the square root of the distance along the plate, assuming the free-stream velocity is constant (Cengel & Cimbala, 2010).

$$\frac{\delta}{x} = \frac{4.91}{\sqrt{Re_x}} \tag{2.19}$$

The shear stress and local friction coefficient, for laminar flow over a flat plate, areshown in Eqs. (2.20) and (2.21) respectively. The shear stress decays following $x^{-1/2}$, as the slope of the velocity $\frac{du}{dy}$, at the wall decreases downstream.

$$\tau_w = 0.33 \frac{\rho U_\infty^2}{\sqrt{Re_x}} \tag{2.20}$$

$$C_{f,x} = \frac{\tau_w}{0.5\rho U_\infty} = \frac{0.664}{\sqrt{Re_x}} \tag{2.21}$$

There are more interactions to consider in the fluid when the flow becomes turbulent, this complicates the solution. Prandlt's Mixing-Length Theory could be used to describe the boundary layer mathematically (Cengel & Cimbala, 2010). The solution for turbulent flow is not shown here, however the boundary layer thickness is given in Eq. (2.22):

$$\frac{\delta}{x} \cong \frac{0.16}{(Re_x)^{\frac{1}{7}}} \tag{2.22}$$

2.3 Rotating Flow Boundary Layer

A Tesla pump uses disks, therefore the boundary layer theory for a spinning disk is more relevant. The boundary layer theory related to the rotation of a disk, for one side of a non-shrouded single spinning disk, is presented here. The process is relatively similar to that for a flat plate, except that there are different boundary conditions and cylindrical polar coordinates apply. Since the laminar flow derivation is simple compared to that of the turbulent solution, only the laminar deviation is shown here along with how the boundary layer thickness is obtained. A brief description of the boundary layer boundary conditions and the process of obtaining the governing equations are shown in section 2.3.1. This is followed by section 2.3.2 with the derivation of the boundary layer thickness for laminar

flow. The critical Reynolds number and turbulent boundary layer thickness is also shown in section 2.3.2.

2.3.1 Rotating Flow Boundary Layer Derivation

The following observations must be considered when looking at the derivation of the governing equations for the flow caused by a rotating disk. The flow regime is controlled by the magnitude of inertia and viscous effects, which is defined in Eq. (2.23) using the local rotational Reynolds number. Therefore, the flow regime is dependent on the angular velocity (ω) of the disk and the disk radius (b) (Childs, 2011).

$$Re_\theta = \frac{\rho \omega b^2}{\mu} \tag{2.23}$$
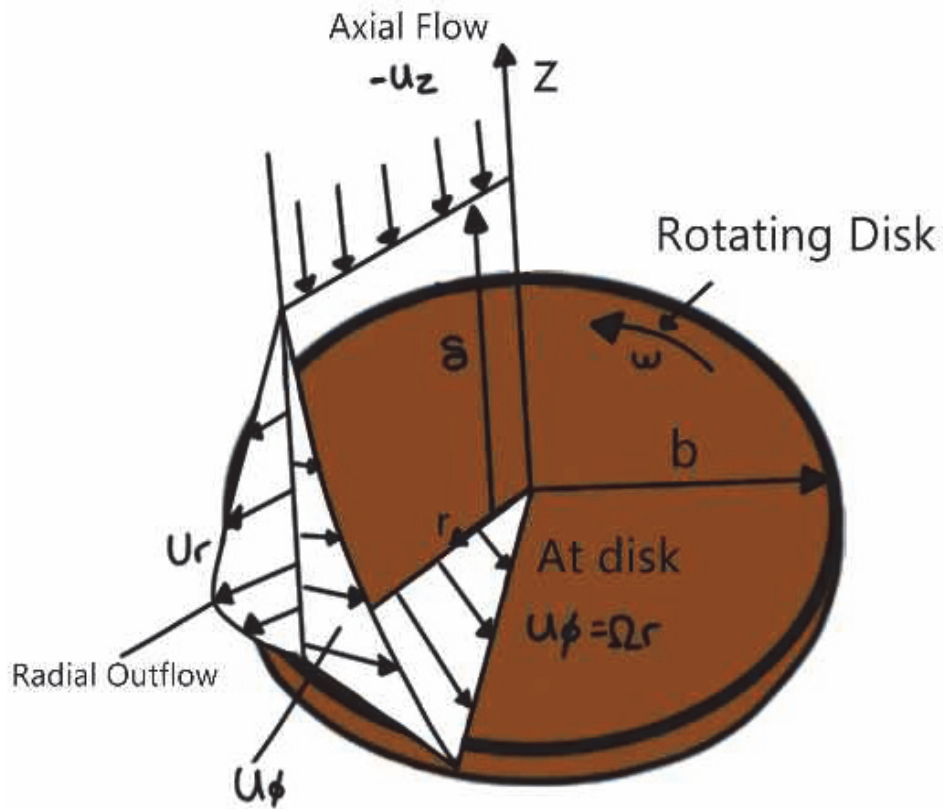
Figure 2.2. Rotating flow due to a spinning disk geometry and flow.

In order to solve this problem, cylindrical polar coordinates are used and the necessary assumptions and boundary conditions required are determined. Figure 2.3 shows the geometry and the velocity profiles above the spinning disk in the various directions. For laminar flow due to a rotating disk the following is assumed (Childs, 2011):

- Steady state flow;

- Axial symmetry;

- Non-slip condition over the disk.

- The tangential velocity (u_ϕ) equals the product of the angular velocity (ω) and the local radius (r), and is considered zero outside the boundary layer, or "free stream".

- The axial flow or velocity (u_z) is considered negative due to the rotation of the disk; it is pulling the fluid in, towards the center of the disk, and should be considered zero at the surface.

- Far from the disk $(z \rightarrow \infty)$: $u_r = 0$ and $u_\phi = 0$

- The value of the axial velocity (u_z), at $z \rightarrow \infty$, is not specified above and should have a (non-zero) negative value to represent the disc pumping effect.

Again, the continuity and Navier–Stokes equations need to be solved for the boundary layer, the simplified equations are presented in Eqs. (2.24) to (2.27). They have been simplified through the following considerations: for a steady flow and axial symmetry conditions, the $\frac{\partial}{\partial \phi}$ and $\frac{\partial}{\partial t}$ terms are automatically equal to zero; and the $\frac{u_r}{r^2}$ and $\frac{u_\phi}{r^2}$ terms generally found in the Navier-Stokes equation can also be ignored since their relative magnitude is smaller than the other viscous forces.

$$\frac{\partial u_r}{\partial r} + \frac{u_r}{r} + \frac{\partial u_z}{\partial z} = 0 \tag{2.24}$$

$$\rho \left(u_r \frac{\partial u_r}{\partial r} + u_z \frac{\partial u_r}{\partial z} - \frac{u_\phi^2}{r} \right) =$$

$$-\frac{\partial P}{\partial r} + \mu \left(\frac{\partial^2 u_r}{\partial r^2} + \frac{1}{r}\frac{\partial u_r}{\partial r} + \frac{\partial^2 u_r}{\partial z^2} \right) \tag{2.25}$$

$$\rho \left(u_r \frac{\partial u_\phi}{\partial r} + \frac{u_r u_\phi}{r} + u_z \frac{\partial u_\phi}{\partial z} \right) =$$

25

$$\mu \left(\frac{\partial^2 u_\phi}{\partial r^2} + \frac{1}{r} \frac{\partial u_\phi}{\partial r} + \frac{\partial^2 u_\phi}{\partial z^2} \right) \tag{2.26}$$

$$\rho \left(u_r \frac{\partial u_z}{\partial r} + u_z \frac{\partial u_z}{\partial z} \right) =$$

$$-\frac{\partial P}{\partial z} + \mu \left(\frac{\partial^2 u_z}{\partial r^2} + \frac{1}{r} \frac{\partial u_z}{\partial r} + \frac{\partial^2 u_z}{\partial z^2} \right) \tag{2.27}$$

The above equations are converted into dimensionless relationships by dividing through using the transformations shown in Eqs. (2.28) - (2.32). The dimensionless variables shown in this section have the subscript * to help identify them.

$$z_* = z \sqrt{\frac{\omega}{\nu}} \tag{2.28}$$

$$u_{r_*}(z_*) = \frac{u_r}{r\omega} \tag{2.29}$$

$$u_{\phi_*}(z_*) = \frac{u_\phi}{r\omega} \tag{2.30}$$

$$u_{z_*}(z_*) = \frac{u_z}{\sqrt{\nu\omega}} \tag{2.31}$$

$$P_*(z_*) = -\frac{P}{\mu\omega} = -\frac{P}{\rho\nu\omega} \tag{2.32}$$

The strategy is to reduce the Navier-Stokes equation to a set of ordinary differential equations that can be solved easily. By subbing in Eqs. (2.28) - (2.32), into Eqs. (2.24) - (2.27), they will be transformed into a set of dimensionless ordinary differential equations; after re-arranging, Eqs. (2.33) to (2.36) are obtained:

$$\frac{du_{z*}}{dz_*} + 2u_{r*} = 0 \tag{2.33}$$

$$\frac{d^2 u_{r*}}{dz_*^2} - u_{z*} \frac{du_{r*}}{dz_*} - u_{r*}^2 + u_{\phi*}^2 = 0 \tag{2.34}$$

$$\frac{du_{\phi*}}{dz_*^2} - u_{z*} \frac{du_{\phi*}}{dz_*} - 2u_{r*}u_{\phi*} = 0 \tag{2.35}$$

$$\frac{d^2 u_{z*}}{dz_*^2} - u_{z*} \frac{du_{z*}}{dz_*} - \frac{dP_*}{dz_*} = 0 \tag{2.36}$$

The corresponding, now transformed, boundary conditions are as follows:

$$u_{r*} = 0, \ \ u_{\phi*} = 1, \ \ u_{z*} = 0, \ \ P_* = 0 \text{ at } z_* = 0$$

$$u_{r*} = 0, \ \ u_{\phi*} = 0 \text{ as } z_* \to \infty$$

The differential equations can now be solved using numerical techniques. Since they are dimensionless, the solution will not be dependent on values of rotational speed and fluid properties, such as density and viscosity. The solution is tabulated in '*Rotating Flow'*, by Childs, on page 88 (Childs, 2011).

Figure 2.3 shows the velocity profiles of the solution to the differential equations presented in Eqs. (2.33) to (2.36). It has been observed that the fluid in contact with the disk surface rotates at the same angular velocity as the disk. This is in accordance with the no-slip condition. The fluid inside the boundary layer just above the surface will also begin to rotate, however cannot maintain the same centripetal acceleration as the disk surface and therefore acquires an outward radial component, pushing it out radially. Essentially, due to conservation of mass, there is zero momentum (non-moving) fluid being drawn in axially, being given momentum in the boundary layer and then pumped radially outward. This type of boundary layer is commonly referred to as an Ekman layer. It is caused by the centrifugal forces from the shear between the rotating disk and the fluid which creates the radial flow in the boundary layer. This radial outflow from the rotation of the disk is called 'pumped flow' since it is forced due to the rotating disk and the viscous or frictional forces on its surface (Childs, 2011).
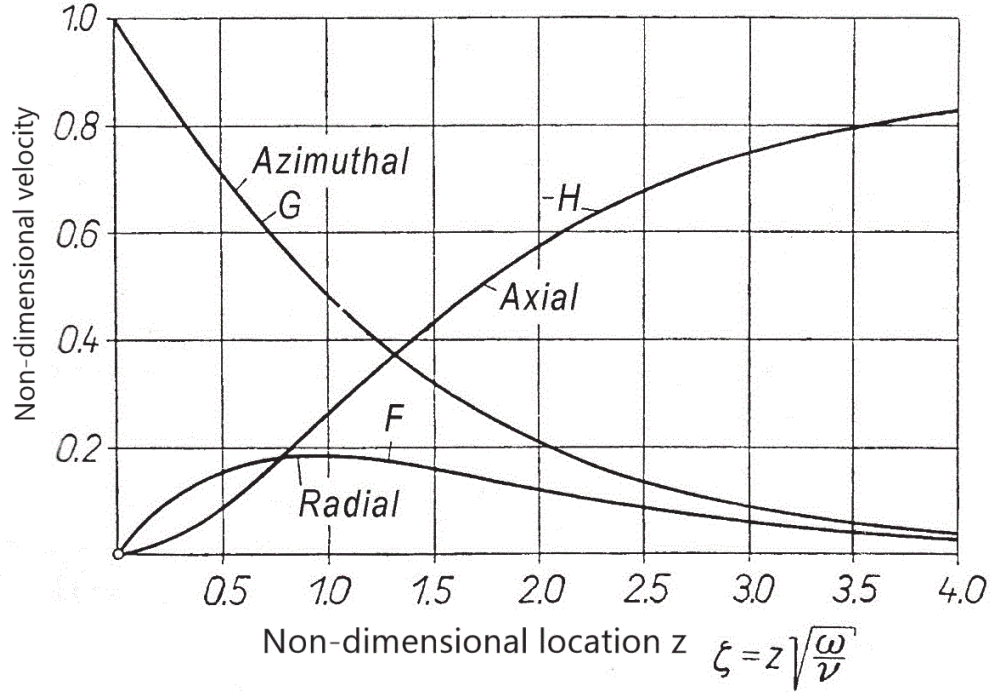
Figure 2.3.Dimensionless laminar flow velocity profiles for a rotating disk (Schlichting & Gersten, 2000).

2.3.2 Boundary Layer Thickness

The definition of a boundary layer for a rotating disk in an infinite fluid is the distance axially away from the rotating disk where the tangential velocity is 1% of the disk speed. Using this definition of a boundary layer, 1% of the tangential velocity, Eq. (2.37) is obtained.

$$u_\phi = 0.01\omega r \tag{2.37}$$

Substituting Eq. (2.37) into the non-dimensional Eq. (2.30) provides Eq. (2.38),

$$u_{\phi*} = \frac{u_\phi}{\omega r} = 0.01 \tag{2.38}$$

The tabulated solution values (Childs, 2011) provide a value for z_* of approximately 5.5. This can now be added into Eq. (2.28) of the non-dimensional boundary conditions to get the boundary layer thickness, Eq. (2.39) (Childs, 2011).

28

$$\delta \approx 5.5 \sqrt{\frac{\nu}{\omega}} \qquad (2.39)$$

This boundary layer thickness relies on the rotational speed of the disk, unlike for a flat plate. Therefore, the larger the rotational speed, the thinner the boundary layer. Also, away from the rotational axis, this boundary layer thickness is independent of position. Therefore, boundary layers in rotating flows have been found to reach a maximum thickness, which is proportional to $\sqrt{\nu/\omega}$, while the stationary boundary layer (on a flat plate for example) will continue growing in a manner proportional to $\sqrt{\frac{\nu x}{u_x}}$.

As previously mentioned, the critical Reynolds number is used to determine the flow regime, laminar or turbulent. The critical rotational Reynolds number for rotating flow has been determined by comparing theoretical analysis and experimental results. Experimentally, the critical rotational Reynolds number depends on the roughness of the disk, where a rougher disk leads to a smaller critical value. The range of experimental values for critical rotational Reynolds number and fully turbulent Reynolds number are compared to the accepted theoretical value for critical Reynolds number in Table 2.1.

Table 2.1. Values of critical Reynolds number for a rotating disk (Childs, 2011).

Critical Reynolds Number (initial breakdown)	2×10^5
Experimental observation Fully Turbulent	$2.12 \times 10^5 \le Re \le 2.7 \times 10^5$
Experimental observation Critical Reynolds number	$1.78 \times 10^5 \le Re \le 2.12 \times 10^5$

Table 2.2, presents the boundary layer thickness and mass flow rate entrained by the boundary layer on only one side of the disk, for laminar and turbulent flow. The mass flow rate entrained by the boundary layer of the disk can prove useful in Tesla pump analysis.

Table 2.2. Comparing rotating laminar and turbulent flow equations.

Laminar			Turbulent*		
Boundary Layer Thickness δ	$\delta = 5.5\sqrt{\dfrac{\upsilon}{\omega}}$	(2.40)	$\delta/r = 0.5261\left(\dfrac{\mu}{\rho\omega r^2}\right)^{\frac{1}{5}}$		(2.41)
Flow entrained by Boundary Layer	$\dot{m} = 2.779\rho b^2\sqrt{\upsilon\omega}$	(2.42)	$\dot{m} = 0.2186\rho\omega b^3 Re_\phi^{-\left(\frac{1}{5}\right)}$		(2.43)

*for 1/7$^{\text{th}}$ power law

Figure 2.4 shows the difference between turbulent and laminar boundary layers in a rotating flow over one disk. The laminar boundary layer thickness is constant except where the fluid is drawn in around the center (not shown on the figure), while the turbulent boundary layer thickness increases outwards exponentially. Similar to the turbulent analysis done for a flat plate, a power law velocity profile in the turbulent region was assumed to obtain Eqs. (2.41) and (2.43) (Childs, 2011).
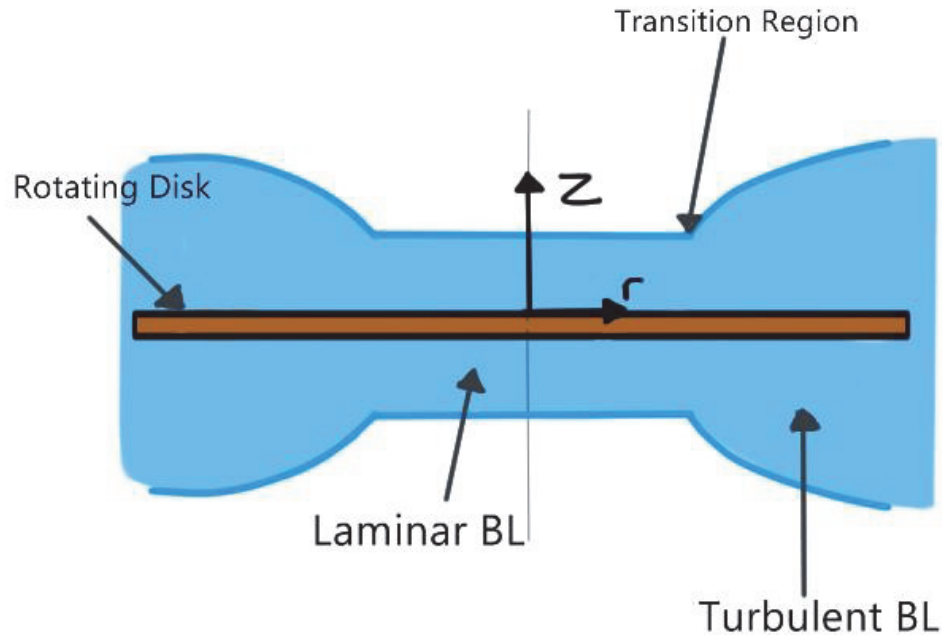
Figure 2.4. Laminar to Turbulent Boundary Layer Transitions on a rotating disk.

2.4 Fully Developed Flow

Due to the small gap spacing found in a Tesla pump and the resulting boundary layer formation for a flat rotating disk, it is possible that the boundary layers formed on two adjacent disk surfaces will eventually collide and merge resulting in a fully developed flow similar to that seen between two flat parallel plates. It is important to note that in a Tesla pump, the disks are ring shaped and therefore the boundary layer will start to form at the inside edge of the disk and grow outward according the flow regime. Figure 2.5 shows a schematic of the flow between two rotating ring shaped disks (*i.e.* the disks in a Tesla pump) where their mutual spacing provided ample room for two separate boundary layers to form. The viscous forces felt by the fluid are the strongest within the boundary layers; the fluid in-between the boundary layers being affected to a lesser degree by the spinning disks. For a smaller gap spacing which would not allow for two individual boundary layers to form, the boundary layers are expected to combine. This is shown in Fig. 2.6, where fully developed flow is therefore occurring. In fully developed flow, the viscous forces between the wall and the fluid are felt much more strongly throughout the gap. It is expected that this type of flow would be more effective compare to the one shown in Fig. 2.5, where only a portion of the fluid feels the viscous effects from the wall.
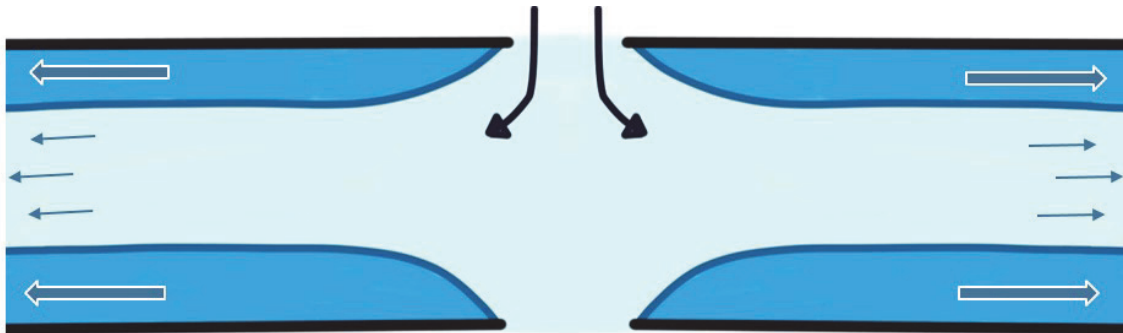
Figure 2.5. Case for two separate boundary layers between the rotating disks.
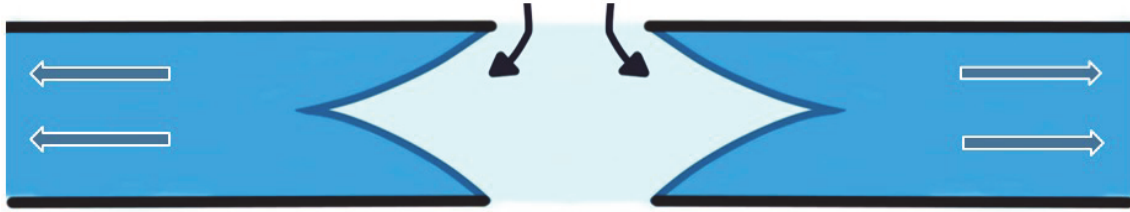
Figure 2.6. Case for fully developed flow between two rotating disks.

The Reynolds number for internal flow is shown in Eq. (2.44). The average velocity (V_{avg}) of the fluid depends on the radius (b) and rotational speed (ω), and the characteristic length (D) would be equivalent to the disk gap spacing (d). The critical value of the Reynolds number for internal flow is 2,300.

$$\text{Re}_{\text{int}} = \frac{\rho V_{avg} D}{\mu} = \frac{\rho b \omega d}{\mu} \qquad (2.44)$$

Chapter 3 Methodology

In this chapter, the design of the prototype pump is presented along with how the testing was performed. The prototype pump is presented in section 3.1 and includes detail regarding the disk pack. The testing loop design, specifics' regarding the testing equipment and setup is presented in section 3.2. Section, 3.3, explains the experimental data acquisition process. The final section, 3.4, presents the uncertainty and error propagation analysis and sources of error.

3.1 Prototype Pump Design

3.1.1 Casing Design

The prototype pump is shown in Fig 3.1, with the inlet through the center in the casing shown on the left, and the outlet on the side seen at the bottom of the picture. The casing is made up of three parts; for the pump side, a stainless steel and a Delrin plastic half, and for the motor side a stainless steel housing. The motor is housed in the cylindrical section on the right in Fig 3.1. The disk pack is driven by the motor through the use of a magnetic coupling, where there is a magnet on either side of the Delrin casing. The thickness of the casing between the magnets is 1.59 mm ($1/16^{th}$ of an inch). Originally, the casing on the pump side was completely made of stainless steel. However, due to eddy current buildup in the metal components, pump performance was severely reduced, and therefore a plastic (non-conductive) portion of the pump casing was implemented. The total size of the prototype sits in approximately a 15 cm by 6.1 cm area.
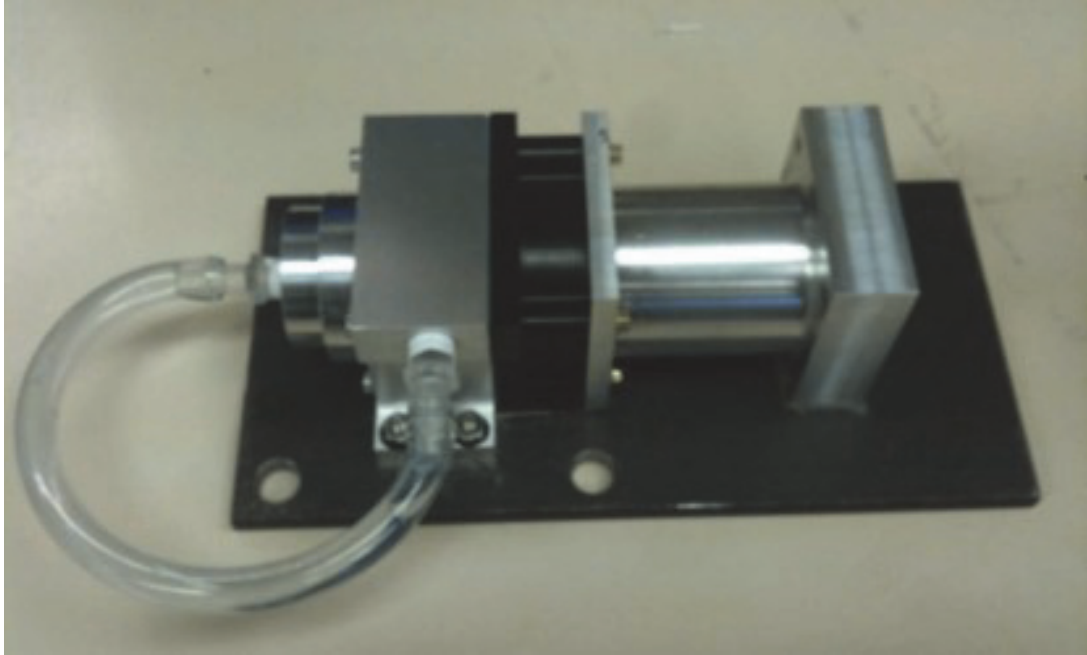
Figure 3.1. Picture of the prototype pump with original casing materials.

The inside of the casing was machined following a log spiral, as shown in Fig. 3.2. A log spiral is a common shape used in pump housings, and is found in nature in animals such as the nautilus shell. This should provide an effective path for the fluid leaving the pump, since it is similar to that of a centrifugal pump. The maximum clearance from the disk pack is approximately 10 mm, with the minimum clearance being approximately 1.6 mm.
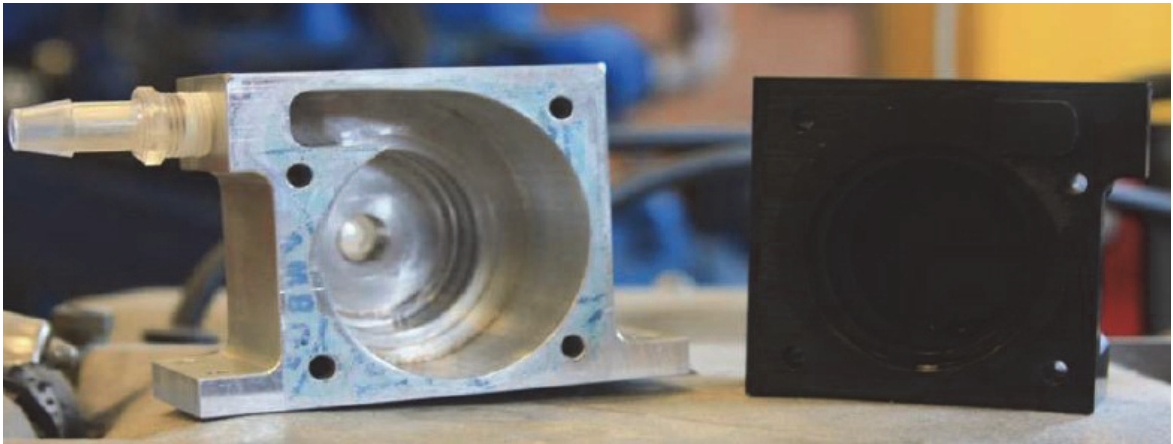
Figure 3.2. Picture of the inside of the old casing.

During this research project, the casing was changed from a stainless steel/Delrin plastic to transparent acrylic, as shown in Fig 3.3. Since, there were suspicions that air was becoming trapped in sections of the casing, the casing was manufactured out of transparent material and replaced. With a transparent casing, any air entrapment could be observed and corrected before testing began. The casing measures approximately 7.65 cm (long) by 6.1 cm (wide) by 51 cm (tall), and is held together with 4 bolts that go through the pump casing and part of the motor enclosure. These bolts are lined up using a circular locating feature that prevents the casing from being assembled incorrectly; this is shown in Fig. 3.4.
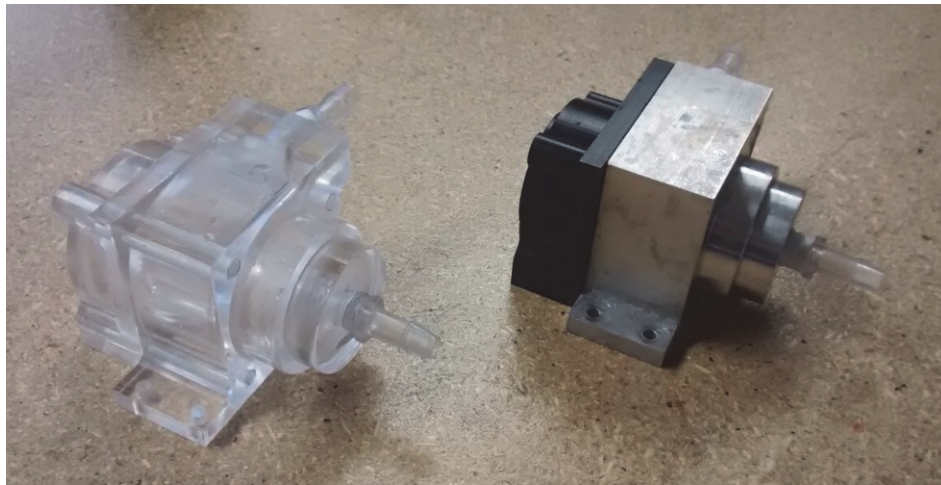
Figure 3.3. New (left) and old (right) casing comparison.
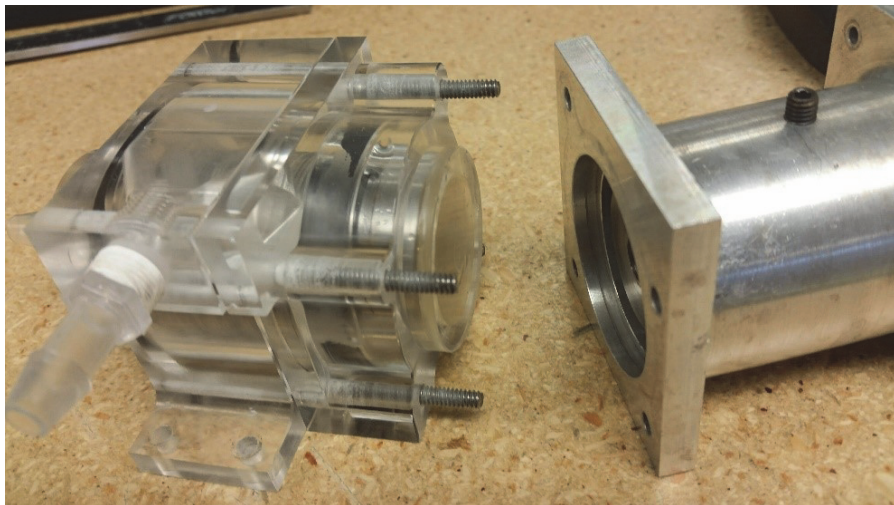
Figure 3.4 Post bolts with circular locating feature.

3.1.2 Disk pack

The disk pack consists of two supports which allow for bearings to be attached on either end and keep all the disks together. The magnet is attached by a bolt through one of the disk pack supports, which can be seen in Fig 3.5. Figure 3.6 shows an exploded view of the disk pack. The disks are attached using three bolts that go through two supports on each end and hold the disks in the middle. These bolts are spaced 120 degrees apart. The bolts are specifically made for this application, as well as the disks and the disk pack supports. The disk pack (section of disks not including supports) averages around 2 cm in length, varying slightly depending on the amount and spacing of disks. The diameter of the disks and disk pack supports are 3.5 cm, and the thickness of each disk is approximately 0.79 mm, or 31.5 thou (where thou is a thousandths of an inch). Figure 3.7 shows the 5 thou thick spacers used within the pump.
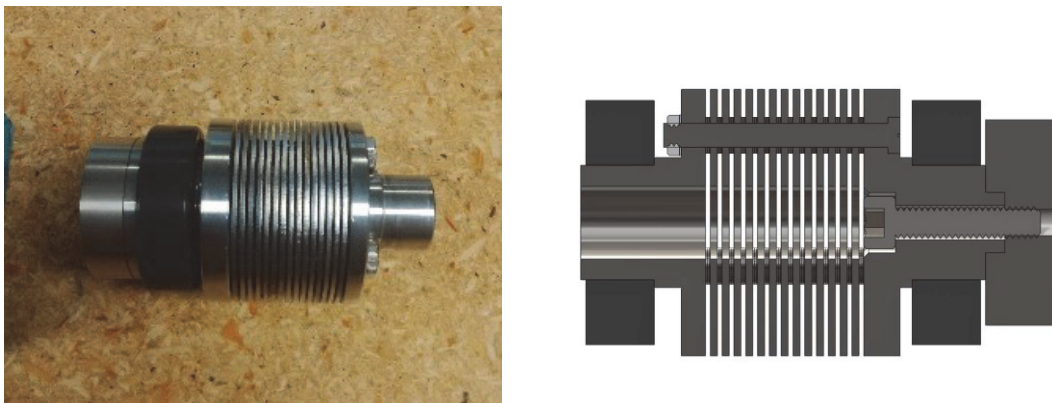
Figure 3.5. Disk pack with bearing and magnetic coupling attached (left), and sliced view CAD of the disk pack showing the bolt attaching the magnet (right).

Figure 3.6. Disk pack exploded view.

Figure 3.7. Spacers, 5 thou thick.

For testing, extra disk pack components were manufactured and disk packs assembled. This lessened the amount of time needed for disassembly and assembly of the pump, specifically when changing the spacing of the disks. Since, the spacers are specially made thin washers, it was time consuming to build the disk packs from scratch. There are approximately 50 to 120 spacers in each disk pack, depending on the spacing. Table 3.1 provides the number of disks per disk pack and Figs. (3.8) to (3.10) show the built disk packs for various spacings. Fig 3.9 shows the 15 thou disk pack with a bearing and the magnet attached.

Figure 3.8. Twenty thou disk pack spacing.

Figure 3.9. Fifteen thou disk pack spacing, with magnet and bearing.
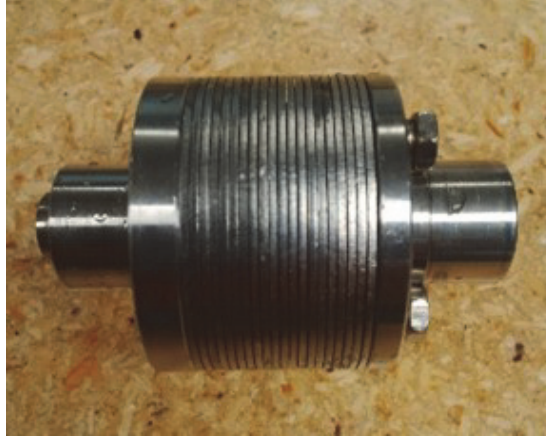
Figure 3.10. Five thou disk pack spacing.

Table 3.1. Number of Disks for each spacing.

Spacing	# of Disks
1 thou	27
3 thou	26
5 thou	20
10 thou	18
15 thou	16
20 thou	15
25 thou	15

The spacers between the disks obstruct the fluid flow through between the disks. Two different extreme assumptions can be made regarding the blockage area, as shown in Fig. 3.11. The first one would be to assume that the fluid's path is straight along the radius of the disk. In this case, the blockage ratio is calculated using Eq. (3.1), where $D_{spacer} = 0.5$ cm is the diameter of the spacers, and $b_{spacer} = 1.14$ cm is the radius at which the spacers are found. The second assumption would be for the fluid to follow a long spiral pattern before exiting the disk gap. The blockage ratio is given Eq. (3.2) where b ($= 1.75$ cm) is the total radius of the disk. For the pump used in the work, $Br_1 = 0.0696$ or nearly 7%, and $Br_2 = 0.2857$ or approximately 28.5%.

$$Br_1 = \frac{3D_{spacer}}{2\pi b_{spacer}} \tag{3.1}$$

$$Br_2 = \frac{D_{spacer}}{b} \tag{3.2}$$
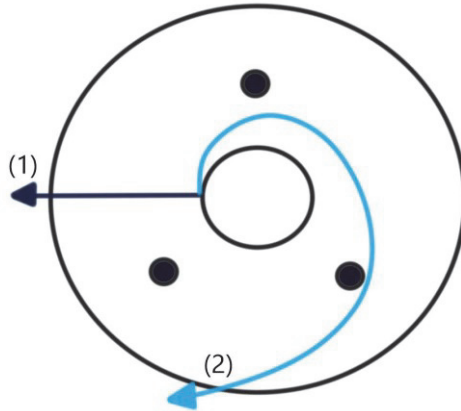
Figure 3.11. Fluid path along rotating disk.

3.1.3 Motor

The electric motor is a Maxon EC-32 15 W brushless motor with integrated sensors, and is shown in Fig. 3.12. The specifications for the Maxon motor are included in Appendix A. The motor has a range of 200 to 7000 rpm, unloaded. The speed of the motor is controlled though an analog signal between 0-10 V. The maximum efficiency of the motor is listed to be 64%. The motor casing is a cylindrical tube which houses the motor, it is approximately 7.3 cm (long) by 5.3 cm (wide) by 5.1 cm (tall). The motor casing was altered due to issues found during preliminary testing. One alteration was due to the motor and drive shaft mechanism turning inside the case. This was corrected with a set screw, through the top of the casing, which can be seen in Fig 3.5. It was later discovered that the motor could be shorted out if the wires from the motor touched the casing, either during assembly or disassembly. Therefore, part of the area of the case where the wires sit was removed and more insulation to the wires was added.

Figure 3.12. Maxon motor on its coupling.

3.2 Testing Loop

3.2.1 Equipment Selection

Data from the undergraduate design group was used as a reference point for equipment selection. The most significant problem was overcoming the low head produced by the pump. Conventional paddle style rotameters would not work since they had been found to produce too much head losses within the system. Another consideration in equipment section was the equipment's use with a fluid more viscous than water and under vibration.

The solution for the flow meter was to select an electromagnetic flow meter since there are no in-flow moving parts, and very little head losses are generated. The maximum range of the flow rate is 6.06 L/min (1.6 GPM). An electromagnetic flow meter works by measuring the voltage through a conductive fluid, as it moves perpendicular though a magnetic field. It relates the measured voltage to the velocity of the fluid. The flowmeter chosen was an in line 'Magmeter' FMG-91 from OMEGA, and is shown in Fig. 3.13. The specifications for the FMG-91 flow meter are shown in Appendix A. There is a minimum liquid

conductivity necessary for the operation of this type of flow meter, which is 5 microSiemens (µS) per cm. This is not an issue for water, since domestic tap water has 500-800 µS/cm; distilled water is 0.5 µS/cm. Therefore, tap water was used for these experiments (Heyda, 2006).
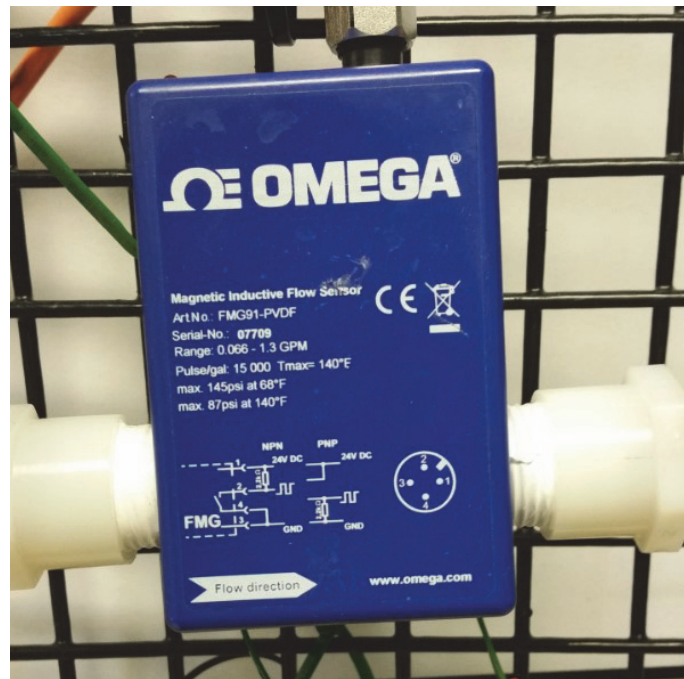
Figure 3.13. Flow meter, FMG-91 from OMEGA.

The pressures measured during preliminary testing by the undergraduate design team provided a rough estimate of the maximum pressure difference across the pump of approximately 2 psi (13.8 kPa). The differential pressure sensor is shown in Fig. 3.14 and is a PX-26 from OMEGA. A differential pressure sensor, in the range of 0-5 psi was chosen for the water tests and the propylene glycol-water mixture used a 0-15 psi range. The pressure sensor specifications are shown in Appendix A. Using a differential pressure sensor simplified the testing loop and was an inexpensive and effective method of measuring the pressure difference across the pump.

Figure 3.14. Differential pressure sensor, PX-26 meter unwired (left), and the pressure sensor in the set up (right).

Figure 3.15, shows a schematic of the testing loop design, with the in-line flow meter, differential pressure sensor, valve, reservoir and pump. The piping is flexible plastic quarter inch tubing, which is used for everything except for a portion for the pressure sensor. The pressure sensor requires one eighth diameter tubing, and rapid prototyped T-type connectors to connect the pressure sensor to the quarter inch tubing of the setup were used. The valve is a needle type with 10 turns, for accurate flow control. The reservoir is a 1 Litre clear plastic container.

After preliminary testing, several things were observed. The most significant being that the flowmeter placement did affect the readings and the pump did not perform well when the suction end had to overcome a large height difference from the reservoir. The solution was to build a stand to attach the equipment and tubing to reduce variation in the results. The completed stand is shown in Fig. 3.16.
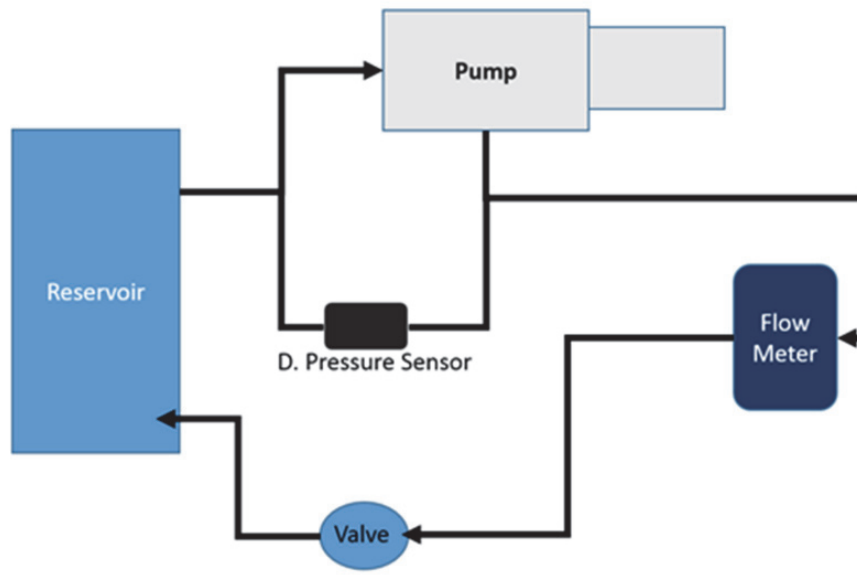
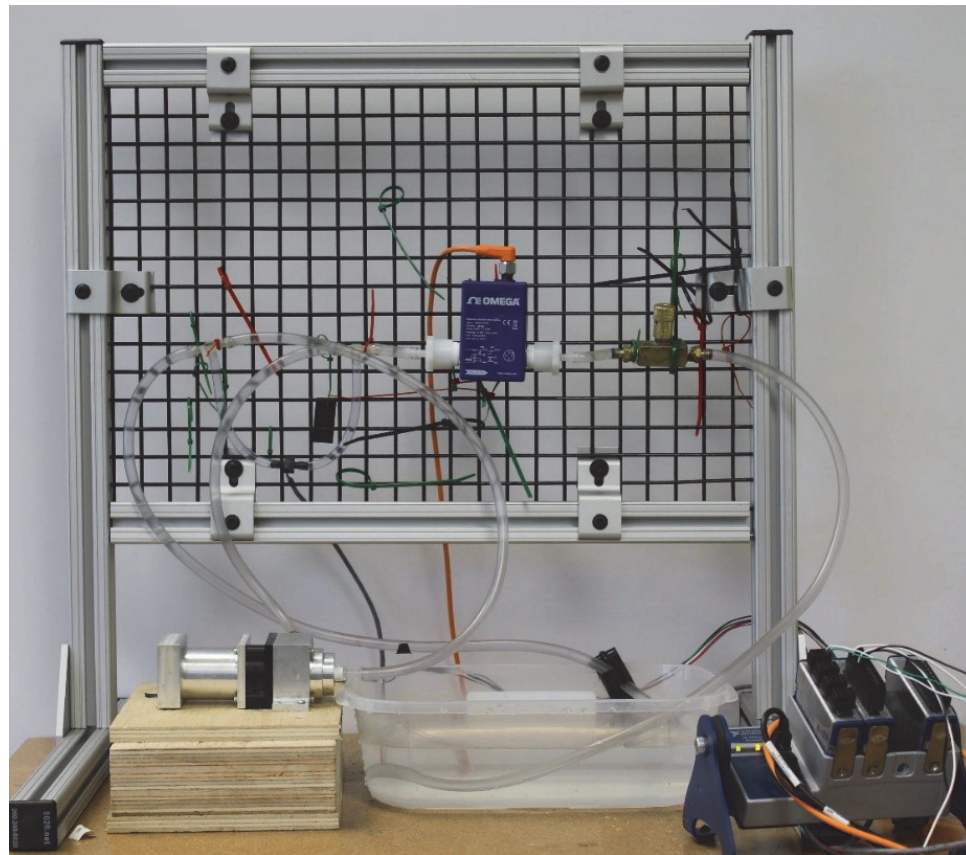**Figure 3.15. Schematic of the testing loop.**

Figure 3.16. Testing loop with stand setup.

44

3.2.2 Electrical Set Up

The electrical and circuitry components were contained in a waterproof box with the motor speed control dial on top. There were minor issues with the circuitry that caused some variation in the readings, such as power supplies not keeping their setting or wires becoming disconnected. These minor issues were resolved by having a small circuit board fabricated. The motor uses two power sources, one for the signal speed input and the other for powering the motor. The power supply for the motor is shown in Fig. 3.17 and the signal speed input was drawn from the flow meter's power supply. Since, the pressure sensor needs a constant known excitation voltage, it was also drawn from the flow meter's power supply. The voltage for the pressure sensor was provided at 8.1 V, and calibrated according to the manufacture's specifications. The variable resistor along with the box that contains the circuity for the setup is shown in Fig. 3.18. A variable resistor with a 10 turn allowance was used for the motor speed control, which allowed for a great deal of control, in the range of ± 5 RPM. (The rough variance in the reading was at most 5 RPM's from observation) It is important to note that the rpm sensor in the motor of the pump worked sporadically and therefore was not used. Since the rotational speed of the motor was only needed when setting up a run, an optical Tachometer was used.

Figure 3.17. Power supply used for motor control, and multimeters.
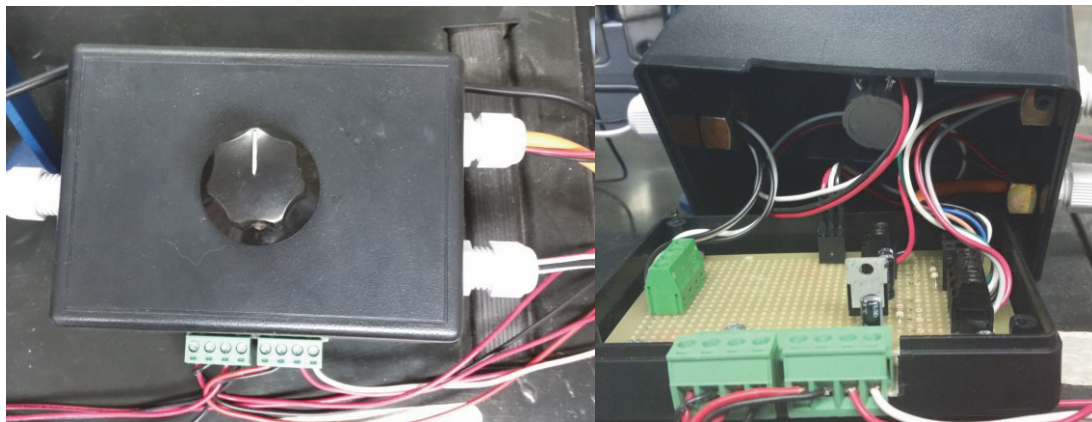
Figure 3.18. Circuit control box (left) with motor speed control dial on top, and the inside of the box (right).

3.2.3 Vibration Testing Set Up

To test the effects of vibration on Tesla pump performance, a Vibration Exciter System (Type 4801) from Brüel & Kjær was used to supply the necessary vibrations. This testing was to determine if cavitation could be induced through vibrations. A picture of the Exciter System's body with the prototype pump is shown in Fig 3.19. An Exciter Control (Type 1047) and Power Amplifier (Type 2707) are used to control the exciter system.

Figure 3.19. Prototype pump on the Vibration Exciter System *i.e.* shaker table.

3.2.4 Data Acquisition

All data was recorded using a National Instruments compact DAQ, 4 slot chassis system, with 2 modules, which are shown in Fig. 3.20. The two modules used are the NI 9435, for the frequency of pulses from the flow meter, and NI 9219 for the analog input from the pressure sensor. The two modules on the far side of the DAQ system shown in Fig. 3.20, are not used. This was connected and read into LabVIEW, which then recorded and saved the data. The block diagram used in LabVIEW is presented in Appendix B

Figure 3.20. DAQ chassis with corresponding modules.

LabVIEW read a voltage signal from the pressure sensor which needed to be converted to provide the pressure in psi. The conversion factor for the differential pressure sensors, was determined by taking the manufacturer's given calibration and converting it to psi/mV as shown in Appendix B. For the 5 psi range, the conversion factor obtained is 123.457 psi/V, for the 15 psi range, 185.185 psi/V.

The flow meter's conversion factor was obtained experimentally using the average frequency output from the flow meter and volume of water, over a minute. The flow meter produces a certain number of pulses per gallon, which for this particular model of flow meter (FMG91-PVDF) was 15000 pulse/gallon.

48

3.3 Experimental Methodology

For the water testing, 3, 5, 10, 15, 20 and 25 thou disk spacing was tested for 4000, 3600, 3000 and 2500 RPM motor speeds. A propylene glycol (PG)-water mixture of 40/60 weight%, was tested for the 5, 10, 15 and 20 thou spacings for 3600, 3000 and 2500 RPM motor speeds. The pump could not consistently reach the 4000 RPM speed for the PG-water mixture, therefore the 4000 RPM motor speed was not tested. The vibration testing was performed for the 5 to 20 thou spacings for 3600 RPM, at frequencies of 500 Hz and 2000 Hz. The procedures for each method of testing are similar except where mentioned otherwise.

For experimental testing, the pump is put together with the disk pack, taking care that the seals and all fasteners are secure. The pump was placed on a wooden block, secured and connected to the inlet and outlet tubing. The power supplies, computer and multimeter are turned on and set accordingly. To prime the pump, a hand pump was used to carefully fill the tubing and pump with the working fluid, while taking care that the tubing for the pressure sensor did not contain air bubbles. The pump motor was then started, and preferably set to a high rotational speed (4000 or 3600 RPM). The rotational speed would be varied occasionally in an attempt to further encourage air out of the system. This process could take up to 2 hours depending on the gap spacing and working fluid. The removal of air combined with waiting allowed the system to stabilize with regards to the flow rate, since the flow meter is sensitive to air bubbles.

Just before starting a test, the rotational speed of the motor was checked using the tachometer and corrected if needed. For each pump operating point, data was recorded over one minute into LabVIEW, and this same test was repeated three times. The three sets of data for each pump operating point were averaged to obtain the data used for the analysis. While the data was being recorded, the current drawn by the motor from the multimeter was physically recorded over the minute. The discharge valve was used to vary the head and flow rate for each run and was turned in increments of one half a turn until almost fully closed. After the valve was turned, at least one minute was allowed for the system to

stabilize before testing began again. Between each run the rotational speed of the motor was checked and adjusted accordingly.

For the testing done under vibration, to determine if vibration will affect the performance of the pump, a couple of changes needed to be made regarding the set up. A major change was allowing for the pump to be re-located onto the vibration exciter (shaker table). The solution was to have the whole setup, including reservoir, be closer to the level of the shaker table. Otherwise issues due to the pump attempting to overcome the large height difference would significantly impact testing. Therefore, the level of the whole setup was lowered for this section of testing. There was still a slight height difference between the pump and the apparatus. A longer length of tubing connecting the pump to the rest of the apparatus was also necessary. The slight height difference and extra lengths of tubing did end up affecting the flow rate and pump head compared to the non-vibration runs. Therefore, non-vibration runs for each disk pack were completed with the pump mounted on the shaker amp, since the losses due to the height differences and extra length of tubing could not be avoided.

3.4 Sources of Error

Typically, there are the normal contributors to error, equipment and human factors. However, a couple of topics have come up after testing was performed which have been shown to be of importance. These issues were found to be air bubbles becoming trapped within the disk pack and setting of the rotational speed.

Small air bubbles within the working fluid can become trapped within the disk pack, which have been found to greatly reduce efficiency (Hasinger & Kehrt, 1963). Hasinger and Kehrt had to take careful and diligent measures to suction out the air bubbles from between the disks; however this would not have been possible for the experiments done for this thesis due to the design of the prototype pump. The air bubbles would also affect the flow meter measurements, by causing fluctuations in the measurements as they passed through. Before the testing would begin the pump would be primed and allowed to run until air was thought to have been removed from the system, typically 2-3 hours was given for the air to

be removed from the system. Figure 3.22 shows the pump before air was removed, while Fig. 3.23 shows the pump after 2-3 hours of continuous operation to remove air. This was the main reason the clear casing was implemented, to be able to observe when air has been removed from within the casing. It is expected that some air may still be trapped within the disk pack during testing, however is likely to not significantly impact the results.
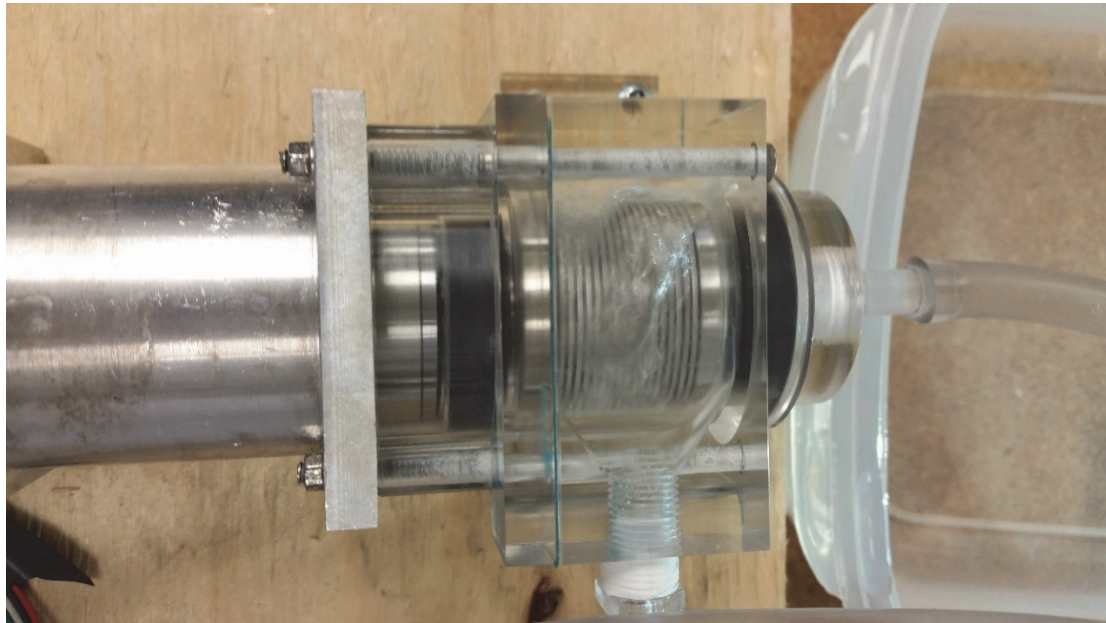
Figure 3.21. Picture of the pump in operation before air was removed.
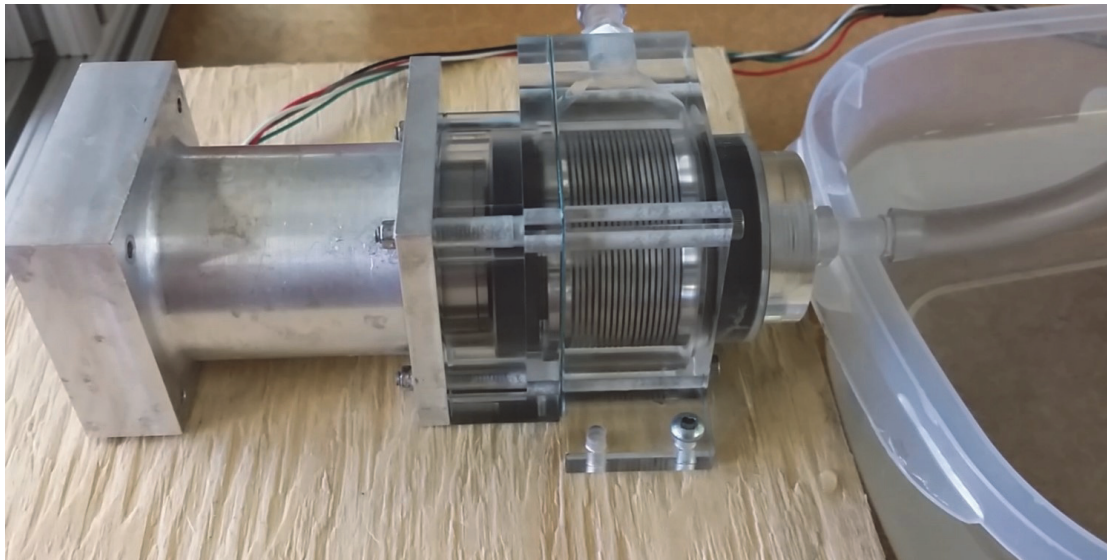
Figure 3.22. Picture of the pump in operation with air removed after waiting for 2-3 hours.

Another source of error would be due to setting the rotational speed, since these value are used for the non-dimensional analysis. An attempt was made to keep the rotational speed constant between runs, however this was not always possible. Either the rotational speed of the motor would slightly change between runs or the rotational speed would be off by up to 10 RPM. Another factor would be that the motor rotational speed was used, not the actual disk pack/rotor speed. This was because the rotational speed of the rotor was difficult to measure due to the design of the prototype, and therefore the disk pack or rotor's rotational speed was assumed to be the same as the motors. It is expected that the rotational speed of the disk pack or rotor is slightly less than the motor's, and would not significantly impact the calculations.

3.4.1 Uncertainty and Error Propagation

The accuracy of the equipment in the setup is shown in Table 3.2, followed by error propagation calculations.

The error propagation from the experimental data is determined using the data from Table 3.2 and Eq. (3.3), for multiplication or division error propagation. The error propagation is then calculated for the motor power, hydraulic power, head, and efficiency; where X is a quantity being calculated that depends on a, b and so forth, which are quantities that have errors which are uncorrelated and random.

$$\frac{\delta X}{|X|} = \sqrt{\left(\frac{\delta a}{a}\right)^2 + \left(\frac{\delta b}{b}\right)^2 \dots + \left(\frac{\delta z}{z}\right)^2} \qquad (3.3)$$

Table 3.2. Accuracy of pump equipment for measurement error.

Equipment	Accuracy	Response time
PX-26-005-DV (pressure sensor)	1% FS = ± 0.05 psi	1 msec
PX-26-015-DV (pressure sensor)	1% FS= $\pm$ 0.15 psi	1 msec
FMG 91 (flow meter)	1% of reading: Max flow range 1.6GPM=6.06 L/min $\rightarrow \pm$ 0.06 L/mim	<100msec
Multimeter (Circuit-Test DMR-1800)	DC Current Accuracy=2% of reading	N/A
Power Supply – EXTECH 382275	Voltage meter ($\pm$ 2% , $+3\ digits$)	N/A
Tachometer (Monarch Pocket Tac Plus 1.4)	Non-contact $\pm$ 0.01 % of reading Approx. $\pm$ 5 RPM from observation during testing	N/A

For any calculations involving the rotational speed, the observed error of ± 5 RPM was used as it was larger then the measurement accuracy of the tachometer. For the calculation of head from Eq. (2.1), the error is solely from the pressure sensor, ± 0.05 psi and $\pm$ 0.15 psi, for the 5 and 15 psi range pressure sensor respectively and is calculated as per Eq. (3.4). While the flow rate measurement is 1% of the value.

$$eps_H = \sqrt{\left(\frac{0.05}{5}\right)^2} = 1\% \text{ of } H \tag{3.4}$$

For the motor power, the current's maximum reading is 2 A, therefore the absolute error is $\pm$ 0.04 A (2% of reading). The voltage was kept constant at 18.8 V, and due to the number of digits of the equipment was accurate to ± 0.05 V (2.6% of reading). Equation (3.5) shows the error propagation.

$$eps_{motor} = \sqrt{\left(\frac{0.04}{2}\right)^2 + \left(\frac{0.05}{18.8}\right)^2} = 2.01\% \text{ of } P_{motor} \tag{3.5}$$

For the hydraulic power, the 5 psi and 15 psi range pressure sensors produce the same result. This is because they both use a 1% full scale accuracy value. However, for the sample calculation, for the 5 psi pressure sensor, the error is ±0.05 psi. For the flow meter, the worst case scenario would be the full scale error, therefore 6.06 L/min ±0.06 L/min. Equation (3.6) shows this error propagation calculation.

$$eps_{hyd} = \sqrt{\left(\frac{0.05}{5}\right)^2 + \left(\frac{0.06}{6.06}\right)^2} = 1.41\% \text{ of } P_{Hyd} \tag{3.6}$$

The efficiency depends on the error of the previous calculations (hydraulic and electrical power), and results into an uncertainty of 2.5% as shown in Eq. (3.7).

$$eps_{eff} = \sqrt{\left(\frac{\varepsilon_{P_{hyd}}}{P_{hyd}}\right)^2 + \left(\frac{\varepsilon_{P_{motor}}}{R_{motor}}\right)^2} =$$

$$\sqrt{(1.41\%)^2 + (2.01\%)^2} = 2.46\% \text{ of } \eta \tag{3.7}$$

Chapter 4 Discussion

The results of tests performed with the prototype Tesla pump are presented here. The relevant boundary layer thickness and Reynolds numbers are presented in Section 4.1. The prototype tesla pump was tested for various parameters; these are shown in Table 4.1. Section 4.2, deals with the results from the water testing and section 4.3, the propylene glycol mixture testing. The impact of vibration on pump performance was analyzed in section 4.4.

Table 4.1. Tests performed for water and propylene glycol. Where ○ are for water, and △ are for the propylene glycol water mixture.

Disk Rotational Speed (RPM) ---------------------- Disk Pack Spacing (thou)	2500	3000	3600	4000
1	○	○	○	○
3	○	○	○	○
5	○ △	○ △	○ △	○
10	○ △	○ △	○ △	○
15	○ △	○ △	○ △	○
20	○ △	○ △	○ △	○
25	○	○	○	○

4.1 Pump Flow Qualification

4.1.1 Rotational Boundary Layer

Using Eqs. (2.38), (2.40) and (2.22) from Chapter 2, the Reynolds number and boundary layer thickness are calculated using relevant experimental parameters and data.

$$\delta = 5.5 \sqrt{\frac{\upsilon}{\omega}} \qquad (2.38)$$

$$\delta/r = 0.5261 \left(\frac{\mu}{\rho\omega b^2}\right)^{\frac{1}{5}} \qquad (2.40)$$

$$Re_\theta = \frac{\rho\omega b^2}{\mu} \qquad (2.22)$$

The calculated rotational Reynolds number and corresponding boundary layer thicknesses as a function of the disk pack rotational speed are shown in Table 4.2, assuming either laminar (Eq. 2.38) or turbulent (Eq. 2.40) flow. For the turbulent case, the boundary layer thickness is calculated for the total disk radius of 3.5 cm. Therefore, the value of turbulent boundary layer thickness in Table 4.2 is the largest since the boundary layer thickness grows according to Eq. (2.40).

Table 4.2. Calculated Boundary Layer Thicknesses for Laminar and Turbulent flow in water.

RPM	Re_θ	Laminar- BL thickness (inch)	Turbulent- BL thickness (inch)
2500	7.76×10^4	0.0134	3.452
3000	9.31×10^4	0.0122	3.33
3600	1.12×10^5	0.0112	3.21
4000	1.24×10^5	0.0106	3.14

It is important to note that the boundary layer thicknesses calculated in Table 4.2 are for a complete disk, while for this Tesla pump, the disk has a hole in the center having a diameter

of 9.4 mm. This hole in the disk will impact the shape of the boundary layer. Since there is now an inside edge to the disk, the boundary layer will form differently. It is hard to estimate analytically by how much the boundary layer thickness will vary compare to a full disk, but the thicknesses should be of the same order of magnitudes as the ones presented in Table 4.2.

For both laminar and turbulent flows, as shown in Table 4.2, as the rotational speed increases the boundary layer thickness decreases, resulting from the increasing angular velocity. For turbulent flow, the boundary layer is much thicker than a laminar boundary layer, similar to what is expected from the boundary layer theory on a flat plate. For the range of rotational speeds used in this thesis, under the assumption of boundary layer flow on rotating disk, the pump appears to be operating under laminar flow, since the rotational Reynolds number is less than 2×10^5 (critical rotational Reynolds number). Since, the rotational Reynolds numbers are close to the critical value it is not certain if the flow regime is purely laminar.

4.1.2 Fully Developed Flow

The flow between the disks could also be treated as internal flow, where fully developed flow would occur between the disks. As mentioned in Chapter 2 section 2.4, if the boundary layers are larger than half a gap spacing, then fully developed flow is expected. The Reynolds numbers for fully developed internal flow are shown in Table 4.3, for the various rotational speeds and gap spacings. These Reynolds numbers were calculated using Eq. (2.44) for the full length of the disk. As the rotational speed and disk gap spacing increases, so does the Reynolds number. The values of Reynolds numbers in Table 4.3, for the rotational speeds and gap spacings are considered laminar since they are below the expected critical value of 2,300.

$$\mathrm{Re} = \frac{\rho \omega b d}{\mu} \qquad (2.44)$$

57

Table 4.3. Internal Flow Reynolds numbers for the various gap spacing's and rotational speed (water).

RPM	Reynolds number						
	1 thou	3 thou	5 thou	10 thou	15 thou	20 thou	25 thou
2500	11.4	34.3	57.2	114.5	171.7	229.0	286.2
3000	13.7	41.2	68.7	137.4	206.1	274.7	343.4
3600	16.5	49.5	82.4	164.8	247.3	329.7	412.1
4000	18.3	54.9	91.6	183.2	274.7	366.3	457.9

4.1.3 Surface Area

The total surface area available is another parameter that is useful in characterizing the Tesla pump's performance. The surface areas for each disk pack are compared in Table 4.4, where the 1 to 25 thou spacing are presented. The last column in Table 4.4 shows the percentage of surface area differences compared to the 25 thou disk pack. The resulting surface area for each disk pack varies depending on the number of disks. It is expected that more surface area would improve the performance of the pump, since there is more area for energy transfer to occur.

Table 4.4 Surface area comparison as a function of the number of disks used in the disk pack.

Spacing (thou)	number of disks in disk pack	total surface area from disks in the disk pack (m^2)	% difference from 25 thou
25	15	0.0280	0%
20	15	0.0280	0%
15	16	0.0299	6.7%
10	18	0.0337	20%
5	20	0.0374	33%
3	26	0.0486	73%
1	27	0.0505	80%

4.2 Water Experiments

The water testing consisted of four rotational speeds and seven disk pack spacings. The effects of changing the rotational speed are presented in section 4.2.1, and the disk pack spacing in 4.2.2. A non-dimensional analysis using experimental data is shown in section 4.2.3. A comparison to Darby et al. (1987) and Hassinger and Kehrt (1963) is presented in section 4.2.4, looking for future improvements to the pump design. The final section 4.2.5 shows a validation of the flow rates obtained experimentally. It is important to note that graphs presented in this thesis do not have error bars if the size of the error bar is than the symbol use to show the data point.

4.2.1 Impact of Pump's Rotational Speed

Figures 4.1 (a) to 4.7 (a), show the pump curves obtained experimentally (head as a function of flow rate) for the prototype pump, which show the effect of rotational speed for the various disk pack spacings. The maximum flow rate obtained was 1.58 L/min and the highest pump head was 3.26 m, obtained at 4000RPM for the 15 thou spacing (Fig 4.5(a)). It can be observed from Figs. 4.1 (a) to 4.7 (a) that the higher the rotational speed, higher pump head and capacity is produced. Figures 4.1 (a) to 4.7 (a), suggest that there is a consistent improvement in performance as rotational speed is increased.

For a centrifugal pump, the mechanical energy is transferred to the fluid along the impeller, where both the pressure and kinetic energy of the working fluid rises. At the entrance of the pump or suction side, the working fluid is being displaced, therefore there is a negative pressure at the entrance of the impeller. This negative pressure at the entrance of the pump or impeller helps to maintain the flow within the system by pulling fresh fluid into the system. For a Tesla pump the rotation of the disk pack transfers energy through the viscous forces between the disk and the working fluid within the boundary layer moving the fluid along the disk. Therefore, as the rotational speed increases there is more mechanical energy transferred to the fluid, which will produce higher pump head and flow rates.

The overall pump efficiency graphs for the various disk pack spacings are shown in Figs. 4.1 (b) to 4.7 (b) comparing the effects of the four different rotational speeds. The maximum efficiency was 3.58 %, which was obtained for 3600 and 4000 RPM for 5 thou, (Fig 4.3 (b)). For the efficiency in Figs. 4.3 (b) to 4.7 (b), 5 to 25 thou, the higher rotational speeds are the least efficient. While the opposite appears for the smaller gap spacings of 1 and 3 thou, where the higher rotational speeds are more efficient, shown in Figs. 4.1(b) and 4.2 (b). In Fig. 4.1 (b), for 1 thou, the efficiency between the various rotational speeds has very little difference, which is due to the excessively small spacing that limits the amount of fluid being pumped. While for 3 thou, shown in Fig. 4.2 (b), there is a more distinct difference with regards to rotational speed. The expensively small spacing will affect the performance and overall efficiency of the pump and is why the 1 thou spacing displays very little effect due to different rotational speeds.

For Fig. 4.4 (b) and 4.6 (b), 10 and 20 thou spacings, between the 2500 RPM and 3000 RPM speeds, there is some improvement regarding the overall pump efficiency, where for the 15 thou spacing (Fig. 4.5 (b)) there is slightly more of an improvement at 2500 RPM compared to the other larger spacings at low flow rates. It is unclear if this slight increase in efficiency at 2500 RPM is due to the 15 thou spacing or not. Regardless, the lower rotational speeds tend to be more efficient for the larger disk pack spacings and this is suspected to be due to better energy utilization that at a higher rotational speed.
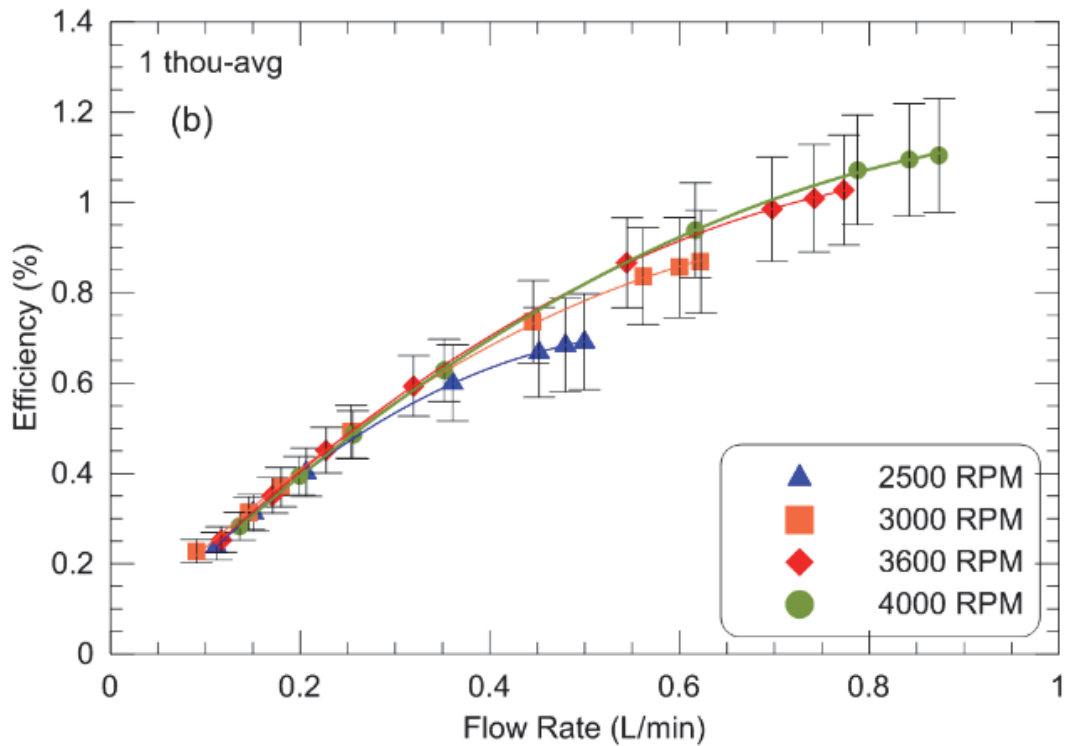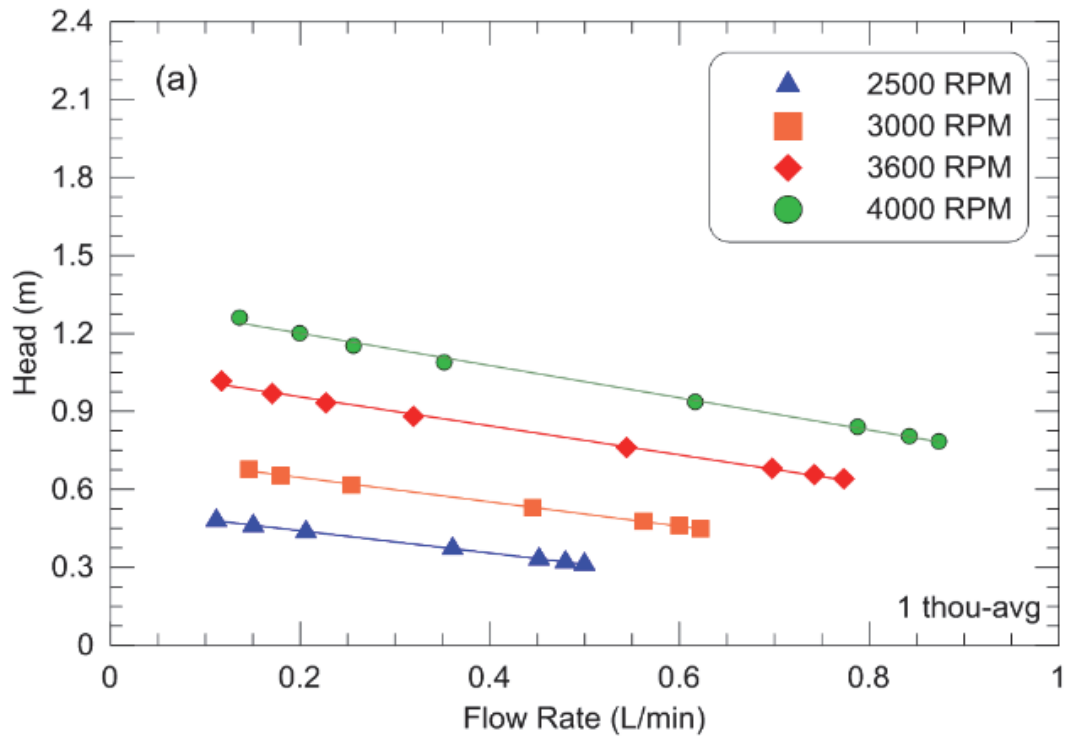
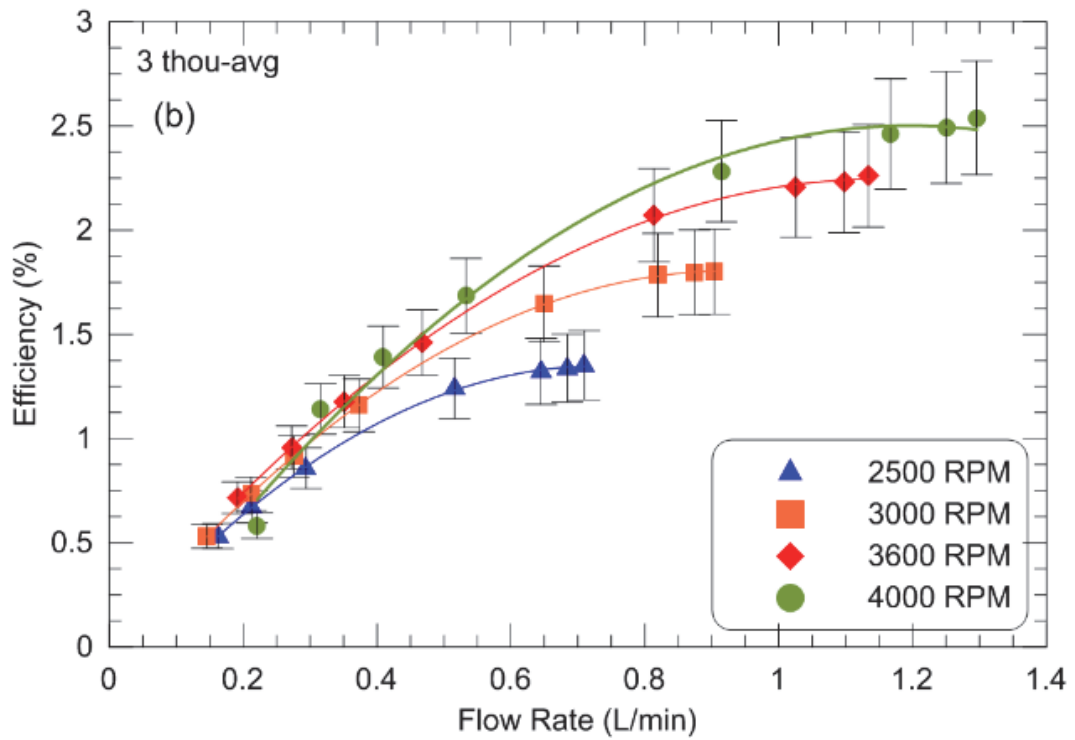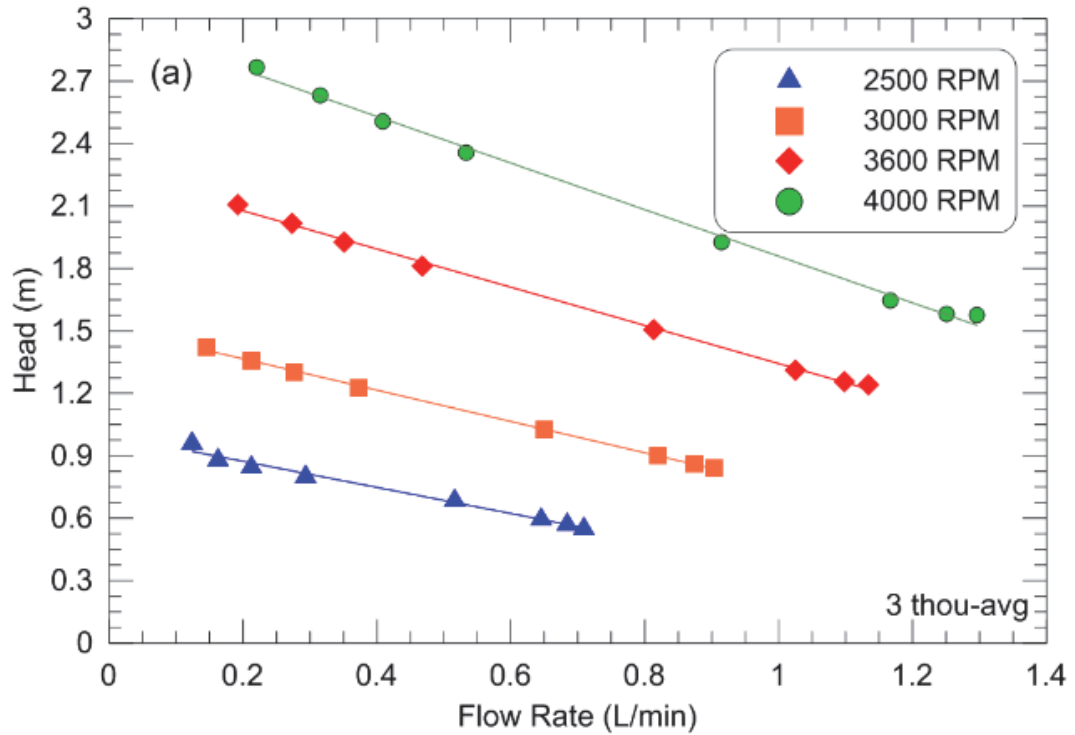**Figure 4.1. 1 thou (a) Head and (b) Efficiency vs. flow rate**
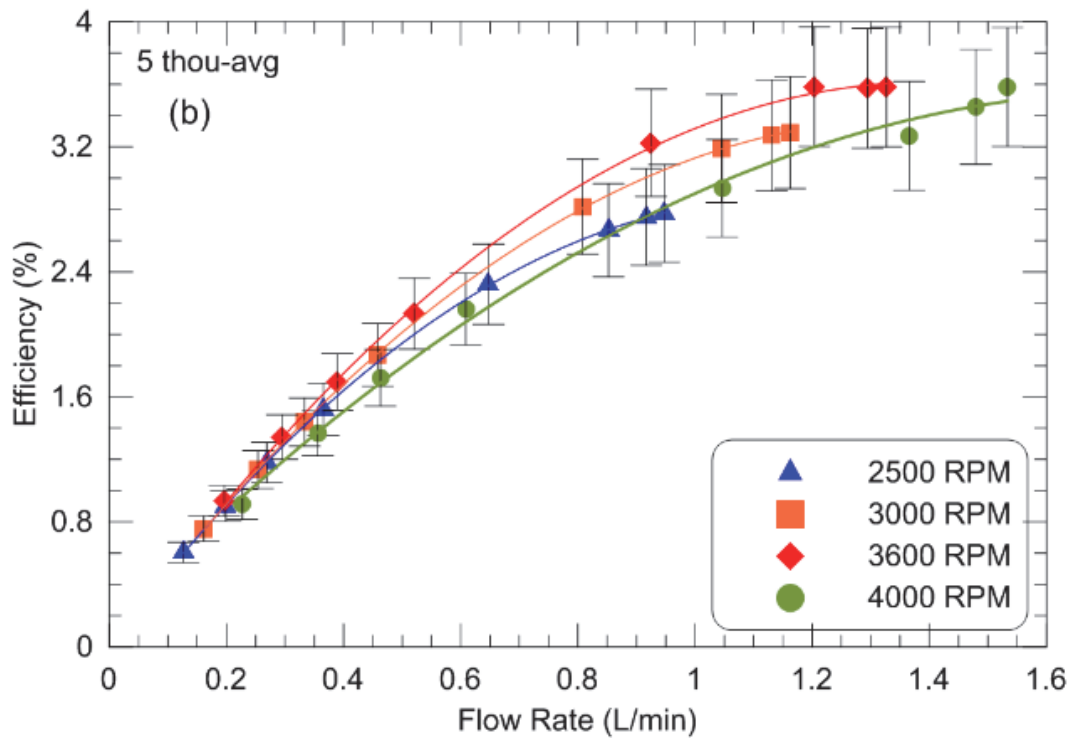
61

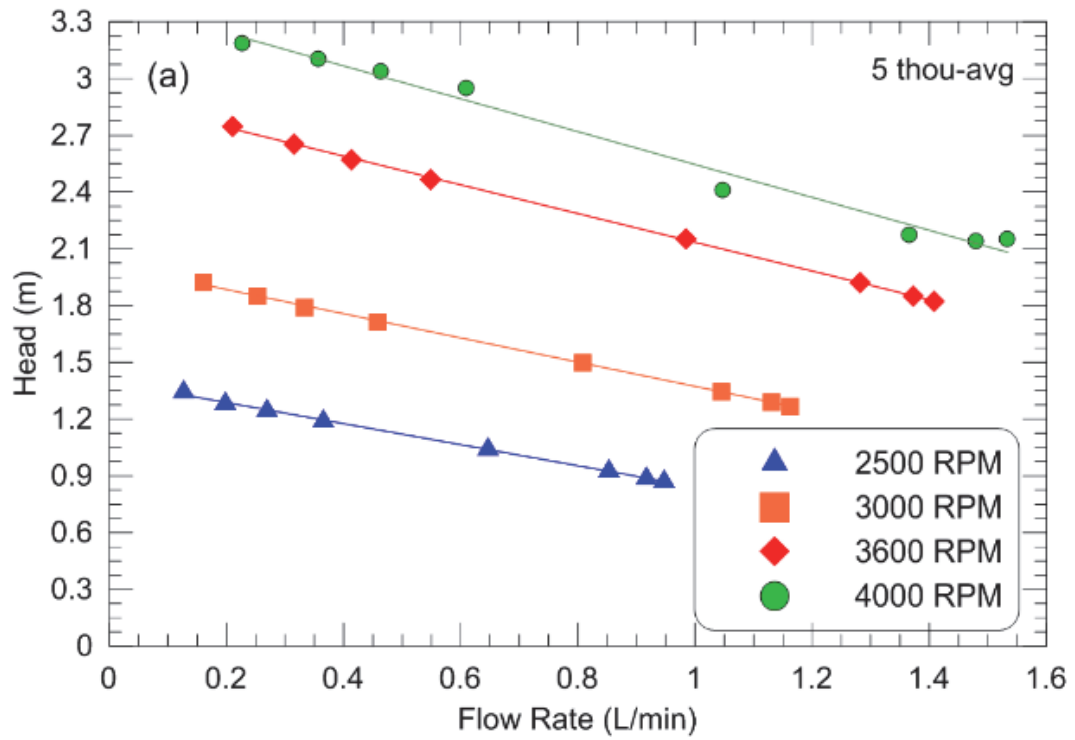**Figure 4.2. 3 thou (a) Head and (b) Efficiency vs. flow rate.**

Figure 4.3. 5 thou (a) Head and (b) Efficiency vs. flow rate.

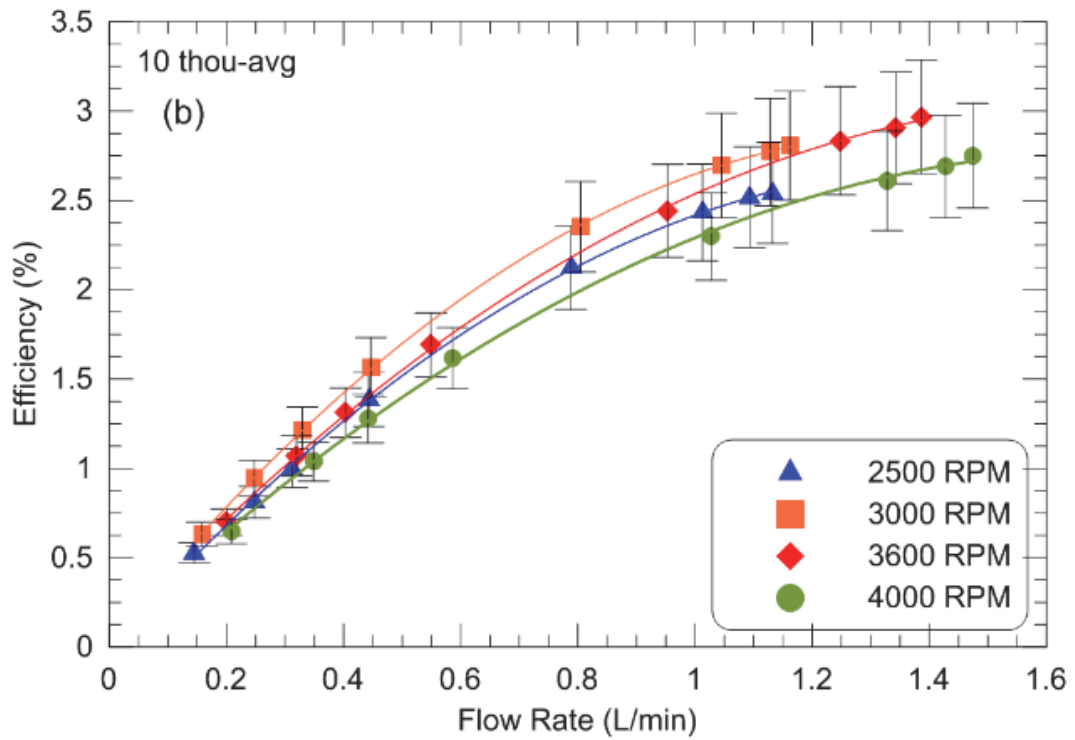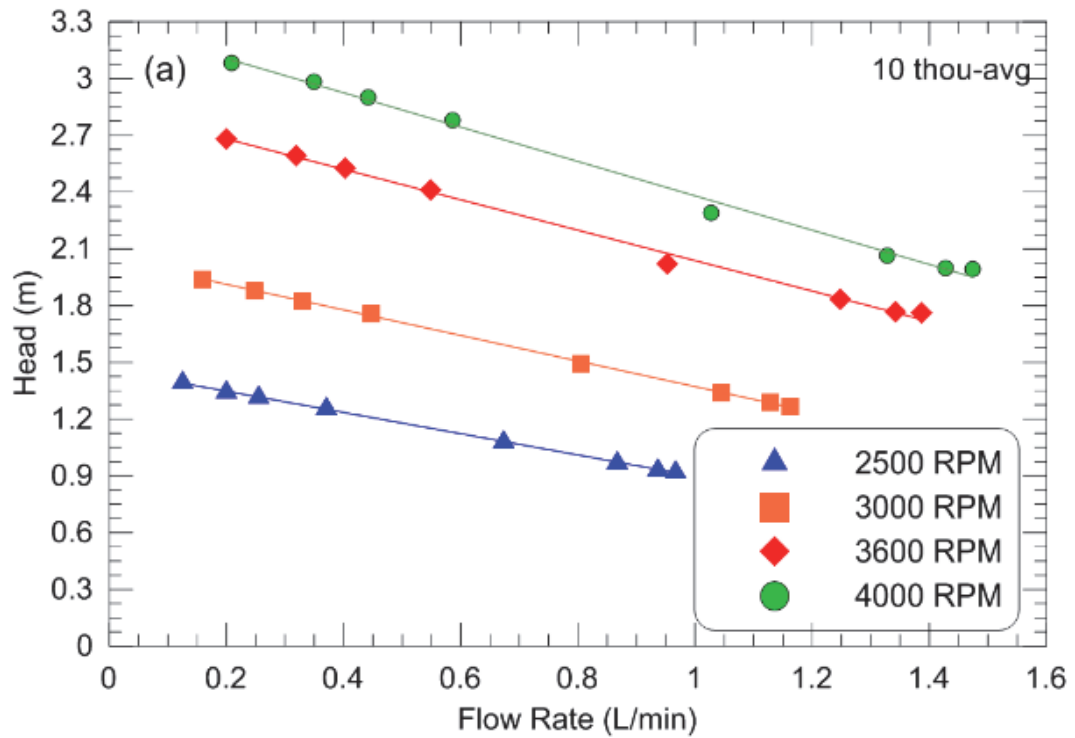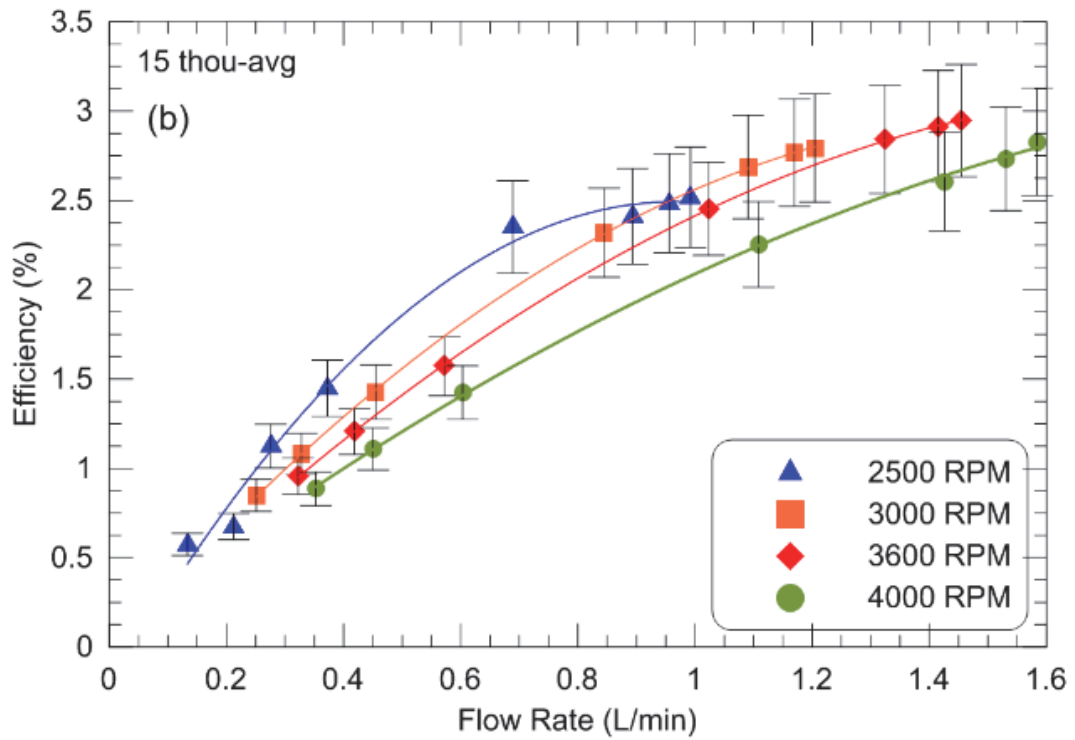**Figure 4.4. 10 thou (a) Head and (b) Efficiency vs. flow rate.**
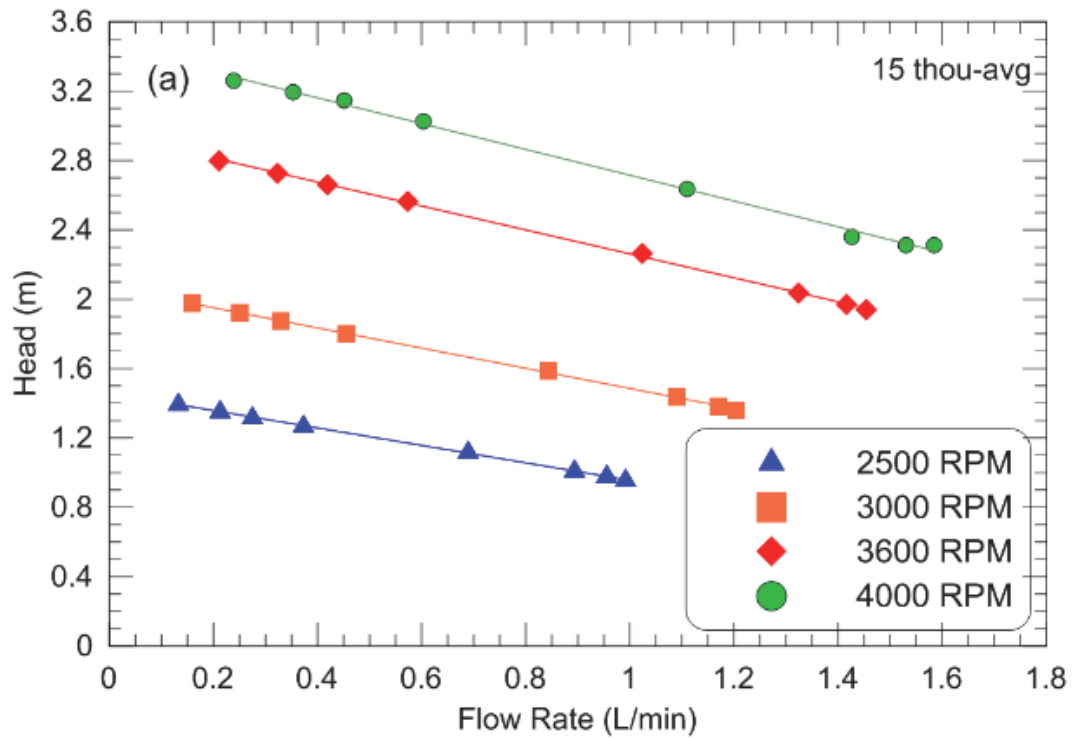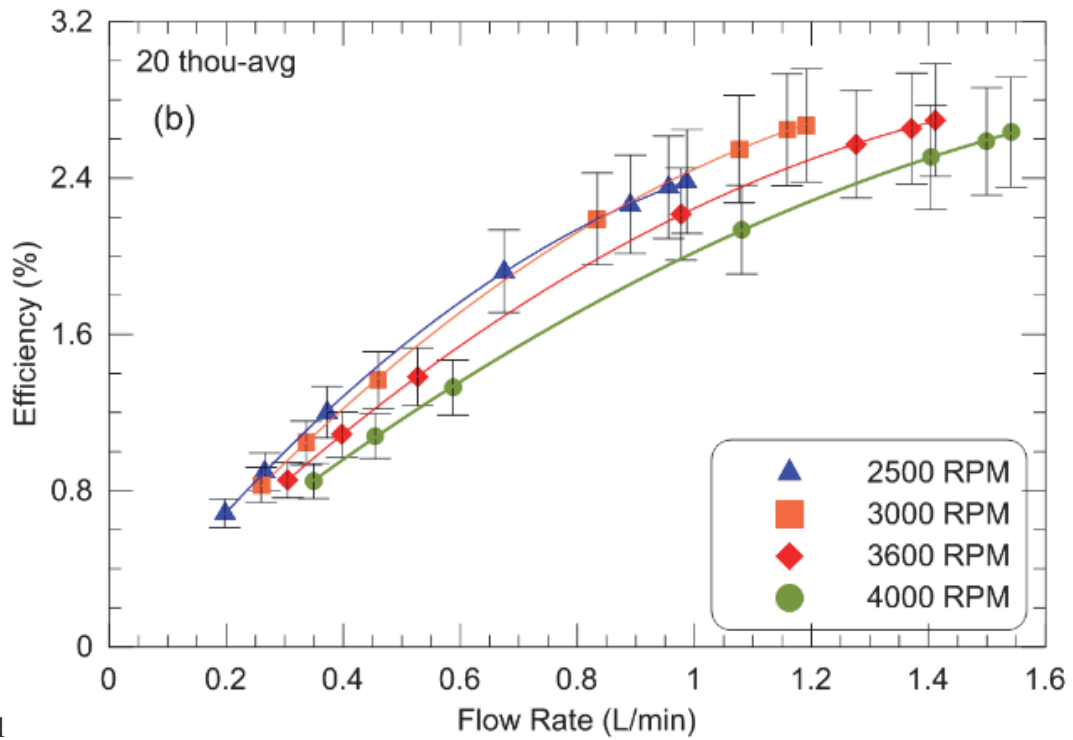
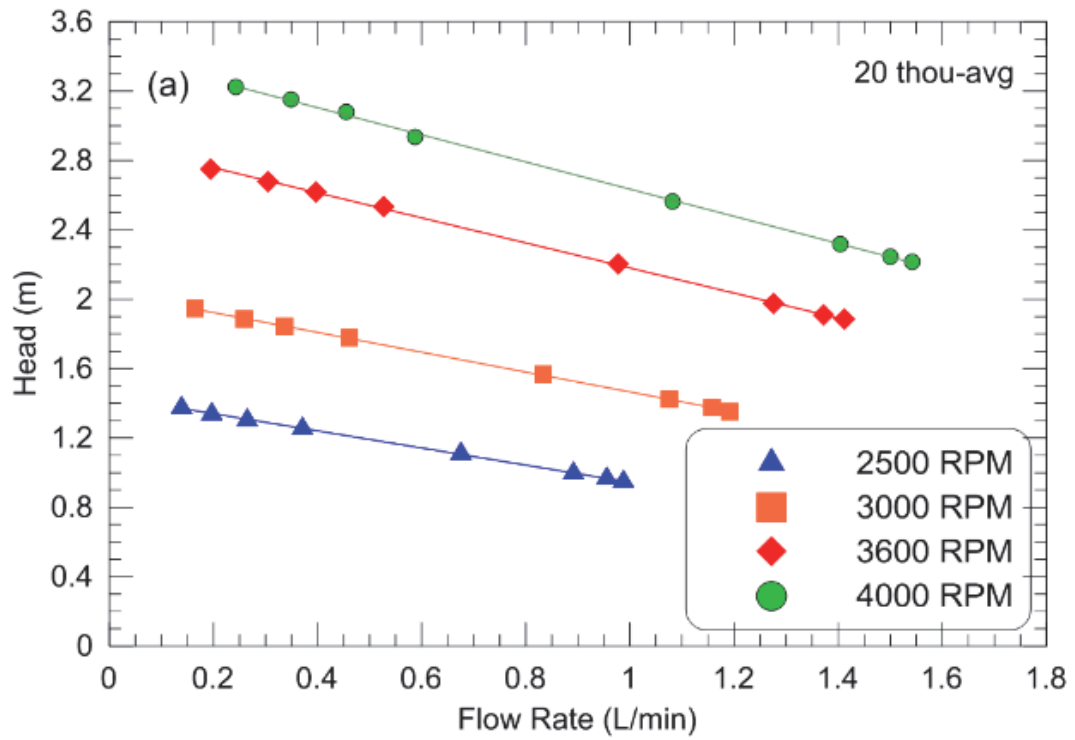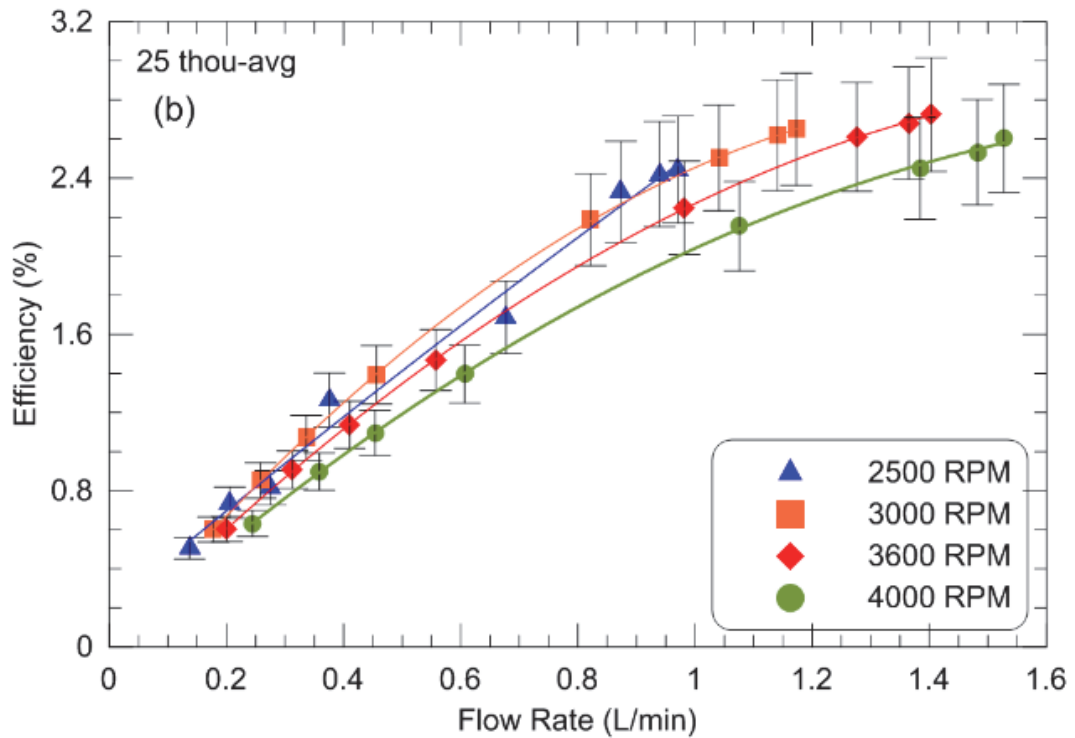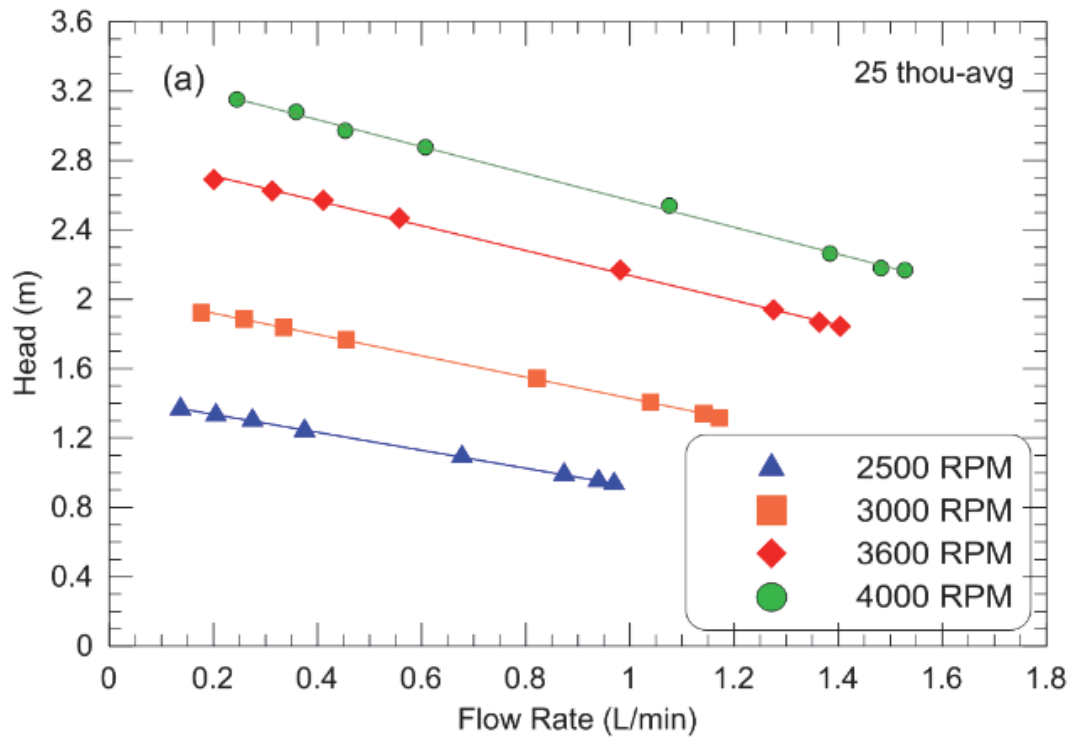**Figure 4.5. 15 thou (a) Head and (b) Efficiency vs. flow rate.**

Figure 4.6. 20 thou (a) Head and (b) Efficiency vs. flow rate.

1

Figure 4.7. 25 thou (a) Head and (b) Efficiency vs. flow rate.

The mass flow rate entrained by the boundary layer on a spinning disk have been calculated and compared to experimental values as shown in Fig. 4.8. Figure 4.8 shows the mass flow rate as a function of rotational speed, comparing the various spacings, where (a) is the experimental data, and (b) is the theoretical data. The theoretical mass flow rates are calculated for one side of the disk using Eq. (2.41), then multiplied by two to obtain the mass flow rate for both sides of a disk and finally multiplied by number of disks in the disk pack.

$$\dot{m} = 2.779 \rho b^2 \sqrt{\nu\omega} \tag{2.41}$$

It is clear that the experimental values are significantly less than the theoretical mass flow rate values, when comparing the scales between Figs. 4.8 (a) and (b). The theoretical mass flow rates do not take into account the disk gap spacings and the effect of the hole in the center of the disks, therefore the theoretical mass flow rates would be larger.

What is true in both cases is that as the rotational speed increases, the flow rate increases. This is also demonstrated with Eq. (2.41) where the mass flow rate increases with the square root of the rotational speed. However, this is not exactly observed with the experimental data. Also, the mass flow rate relationship of Eq. (2.41) is for a rotating disk within an infinite fluid, where the fluid is not bounded. Due to the disk pack being bounded within a casing the mass flow rate is not expected follow the same trend for a non-bounded single disk.
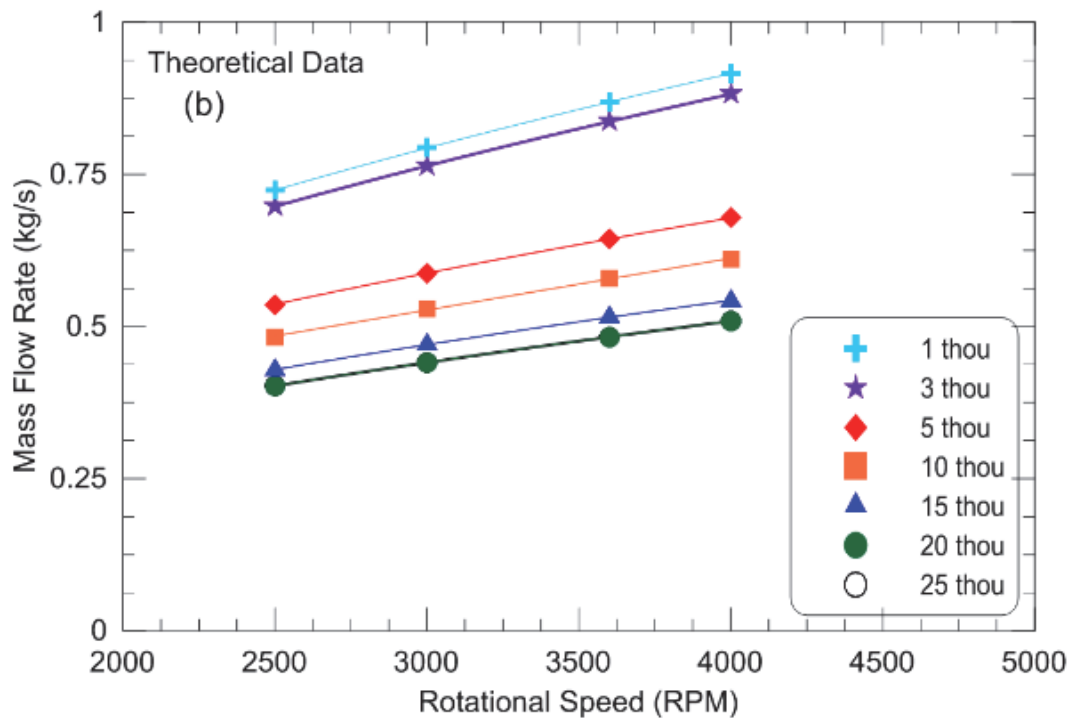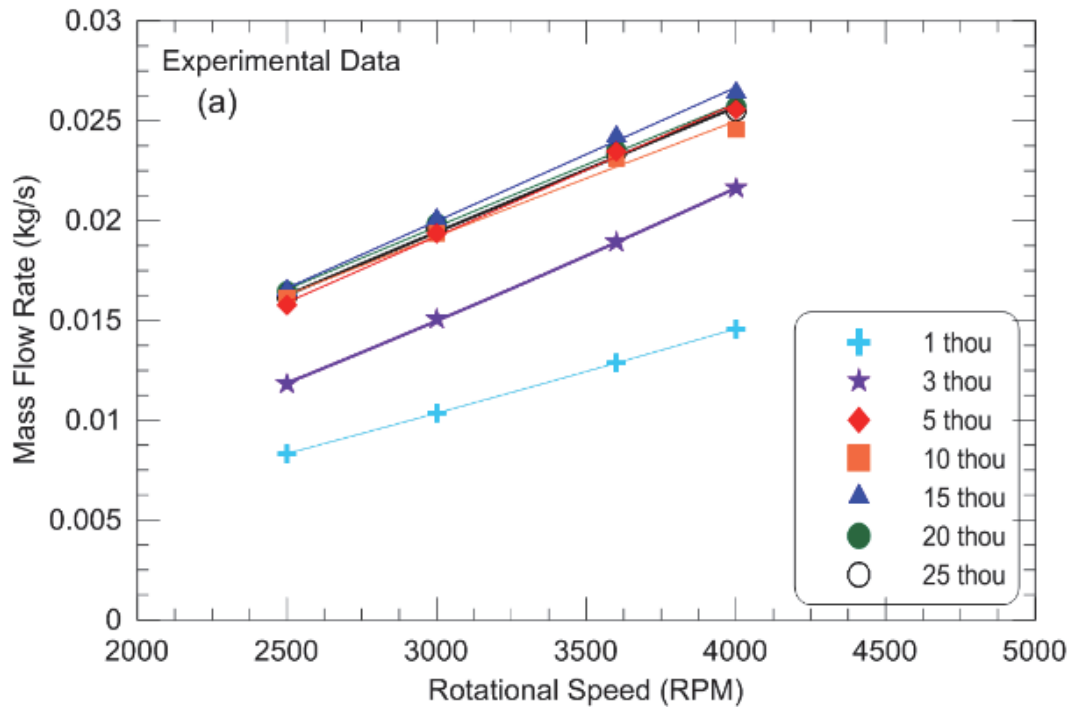
Figure 4.8. Flow Rate as a function of Mass Flow rate for (a) experimental and (b) theoretical.

4.2.2 Impact of Disk Pack Spacing on Pump Performance

Figures 4.9 (a) to 4.12 (a) show the pump head vs. flow rate obtained experimentally for the prototype pump, displaying the effect of various disk pack gap spacings for each rotational speed. The least performant spacing according to Figs. 4.9 (a) to 4.12 (a) is the 1 and 3 thou, which is due to the gap spacing limiting the flow through the disk pack. For the 5 to 25 thou spacings, it becomes harder to determine which is the most performant spacing.

It is expected that fully developed flow between the disks is occurring for the 5 to 20 thou gap spacings, since the calculated boundary layers are larger than half a gap spacing. For example, for 4000 RPM, the boundary layer thickness for one disk is 10.6 thou (from Table 4.2), where only the 25 thou gap spacing could easily allow for two boundary layers to fit in-between the disks. The 15 thou spacing is likely the largest spacing where true fully developed flow would occur and has 6.7% more surface area than the 20 thou spacing. The combination of both of these factors is likely what improves the performance of the 15 thou spacing.

Figures 4.9 (b) to 4.12 (b) shows the efficiency vs. flow rate obtained experimentally for the prototype pump. These figures show the effect of the different disk pack spacings with regards to efficiency for the various rotational speeds. Figs. 4.9 (b) to 4.12 (b) show the 5 thou spacing consistently as the most efficient, obtaining a maximum efficiency of 3.58%, at 4000 and 3600 RPM. The 15 thou spacing obtains a maximum efficiency of 2.95%, as does 10 thou, while 20 thou is approximately 2.70% at 3600 RPM. The 15 thou spacing is somewhere in the middle range of efficiency, regardless of being the most performant compared to other spacings. There is more variation in the efficiency for the 5 to 25 thou spacings compared to the pump's performance overall variation. This suggests that the motor or shaft coupling could be impacting the overall efficiency, since the power drawn from the motor is relevant in determining the overall pump efficiency.
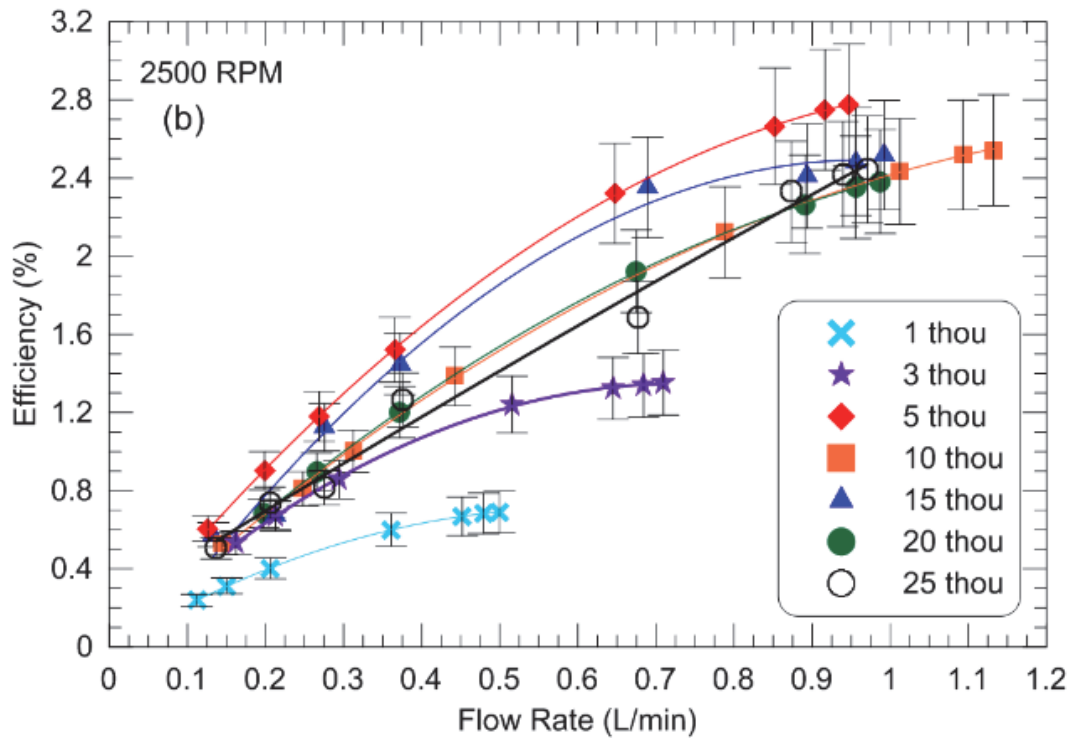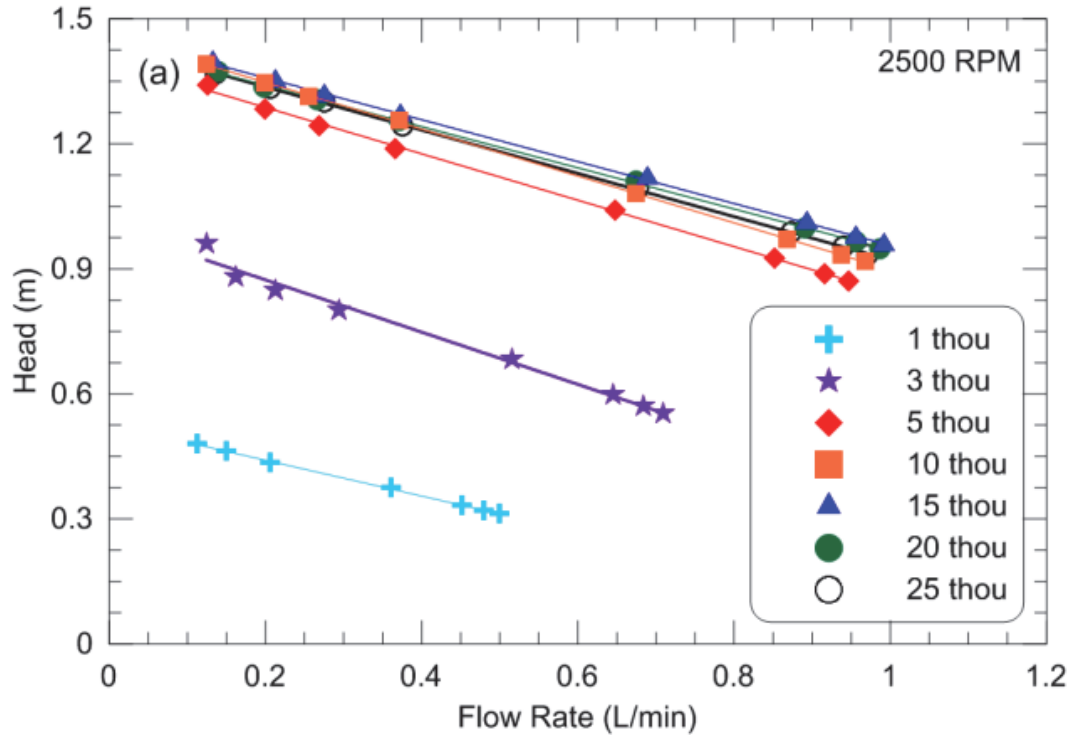
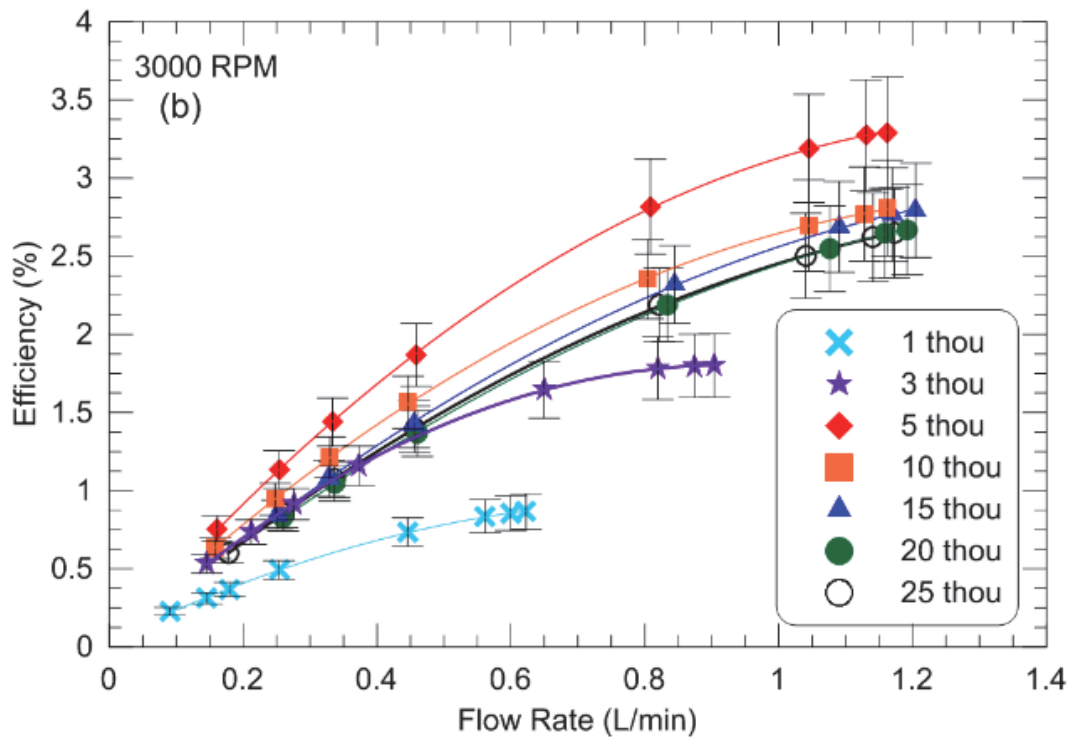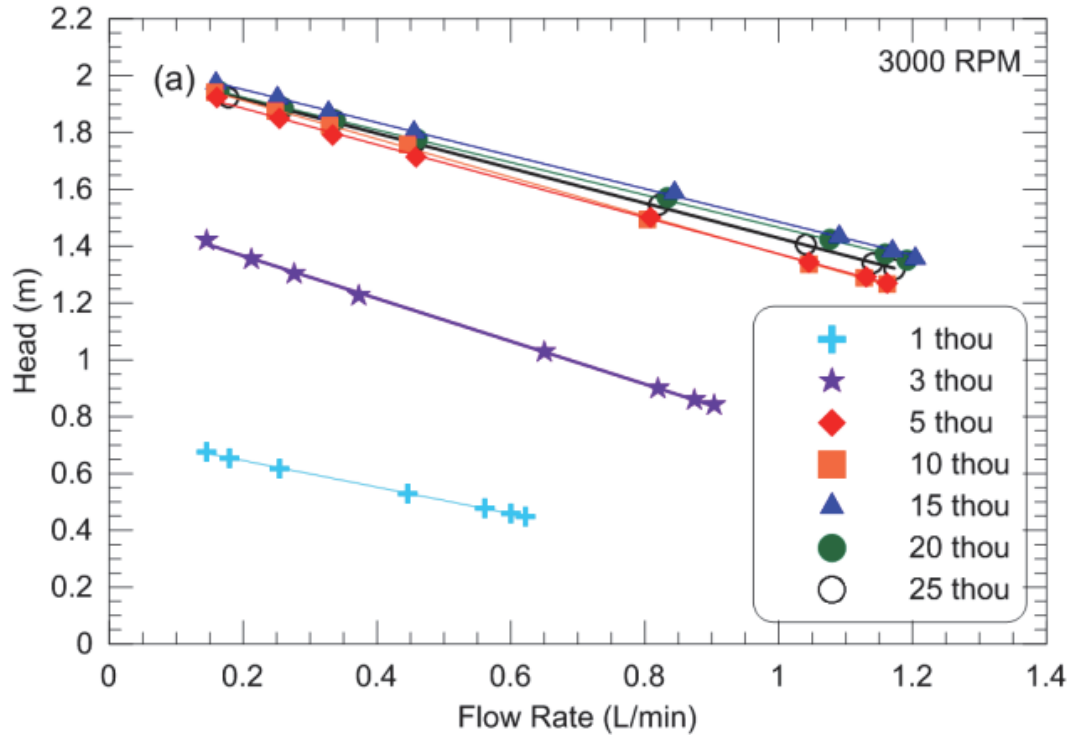**Figure 4.9. 2500 RPM (a) Head and (b) Efficiency vs. flow rate.**

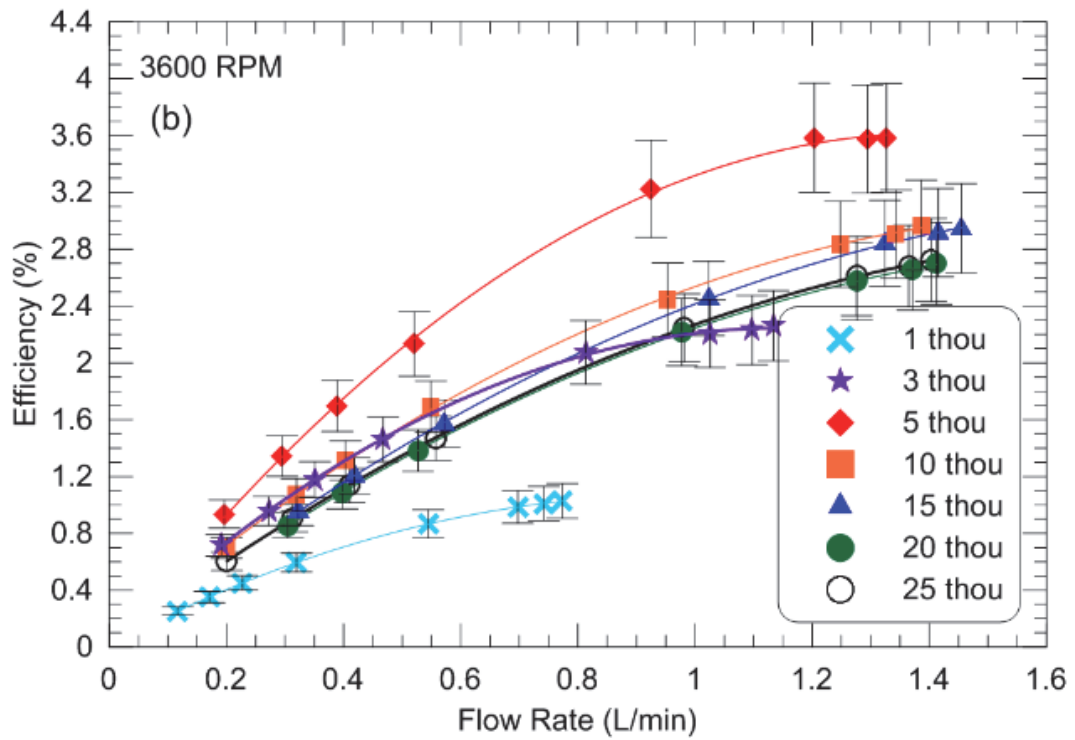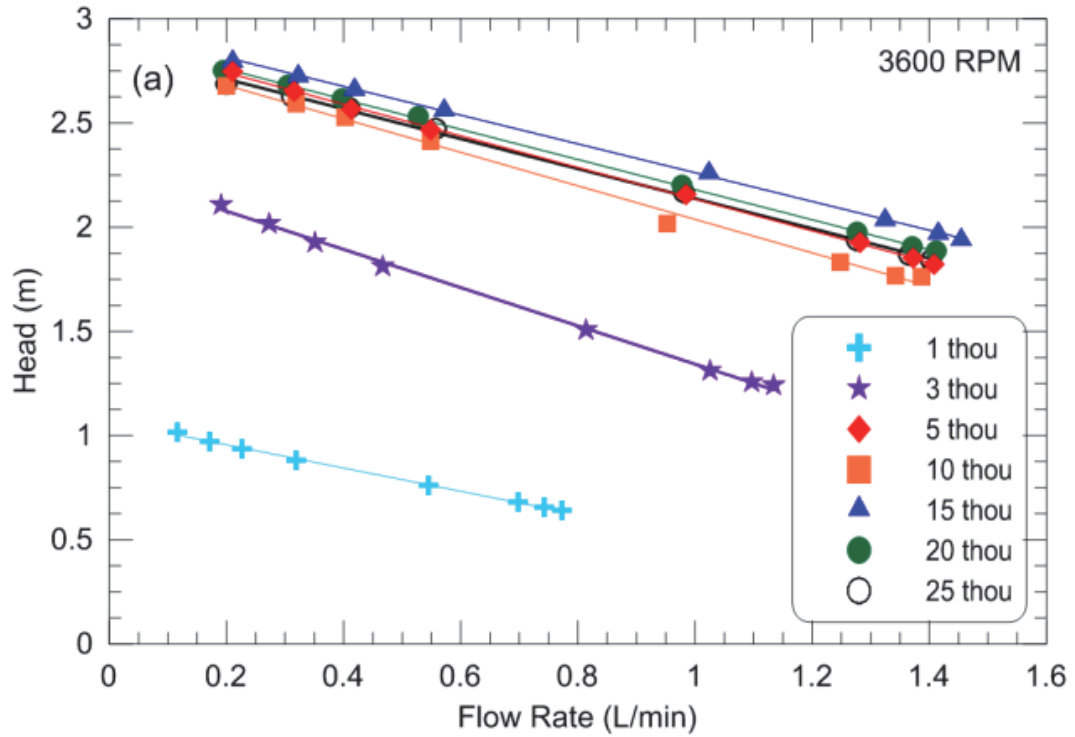71

Figure 4.10. 3000 RPM (a) Head and (b) Efficiency vs. flow rate.

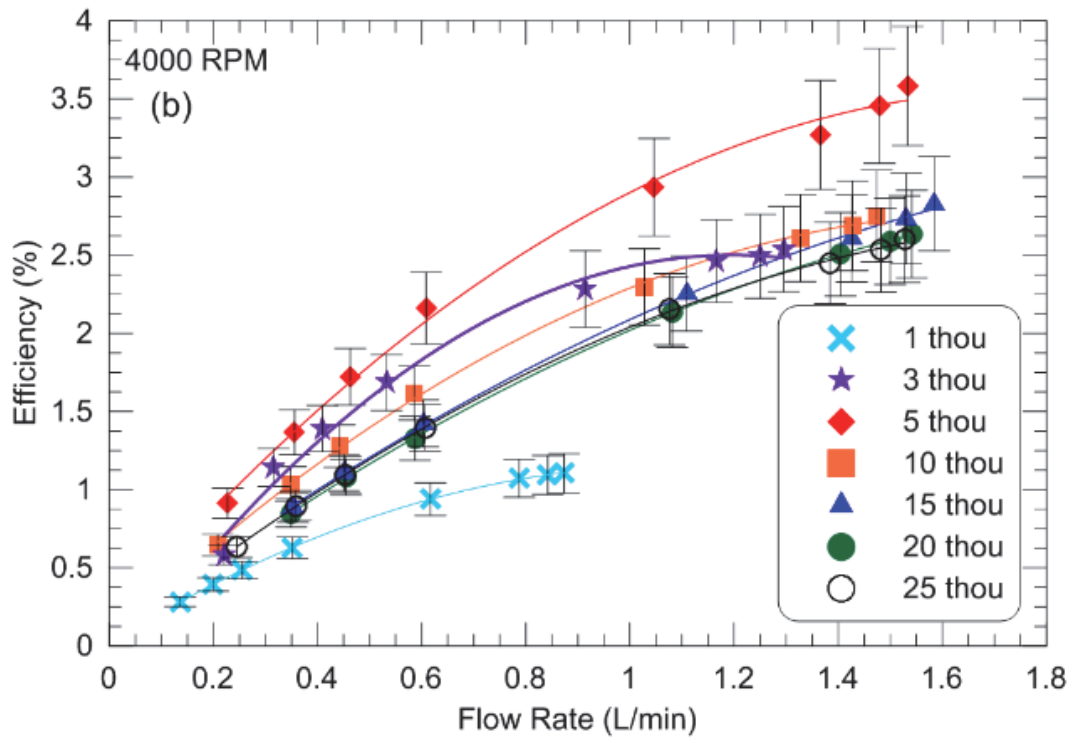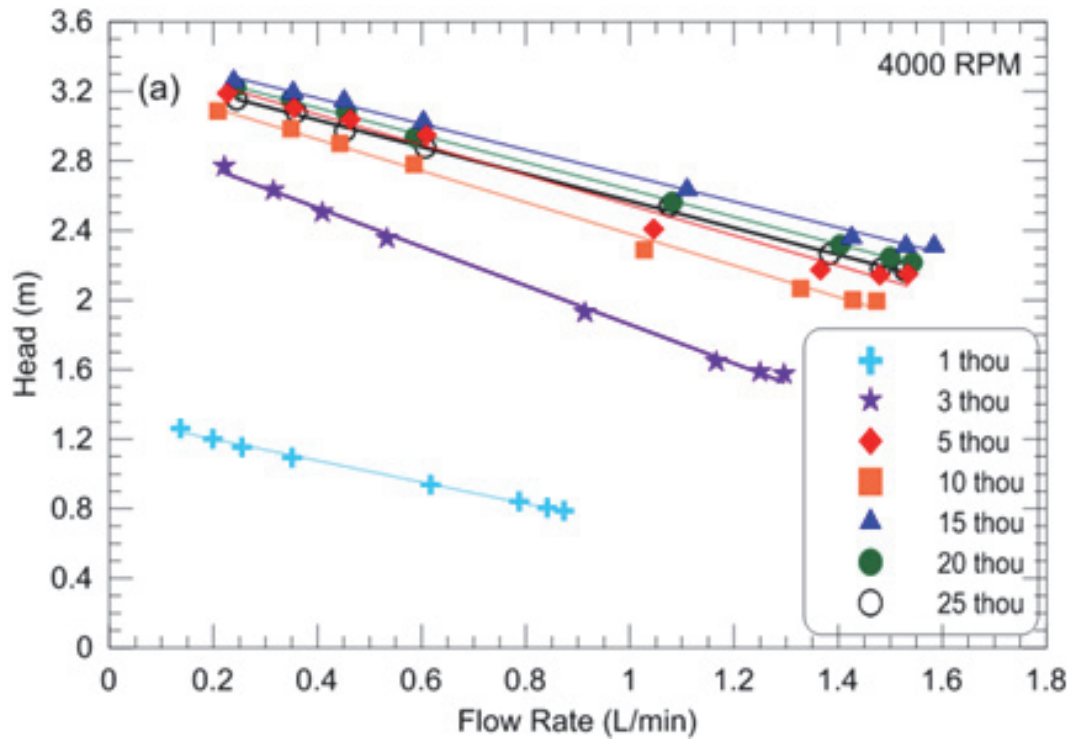**Figure 4.11. 3600 RPM (a) Head and (b) Efficiency vs. flow rate.**

Figure 4.12. 4000 RPM (a) Head and (b) Efficiency vs. flow rate.

4.2.3 Non-Dimensional Analysis

The data from the previous sections can be converted to dimensionless coefficients for later comparison to other pumps. Figure 4.13 shows a plot of experimental data from Timár (2005), head vs. flow coefficients for a centrifugal pump, showing a characteristic pump curve. The Reynolds number was calculated using Eq. (4.1), with density (ρ), rotational speed (n), impeller diameter (D), and dynamic viscosity (μ). In Fig 4.13, it can be seen that there is no effect due to rotational speed for a centrifugal pump (tests done between 1200 to 2000 RPM).

$$\text{Re} = \frac{\rho n D^2}{\mu} \tag{4.1}$$

Figure 4.14 shows the effect of rotational speed on the Head (C_H) vs. the Capacity (C_Q) coefficients, for various disk pack spacings on the Tesla pump used in this study. The 1 thou spacing in Fig. 4.14 (a) for the various rotational speeds is identical, while the other spacings Fig. 4.14 (b-g) all show some variation in them. The 4000 RPM rotational speed for 5 to 25 thou spacings tends to be less performant compared to the other rotational speeds. A Tesla pump's operation is similar to a centrifugal pump, the same dimensionless relationships are used; it is expected that, for each disk pack's spacing, there would be one characteristic curve for all rotational speeds as long as the flow regime remains similar between the disks. According to Table 4.3, the flow in the Tesla pump tends to be laminar rather than turbulent, unlike for the centrifugal pump example in Fig 4.13. Figures 4.14 (b-g) suggest that for this Tesla pump, that the flow regime is similar to a certain degree, but not perfectly since the dimensionless pump curve to not collapse perfectly onto each other.
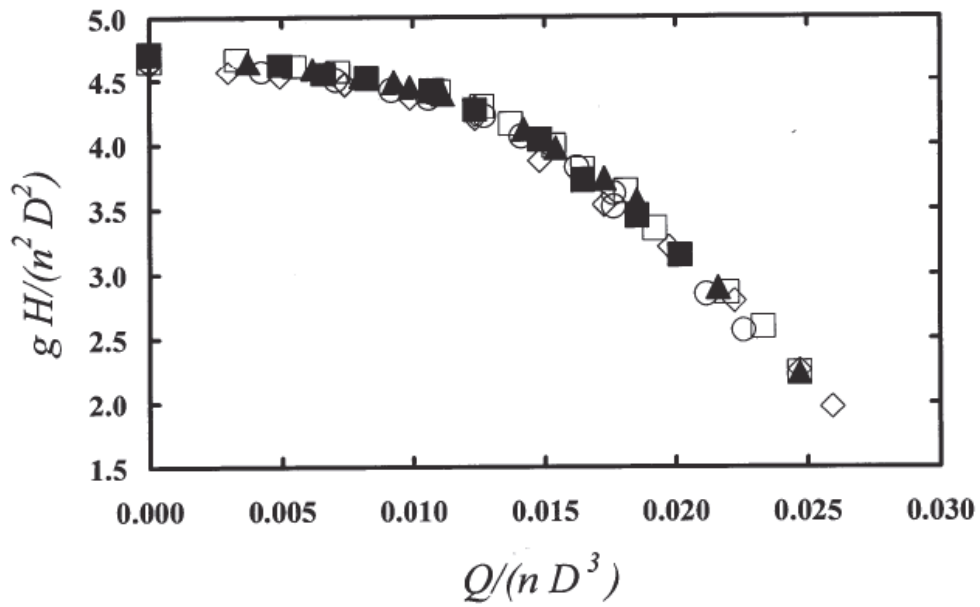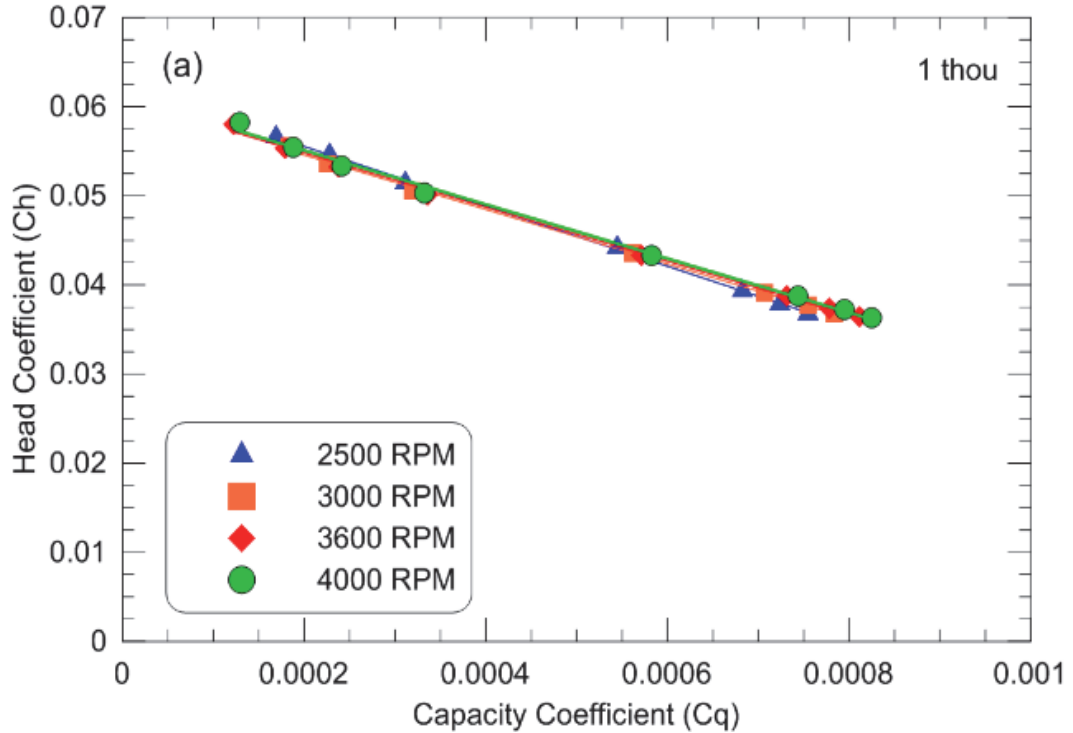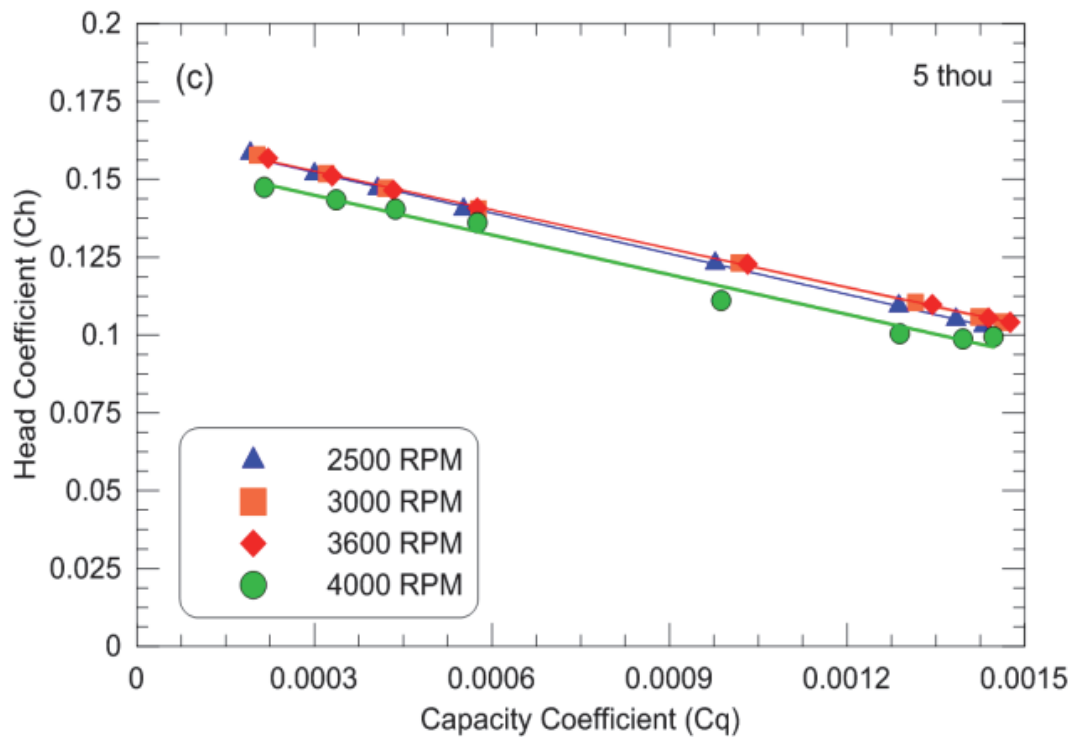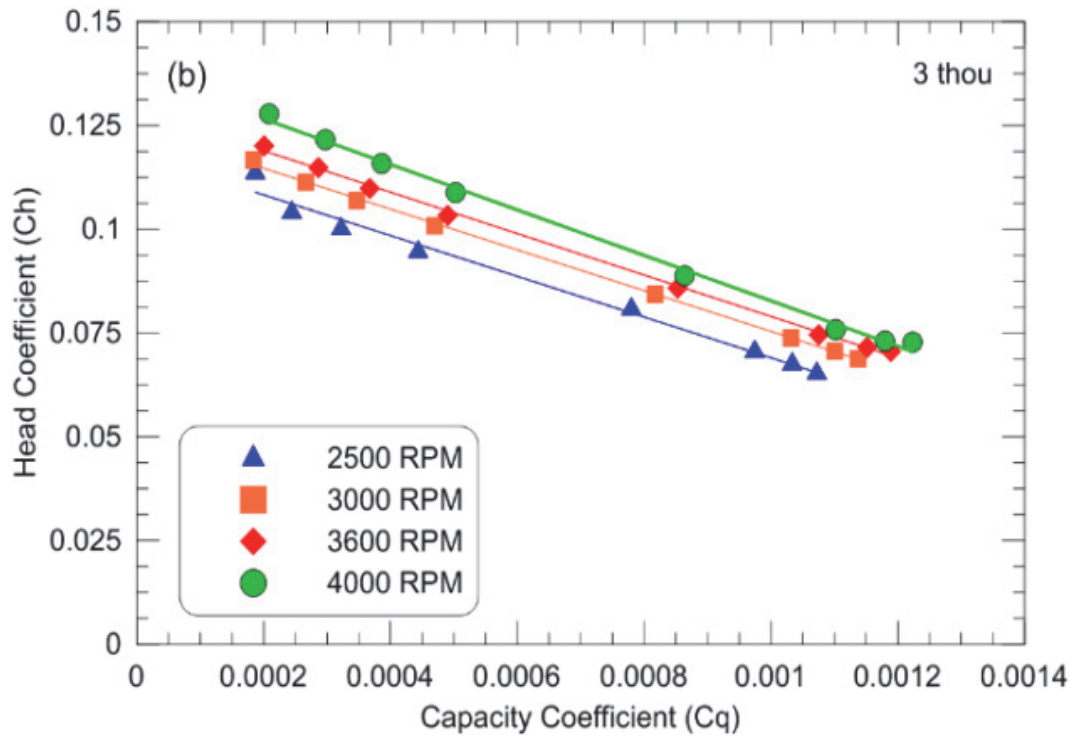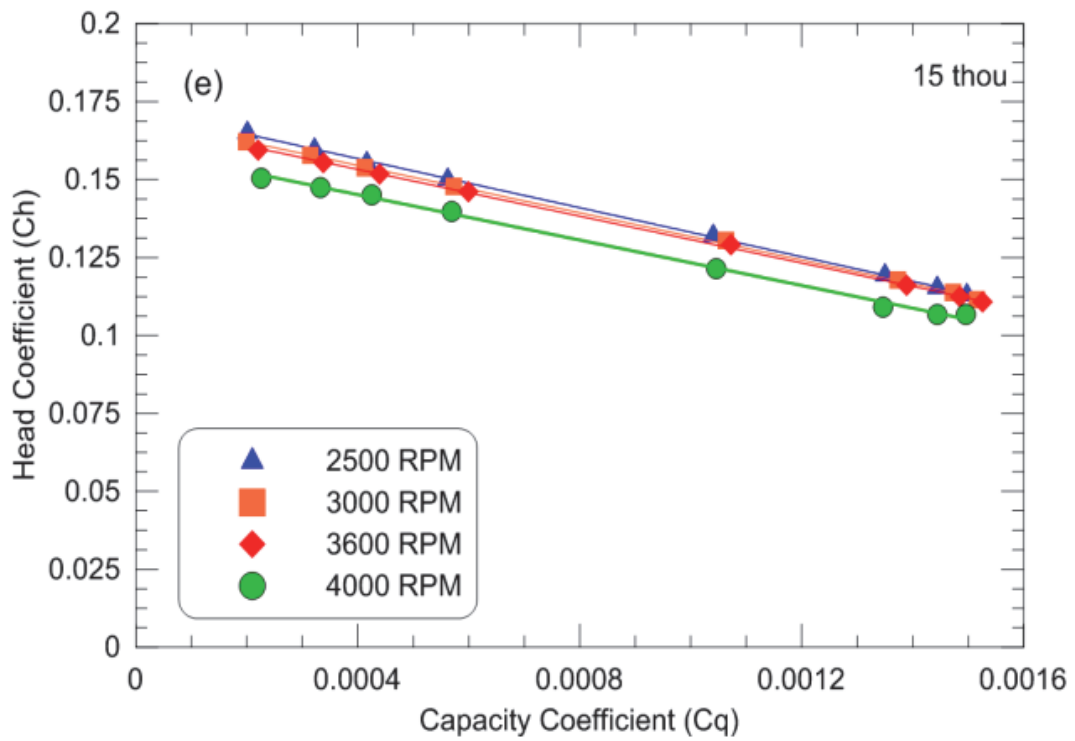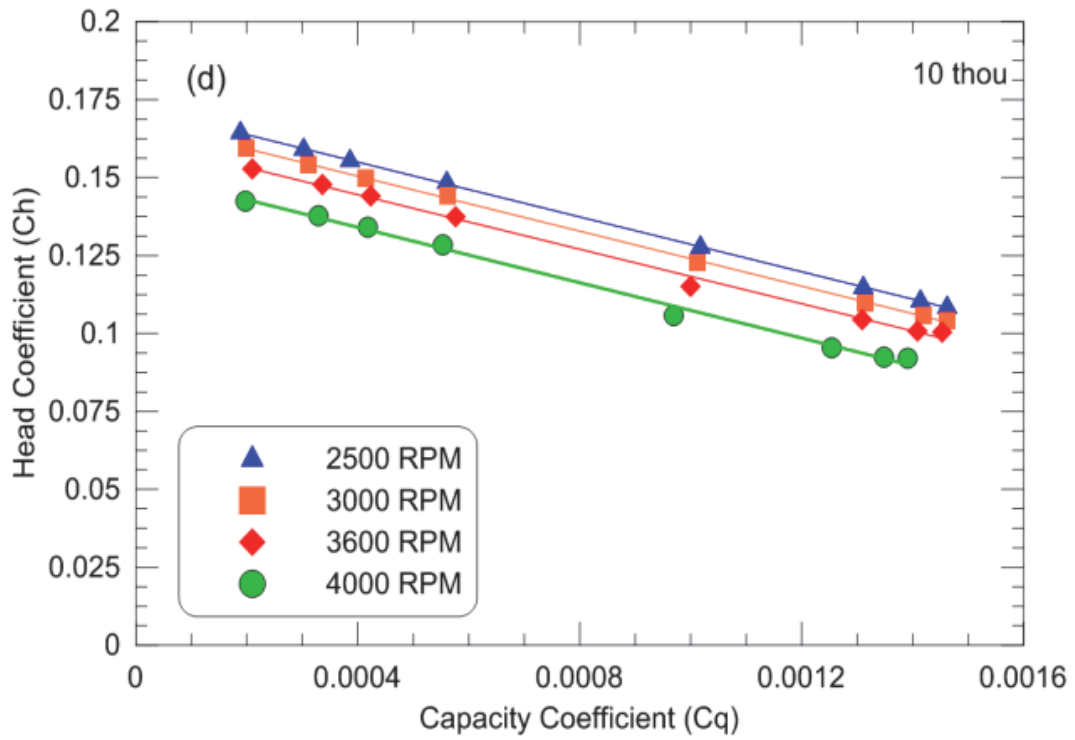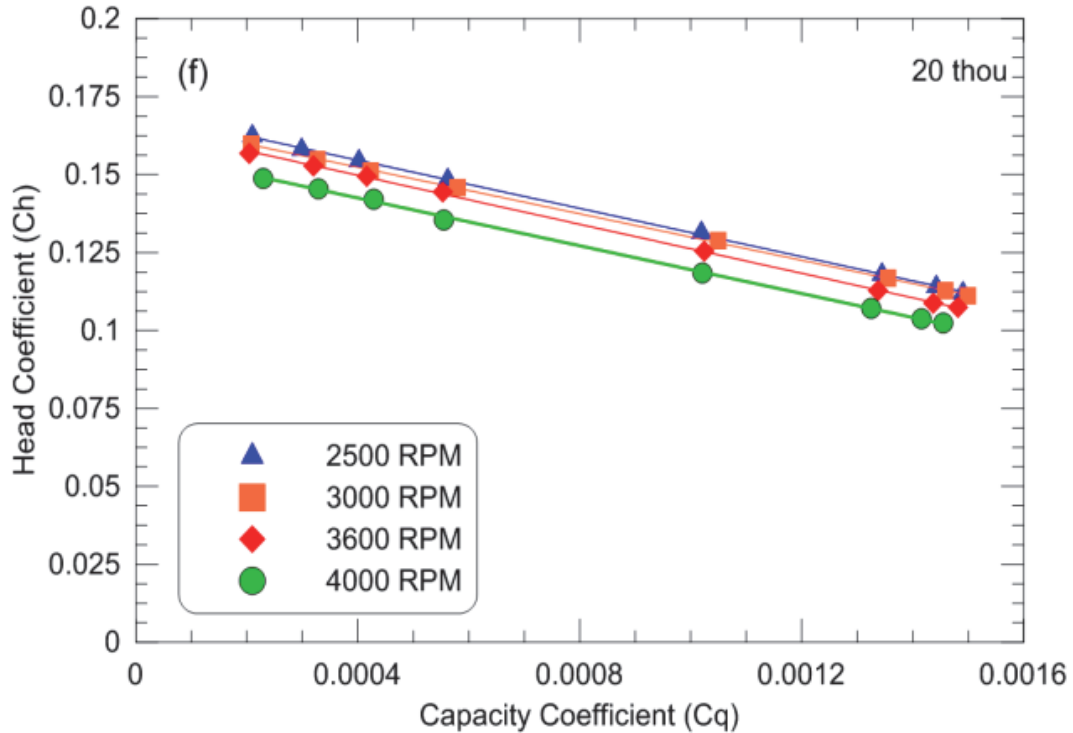
Figure 4.13. Head coefficient as a function of the flow coefficient for centrifugal pump, for 1200 to 2000 RPM, with corresponding Reynolds numbers, 410,000 to 680,000. (Timár, 2005)

(b) 3 thou

2500 RPM
3000 RPM
3600 RPM
4000 RPM

(c) 5 thou

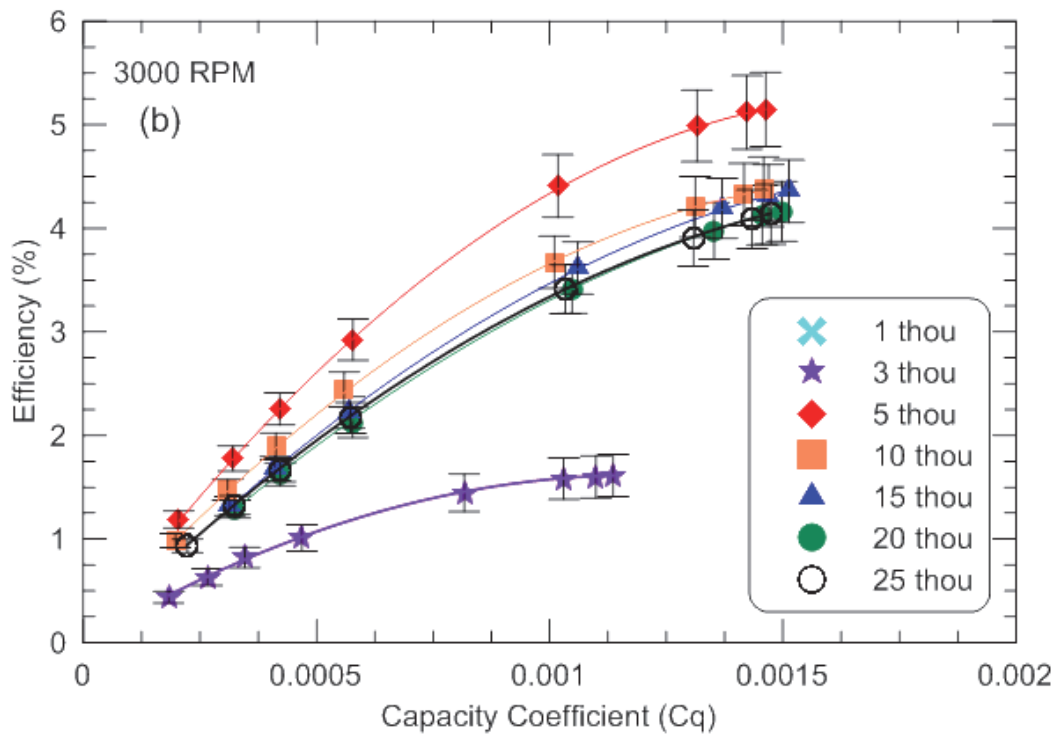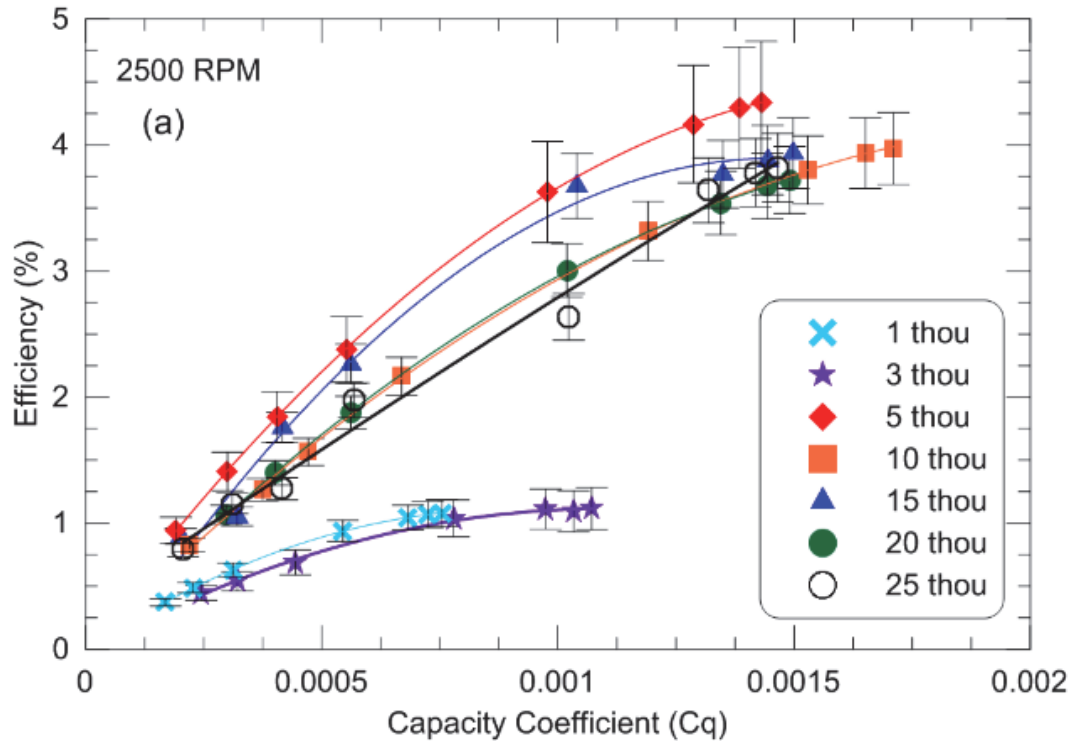2500 RPM
3000 RPM
3600 RPM
4000 RPM

77

Figure 4.14. Head vs. capacity coefficient, rotational speed comparison, for (a) 1 thou, (b) 3 thou, (c) 5 thou, (d) 10 thou, (e) 15 thou, (f) 20 thou, (g) 25 thou.

In order to make a reasonable comparison of this work to other studies, the dimensionless parameters were used to calculate the mechanical (η_{mech}) or the disk pack/rotor efficiency, rather than the overall pump efficiency (η_{tot}), which includes the motor electrical to mechanical efficiency. All the efficiencies shown in this section will be higher due to the motor's efficiency of 64% not contributing to the analysis. The pump's efficiency vs. capacity coefficient as a function of the disk pack spacing is show in Fig 4.15, for all four rotation speeds.

Figure 4.16 shows the pump efficiency as a function of the capacity coefficient for the different disk pack gap spacings by combining all the data irrespective of the pump rotational speed in a way similar to Fig. 1.5 in Chapter 1. Fig. 4.15 clearly show that the 5 thou spacing is the most efficient. The efficiency curves are not complete compared to other studies such as Darby et al. (1987) (Fig 1.5); not showing the downward trend at higher flow rate. The error bars in Fig 4.16 are not shown to due to the number of data points and the cluttering of the graph.
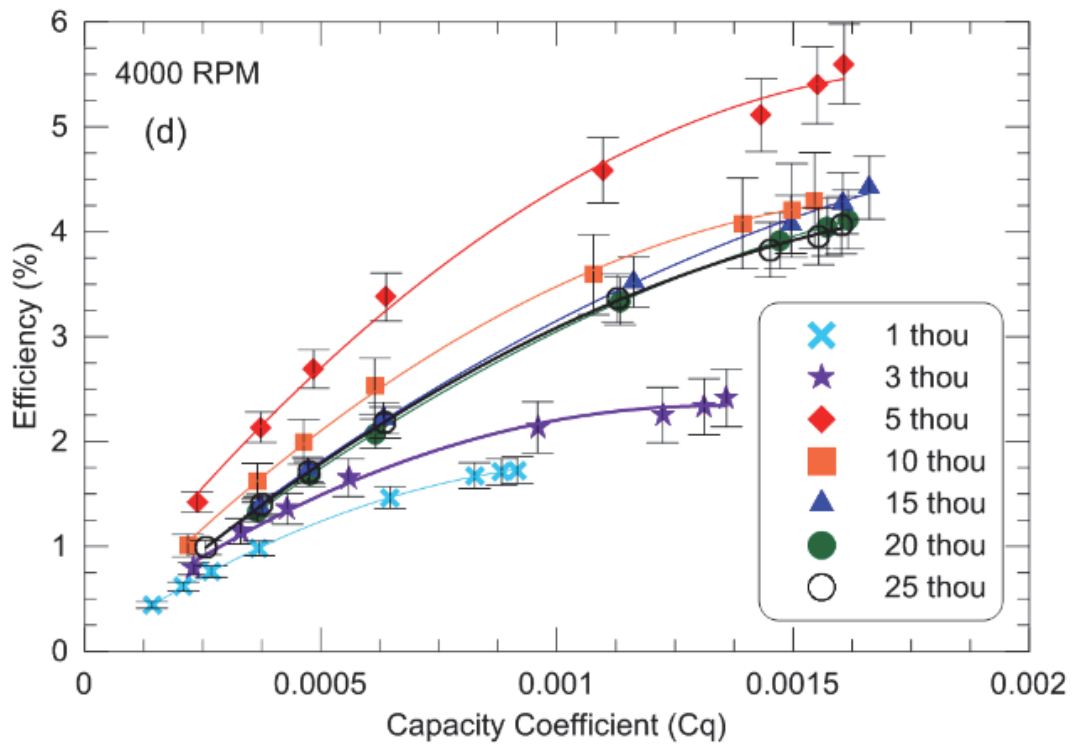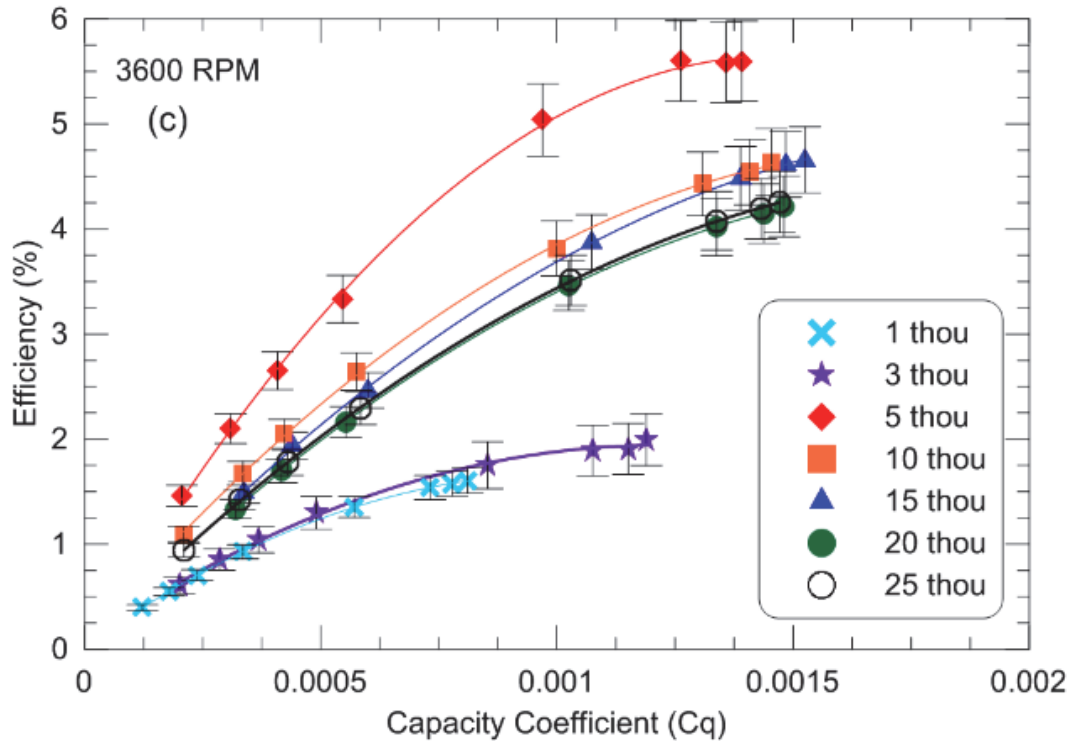
Figure 4.15. Capacity coefficient vs. Pump Efficiency, (a) 2500 RPM, (b) 3000 RPM, (c) 3600 RPM, and (d) 4000 RPM spacing comparison.

81
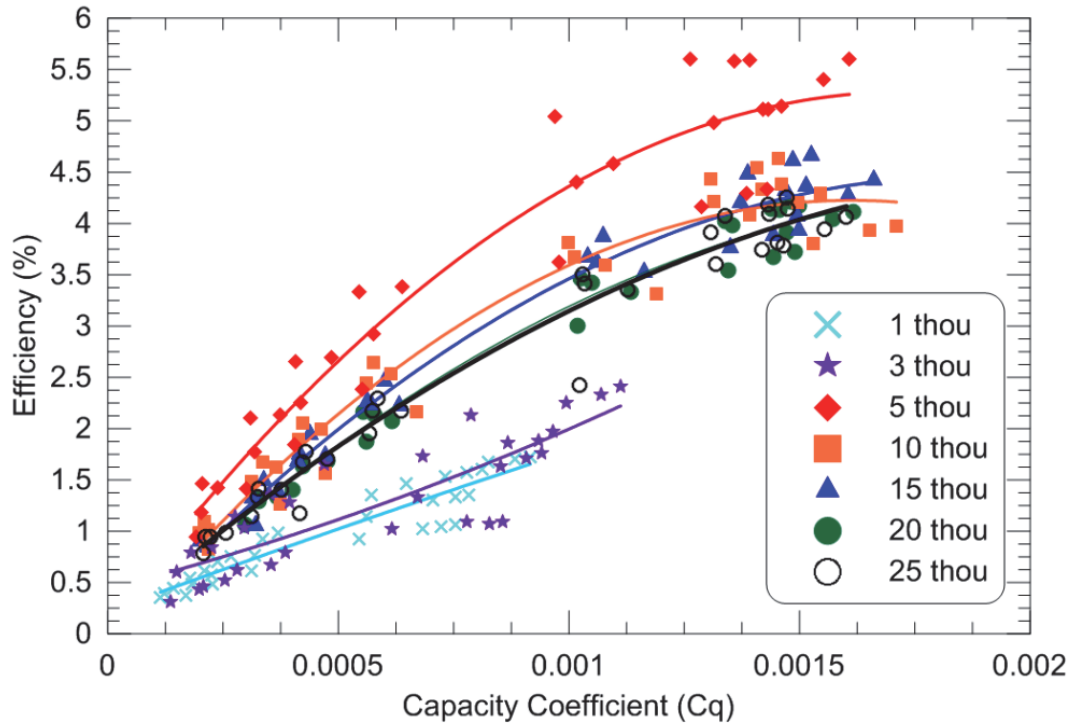
Figure 4.16. Characteristic Curve for Rotor Efficiency vs. Capacity coefficient, spacing comparison.

4.2.4 Study Comparison

As mentioned in the literature review of Chapter 1, the study performed by Darby et al. (1987) is similar to that of the work performed in this thesis, albeit using larger disks in their Tesla pump. Hasinger and Kerht (1963) is another similar study, although that the disk pack/rotor design is different. Table 4.5 shows the differences between these three studies, including the work presented in this thesis. There are both geometrical and rotational speed differences between these studies.

Table 4.5. Darby et al. study and the prototype pump dimensional and parameter comparison.

	(Darby et al., 1987)	(Hasinger & Kehrt, 1963)	Prototype pump
Diameter	14 in (35 cm)	4 in (10.6 cm)	1.38 in (3.5 cm)
Thickness	0.149 in (0.378 cm)	0.005 in (0.0127 cm)	0.0315 in (0.80 cm)
Gap (varies)	0.136 in (0.345 cm), 0.330 in (0.838 cm), 0.689 in (1.75 cm), 1.527 in (3.88 cm)	0.0053 in (0.0135 cm)	0.001 in (0.0254 mm), 0.003 in (0.0752 mm), 0.005 in (0.0127 cm), 0.010 in (0.0254 cm), 0.015 in (0.0381 cm), 0.020 in (0.0508 cm), 0.025 in (0.0635cm)
Gap/Diameter ratio	9.71×10^{-3}, 0.0236, 0.0492, 0.109	1.33×10^{-3}	7.24×10^{-4}, 3.62×10^{-3}, 7.25×10^{-3}, 0.0109, 0.0145, 0.0181
Rotational Speeds	300 to 2750 RPM	2400 to 5090 RPM	2500 to 4000RPM
Number of disks (corresponds to given gap spacing's)	11, 8, 5, 3 disks	174 disks	27, 26, 20, 18, 16, 15 disks
Maximum Disk Pack Efficiency	30 %	65%	5.6%
Maximum Head Coefficient	0.09	1.8	0.165
Maximum Capacity Coefficient	0.006	0.1	0.0015
Disk Pack Fastening	5 bolts	N/A	3 bolts

In Darby et al., the size of the disks (diameter and thickness) is larger, and the rotational speed was less than the prototype pump study performed here. This affects both the dimensionless coefficients and specific speed. The maximum capacity coefficient for Darby et al.'s study was approximately 0.006, and the maximum head coefficient was 0.09 (Darby et al., 1987), while the prototype study performed in this thesis obtained capacity and head coefficients of 0.0015 and 0.165, respectively. It is clear that this study produced larger values of dimensionless pump head, yet obtaining lower capacity coefficients than Darby et al.'s pump. The variable that has caused the largest differences between these studies would likely be the rotational speed and larger disk diameter.

In the other study, by Hasinger and Kehrt (1963), the design of the pump was different in that the disks are at an angle from the entrance/shaft and are more cone shaped than flat, which is shown in Fig. 1.3. The purpose of such a design was to utilize mixed and axial flow to create lower inlet velocities but yet higher inlet flow rates (Hasinger & Kehrt, 1963). This was to prevent cavitation at the entrance and therefore inside the pump as well. This design is not of a traditional Tesla pump; however, the results are interesting. Capacity and pressure coefficients of 0.1 and 1.8 where obtained, respectively.

The pump efficiency for this prototype pump study is significantly less than that found by Darby et al. This study obtained a maximum efficiency of 5.6%, where Darby et al. obtained around 30%. With the altered disk pack design, Hassinger and Kehrt obtained higher pump efficiencies of up to 65%. This suggests that Hasinger and Kehrt's disk pack design could be an improvement of the conventional Tesla pump. Both of the studies used a larger disk diameter which increases the surface area and in turn the performance of the pump. Therefore, it would be beneficial to look at lower rotational speeds and possibly larger disk pack spacings.

Darby et al. had the largest gap to disk radius ratio (d/D); however Hasinger and Kehrt's pump produced the highest head and capacity coefficients with a gap to diameter ratio less than Darby et al. It is difficult to compare Darby et al., and Hasinger and Kehrt disk gap/diameter ratio when Hasinger and Kehrt's rotor design is different. However, due to efficiency and flow rates obtained by Darby et al. compared to the prototype pump used in this work, it may be ideal test a larger disk diameter and gap spacings.

Another factor contributing to the large difference in efficiency is suspected to be caused by the casing design, specifically the inlet and outlet. The Tesla turbine studies from Chapter 1 suggest that the inlet design is also important for performance. Air trapped between the disks and obstructing flow could be a factor as well, however it appears that most of the air that could have been trapped in the pump was bleed out before actual testing was done.

The method of fastening the disks together was similar between Darby et al. and this prototype pump, in that they both used bolts which passed through all of the disks. Darby et al. used five bolts where the prototype pump uses three. The method of using bolts to fasten the disks together blocks a portion of the flow between the disks. Since Darby et al. did not depict how the five bolts where placed through the disks in their system, a quantitative comparison cannot be made. However, it can be deduced that using five bolts would obstruct the flow more compare to three, where the three bolts for the prototype pump produce up to 28% blockage as calculated earlier.

4.3 Propylene Glycol Mixture Testing

A PG-water mixture of 40/60 weight percent was used to study the effects of viscosity on the prototype Tesla pump performance. The glycol/water mixture was used since it is readily available and typically used as a heat transfer fluid. Only four of the disk pack spacings were tested with the PG-water mixture: 5, 10, 15 and 20 thou along with three rotational speeds: 2500, 3000, and 3600 RPM. The 4000 RPM rotational speed was not performed with the PGM due to a lack of consistency in which the motor could sustain that speed. Essentially, the load on the motor was too great for the pump to reach and sustain the 4000 RPM speed.

Table 4.6 compares the density and viscosity of water, PG and the PG-water mixture. The pump would not run with pure PG, since the motor could not handle the increased load.

Table 4.6. Comparing density and viscosity of water, PG and the PG-water mixture. Data from (The Dow Chemical Company, 2016)

	water	PG	PG-water mix
Density (kg/m^3)	998	1040	1032
Viscosity (cp)	0.89	42	4.5

The boundary layer thickness and Reynolds numbers for the PG-water mixture are shown in Table 4.7. These boundary layer thicknesses are again calculated for the full radius of the disk. From Table 4.7, the Reynolds numbers are less than those for water (Table 4.2) due to the increased viscosity. The boundary layer thicknesses for the PG-water mixture under the laminar flow regime are larger than that of water, while the turbulent thicknesses for the PG-water mixture are less than that for water. This is due to the different properties of the PG-water mixture compared to just water. For a more viscous fluid there would be more resistance to any forces applied to the fluid compared to that of a less viscous fluid, therefore a laminar boundary layer would be thicker since it would be more difficult to accelerate the fluid. For a turbulent boundary layer, it would become difficult for it to expand like that for water due the increased resistance of the fluid. The testing performed was assumed to be laminar flow, according to the Reynolds numbers, in Table 4.7, which are less than the critical rotational Reynolds number (2×10^5.)

Table 4.7 Rotational Reynolds number and boundary layer thickness for turbulent and laminar flow, for the PG-water mixture.

RPM	$\mathbf{Re_\theta}$	Laminar- BL thickness (thou)	Turbulent- BL thickness (inch)
2500	3.30×10^4	20.5	2.58
3000	3.96×10^4	18.8	2.49
3600	4.76×10^4	17.1	2.40

Table 4.8 shows the Reynolds numbers assuming internal flow between the disks, for the rotational speeds and gap spacings tested for the PG-water mixture. The Reynolds numbers are larger than that for the water, however are still laminar.

Table 4.8. Internal Flow Reynolds numbers for the various gap spacing's and rotational speed (PG-water mixture).

RPM/Gap Spacing	Reynolds number			
	5 thou	10 thou	15 thou	20 thou
2500	129.2	258.5	387.7	516.9
3000	155.1	310.2	465.3	620.3
3600	186.1	372.2	558.3	744.4

4.3.1 Impact of Pump's Rotational Speed

Figures 4.17 (a) to 4.20 (a) show the head vs flow rate curves for various spacings showing the effects of rotational speed. The overall effect of rotational speed with the PG-water mixture produce similar trends to that of the water testing; however, the resulting flow rates are slightly less and the pump head is larger. The maximum flow rate obtained for PG-water was 1.23 L/min and the pump head 3.22 m for the 15 thou operating at 3600 RPM (Fig 4.19 (a)), while for water the maximum flow rate was 1.45 L/min and pump head was 2.8 m. When comparing the 3600 RPM rotational speed to the rest (2500 and 3000 RPM) in Figs. 4.18 (a) to 4.20 (a), the difference in performance due to rotational speed is more significant. The 15 thou spacing at the highest rotational speed tested is the most performant spacing for the PG-water mixture as well as for water.

The effects of rotational speed on the pump efficiency for the PG-water mixture at various spacings are shown in Figs. 4.17 (b) to 4.20 (b). The efficiencies for the PG-water mixture runs are less than that for water, where the maximum efficiency obtained was 2.54% (2500 RPM, 20 thou) and for water was 3.58 % (4000 RPM, 5 thou). Since, the working fluid is more viscous, more energy is needed to overcome the shear stresses to accelerate the working fluid.

For the smallest spacing of 5 thou, in Fig 4.17 (b), the differences between the three rotational speeds are almost negligible. For Figs. 4.18 (b) to 4.20 (b), the slowest rotational speed (2500 RPM) is the most efficient, which is due to better utilization of energy compared to the higher rotational speeds.
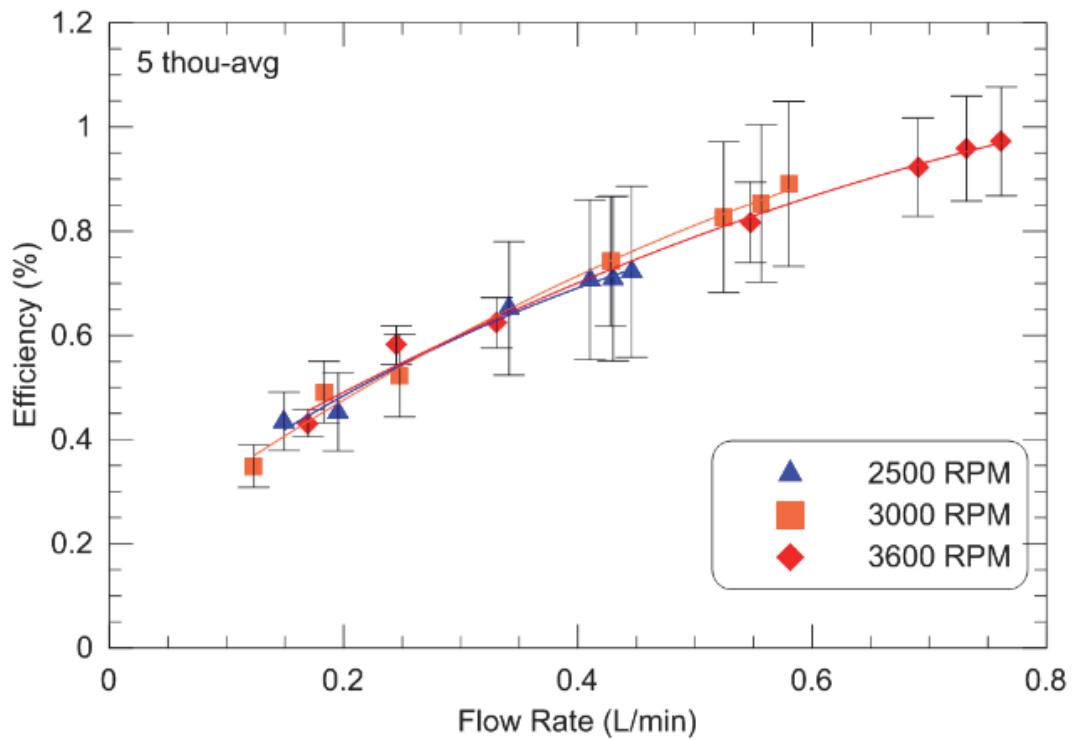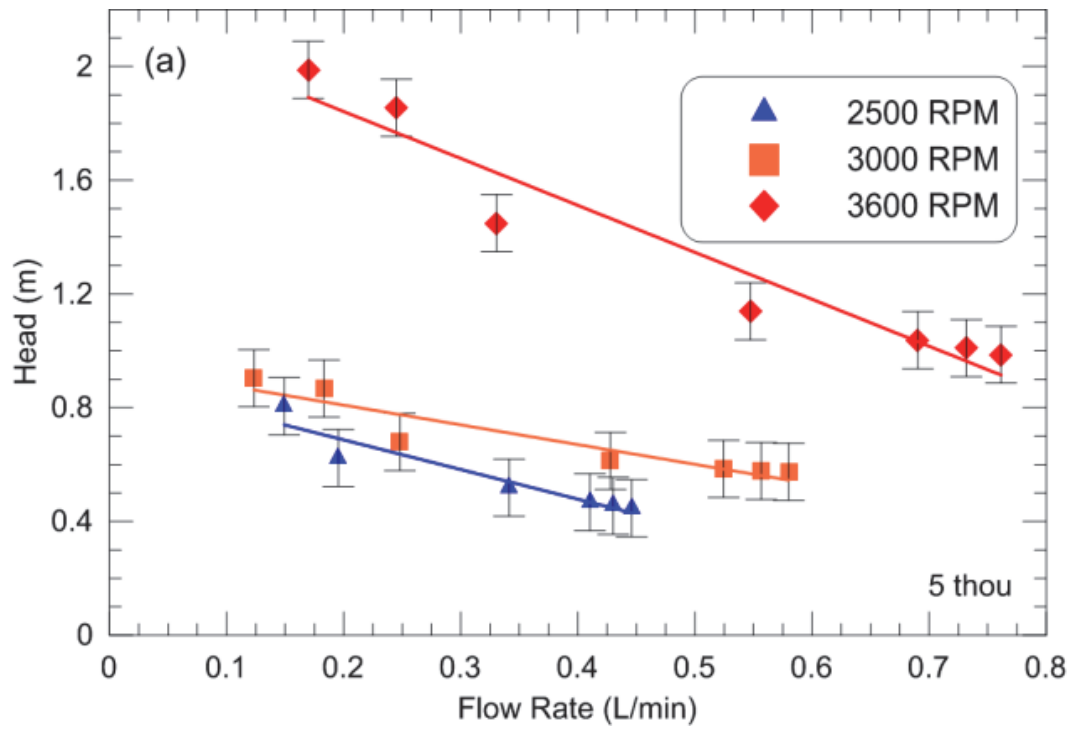
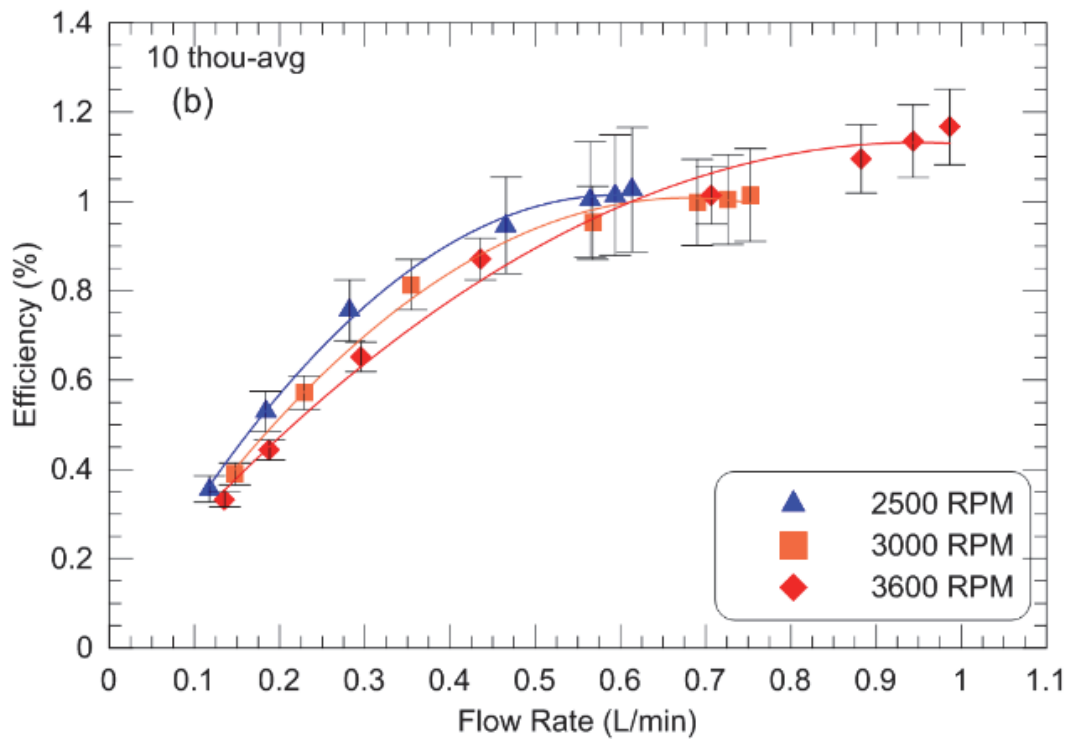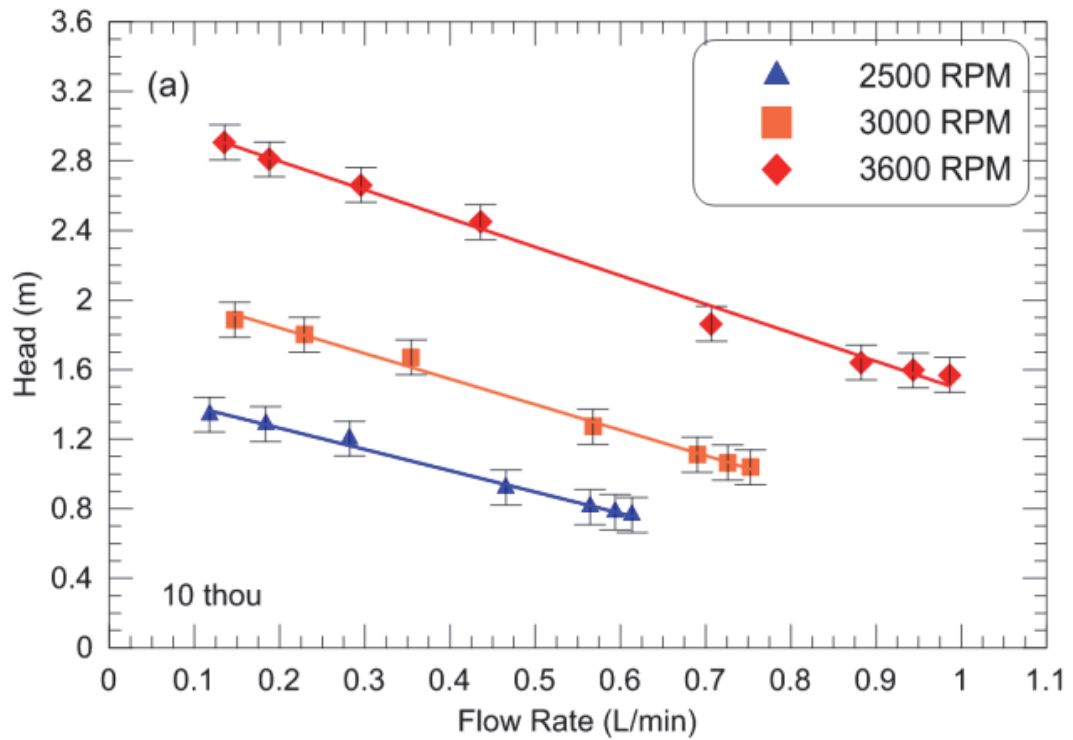**Figure 4.17. PG-water 5 thou (a) Head and (b) Efficiency vs. flow rate.**

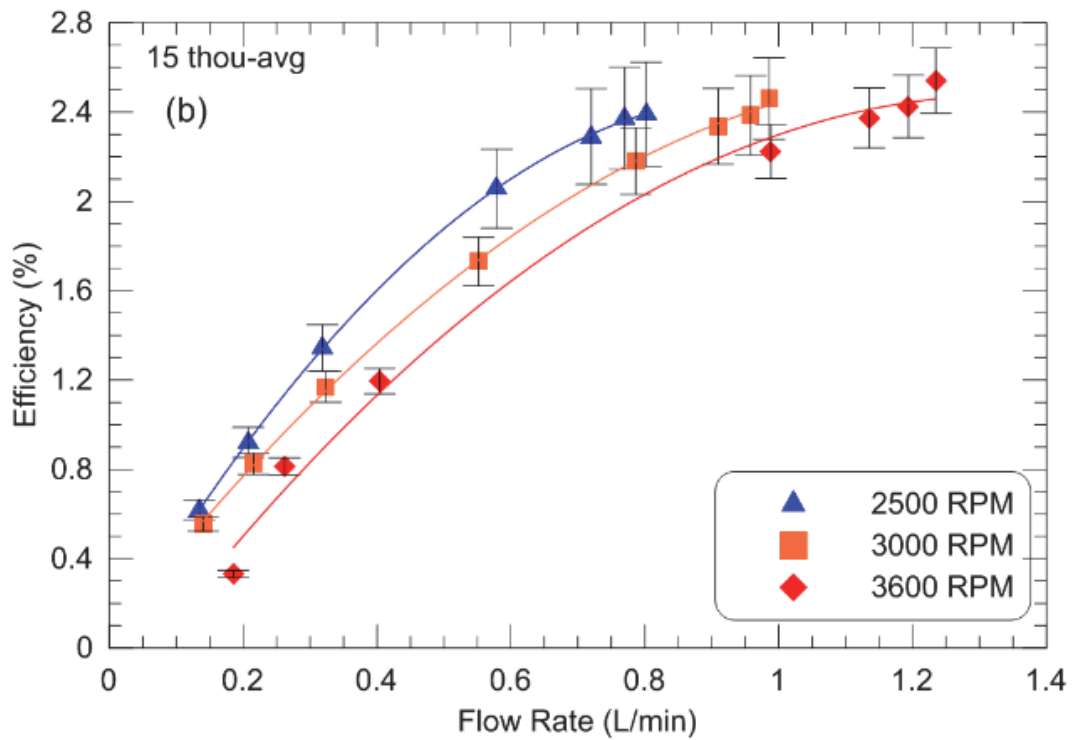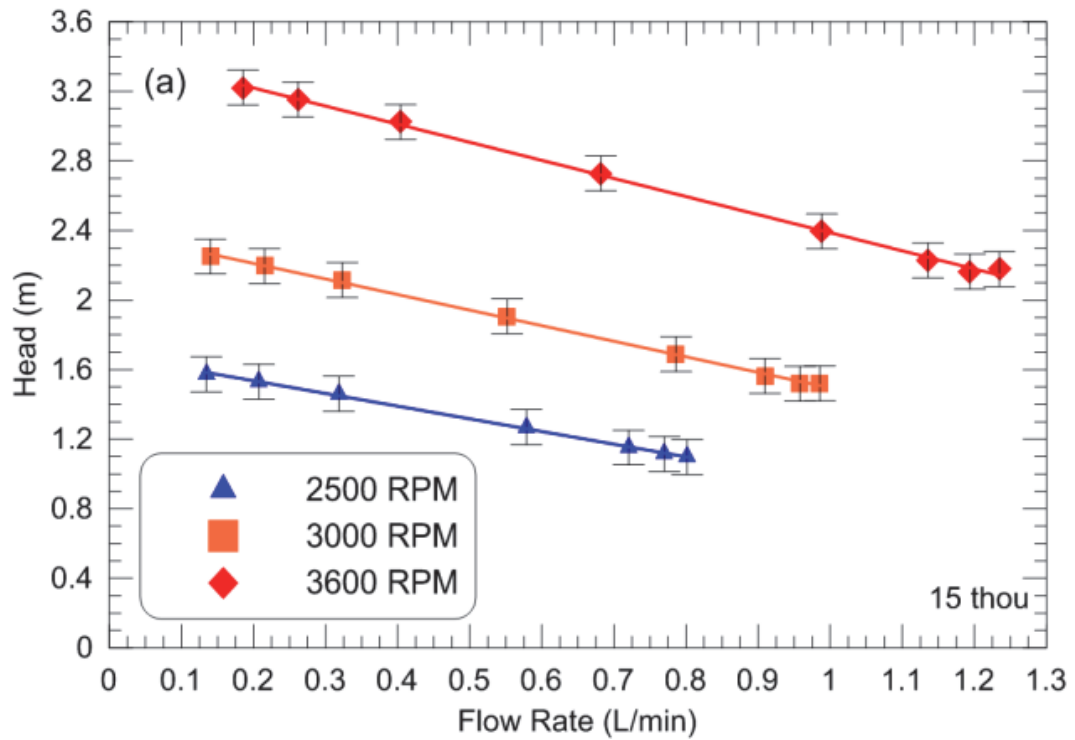**Figure 4.18. PG-water, 10 thou (a) Head and (b) Efficiency vs. flow rate.**

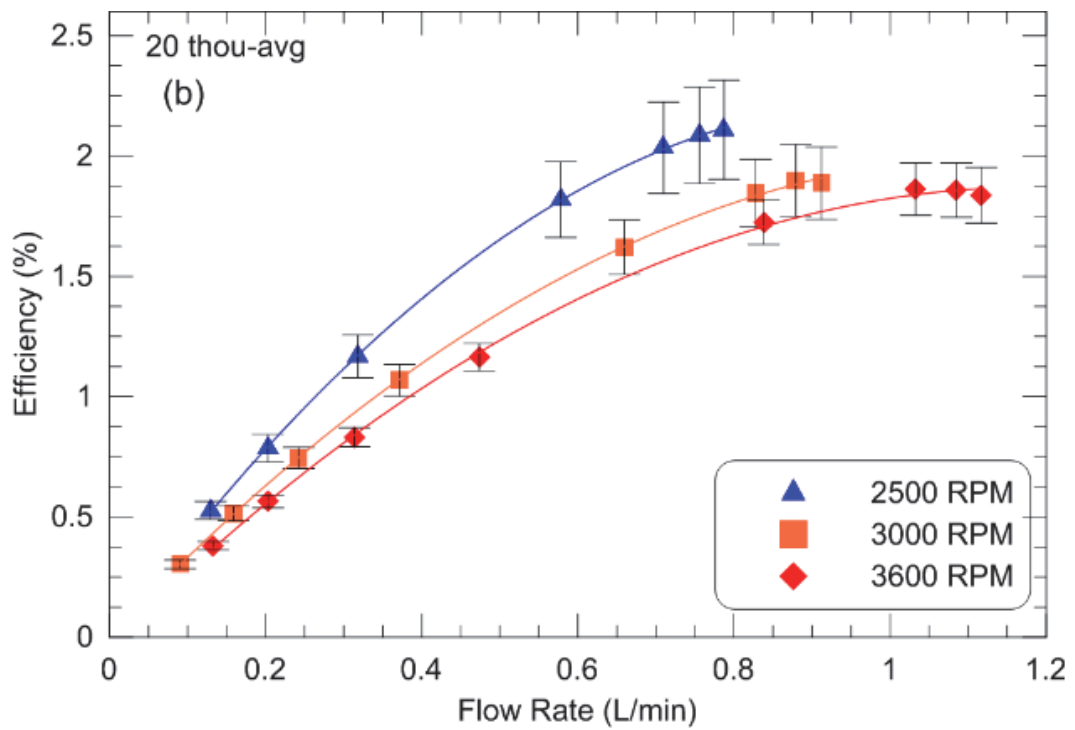**Figure 4.19. PG-water, 15 thou (a) Head and (b) Efficiency vs. flow rate.**
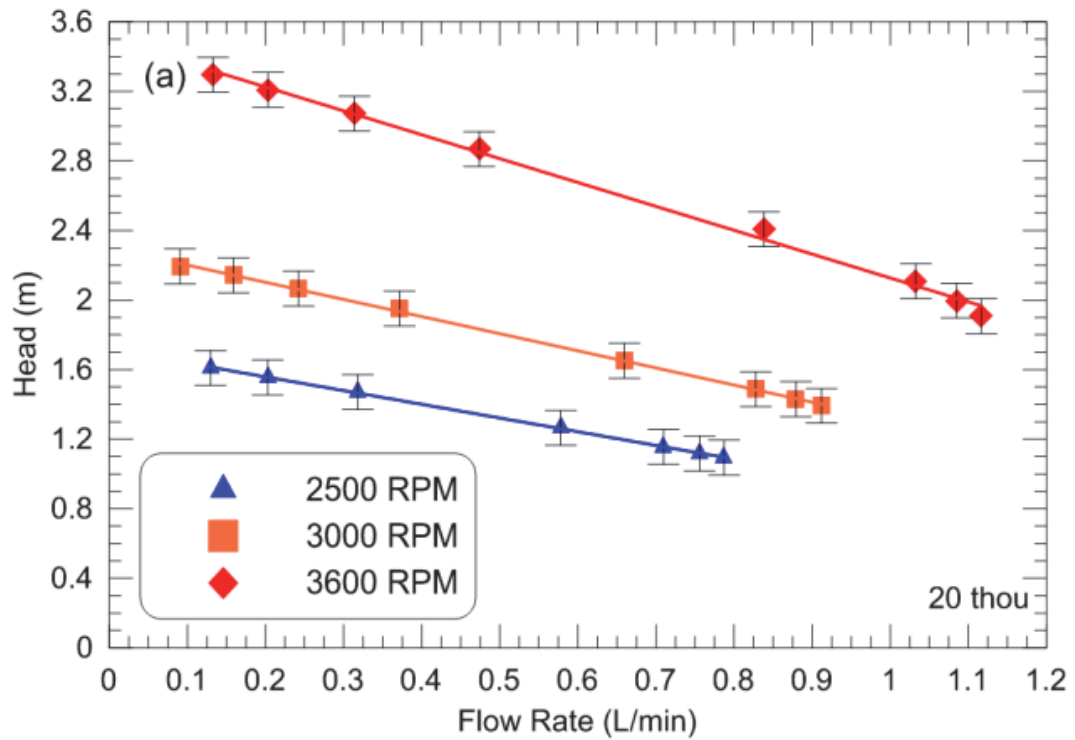
90

Figure 4.20. PG-water, 20 thou, (a) Head and (b) Efficiency vs. flow rate.

4.3.2 Effect of Disk Pack Spacing

Figures 4.21 (a) to 4.23 (a) show head vs. flow rate plots for the various rotational speeds comparing different disk pack spacings for the PG-water mixture. The 15 thou spacing appears to be the most performant spacing, producing the highest pump head and capacity within the measurement error. The 20 thou spacing in Fig. 4.21 (a) for 2500 RPM does appear to be just as performant as the 15 thou. However, as the rotational speed increases the 20 thou spacing becomes less performant compared to the 15 thou as shown in Figs. 4.22 (a) and 4.23 (a), for 3000 and 3600 RPM respectively. The minimum laminar boundary layer thickness from Table 4.7 is 17.1 thou for 3600 RPM. Therefore, fully developed flow is occurring between the disks since the boundary layer thickness is larger than half a gap spacing. For the water tests, the performance of the 15 thou spacing was closer to the other spacings compared to tests with the PG-water mixture. There is a similar trend where the 15 thou spacing is still the most performant between the water and PG-water tests. The increased viscosity tends to produce a larger observable difference between the spacings compared to that observed from water.

The efficiency vs. flow rate when comparing the various disk pack spacings for various rotational speeds is shown in Figs. 4.21 (b) to 4.23 (b). The trends for the PG-water mixture are different than those found in section 4.2.2 for the water tests. Figures 4.21 (b) to 4.23 (b) show that the 15 thou spacing is the most efficient spacing within the measurement error, while 5 thou is the least effective. This could be due to the increased viscosity compared to water which renders the 5 thou spacing to narrow for proper flow of the more viscous PG-water mixture (increasing the force needed to accelerate the fluid). As for the 20 thou spacing, the difference in efficiency from the 15 thou spacing would be due to the increased surface area compared to the 20 thou spacing.
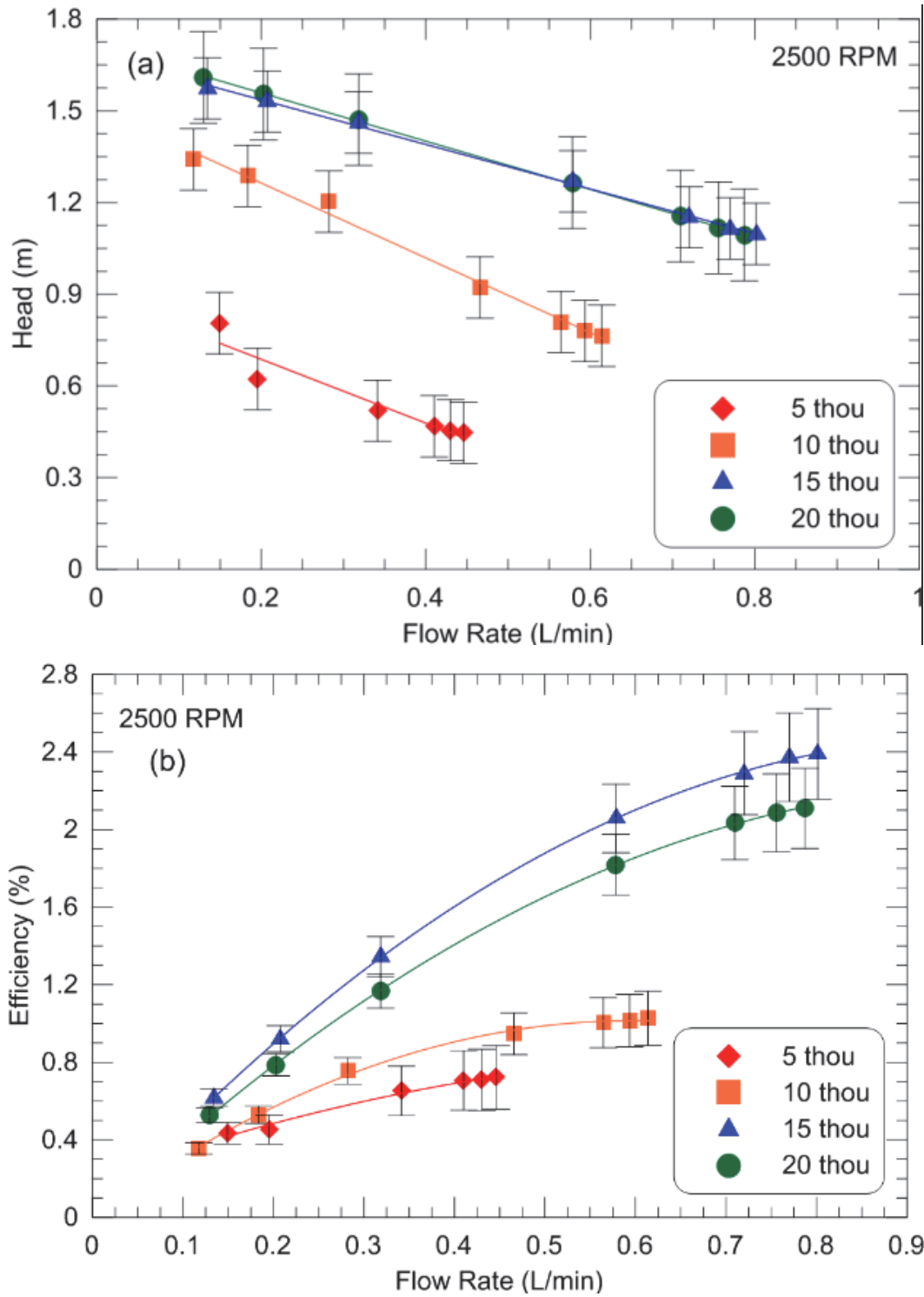
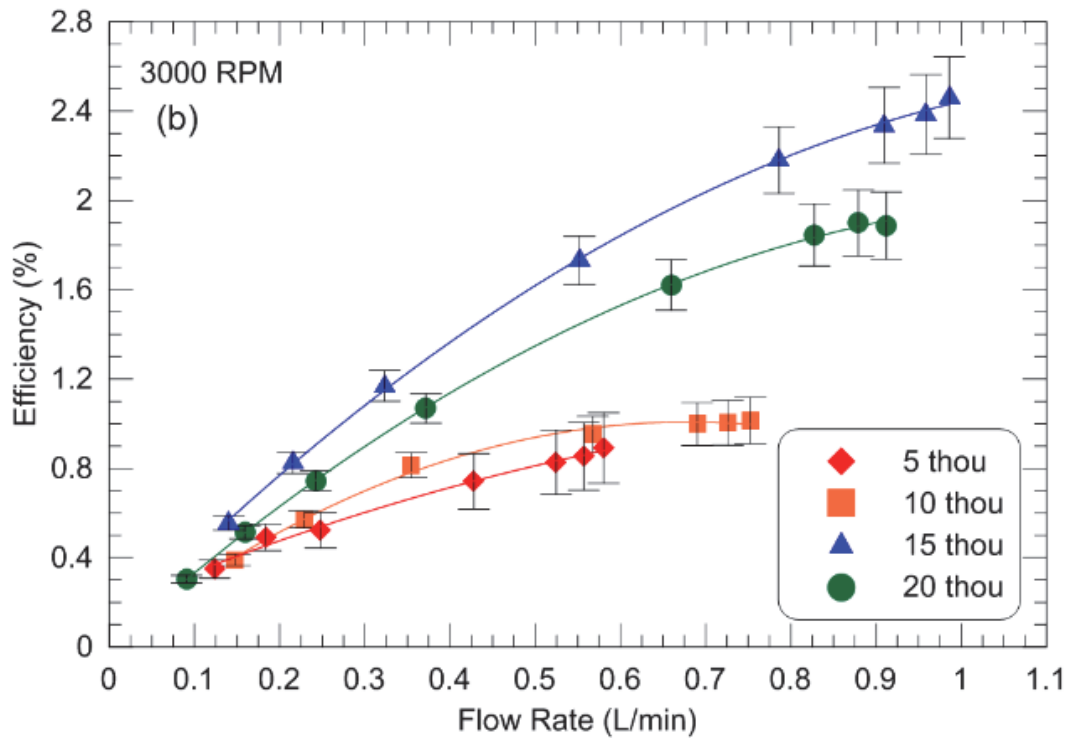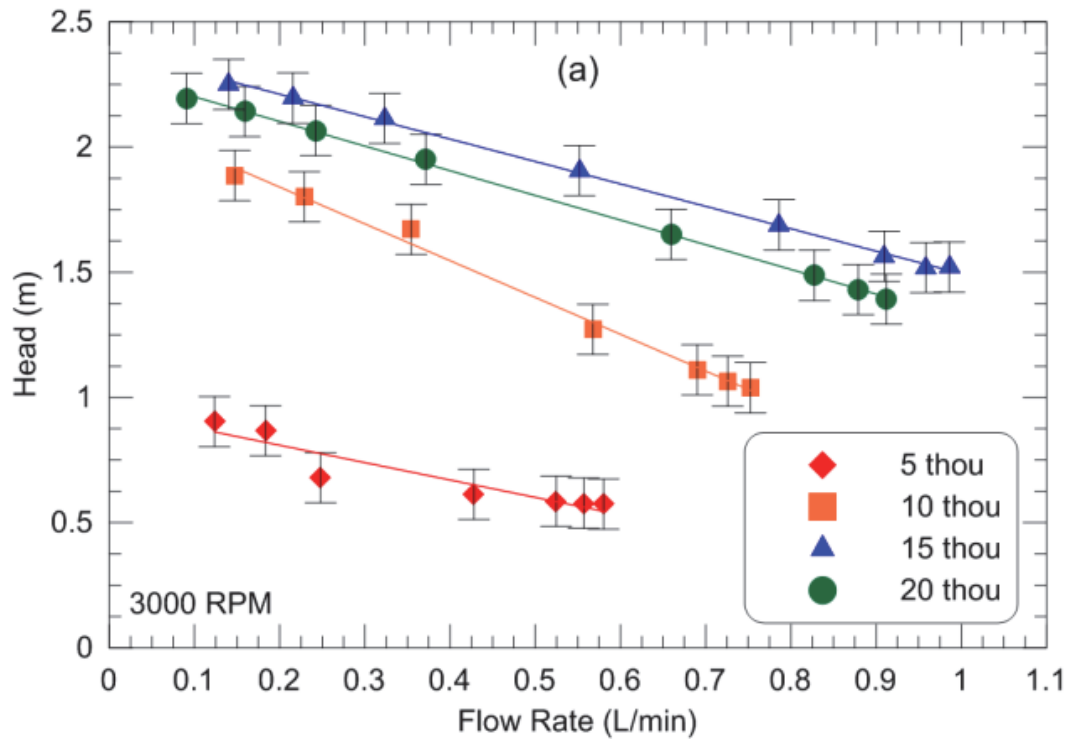**Figure 4.21. PG-water, 2500 RPM (a) Head and (b) Efficiency vs. flow rate.**

93

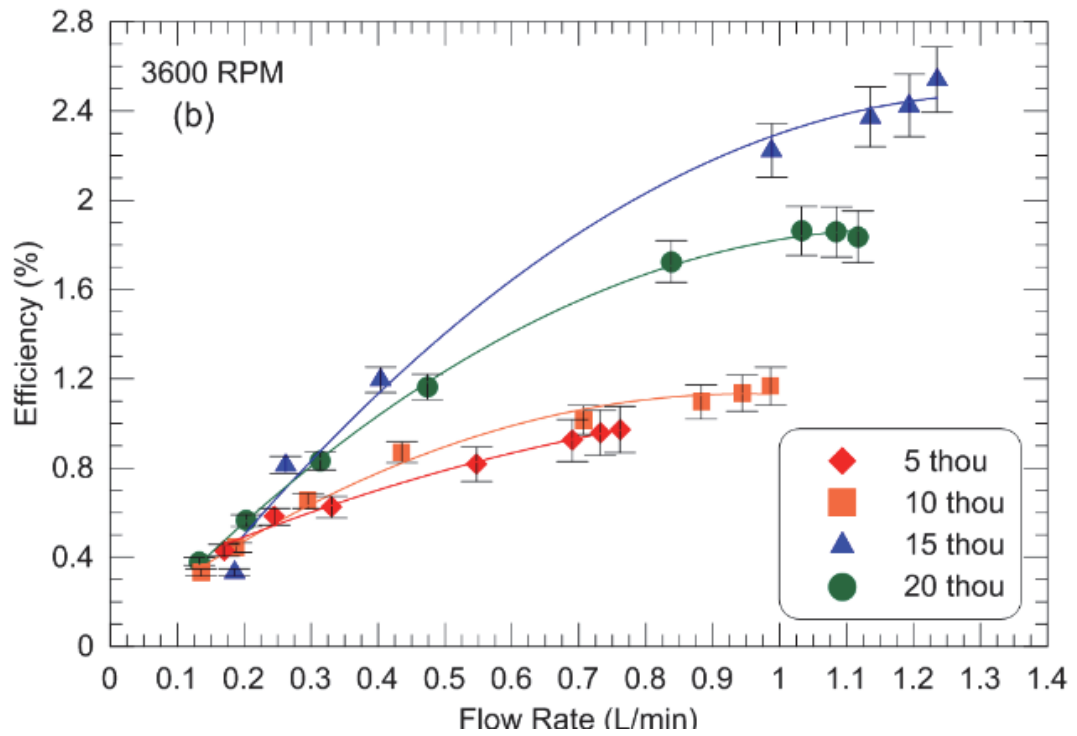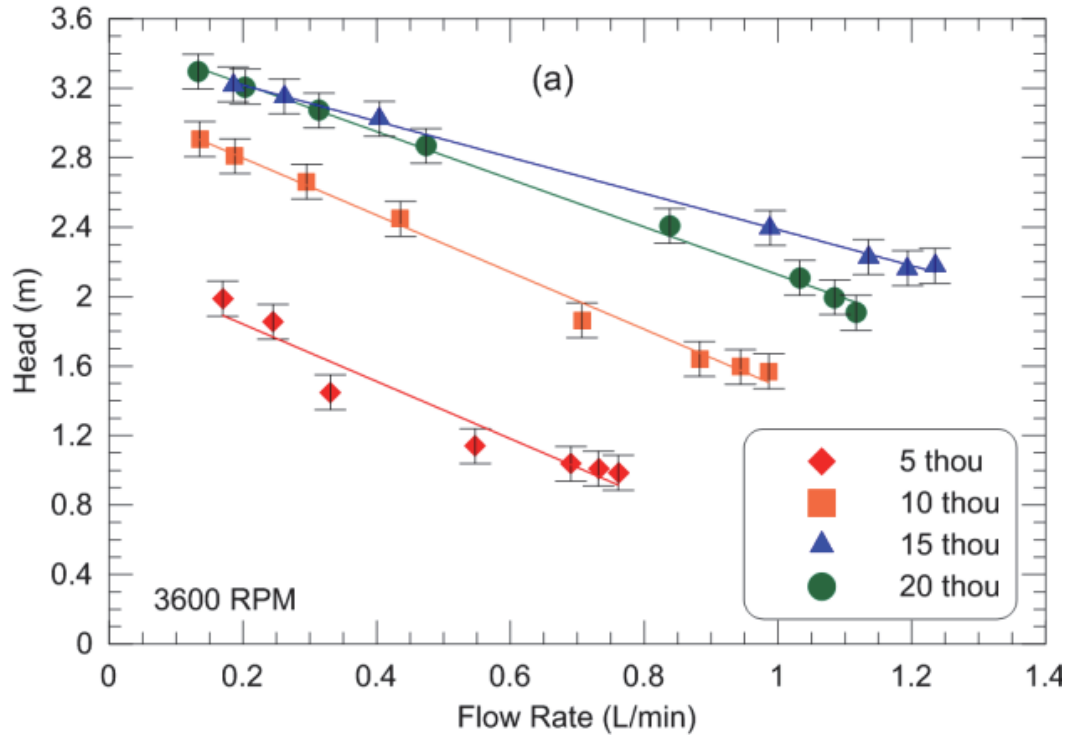**Figure 4.22. PG-water, 3000 RPM (a) Head and (b) Efficiency vs. flow rate.**

Figure 4.23. PG-water, 3600 RPM (a) Head and (b) Efficiency vs. flow rate.

4.3.3 Non-Dimensional Rotational speed

Figure 4.24 compares the water and PG-water head and flow coefficients for the various disk pack spacings, with regards to the effect of rotational speed. This is similar to what was presented in section 4.2.3, where the rotational speed should not play a factor and a characteristic curve should appear if the flow regime is similar between all the tests and disk pack configurations. Figure 4.24 (c), 15 thou spacing, the PG-water mixture obtains higher head and capacity coefficients than water, further suggesting that 15 thou is an ideal spacing. In Fig. 4.24, for the PG-water mixture, as the spacing increases, the head and capacity coefficients improve compared to water. The slope of the characteristic curve (or line in this case) for the PG-water mixture when compared to water are steeper, at least in Figs. 4.24 (b) to (d). This is due to the effect of the increased viscosity compared to water, where there is a steep drop in capacity and head coefficients.

In Fig 4.24 (a), for the 5 thou spacing, there is considerable variations between expected trends. For the 5 thou spacing, this huge variation could be due to a couple of factors, where one is air becoming trapped within the disk pack and the other being that the nature of the flow is different for each rotational speed. The other spacings show a reasonable agreement with regards to a characteristic curve, negating the effect of rotational speed on the head and capacity coefficients.
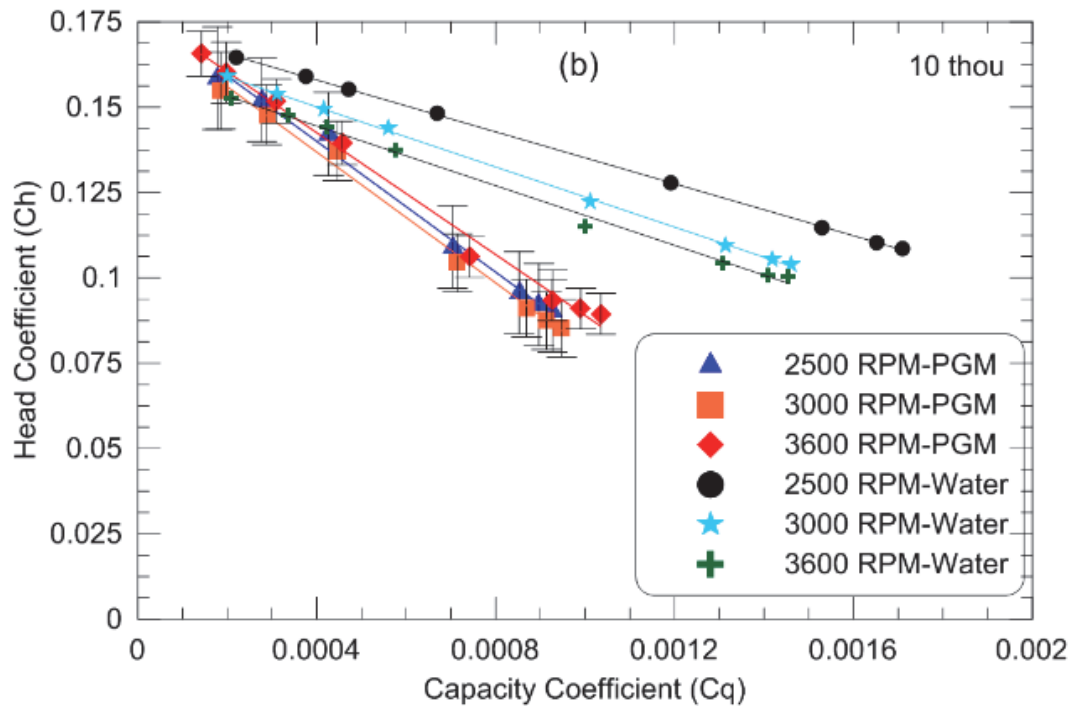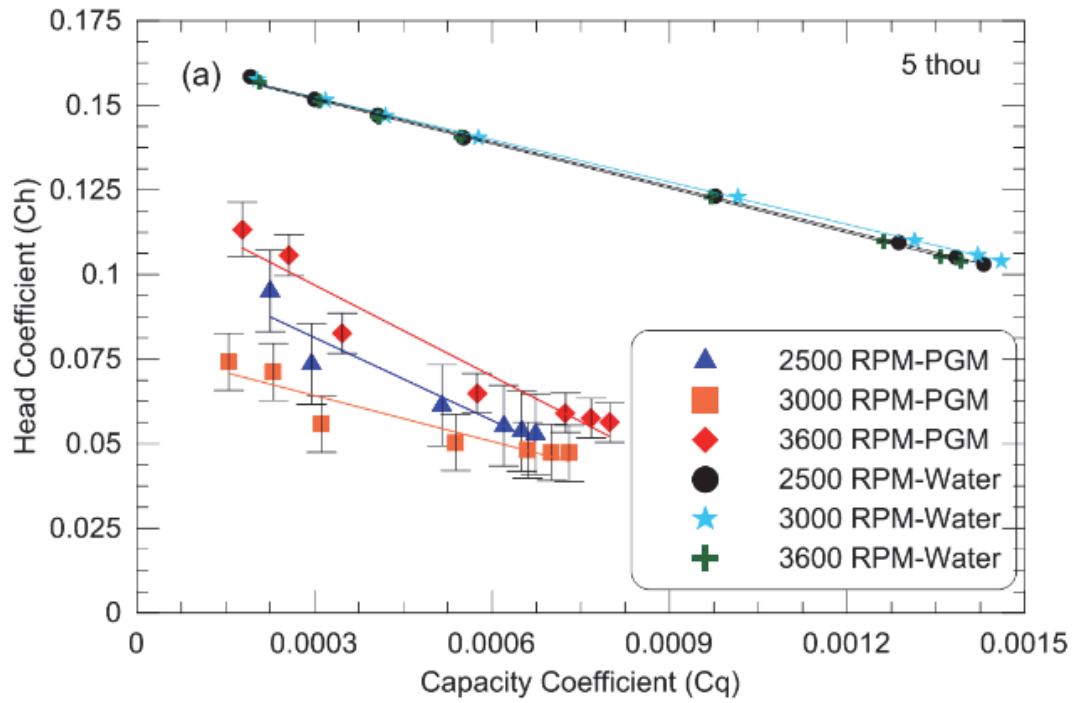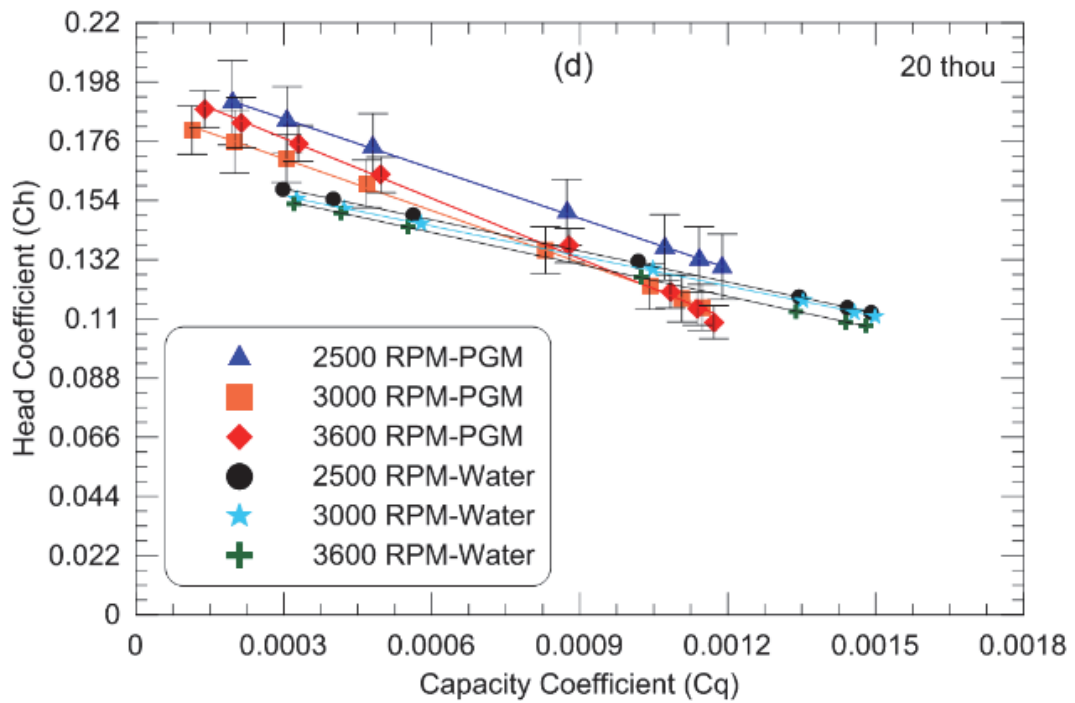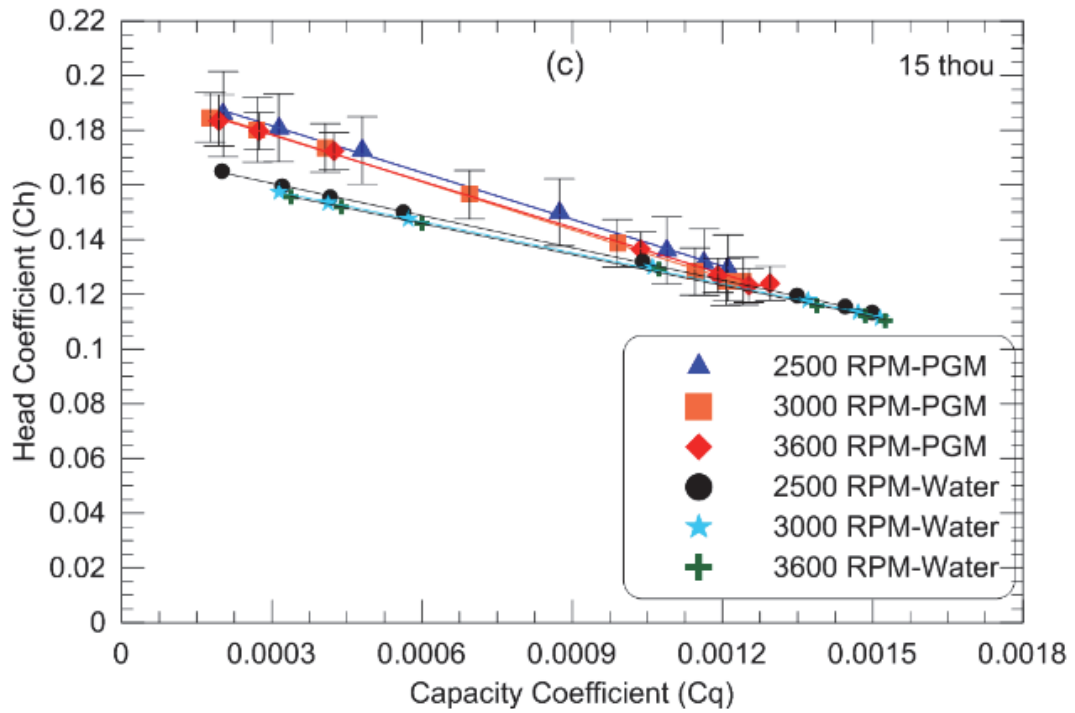
Figure 4.24. PGM, head vs. flow rate, rotational speed comparison for (a) 5 thou, (b) 10 thou, (c) 15 thou, (d) 20 thou.

98

4.4 Vibration Tests

The vibration tests were done under the two vibrational frequencies, 500 and 2000 Hz, as well as under no vibration for comparison. It is important to note that these tests were done with the pump sitting slightly below the flow meter and pressure sensor. This height was minimized, however, the height difference still effects the results. Therefore, when compared to the other water runs in section 4.2, these runs will produce less pump head and capacity. The results presented here will show the effect of vibration frequency on the pump and determine if cavitation is induced.

Figures 4.25 (a) and 4.28 (a), show the effects of two frequencies on the head and flow rate of the prototype pump for the 3600 RPM motor speed. There is little to no difference in pump head and flow rate due to various vibrational frequencies. Suggesting that cavitation is not induced, otherwise there would be large differences between the vibration and non-vibration runs.

Figures 4.25 (b) to 4.28 (b), shows the efficiency vs. flow rate for the vibration and non-vibration runs. The 20 thou spacing results, Fig. 4.28 (b), show the most deviation from the non-vibration runs, compared to the other spacings. The 5 thou spacing has the least deviation from the non-vibration run. Figs. 4.27 (b) and 4.28 (b), the 10 and 15 thou spacings do deviate from the non-vibration runs, however there is no clear trend suggesting this is likely due to experimental or human error.

In theory, the boundary layer can be affected by vibration (Cengel & Cimbala, 2010). However, it should only effect when the transition from laminar to turbulent flow occurs. Since the flow regime is clearly laminar, a transition to turbulence is not expected to occur yet. Regardless, if transitional flow was induced the flow would still become fully developed. It was expected that vibration would not significantly impact the performance of the pump, and has been shown not to according to Figs. 4.25 to 4.28. The vibration also was found to help remove the air trapped in the disk pack, which has been shown in Hasinger and Kehrt to impact performance.

Figure 4.25. 5 thou, (a) Head and (b) Efficiency vs. flow rate, effect of vibration frequency.

Figure 4.26. 10 thou, (a) Head and (b) Efficiency vs. flow rate, effect of vibration frequency.
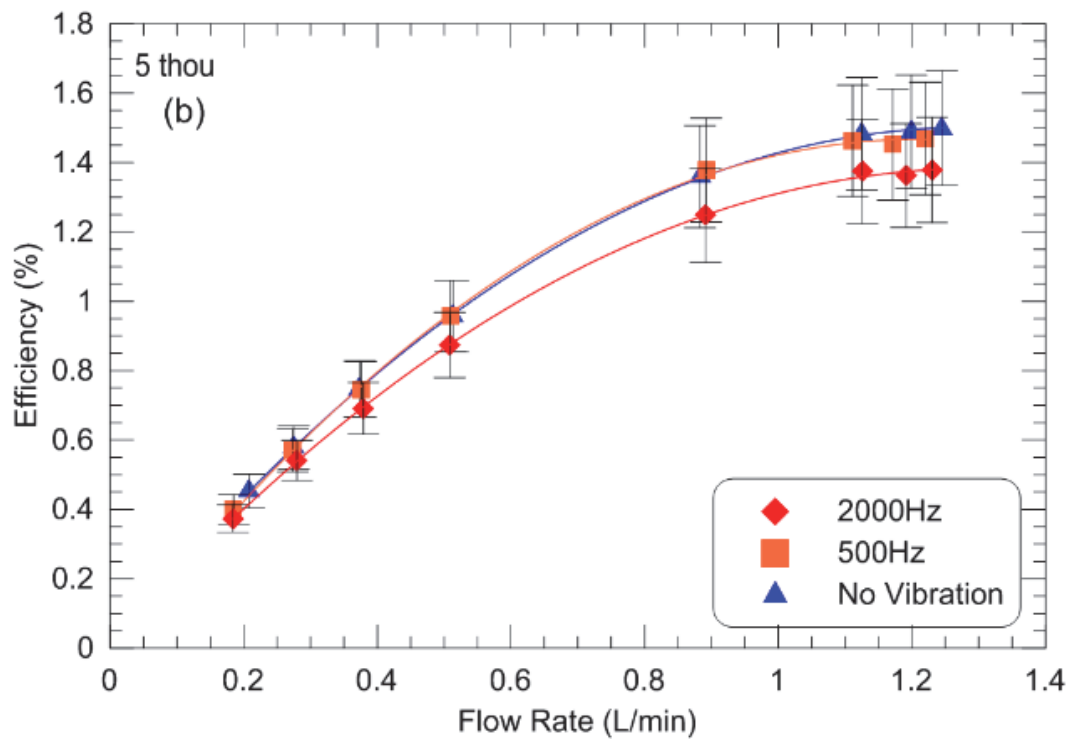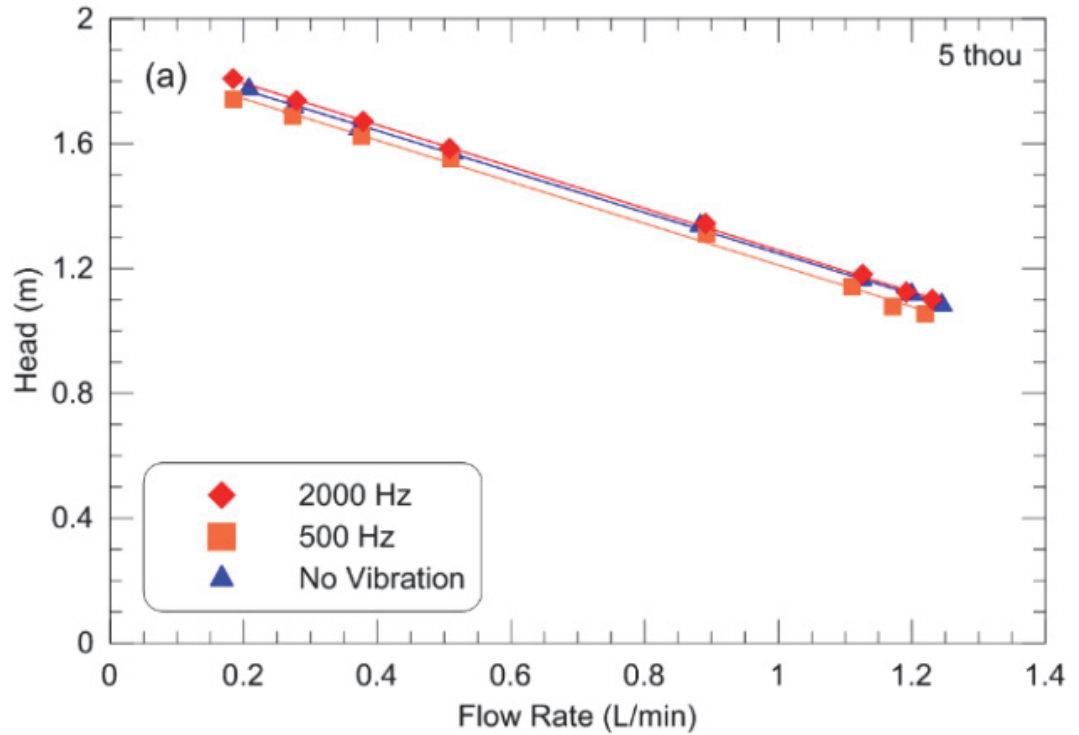
101

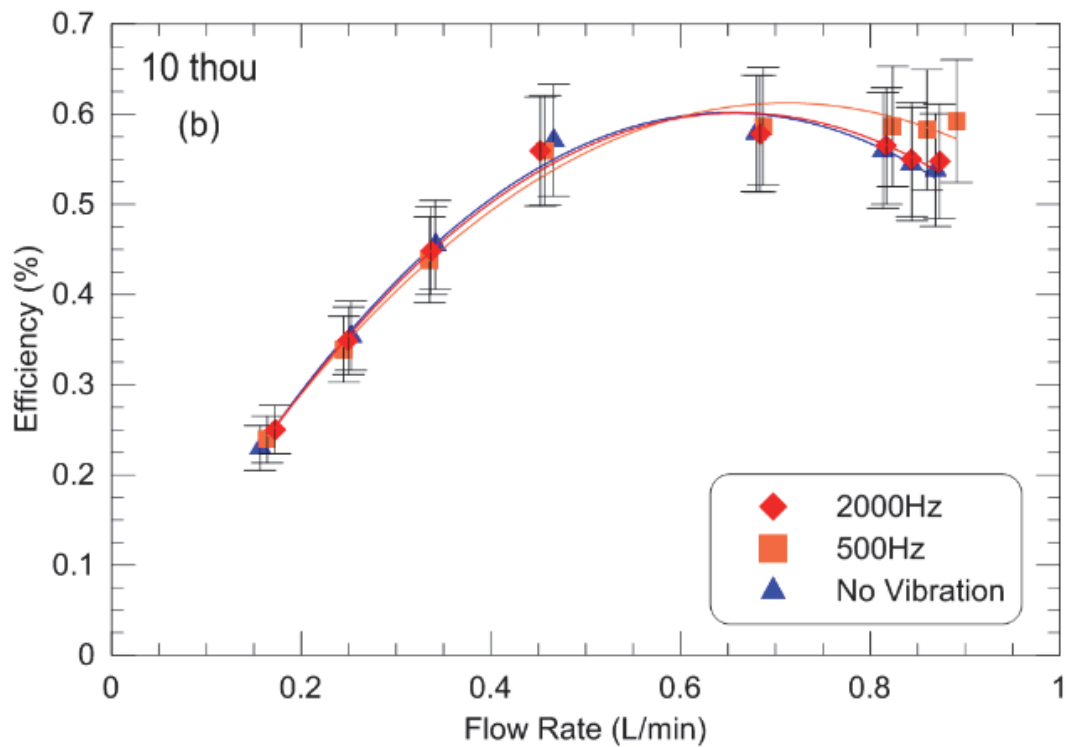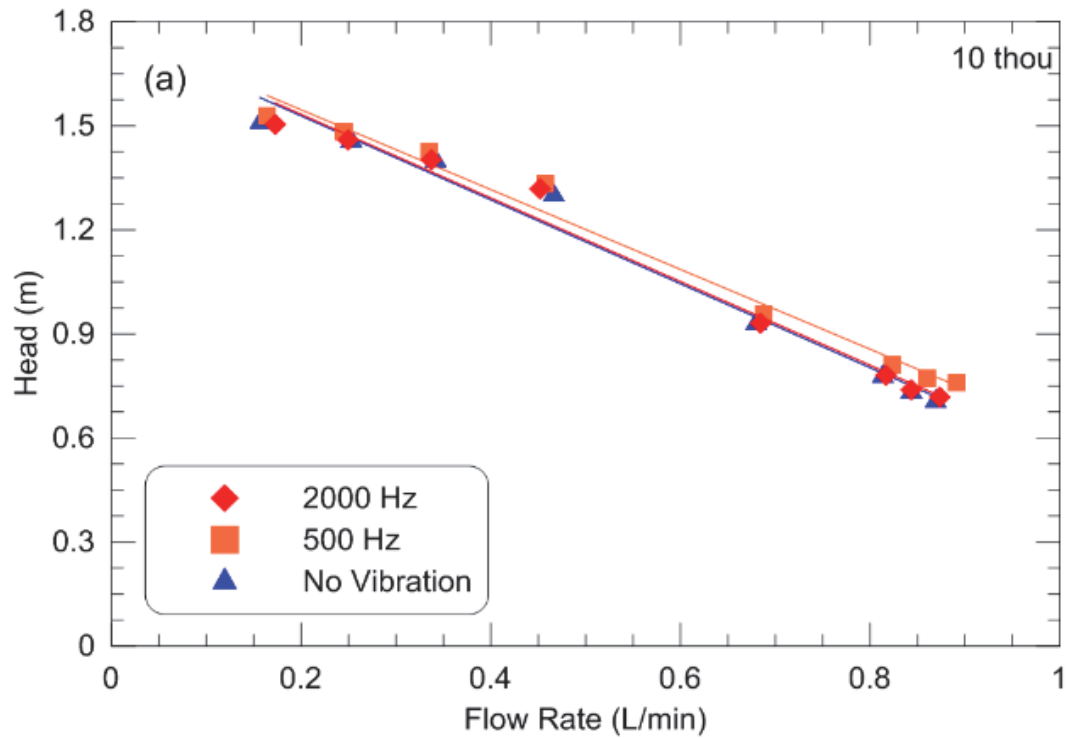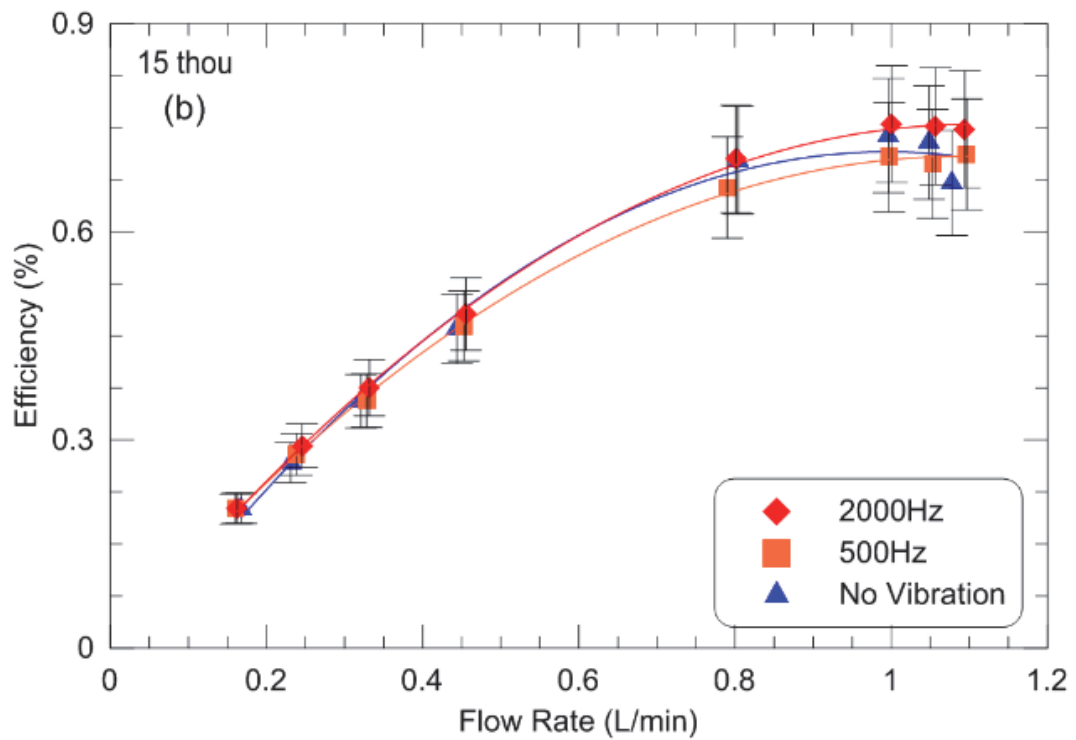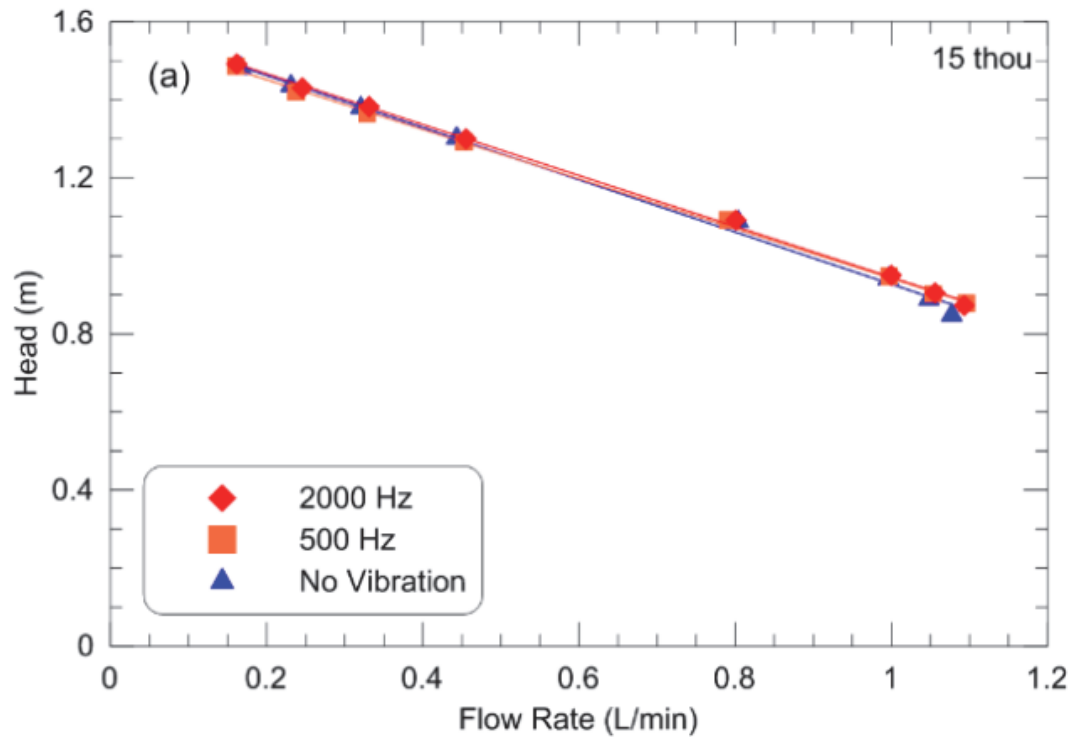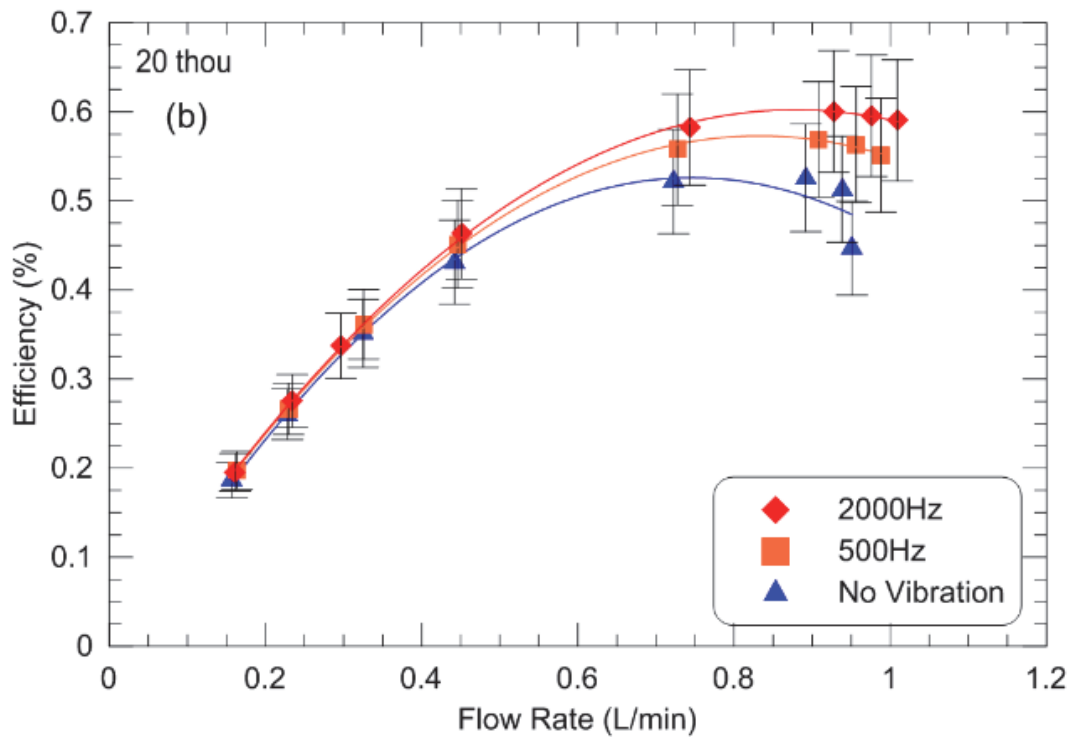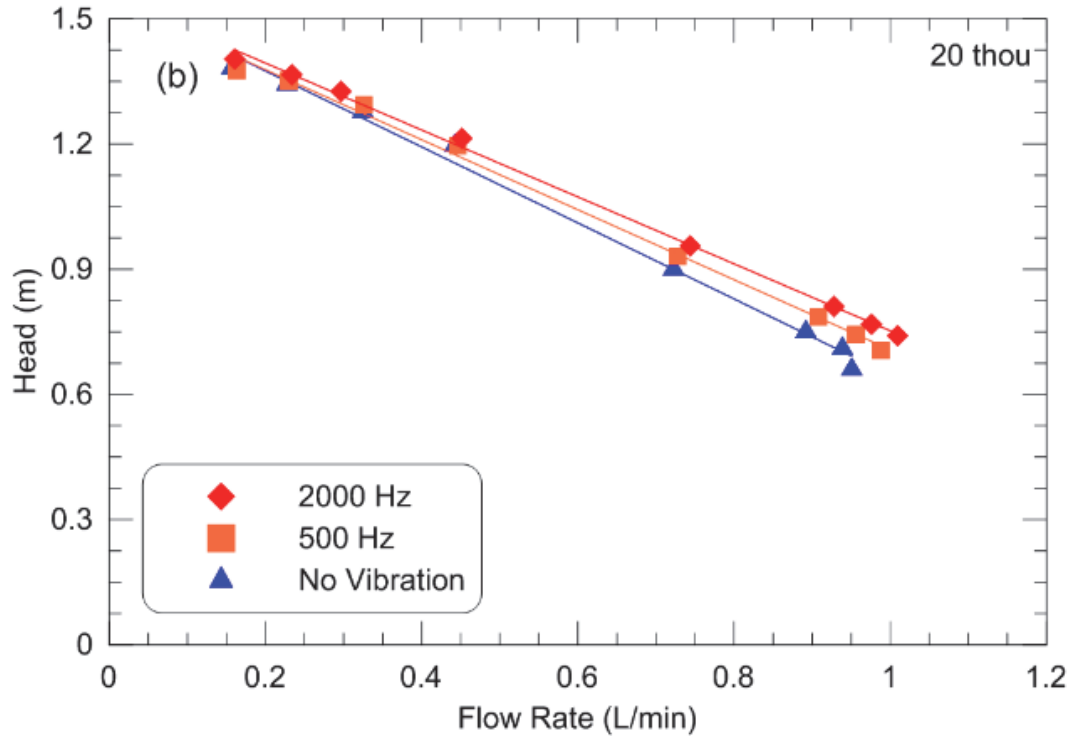**Figure 4.27. 15 thou, (a) Head and (b) Efficiency vs. flow rate, effect of vibration frequency.**

Figure 4.28. 20 thou, (a) Head and (b) Efficiency vs. flow rate, effect of vibration frequency.

103

4.5 Conclusion

This chapter presented the experimental results obtained when testing with water, PG-water mixture, and under vibration. It was as rotational speed increases, the pump produces higher head and flow rates. The efficiency for the higher rotational speeds was less compared to the lower speeds, where the lower speeds have better energy utilization compared to the higher speeds. The 15 thou spacing has been shown to be the most effective; however, was not the most efficient spacing for the water tests. The 25 thou spacing would allow for a laminar boundary layer to fit on either side in the gap between the disks, which would be at 4000 RPM for water. Since, the boundary layer thicknesses are generally larger than half of the gap spacing, this suggests that fully developed flow was occurring between the disks. The 15 thou spacing was the most performant compared to the other spacings since this was the spacing where fully developed flow occurs and possesses a slightly larger surface area than the 20 and 25 thou spacings.

An increase in the boundary layer thickness was observed for the PG-water mixture due to the increased viscosity compared to water. The increase in the thickness of the boundary layers was due to the increased resistance to forces applied to the fluid. The increased viscosity highlighted the effectiveness of the 15 thou disk pack spacing with regards to performance and efficiency.

The effect of vibration on a Tesla pump was shown to make little to no difference and cavitation was not induced. The difference between the vibration and non-vibration runs was contributed to experimental error.

The non-dimensional analysis for the head and capacity coefficients was shown to produce a characteristic curve for the Tesla pump. This was similar to what occurs for a centrifugal pump, and since a Tesla pump operates similarly, a characteristic curve for the prototype pump was expected. For the Tesla pump tested in this work, the characteristic curve was obtained for a laminar flow regime.

From section 4.2.4, presenting the comparison of Hasinger and Kehrt, Darby et al., and this thesis results, several ideas for improving the performance of the prototype pump where

determined. The largest problem with the performance of the prototype Tesla pump was its efficiency, which was considerably lower than the other studies. The prototype pump reached a maximum efficiency of 5.6%, where Darby et al. obtained 30% and Hasinger and Kehrt obtained efficiencies up to 65%. Air bubbles becoming trapped between the disks was mentioned to be an issue with regards to Tesla pump performance by Hasinger and Kehrt, and was likely a factor contributing to the lower efficiencies. It is recommended that a larger disk pack spacings and diameters be tried for the prototype pump, along with slower rotational speeds. The volute and casing design for the prototype pump was expected to be a major factor contributing to the decreased efficiency compared to the other studies. The impact of changes to the volute design has not been analysed in this MASc project.

Chapter 5 Computational Fluid Dynamics

A working numerical model of the Tesla pump developed during this research work and preliminary simulation results are presented here. The results from various steps of the model's production are compared to experimental data to validate the simulation as it was gradually improved. The working full size model is not an exact reproduction of the pump and disk pack, however is a good representation of the pump system. Section 5.1 describes the process the geometry and mesh went through to obtain the full size model. A brief description of how the simulation in CFX was set up is presented in section 5.2 and contains a visual analysis of selected simulations and results comparing the experimental and simulation results.

5.1 Geometry and Mesh

ANSYS 15.0, with the CFX module, a fluid dynamics computational program, was used to set up the pump simulation. The geometry was built in Solidworks and imported to ANSYS, where the simulation was then set up.

5.1.1 Geometry

A simplified model was first built to verify assumptions made for the simulation, after which the model was gradually improved. The very first model consisted of one disk within a cylindrical shaped volute, with outlet and inlet tubes, such as that shown in Fig. 5.1. The disk(s) in the simulations are empty space which has been removed from the rest of the model, since only the fluid domains are modeled. Figure 5.2 shows the one disk geometry with the realistic volute.

A four disk model with an improved volute design is shown in Fig. 5.3. It contains an isometric view and a cross sectional view showing the disks. The brown cylinder within the main volute is a rotating boundary; this was the method used to simulate the rotation of the disks.
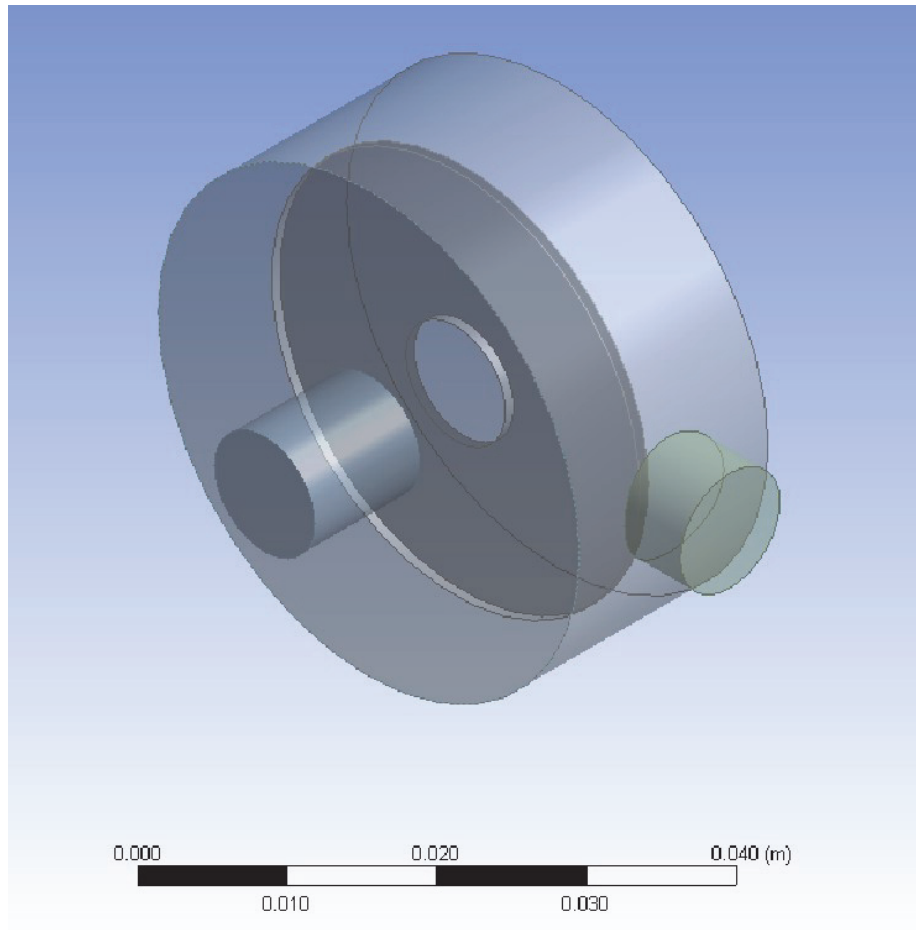
Figure 5.1. Original 1 disk volute with hidden rotating boundary.
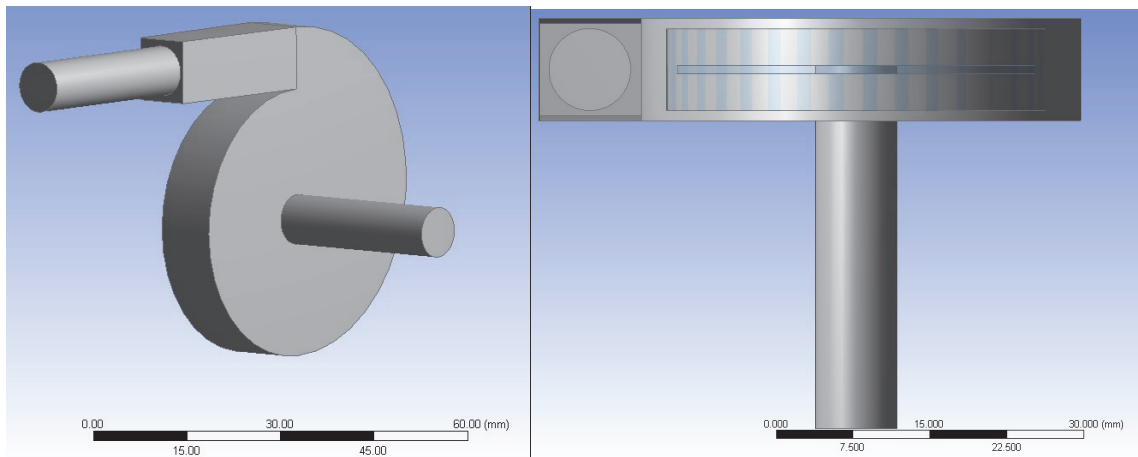
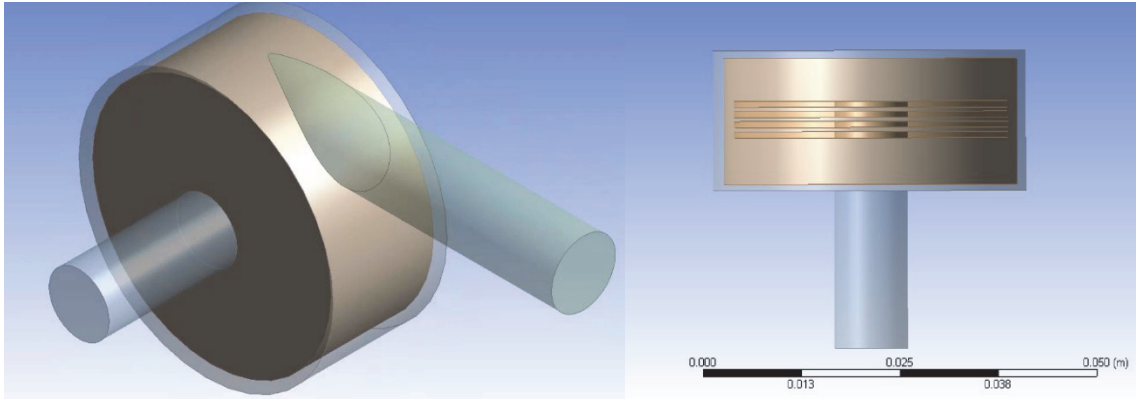
Figure 5.2. 1 disk model with realistic volute design. (left) Isometric and (right) cross section view.

Figure 5.3. Four disk volute geometry for the Tesla pumps simulation (left) isometric view, (right) cross section.

Figure 5.4 shows the 10 disk geometry for the 20 thou spacing. The 10 disk model has the realistic volute which will be used for the full sized disk packs. Figures 5.5 and 5.6 show the full size disk pack geometry for the 20 and 15 thou spacings, respectively. A cross sectional view of the full size disk packs, which was zoomed in on the disks for 15 and 20 thou are shown in Figs. 5.7 and 5.8. There are 15 disks in the 20 thou disk pack and 16 in the 15 thou, only a one disk difference.
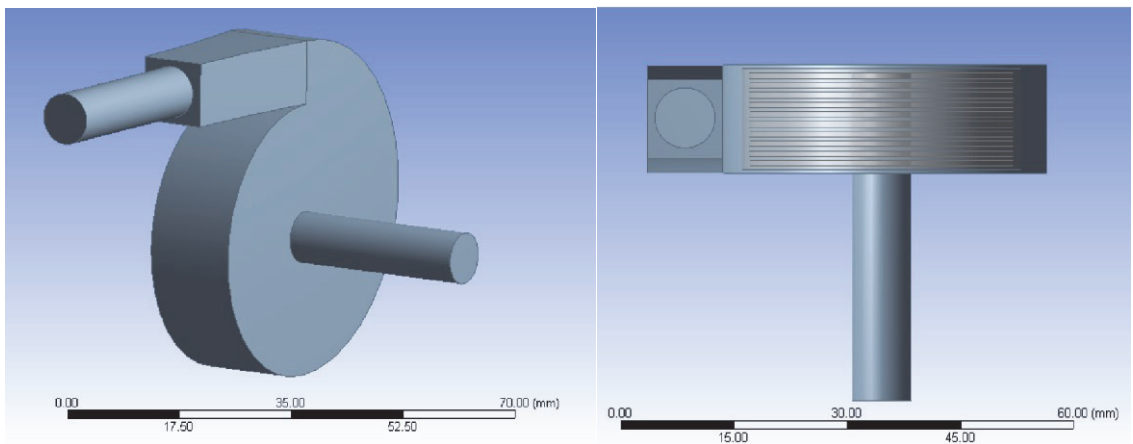
Figure 5.4. 10 disk, 20 thou spacing with Realistic volute design. (left) Isometric and (right) a cross section of the disks.
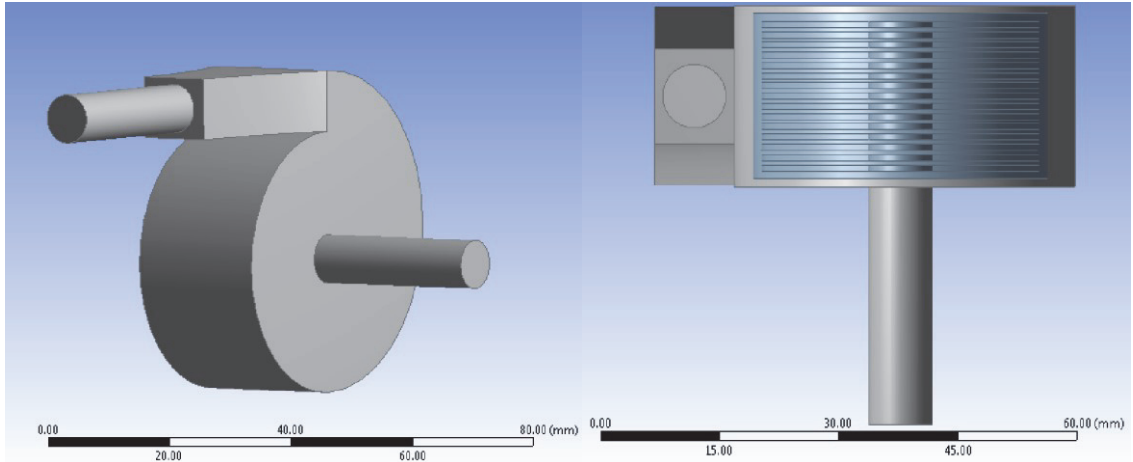
Figure 5.5. Full size disk pack, realistic volute of the 20 thou spacing (15 disks) Tesla pump model. (left) Isometric and (right) a cross section of the disks.
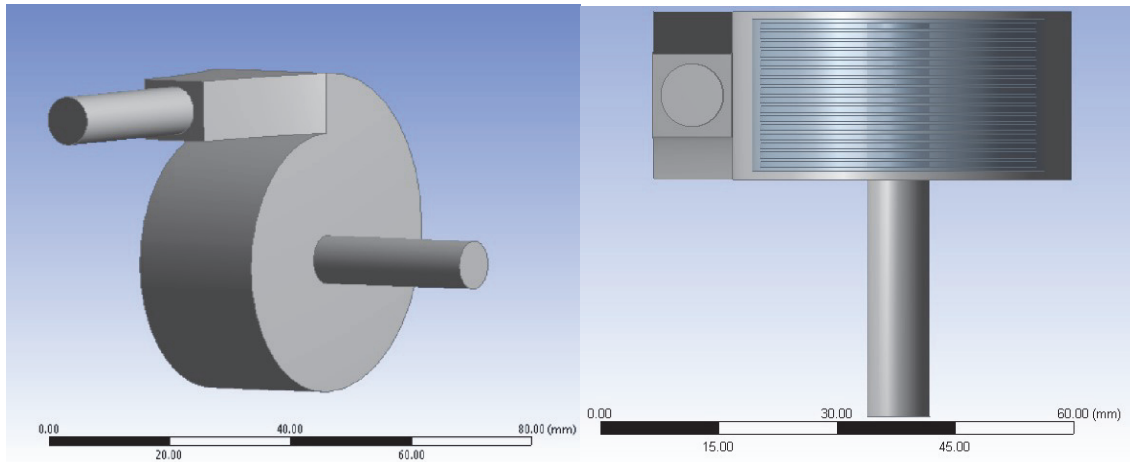
Figure 5.6. Full Size disk pack, realistic volute for the 15 thou spacing (16 disks) Tesla pump model. (left) Isometric and (right) a cross section of the disks.
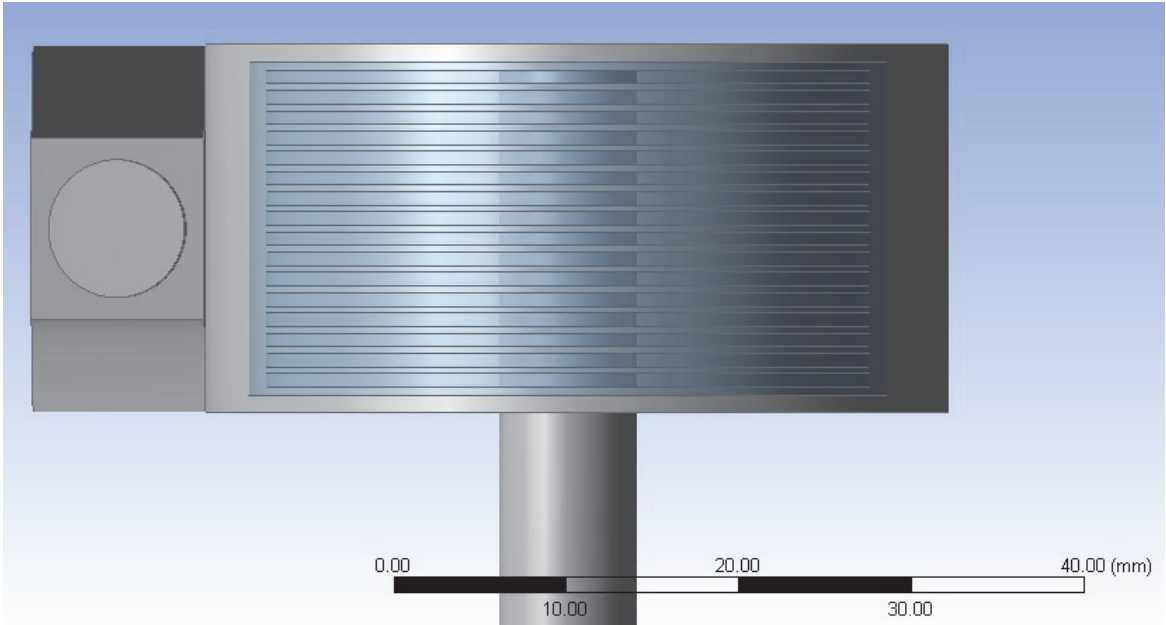
Figure 5.7. 15 thou spacing 16 disk, full size disk pack.
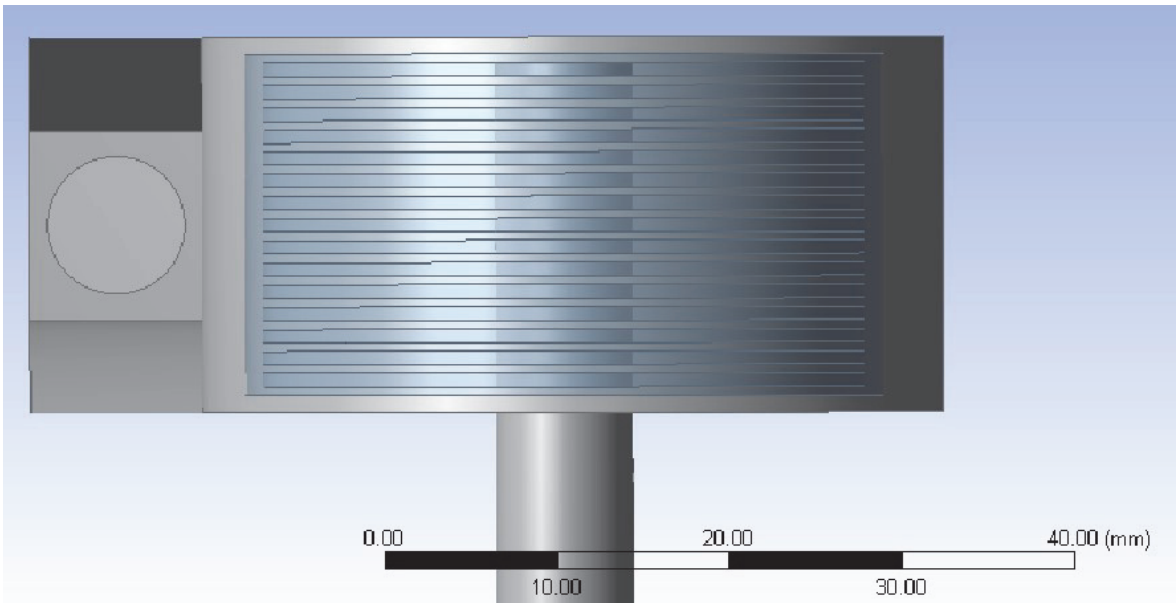
Figure 5.8. 20 thou spacing 15 disk, full size disk pack.

The four disk and ten disk models were used to ensure the simulation was functioning as expected as more disks were added. It was then altered gradually to have a realistic volute design and contain more disks. The diameter and thickness of the disks were made to be representative to that of the prototype pump, 3.5 cm in diameter and 0.79 mm thick. The

disks where centered within the volute and made concentric to the inlet, as they are in the prototype pump. The outlet and inlet tubes were 8 mm in diameter and the length of the exit and entrance tubing was 30 cm from the volute. The thickness of the volute could be easily altered to contain the corresponding number of disks, and maintain the specified following spacings between the volute, rotating boundary and disk pack. The total space between the volute and disks was 1.5 mm on either side of the disk pack. The space between the volute and the rotating boundary was 0.5 mm and between the disks and the rotating boundary was 1 mm on either side. Therefore, the total width of the model will depend on the disk gap spacing and the number of disks. The width of the outlet of the scroll is adjusted to accommodate the cylindrical outlet. These dimensions were used for all simulations, except for the ones containing one disk, where 4.6 mm where allowed on either side of the disks. The space between the volute and rotating boundary was 1 mm, and 3.6 mm between the disk and rotating boundary for the one disk realistic volute. This was because a 10 mm thick volute was necessary for the 8 mm outlet tube to fit.

5.1.2 Mesh

Figure 5.9 shows the mesh for the 1 disk realistic volute model, while Fig. 5.10 provides a zoomed in view of the mesh around the disk. The inflation layer can be seen around the single disk in both Figs. 5.9 (right) and 5.10.

Figure 5.9. 1 disk, real volute mesh. (left) Isometric view and (right) and cross section.

Figure 5.10. One disk realistic volute cross section view zoomed in on the disks.
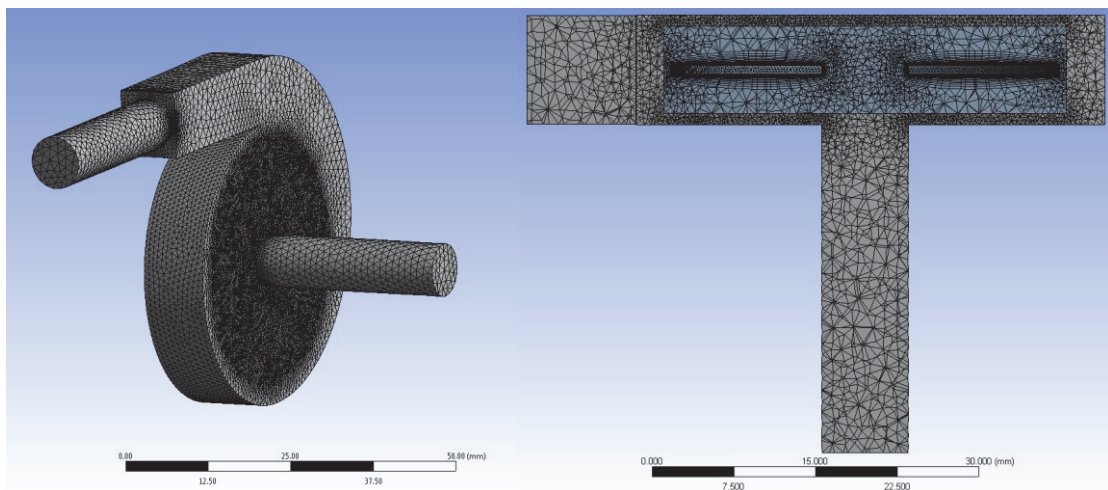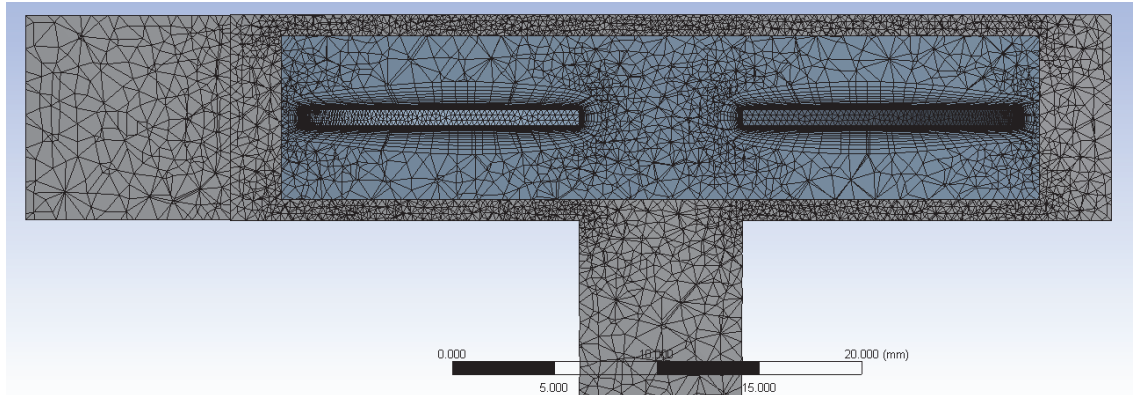
Figure 5.11 shows the mesh for the 10 disk, 15 thou spacing realistic volute model. Figure 5.12 is a zoomed in view of the mesh around the 10 disk 15 thou disk pack.
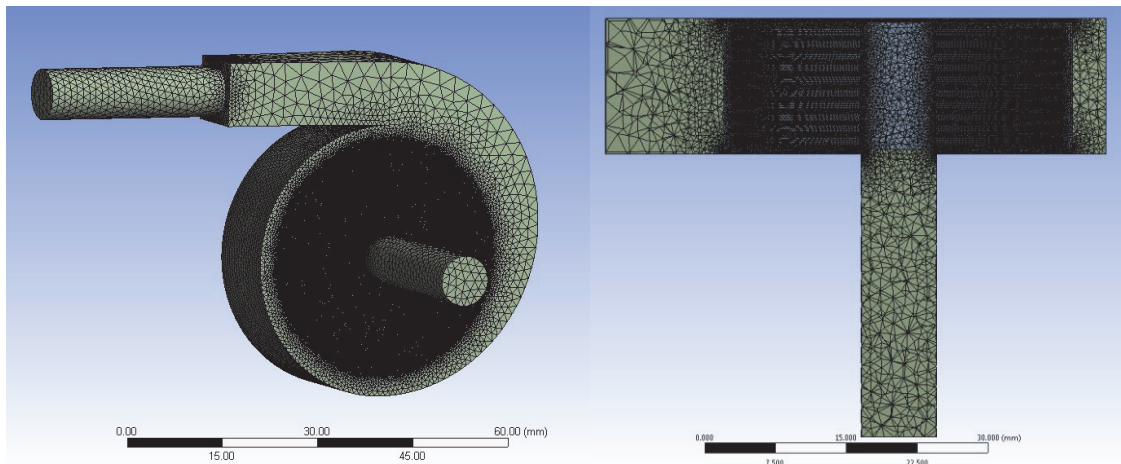
Figure 5.11. 10 disk, 20 thou spacing mesh. (left) full and (right) cross sectional view.
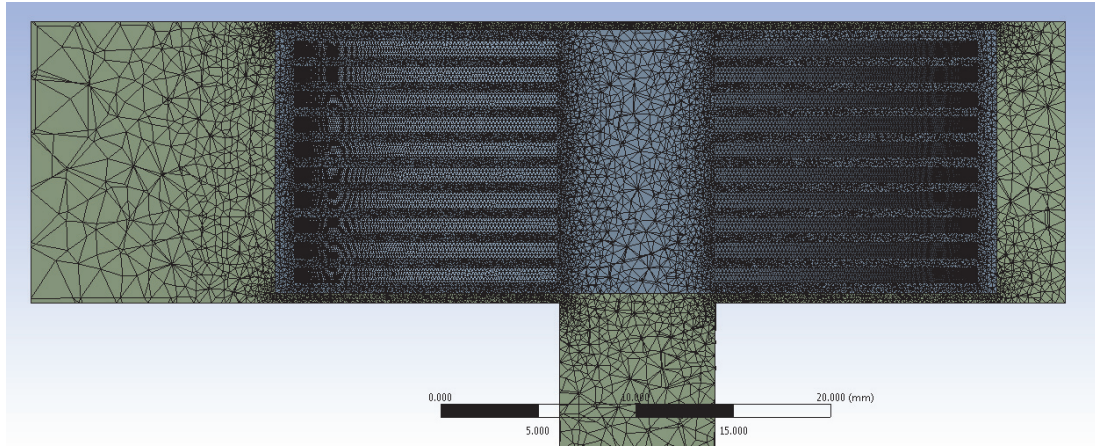
Figure 5.12. 10 disk, 20 thou spacing realistic volute cross section zoomed in on the disks.

The 20 thou and 15 thou full size models are shown in Figs. 5.13 and 5.14, respectively. The mesh around the disk packs for the 20 and 15 thou spacings for the full size models are shown in Figs. 5.15 and 5.16, respectively.
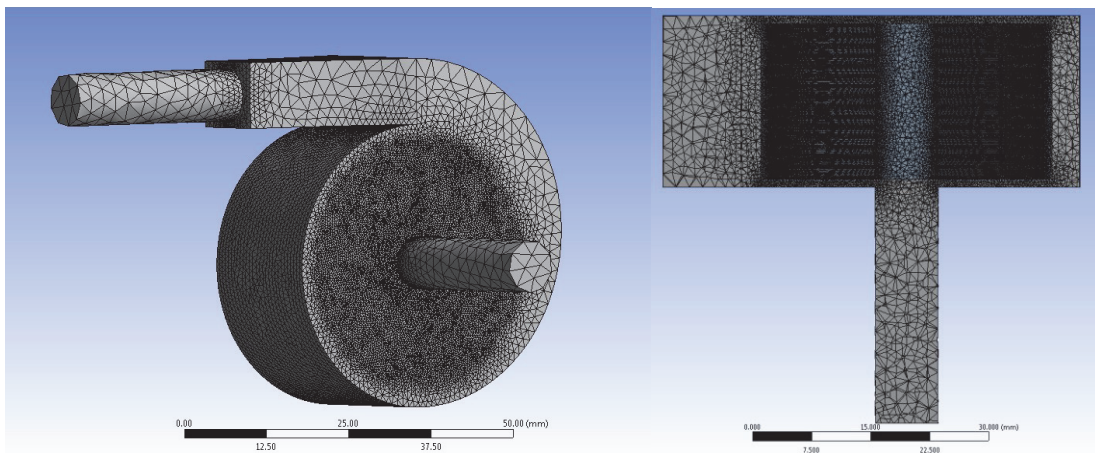
Figure 5.13. Full size, 20 thou spacing realistic volute mesh. (left) full view and (right) cross sectional view.
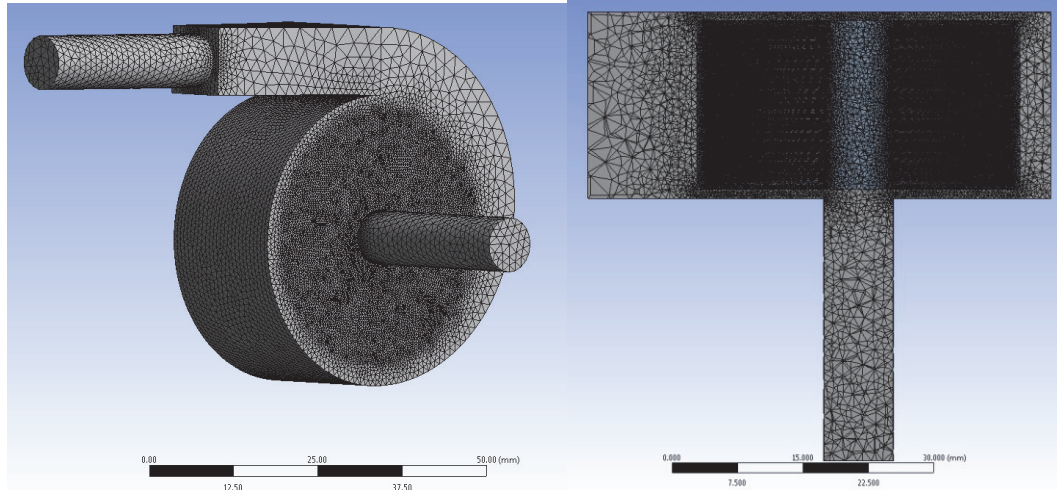
Figure 5.14. Full size 15 thou spacing realistic volute mesh. (left) full view and (right) cross sectional view.

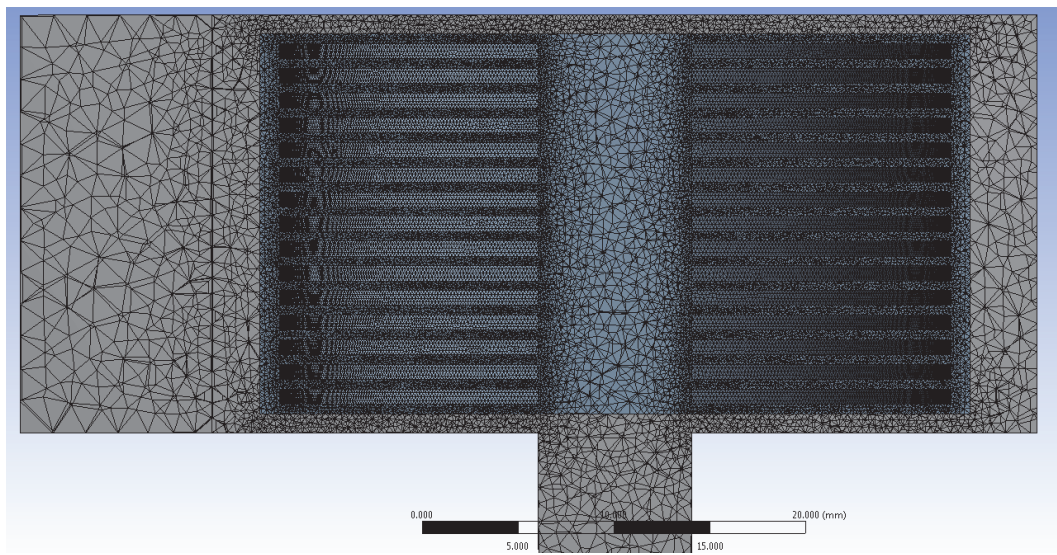**Figure 5.15. Full size disk pack 20 thou, realistic volute cross section zoomed in on the disks.**
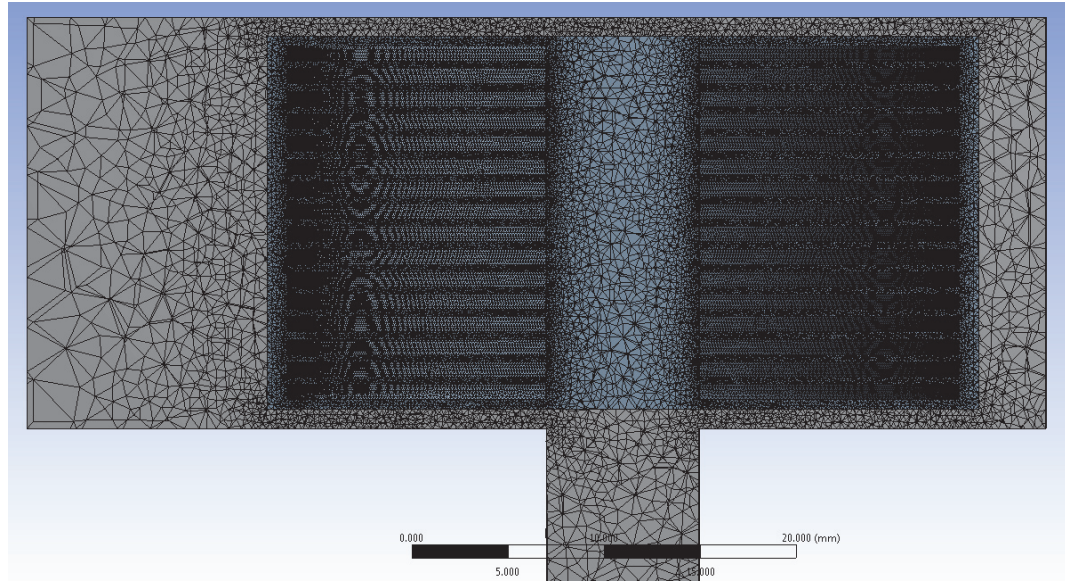
Figure 5.16. Full Size 15 thou spacing, realistic volute cross section zoomed in on the disks.

Table 5.1 displays the node and element counts for the various simulation models presented in this section. The original 1 disk model element and node count was similar to the real volute 1 disk model presented in Figs. 5.2 and 5.9 and therefore was not shown here. When meshing the models, there were a few problems with models that contained more than one disk. For a one disk simulation, it could be meshed so that the boundary layer around the disk could be better observed. However, it was very difficult to get an inflation layer between disks and still keep the number of elements manageable. There was a sudden increase observed in the amount of elements and nodes between the 20 and 15 thou full size spacing models. The smaller two spacings, 5 and 10 thou, which were originally to be modeled were not simulated. The other simulations were expected to still produce reasonable results, however may not produce boundary layers that could be observed. For the single disk simulations, it took 3 or more hours to run the simulation and the full size disk packs, up to 3 days. This was done on a Dell Precision T1600 with an Intel Xeon CPU E31245 at 3.30 GHz and 16 GB of memory. A mesh study was not performed since the simulations were already lengthy and this was not part of the project. The main purpose of this project was to determine if the prototype pump could be modeled and if it could produce physical results.

115

Table 5.1. Nodes and element counts for the various simulation models.
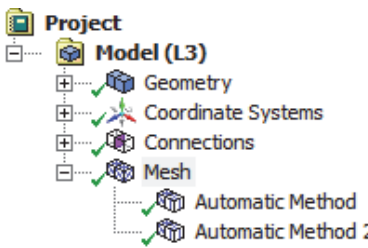
Mesh Model	Nodes	Elements
1 disk Real Volute	293,198	970,290
10 disk, 20 thou spacing, Real Volute.	1,834,709	8,696,046
Full Size disk pack, 20 thou spacing, Real Volute.	2,303,938	10,950,979
Full Size disk pack. 15 thou spacing, Real Volute.	3,746,224	17,690,606

The one disk simulation used the Advanced Size Function setting of Proximity and Curvature and used inflation layers around the disk. The settings for the inflation layer are shown in Fig. 5.17, where first layer thickness was selected and set to 3×10^{-3} mm with a maximum of 25 layers.
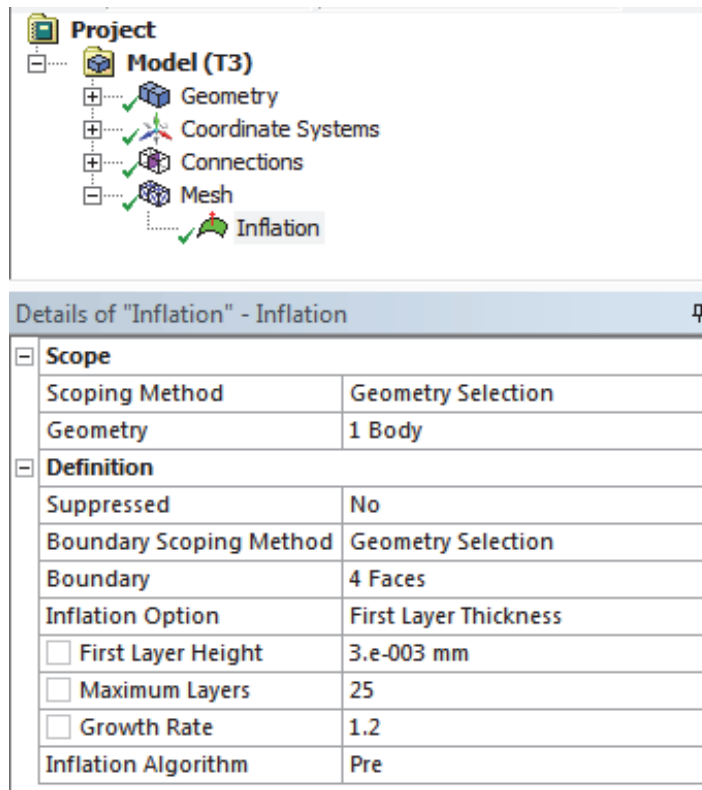
Figure 5.17. One disk inflation layer mesh set up.

Figure 5.18 shows an example (15 thou full size disk pack) of the typical settings for the mesh in the disk pack models. The first Automatic Method under Mesh is for the outer volute casing, while the second mesh method was used for the rotating boundary and thus the disks. No inflation layers were implemented around the disks due to issues getting it to work within the small spaces and in order to keep the number of elements down.

Details of "Mesh"	
Defaults	
Physics Preference	CFD
Solver Preference	CFX
Relevance	0
Sizing	
Use Advanced Size Function	On: Proximity and Curvature
Relevance Center	Medium
Initial Size Seed	Active Assembly
Smoothing	Medium
Transition	Slow
Span Angle Center	Fine
Curvature Normal Angle	Default (18.0 °)
Num Cells Across Gap	Default (3)
Min Size	Default (2.7767e-002 mm)
Proximity Min Size	Default (2.7767e-002 mm)
Max Face Size	Default (2.77670 mm)
Max Size	Default (5.55350 mm)
Growth Rate	Default (1.20)
Minimum Edge Length	10.0 mm
Inflation	
Patch Conforming Options	
Triangle Surface Mesher	Program Controlled
Patch Independent Options	
Topology Checking	Yes
Advanced	
Defeaturing	
Statistics	
Nodes	3746224
Elements	17690606
Mesh Metric	None

Figure 5.18.Typical mesh set up for the 10 full size disk packs.

117

5.2 Simulation

The domains and boundaries are set up in CFX according to Fig. 5.19 where the setup was similar for every model. The boundary conditions and inputs where from experimental data, where two different inlet/outlet conditions were compared. The first method used conservation of mass, with the mass flow rate in set to be equal to the mass flow rate out. For the second method, the mass flow rate was set at the inlet and the pressure at the outlet was set to zero, since the pressure difference between the inlet and outlet was going to be used for analysis. The rotational speed of the rotating boundary was set in radians per second, and the results presented in this thesis are for 3000 RPM (314.16 rad/sec). The frame change/mixing model for the interface between the rotating domain and volute was set to frozen rotor, and according to Fig. 5.19, was called "Default Fluid Fluid Interface". Two flow rates from the experimental data were selected as input for the simulations from the corresponding data sets and are presented in Table 5.2. The flow rates selected from the experimental data was the middle value and the highest flow rate from each data set.

Table 5.2 Mass flow rates used for each model, where results are shown.

Model Real Volute	Corresponding mass flow rates tested (kg/s)
One disk	7.67×10^{-3} kg/s
10 disk, 20 thou spacing	0.01987 kg/s, 7.67×10^{-3} kg/s
Full size 20 thou spacing	0.01987 kg/s, 7.67×10^{-3} kg/s
Full size 15 thou spacing	0.02008 kg/s, 0.01408 kg/s

For both the Casing and Rotating domains, the heat transfer option was set to 'none', and the turbulence model was set to Shear Stress Transport (SST); although it has been determined from the Re number calculations that the flow would more likely be laminar, the SST model was used to capture any early appearance of transition to turbulence. The walls and disk surfaces were set to no slip smooth walls, which was the default setting. The simulation was then allowed to run for a 1000 iterations or until the convergence criteria

was met, this was kept at the default value of 1×10^{-4} RMS for everything. An average of the data across a line at the center of the inlet and outlet tubes where taken as the local pressure values in CFX post processing. One hundred data points along the line was averaged, and the difference between the inlet and outlet calculated to obtain the pump head.
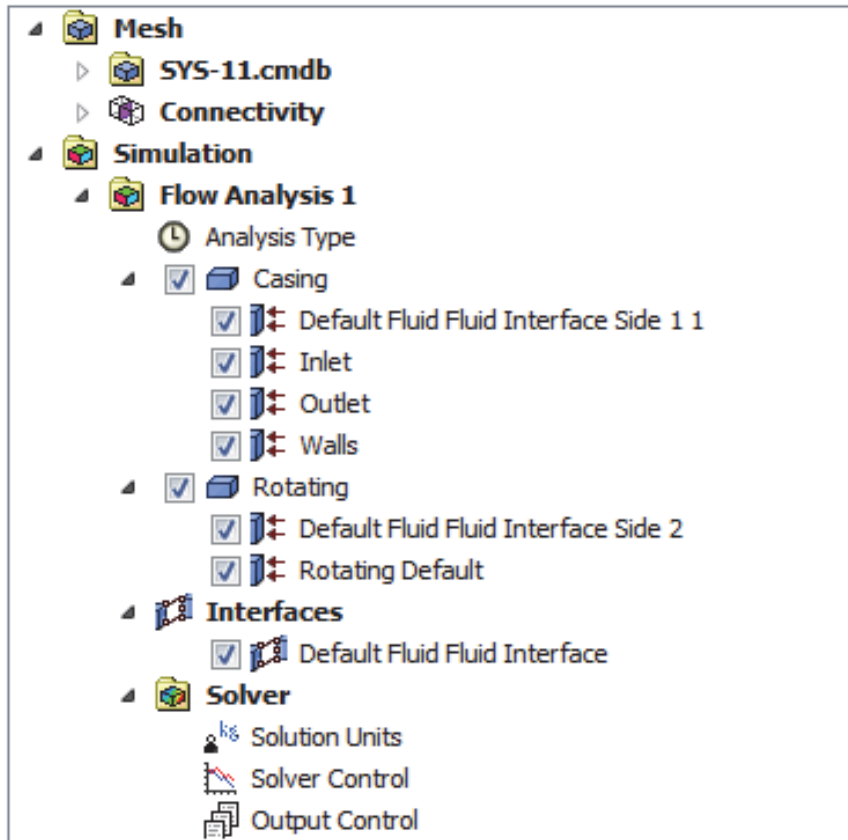
Figure 5.19. Domain list 20 thou for simulation set up.

5.3 Results

The results of the single, 10 disks and full size simulations for the realistic volute design are shown in this section. Only one of the rotational speeds (3000 RPM) was used in the study. The one disk simulation results are shown in section 5.3.1. The difference between the local pressure at the inlet and outlet from the simulation where converted to pump head, where these results are compared to the corresponding experimental values. Contours of the velocity and pressure around the disks were also analysed and are presented in section

5.3.2. Finally, a brief conclusion of the findings, with regards to the CFD work is presented in section 5.4.

5.3.1 One Disk Simulation

The very first model consisted of one disk realistic volute. Figures 5.20 and 5.21 show the velocity profile for the one disk simulation with the realistic volute shape where a boundary layer can be observed. Figure 5.21 is a zoomed in version of Fig. 5.20 to better show the boundary layer. The boundary layer from Fig. 5.21 is approximately 8 thou (0.2 mm) thick near the end of the disk, which is smaller than that obtained in Chapter 4 for both laminar and turbulent boundary layers. The hole in the center of the disk causes the boundary layer to start to form similar to that on a flat (stationary) plate. Since this is a shrouded ring shaped disk, the boundary layer may not form similar to a full rotating disk in an infinite fluid. However, it should be laminar according to the Re number calculation with a thickness having an order of magnitude of 12 thou.
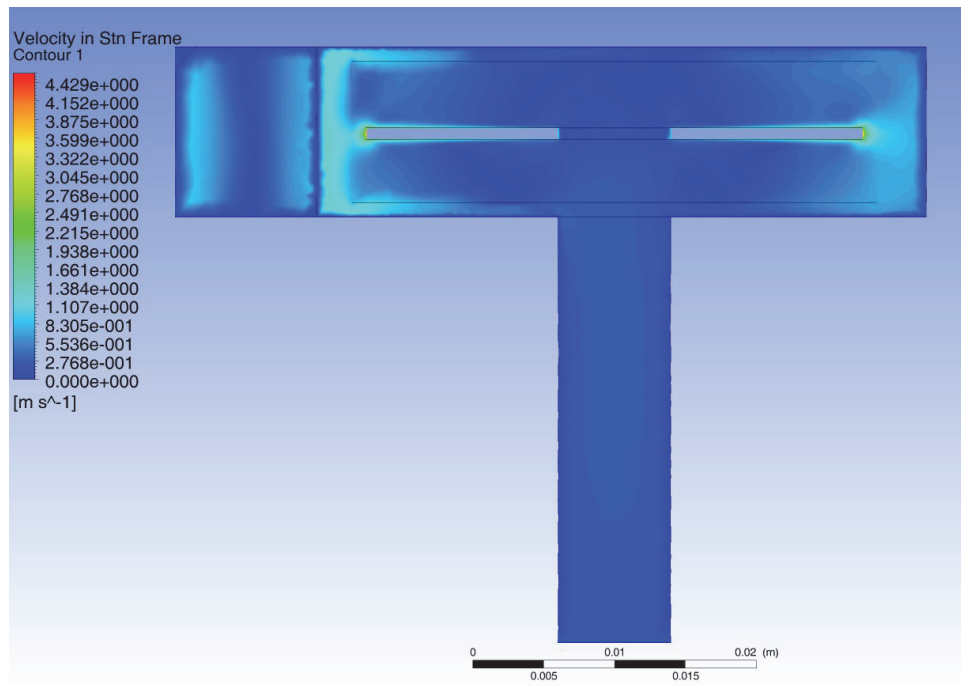
Figure 5.20. Real volute single disk, velocity contour plot.
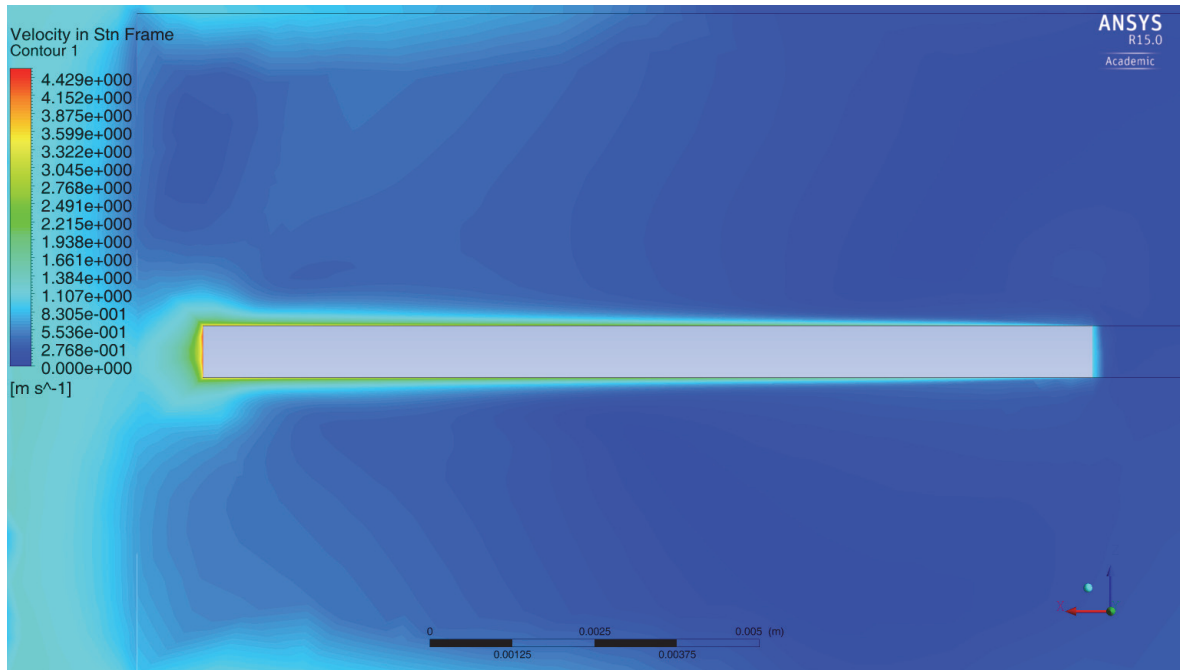
Figure 5.21. Zoomed in velocity profile for the one disk realistic volute simulation.

Figures 5.22 and 5.23 show the pressure contour plots, again with a boundary layer similar to what is observed in the velocity contours. The pressure contour plot in Fig 5.23 shows that the pressure has increased from the inlet to the outlet. Near the edge of the disk the pressure is less than its surroundings, and increases further away from the disk. The fluid within the boundary layer is being pushed outwards from the center of the disk creating a low pressure area and from this motion the pressure is increased further away from the disk; which is what a pump should be doing. The largest pressure drop along the disk from Fig. 5.23 is approximately 11 kPa where the vaporization pressure of water at room temperature (21°C) is approximately 2.4 kPa. This indicates that cavitation is not going to occur, since the pressure drop, from atmosphere, does not reach the pressure of vaporization at room temperature.

121

Figure 5.22. One disk real volute pressure contour plot.

Figure 5.23. One disk real volute pressure contour plot zoomed in version.

5.3.2 Results for the Disk Pack Simulations

The results comparing the disk pack simulations at 3000 RPM, using the flow rates presented in Table 5.3, are presented in this section. Starting with the velocity and pressure contours for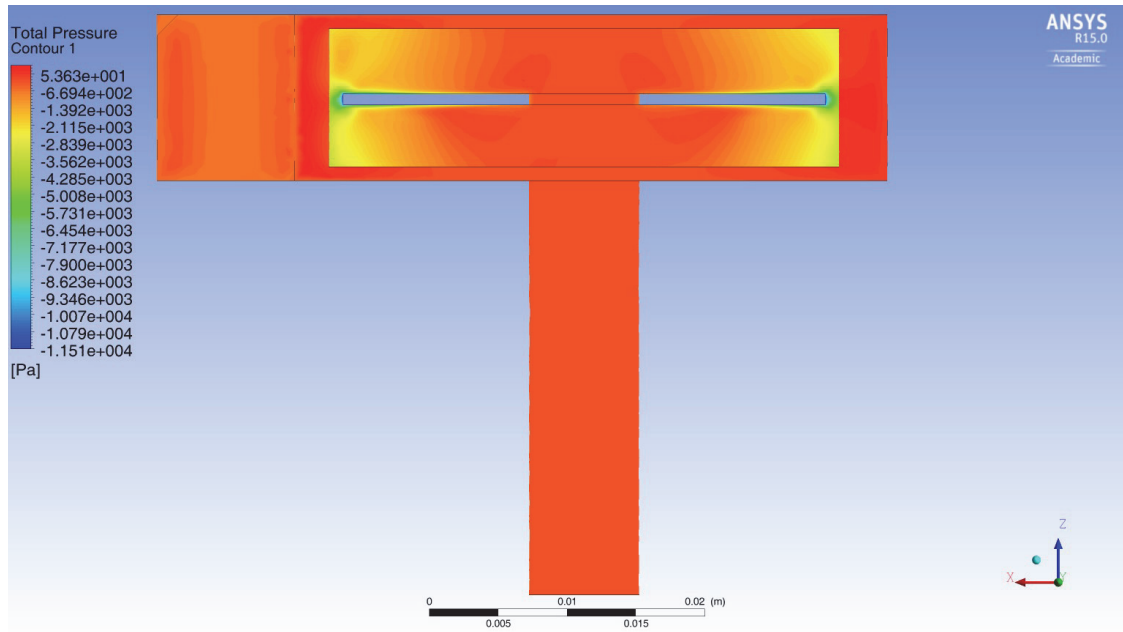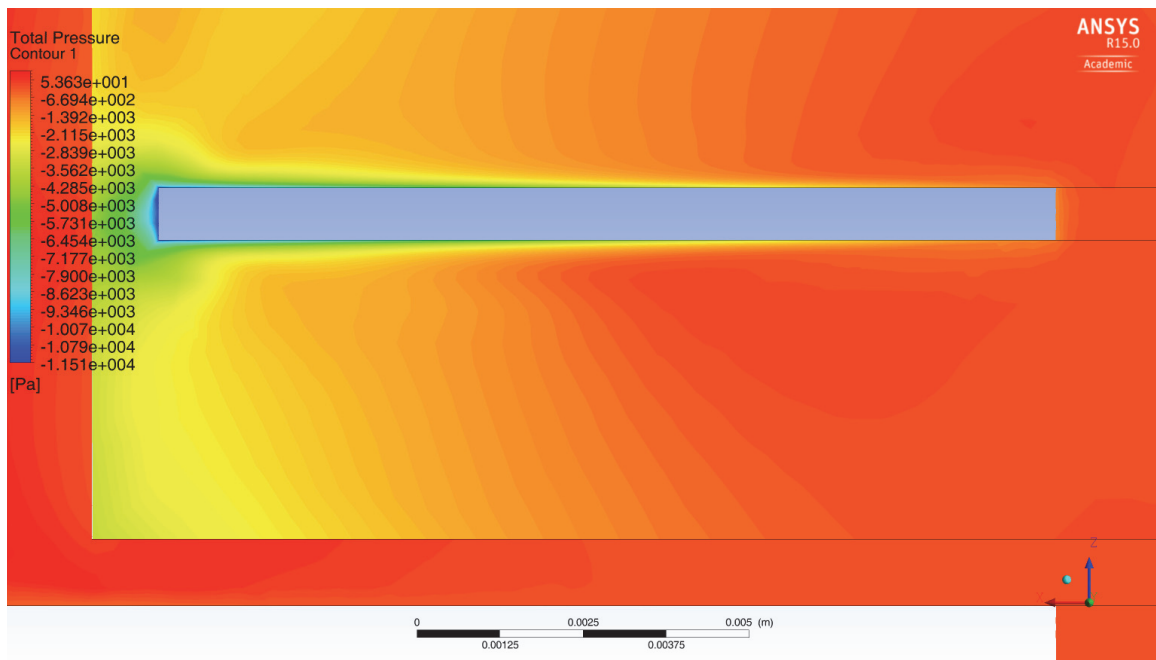 the highest flow rates, to show what is going on within each model for the two spacings. This is followed by comparing the pressure difference across the pump to experimentally obtained values, also comparing the two flow rates.

Table 5.3. Flow rates used for the various simulations models presented in section 5.3.2.

Model Real Volute	Corresponding mass flow rates tested (kg/s)
10 disk, 20 thou spacing	$0.01987, 7.67 \times 10^{-3}$
Full size 20 thou spacing	$0.01987, 7.67 \times 10^{-3}$
Full size 15 thou spacing	$0.02008, 0.01408$

Figure 5.24 shows the local pressure contour plot for the highest flow rate and a disk pack spacing of 20 thou, for the 10 disks simulation. Figure 5.25 shows the velocity contour plot for the same case. The rotational domain can be easily seen in Figs. 5.24 and 5.25. The velocity can be observed to be increasing along the length of the disk, similar to a real life pump.

The local pressure contour plot for the 15 thou full size disk pack with 16 disks is shown in Fig. 5.26, while the velocity profile is shown in Fig. 5.27. The pressure and velocity contour plots for the 20 thou full size disk pack is shown in Figs. 5.28 and 5.29, respectively. The combination of the pressure and velocity profile, Figs. 5.24 to 5.29, shows that the simulated rotation of the disks is accelerating the working fluid as it is drawn in and pushed out of the pump.

There are some anomalies in the flow pattern which can be observed for all the simulations such as to the left near the rotating boundary in Fig 5.25, there are spots where the fluid

appears to be nearly stagnant. This is expected to be due to the quality of the mesh and not meeting the convergence criteria.
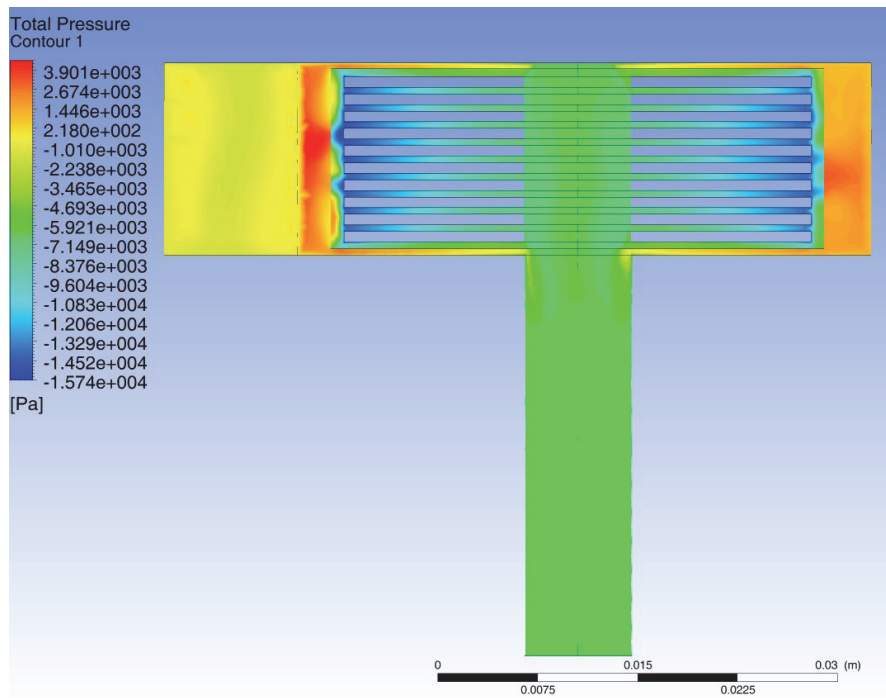
Figure 5.24. 10 disk 20 thou, 3000RPM, real volute design local pressure profile side view for 0.01987 kg/s.
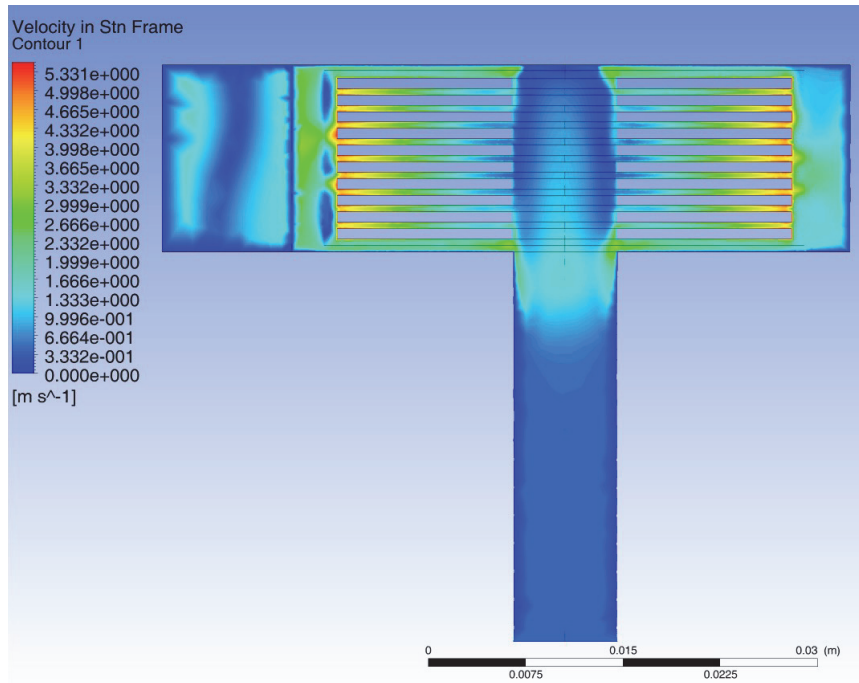
Figure 5.25. 10 disk 20 thou, 3000RPM real volute design, cross section velocity profile in direction of rotation 0.01987 kg/s.
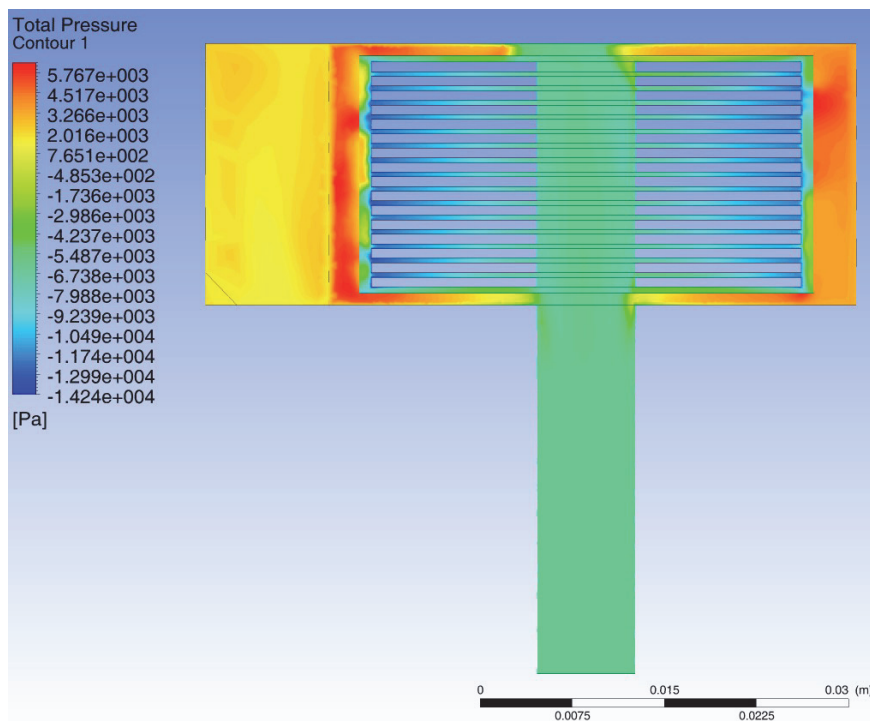
Figure 5.26. Full size disk pack, 15 thou spacing pressure contour plot for 0.02008 kg/s.
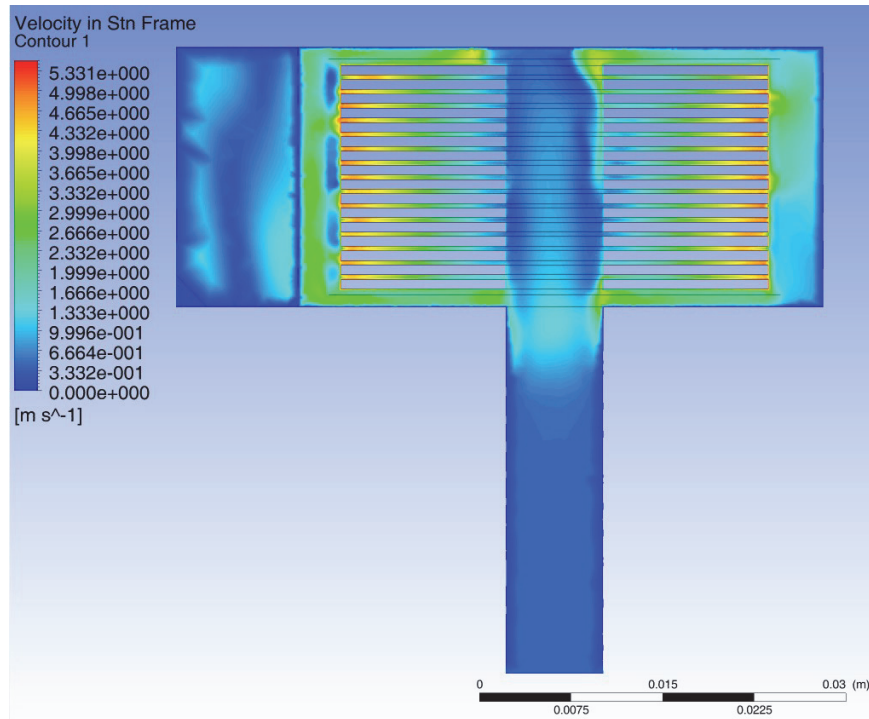
Figure 5.27. Full size disk pack, 15 thou spacing velocity profile for 0.02008 kg/s.
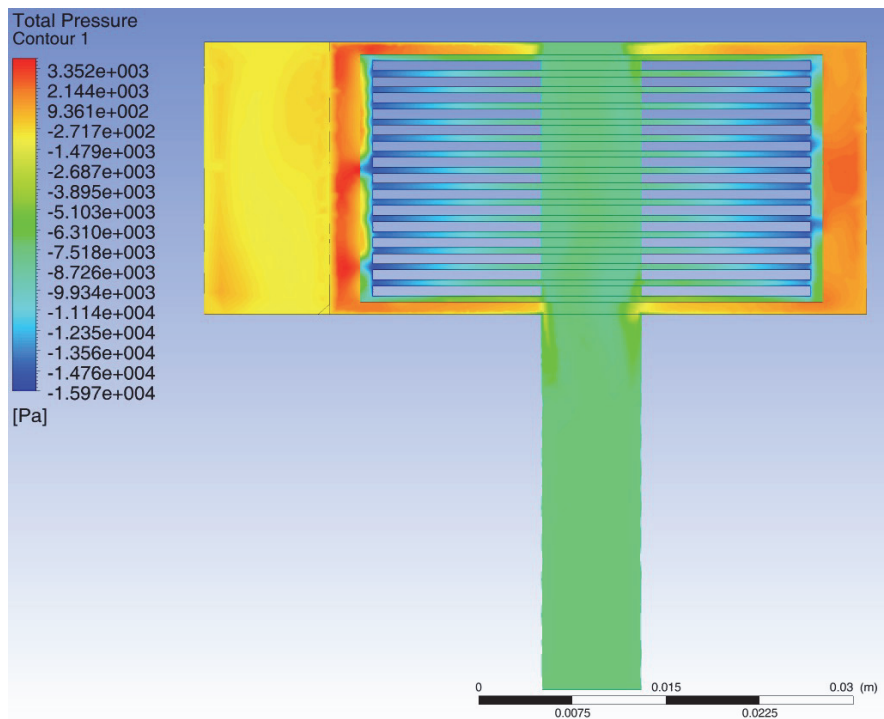
Figure 5.28. Full sized disk pack, 20 thou spacing pressure contour plot for 0.01987 kg/s.

126
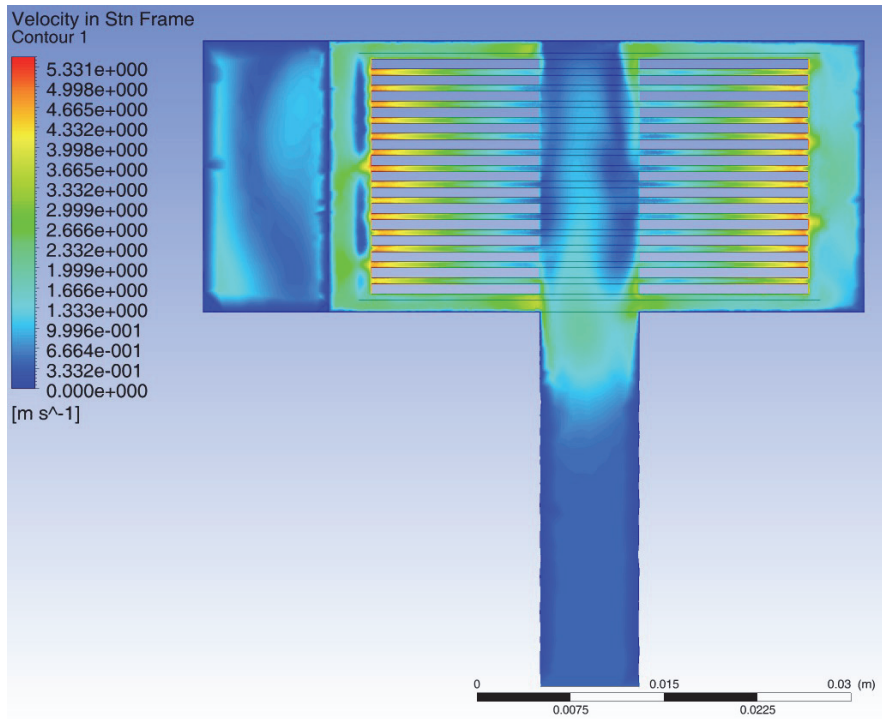
Figure 5.29. Full sized disk pack, 20 thou spacing velocity contour plot 0.01987 kg/s.

When looking at the velocity contours in Fig 5.30, the area between the disks close to the center appears to display boundary layers. There are still areas in the middle of the space between the disks where the fluid is not moving. The area of stagnation (dark blue) between the disks eventually disappears, suggesting the boundary layers are combining and developing into fully developed flow. This is suspected to occur based off the boundary layer thickness calculated in Chapter 4, Table 4.1. However, due to the mesh quality, the development of the boundary layers near the center edge of the disk is not clear or observed consistently.
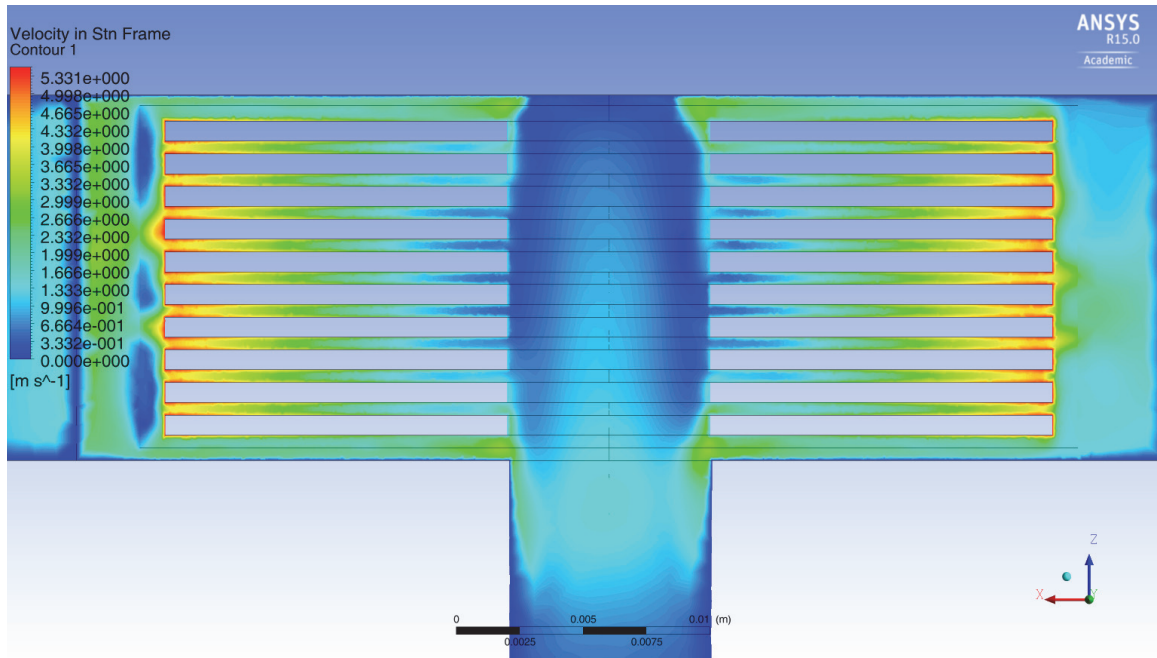
Figure 5.30. Zoomed in velocity contour for the 10 disk, 20 thou spacing.

Figure 5.31 shows the velocity contour plot in the *y*-direction for the 10 disk, 20 thou model. It looks similar to the overall velocity contour plot in Fig. 5.20, where the fluid is accelerating along the disk. The difference from the left to the right velocity is due to the simulated rotation of the disks, where the left side has a positive magnitude of velocity and the right is negative. Figure 5.32 shows the velocity contour for the same simulation in the *x*-direction, where there is little difference in the velocity along the disk, although the magnitude of *x*-velocities are smaller than the *y* ones. This suggests that the velocity is dominated by the rotation of the disk (*y*-direction).

Figure 5.31. 10 disk 20 thou, velocity contour in the *y* direction.

Figure 5.32. 10 disk 20 thou, velocity contour for the *x* direction.

Two different types of boundary conditions were tested. Method 1 assumed the inlet and outlet flow rates were equal. Method 2 assumed that the pressure out was equal to zero, while providing a mass flow rate in. This was done at 3000RPM for the 3 disk pack models at the two different flow rates as presented in Table 5.3.
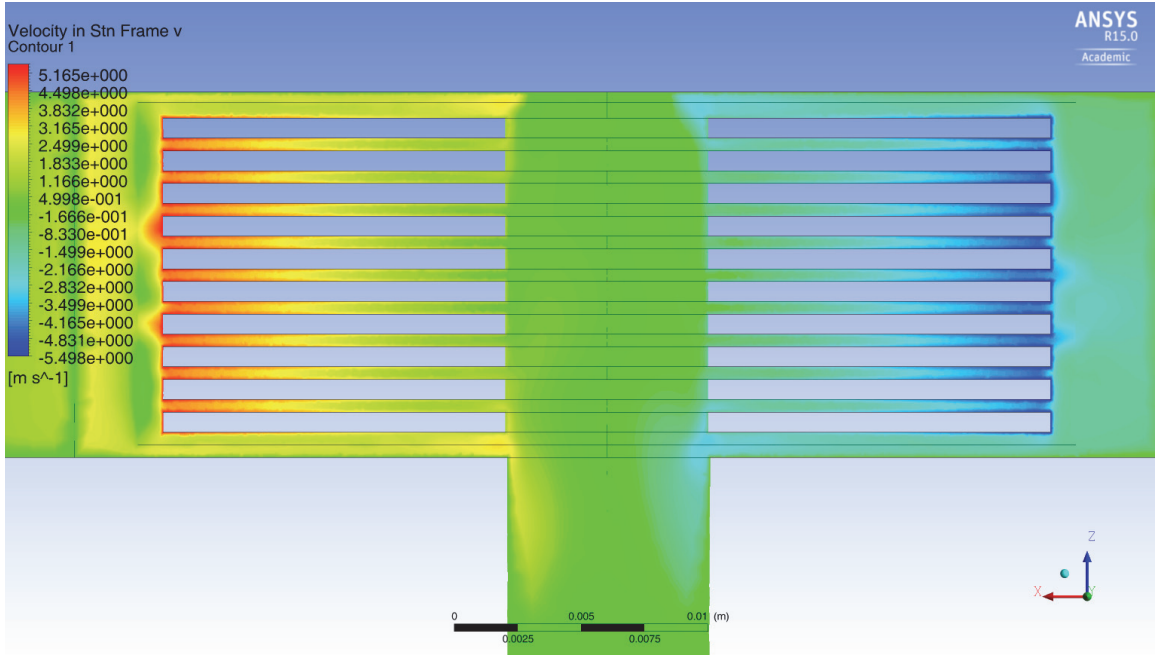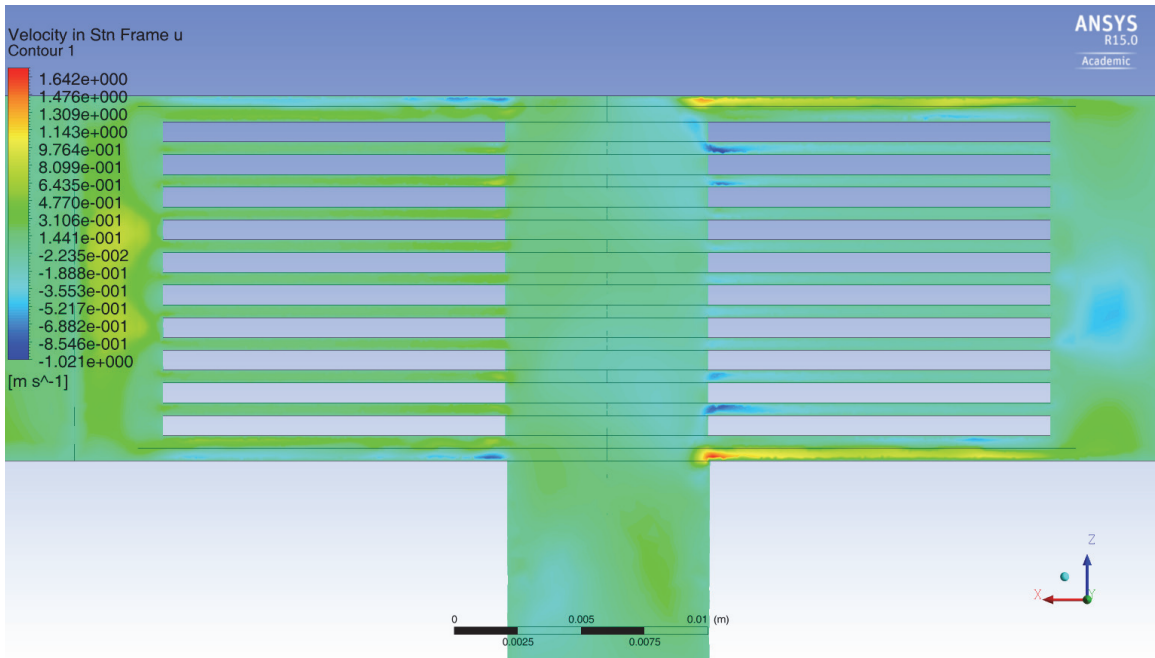
Table 5.4, provides results for the 10 disk simulations for 20 thou, at 3000RPM, for the two boundary conditions. From Table 5.4, the different boundary conditions did not significantly impact the results, with percent differences of 0.1 % and 0.04 %. Therefore, either set of boundary conditions may be used, especially since the data used (mass flow rates) were the same in both cases.

For the 10 disk model there is two thirds of a full disk pack, where a full disk pack is 15 disks. The difference between two thirds of the experimental value and the simulation results is 31% and 40 % difference. This is reasonable for a first attempt at a working simulation of a Tesla pump, since it is on the same scale as the experimental data.

Table 5.4. Ten disk real volute design, 20 thou spacing results, 3000RPM.

Experimental Mass Flow Rate (kg/s)	Method 1 head (m)	Method 2 head (m)	% Difference between boundary conditions	2/3 Experimental value of Head (m)	% Diff for 2/3 Exp. and Sim.
0.01987	0.6581	0.6574	0.11 %	0.901	31%
0.00767	0.8165	0.8162	0.03 %	0.544	40%

Table 5.5 presents the data obtained from the simulation for the 20 thou disk pack at 3000 RPM. In Table 5.5, the difference between the simulation and experimental data is 57% and 58% for the two flow rates selected. Compared to the 10 disk simulation results from Table 5.4, the full disk pack simulation produces higher values of pump head. The increase in pump head from the 10 to 15 disk simulations is due to the increase in surface area; confirming that the simulation is working as expected since there is slightly more surface area for energy exchange (mechanical to hydraulic) to occur. The fact that surface area is impacting the performance of the pump in the simulation is promising.

130

Table 5.5. Full Size Disk Pack (15 disk), 20 thou spacing simulation results, 3000RPM.

Experimental Mass Flow Rate (kg/s)	Mass flow rate in=out resulting head (m)	Experimental head value (m)	% difference
0.01987	0.7499	1.3520	57 %
0.00767	0.9791	1.7744	58 %

Additionally, the results for the 15 thou disk pack with 16 disks is shown in Table 5.6. The difference between the simulation and experimental head is 41% and 44 % for the full size 15 thou simulation. The percent difference for the 15 thou full size disk pack is less than that of the 20 thou at 57% and 58% (Table 5.5).

Due to the simulation using the input from the experimental runs, it is expected that the same sort of trends and patterns will occur between disk pack spacings. The 15% difference between the 20 and 15 thou full disk pack simulation results could suggest that the 15 thou spacing is more effective than 20 thou, similar to what was found in Chapter 4. However, simulations for the other spacings would be necessary to confirm this, as well as a mesh independence study and better convergence during the simulations.

Table 5.6, Full Size Disk pack, 15 thou (16 disks) spacing simulation results 3000RPM.

Experimental Mass Flow Rate (kg/s)	Mass flow rate in=out resulting head (m)	Experimental head value (m)	% difference
0.02008	0.8969	1.3591	41 %
0.01408	1.0134	1.5879	44 %

5.4 Conclusion

The work done in attempting to simulate the prototype Tesla pump produced relatively reasonable results in that the results compared reasonably to the experimental data. However, there is more work needed to improve the simulation such that it could be used for design analysis. Firstly, a mesh independence study needs to be performed and the issues with meshing between the disks need to be addressed. The set residual Root Mean Square (RMS) error value was not always being met and the typical values of residual RMS

obtained were on the order of 10^{-3} for 1000 iterations. Therefore, the simulation may not have always converged fully to this set criterion. It is recommended that a mesh independence study be performed, and each simulation be ran and properly monitored to know if it has truly converged. It is important to note that the purpose of this part of the study was to investigate if a working simulation of the prototype pump would produce similar results to the experimental study.

The one disk simulation produced a turbulent boundary layer, which was likely due to the turbulence model selected. Both the velocity and pressure contour plots for the disk pack simulations showed increasing velocity. The velocity contour plots for the disk pack simulations showed the boundary layer formation at the center edge of the disks, similar to the formation of fully developed flow between flat plates. For the full sized disk pack simulations for 15 and 20 thou, the 15 thou spacing was found to be more effective than the 20 thou. However, this may partly be due to using experimental flow rates as input variables to the simulations. For the 15 thou simulation the difference from experimental and the simulation pump head values was approximately 15% less, suggesting that 15 thou is more effective. Overall, the simulation produces results similar to the experimental results obtained from the prototype pump; however, work still needs to be done to improve the quality of the simulation.

Suggestions for further work would include running the simulations under laminar flow physics, since the experimental analysis suggests the flow is laminar. A pump curve could be produced with flow rates as input and pump head as the output, after the improvements are made to the simulation. The pump curves produced could then be used to further analyse the performance of the prototype Tesla pump with various volute designs or disk packs.

Chapter 6 Conclusion

The work presented here helps to further understand how a Tesla pump works, through studying it under varying operational conditions. Various motor speeds and disk pack spacings were tested with the possibility of determining optimal operational parameters. The same testing was performed utilizing a more viscous working fluid, propylene glycol water mixture, to analyze the effects of viscosity. A study of the effects of vibration frequency was also performed. In addition, a CFD model of the pump was made that compared to experimental data to be used in the future to look at the impact of different casing geometries.

The prototype pump testing rig included an electromagnetic flow meter, a differential pressure sensor, discharge valve, motor control, reservoir, and a DAQ with relevant modules. A stand where the rig equipment could be fastened to was created and a clear acyclic pump casing was machined. The clear casing was to observe the disk pack and air bubbles within the pump, this did help in the removal of air bubbles within the casing.

Chapter 4 presented the experimental results for the testing of the prototype pump with water, PG-water mixture and under vibration. The 15 thou spacing has been shown to be the most performant; however, was not the most efficient spacing for the water tests. The 15 thou spacing is the most performant compared to the 20 or 25 thou spacings, due to possessing a slightly larger surface area in comparison. The boundary layer thicknesses are generally larger than half of the gap spacing which points to the fact that fully developed flow occurs between the disks. The PG-water mixture highlighted the effectiveness of the 15 thou spacing and obtained the highest efficiencies out of the other four spacings tested. An increase in the boundary layer thickness was observed for the PG-water due to the increased viscosity compared to water.

As the rotational speed increases, the pump produces higher head and flow rates. The efficiency for the higher rotational speeds was less compared to the lower speeds, where the lower speeds better utilize energy compared to the higher rotational speeds.

The effect of vibration on a Tesla pump was shown to make little to no difference, which indicates that cavitation was not induced due to vibrations. Any difference between the vibration and non-vibration runs was more than likely the results of experimental error.

The non-dimensional analysis for the head and capacity coefficients has shown to produce a characteristic curve for the Tesla pump. This is similar to what occurs for a centrifugal pump, and since a Tesla pump operates similarly, a characteristic curve for the prototype pump for each spacing was observed for laminar flow.

From visual analysis of the CFD results for the one disk simulation, a boundary layer of approximately the same laminar thickness was produced. Both the velocity for the disk pack simulations showed increasing velocity along the disks as well as the merging of the boundary layer into a fully development flow profile. The preliminary results from the CFD study compared reasonably with the experimental data, however more work is needed improve the simulation and confirm findings.

6.1 Recommendations

From the comparison of Hasinger and Kehrt, Darby et al., and this thesis results, several ideas for improving the performance of the prototype pump where determined. The largest problem with the performance of the prototype Tesla pump was its efficiency, which was considerably lower than the other studies. The prototype pump reached a maximum rotor efficiency of 5.6%, where Darby et al. obtained 30 % and Hasinger and Kehrt obtained efficiencies up to 65%. The difference in efficiency is expected to be due in large part to the volute design. Therefore, it is suggested that the volute design be improved, possibly by using the findings from the Tesla turbine studies presented in Chapter 1, section 1.1.4. It is also recommended that larger diameters be analysed for the prototype pump, along with slower rotational speeds based on what was observed from the study comparison.

The literature review indicated that the volute design, especially the inlet and outlet could affect Tesla pump performance. This was the main purpose of developing a CFD model, to test different volute designs in the future. The work done in attempting to simulate the prototype Tesla pump, produced relatively reasonable results; however, more work is

required to improve the simulation and to validate these results. Firstly, a mesh independence study needs to be performed, and the issues with the mesh between the disks need to be addressed. The set residual Root Mean Square (RMS) error value was not always being met during the simulations, therefore the simulation may not have always converged. It is recommended to confirm that the simulation has converged, possibly by trying different boundary conditions which would not cause convergence issues and running the simulations for a larger number of iterations. Suggestions for further work would include running the simulations under laminar flow physics, since the flow within the pump has been determined to be laminar. Pump curves could later be produced from the numerical study and used in further analyse of the prototype Tesla pump.

References

Amaral-Teixeira, J., & Spence, R. (2009). A CFD parametric study of geometrical variations on the pressure pulsations and performance characteristics of a centrifugal pump. *Computer and Fluids, 38*, 1243-1257. doi: 10.1016/j.compfluid.2008.11.013

Benton, E. R. (1966). On the flow due to a rotating disk. *Journal of Fluid Mechanics, 24*(04), 781-800. doi: http://dx.doi.org/10.1017/S0022112066001009

Cengel, Y. A., & Cimbala, J. M. (2010). *Fluid Mechanics: Fundamentals and Applications* (2nd ed.): McGraw-Hill.

Childs, P. (2011). *Rotating flow*. Amsterdam ; Boston: Elsevier. doi:http://dx.doi.org/10.1016/B978-0-12-382098-3.00009-3

Cochran, W. G. (1934). The flow due to a rotating disk. *Mathematical Proceedings of the Cambridge Philosphical Society, 30*, 365-375. doi: 10.1017/S0305004100012561

Crowe, C. T., Elger, D. F., & Roberson, J. A. (2005). *Engineering Fluid Mechanics* (8th ed.): John Wiley & Sons. Inc.

Darby, R., Morrison, G., & Roddy, P. (1987). Performance charaterisitics of a multiple-disk centrifugal pump. *Journal of Fluids Engineering, 109*(1), 51-57.

Engin, T., Özdemir, M., & Çeşmeci, Ş. (2009). Design, testing and two-dimensional flow modeling of a multiple-disk fan. *Experimental Thermal and Fluid Science, 33*(8), 1180-1187. doi: 10.1016/j.expthermflusci.2009.07.007

Furukawa, H., & Watanabe, T. (2009). Flows around rotating disks with and withour rim-shroud gap. *Experiments in Fluids, 48*(4), 631-636. doi: 10.1007/s00348-009-0785-4

Gauthier, G., Gondret, P., Moisy, F., & Rabaud, M. (2002). Instabilities in the flow between co-and counter-rotating disks. *Journal of Fluid Mechanics, 473*, 1-21. doi: 10.1017/S0022112002002525

Greif, R., Humphery, J. A. C., Schuler, C. A., Usry, W., & Weber, B. (1990). On the flow in the unobstucted space between shrouded corotating disks. *Physics of Fluids A: Fluid Dynamics, 2*(10), 1760-1770. doi: 10.1063/1.857703

Guha, A., & Sengupta, S. (2013a). Analyitical and computational solutions for three-dimensional flow-field and relative pathlines for the rotating flow in a Tesla disc turbine. *Computers and Fluids, 88*, 344-353. doi: http://dx.doi.org/10.1016/j.compfluid.2013.09.008

Guha, A., & Sengupta, S. (2013b). The fluid dynamics of the rotating flow in a Tesla disc turbine. *European Journal of Mechanics - B/Fluids, 37*, 112-123. doi: 10.1016/j.euromechflu.2012.08.001

Guha, A., & Smiley, B. (2010). Experiment and analysis for an improved design of the inlet and nozzle in Tesla disc turbines. *Proceedings of the Institution of Mechanical Engineers, Part A: Journal of Power and Energy, 224*(2), 261-277. doi: 10.1243/09576509jpe818

Harikishan, G., & Shyam, K. (2013). Desgin and Operation of Tesla Turbo machine- A state of the art review. *International Journal of Advanced Transport Phenomena, 2*(1), 7-14.

Hasinger, S., & Kehrt, L. (1963). Investigation of a Shear-Force Pump. *Journal of Engineering for Power, 85*(3), 201-207.

Heyda, M. (2006). A Practical Guide to Conductivity Measurement Retrieved March 16, 2016, from http://www.mbhes.com/conductivity_measurement.htm

Hoya, G. P., & Guha, A. (2009). The design of a test rig and study of the performance and efficiency of a Tesla disc turbine. *Proceedings of the Institution of Mechanical Engineers, Part A: Journal of Power and Energy, 223*(4), 451-465. doi: 10.1243/09576509jpe664

Hsieh, M. K., & Huang, R. F. (2011). Phase-resolved flow characterisitics between two shreouded co-rotating disks. *Experiments in Fluids, 51*(6), 1529-1547. doi: 10.1007/s00348-011-1168-1

Humphrey, J. A. C., Shuler, C. A., & Webster, D. R. (1995). Unsteady Laminar Flow Between Pair of Disks Corotating in a Fixed Cylindrical Enclosure. *Physics of Fluids, 7*(6), 1225-1240.

Miller, G. E., & Fink, R. (1999). Analysis of Optimal Design Configurations for a Multiple Disk Centrifugal Blood Pump. *Artificial Organs, 23*(6), 559-565.

Rice, W. (1963). An analytical and Experimental Investigation of Mulitple Disk Pumps and Compressors. *Journal of Engineering for Power, 85*(3), 191-200. doi: 10.1115/1.3675253

Rogers, M. H., & Lance, G. N. (1959). The rotationally symmetric flow of a viscous fluid in the presence of an infinite rotation disk. *Journal of Fluid Mechanics, 7*(04), 617-631. doi: http://dx.doi.org/10.1017/S0022112060000335

Rossetti, A., Pavesi, G., & Ardizzon, G. (2010). A new two stage miniature pump: Design, experimental characterization and numerical analyses. *Sensors and Actuators A: Physical, 164*(1-2), 74-87. doi: 10.1016/j.sna.2010.09.003

Schlichting, H., & Gersten, K. (2000). *Boundary Layer Theory* (8th rev. ed.). New York: Springer.

The Dow Chemical Company. (2016). Propylene Glycols - Viscosities of Aqueous Solutions Retrieved April 28, 2016, from http://dowac.custhelp.com/app/answers/detail/a_id/7472

Timár, P. (2005). Dimensionless Characterisitics of Centrifugal Pump. *Chemical Papers, 59*(6(b)), 500- 503.

Yamaguchi, K., Wang, B., Okamoto, K., & Teramoto, S. (2014). Loss Mechanisms in Shear-Force Pump With Multiple Corotating Disks. *Journal of Fluids Engineering, 136*(8). doi: 10.1115/1.4026585

Appendix A: Specification Sheets For the Equipment

ELECTROMAGNETIC FLOWMETER
With PVDF and 316L Construction

FMG90 Series

1 YEAR WARRANTY CE

- ✔ No Moving Parts or Obstructions
- ✔ Independent to Changes of Temperature, Pressure, Viscosity
- ✔ Lightweight and Compact Design
- ✔ PVDF and 316L Wetted Parts
- ✔ Fast Response (<100 ms)

OMEGA's FMG90 Series electro-magnetic flow sensor for conductive liquid media was developed for OEM applications and does not contain any moving parts. FMG90 series is the most economic electromagnetic flowmeter due to the cost optimized plastic construction. Its design is compact and lightweight. Six flow ranges are available. Changes in temperature, density, viscosity, concentration or electrical conductivity of the medium do not affect the output signal. The sensor is intended for continuous measurement of flow rates or for dosing/batching of liquids with a minimum conductivity of 20 µS/cm.

FMG94-PVDF shown actual size.

SPECIFICATIONS
Materials:
Electrodes and Grounding Rings: Stainless steel 316L
Measuring Pipe and Process Connections: PVDF
O-Rings: EPDM
Housing: ABS
Accuracy: 1% of reading

Repeatability: 1%
Minimum Conductivity of Medium: Water and other conductive liquids/ 20 µS/cm
Medium Temperature: -10 to 60ºC (14 to 140°F) (non-freezing)
Ambient Temperature: 5 to 60ºC (41 to 140°F)
Maximum Working Pressure:
145 psi at 20ºC (68°F)
116 psi at 40ºC (104°F)
87 psi at 60ºC (140°F)
Response Time: <100 ms
Indications: Red LED – power, green LED – flow

Signal Shape: Square wave frequency, can be connected as PNP or NPN open collector pulse duty ratio 50:50, maximum signal current 25 mA
Electrical Data:
Supply: 24 Vdc ±15%
Consumption: 0.6 W
Protection Measures: Short-circuit proof and polarity protection
**Connection:** 4 pin plug connector M12 x 1
**Class:** NEMA 4 (IP65) (with attached cable socket)

Model No.	FMG91-PVDF	FMG92-PVDF	FMG93-PVDF	FMG94-PVDF	FMG95-PVDF	FMG96-PVDF
Size	DN 8	DN 8	DN 15	DN 20	DN 20	DN 25
Process Connection	½–14 NPT	½–14 NPT	¾–14 NPT	1–11.5 NPT	1–11.5 NPT	1¼–11.5 NPT
Inner Diameter	7.9 (0.31)	7.9 (0.31)	14 (0.55)	18 (0.71)	18 (0.71)	25 (0.98)
Flow Range GPM	0.066 to 1.3	0.26 to 5.3	0.66 to 13.2	1.3 to 26.4	2.6 to 53	3.3 to 66
Signal Output Starts At	0.02 GPM	0.07 GPM	0.27 GPM	0.52 GPM	1.05 GPM	1.3 GPM
Maximum Flow Rate	1.6 GPM	6.6 GPM	15.8 GPM	31.7 GPM	63.4 GPM	79.3 GPM
Pulse Rate (pulse/gal)	15000	3000	1500	750	380	300

Pressure Drop
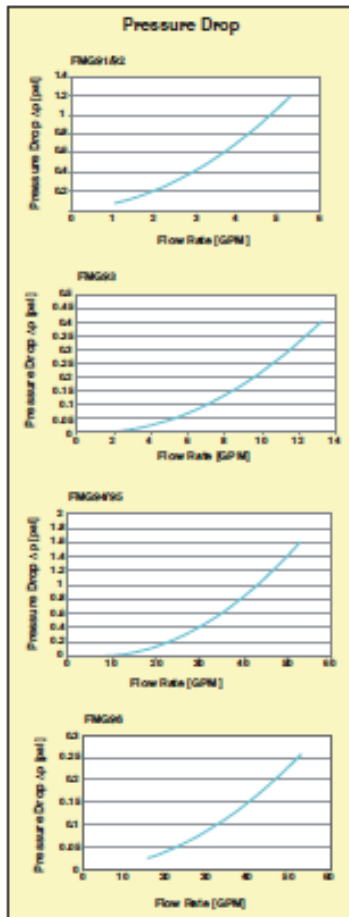
FMG91-PVDF thru FMG95-PVDF

Dimensions: mm (inch)
Ø = Diameter
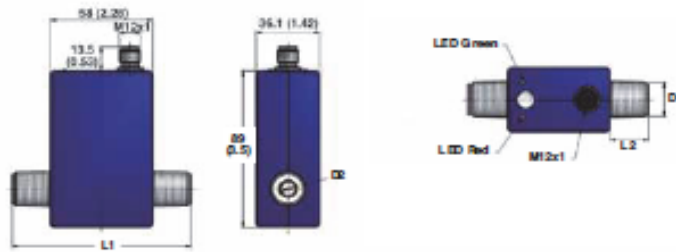
Model No.	L1	L2	D1	D2
FMG91-PVDF	4 ± 0.02	0.83 ± 0.01	½ - 14 NPT	Ø 0.31
FMG92-PVDF	4 ± 0.02	0.83 ± 0.01	½ - 14 NPT	Ø 0.31
FMG93-PVDF	4.02 ± 0.02	0.83 ± 0.01	¾ - 14 NPT	Ø 0.55
FMG94-PVDF	4.41 ± 0.02	0.98 ± 0.01	1 - 11.5 NPT	Ø 0.71
FMG95-PVDF	4.41 ± 0.02	0.98 ± 0.01	1 - 11.5 NPT	Ø 0.71

FMG96-PVDF
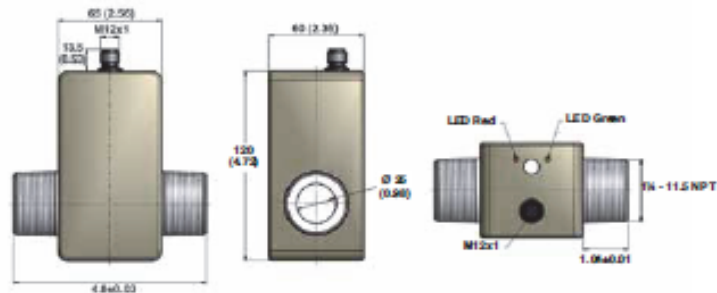
To Order

Model No.	Model No. with BSP	Description (cable sold separately)
FMG91-PVDF	FMG91-PVDF-BSP	Electromagnetic flow meter ½ NPT, 0.07 to 1.3 GPM
FMG92-PVDF	FMG92-PVDF-BSP	Electromagnetic flow meter ½ NPT, 0.26 to 5.3 GPM
FMG93-PVDF	FMG93-PVDF-BSP	Electromagnetic flow meter ¾ NPT, 0.66 to 13.2 GPM
FMG94-PVDF	FMG94-PVDF-BSP	Electromagnetic flow meter 1 NPT, 1.3 to 26.4 GPM
FMG95-PVDF	FMG95-PVDF-BSP	Electromagnetic flow meter 1 NPT, 2.6 to 53 GPM
FMG96-PVDF	FMG96-PVDF-BSP	Electromagnetic flow meter 1¼ NPT, 3.3 to 66 GPM

Accessories

Model No.	Description
M12C-PVC-4-R-F-5	5 m (16.4') cable with right angle M12 x stripped leads
M12C-PVC-4-R-F-10	10 m (32.8') cable with right angle M12 x stripped leads
PSU-93	Unregulated power supply

Comes complete with operator's manual (cable sold separately).

Ordering Example: *FMG91-PVDF*, electomagnetic flowmeter with ½ NPT connections and 0.07 to 1.3 GPM range with *M12C-PVC-4-R-F-5* 5 m (16.4') cable with right angle M12 connector.

omega.com®
ΩOMEGA®

PX26 SERIES
Pressure Transducers

INSTRUCTION SHEET
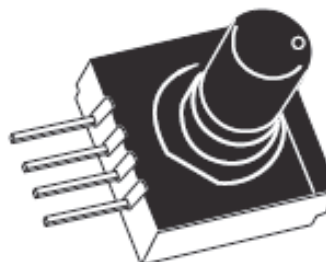
M1608/1204

Shop online at: omega.com   e-mail: info@omega.com
For latest product manuals: omegamanual.info

GENERAL INFORMATION

OMEGA's Pressure sensors are four-active piezoresistive bridge devices. When pressure is applied, a different output voltage proportional to that pressure, is produced.

Wet/Wet Differential Pressure Sensors simultaneously accept independent pressure sources. Gage Pressure Sensors provide a form of differential pressure measurement in which atmospheric pressure is used as a reference.

The PX26 is available in variety of PSI ranges and as differential and gage sensors:

MODEL NUMBER (GAGE)	RANGE	MODEL NUMBER (DIFFERENTIAL)	RANGE
PX26-001GV	0-1 PSIG	PX26-001 DV	0-1 PSID
PX26-005GV	0-5 PSIG	PX26-005DV	0-5 PSID
PX26-015GV	0-10 PSIG	PX26-015DV	0-15 PSID
PX26-030GV	0-30 PSIG	PX26-030DV	0-30 PSID
PX26-100GV	0-100 PSIG	PX26-100DV	0-100 PSID
PX26-250GV	0-250 PSIG	PX26-250DV	0-250 PSID

UNPACKING

Remove the packing list and verify that all equipment has been received. If there are any questions about the shipment, please call OMEGA Customer Service Department at 1-800-622-2378 or 203-359-1600. We can also be reached on the Internet at omega.com   e-mail: info@omega.com

Upon receipt of shipment, inspect the container and equipment for any signs of damage. Take particular note of any evidence of rough handling in transit. Immediately report any damage to the shipping agent.

NOTE:

The carrier will not honor any claims unless all shipping material is saved for their examination. After examining and removing contents, save packing material in event reshipment is necessary.

MEDIA COMPATIBILITY

Input media are limited to those media which will not attack polyester, flurosilicon, or silicon, such as oils, lacquer thinner, hydraulic fluid, most petroleum products, water and salt water. Not recommended for freons.

SOLDERING

Limit soldering temperature to 600°F (315°C) for 10 seconds duration maximum.

ELECTRICAL CONNECTION

NOTCHED (PIN 1)

METER

| 1 |
| 2 |
| 3 |
| 4 |
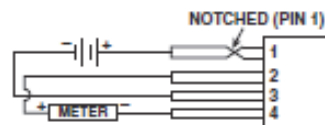
WARNING! READ BEFORE INSTALLATION

Fluid hammer and surges can destroy any pressure transducer and must always be avoided. A pressure snubber should be installed to eliminate the damaging hammer effects.

Fluid hammer occurs when a liquid flow is suddenly stopped, as with quick closing solenoid valves. Surges occur when flow is suddenly begun, as when a pump is turned on at full power or a valve is quickly opened.

Liquid surges are particularly damaging to transducers if pipe is original empty. To avoid damaging surges, fluid lines should remain full (if possible), puts should be up to power slowly, and valves opened slowly. To avoid damage from both fluid hammer and surges, a surge chamber should be installed, and a pressure snubber should be installed on every transducer.

Symptoms of fluid hammer and surges damaging effects:
a) Pressure transducer exhibits an output at zero pressure (large zero offset). If offset is less than 10% FS, user can usually re-zero meter, install proper snubber and continue monitoring pressures.
b) Pressure transducer output remains constant regardless of pressure.
c) In severe cases, there will be no output.

140

SPECIFICATIONS

EXCITATION:	10Vdc, 16Vdcmax @ 2mA
OUTPUT:	100mV, 1 10mV/V
	(16.7mV, 1.67mV/V for
	1 PSI range)
	(50mV, 5mV/V for 5PSI range)
ACCURACY:	1% FS
LINEARITY:	1.0% FS BFSL
HYSTERESIS & REPEATABILITY:	0.2% FS
ZERO BALANCE:	±1.5mV
SPAN TOLERANCE:	±3.0 mV
STORAGE TEMPERATURE:	-67° to 212°F (-55° to 100°C)
OPERATING TEMPERATURE:	-40 to 185°F (-40° to 85°C)
COMPENSATED TEMPERATURE:	32° to 122°F (0° to 50°C)
THERMAL EFFECTS:	ZERO: 1 mV
(25 to 50°C, 25 to 0°C)	SPAN: 1% Rdg
PROOF PRESSURE:	20 PSI for 1 and 5 PSI range
	45 PSI for 15 PSI range
	60 PSI for 30 PSI range
	200 PSI for 100 PSI range
	500 PSI for 250 range
INPUT RESISTANCE:	7.5k Ω
OUTPUT RESISTANCE:	2.5k Ω.
RESPONSE TIME:	1 msec.
SHOCK:	Qualified to 150 G
VIBRATION:	Qualified to 2kHz @ 20 G sine
GAGE TYPE:	Silicon sensor
WETTED PARTS:	Polyester, Silicon, flurosilicon
MATING CONNECTOR:	CX136-4, not included
PRESSURE PORT:	0.20" dia. & 0.25" collar dia.
ELECTRICAL CONNECTION:	Pin 1 +EXC (notched)
	Pin 2 +OUT
	Pin 3 −EXC
	Pin 4 −OUT
WEIGHT:	Approx 0.07 oz (2 gm)
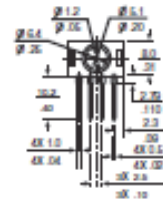
Gage Sensor

Pressure is applied to Port P2

Port P 1 vents to ambient pressure
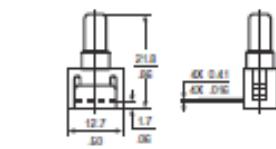
Differential Sensor

Port P 1 is near terminals.

PORT P2

PORT P1

The EC 32 flat with integrated electronics is a brushless, speed-controlled 1-quadrant drive. It is available as 15 watt version and in 2-wire or 5-wire variants as follows:

Order number		Variant	Nominal speed [rpm]	Output [W]
IP 40	IP 00			
353400	353324	2-wire	3000	15
353401	353325	2-wire	6000	15
353399	349801	5-wire «Enable»	6000	15
370418	370417	5-wire «CW/CCW»	6000	15

Functions

- Commutation with Hall sensors
- Digital speed control
- Speed range: 200…7'000 rpm (depending on variant)
- Current limitation, non-adjustable
- Overvoltage and undervoltage switch-off
- Overvoltage protection
- Blockage protection, temperature monitoring
- Inverse polarity protection

2-wire variant
- Speed proportional to supply voltage

5-wire variant
- Set value speed through analog signal 0…10 V
- 2-wire operation possible
- Versions:
  - «Enable» TTL level-compatible
  - Direction preselection «CW/CCW» TTL level-compatible
- Speed monitor delivers speed-proportional frequency signal

Contents

maxon motor ag   Brünigstrasse 220   P.O.Box 263   CH-6072 Sachseln   Phone +41 41 666 15 00   Fax +41 41 666 16 50   www.maxonmotor.com

142

maxon motor

maxon motor ag Brünigstrasse 220 P.O. Box 263 CH-6072 Sachseln Phone +41 41 666 15 00 Fax +41 41 666 16 50 www.maxonmotor.com

READ THIS FIRST

These instructions are intended for qualified technical personnel.

Prior commencing with any activities...

- you must carefully read and understand this manual and
- you must follow the instructions given therein.

The EC 32 flat with integrated electronics is considered as partly completed machinery according to EU Directive 2006/42/EC, Article 2, Clause (g) and is intended to be incorporated into or assembled with other machinery or other partly completed machinery or equipment.

Therefore, you must not put the device into service,...

- unless you have made completely sure that the other machinery – the surrounding system the device is intended to be incorporated to – fully complies with the requirements stated in the EU directive 2006/42/EC!
- unless the surrounding system fulfils all relevant health and safety aspects!
- unless all respective interfaces have been established and fulfil the stated requirements!

Safety Guidelines

Qualified personnel	Do not engage with any work unless you possess the necessary skills.
Legal requirements	Observe any regulation applicable in the country and/or at the site of implementation with regard to health and safety/accident prevention and/or environmental protection.
	Make sure that all associated devices and components are installed according to local regulations.
Additional safety equipment	Be aware that, by principle, an electronic apparatus can not be considered fail-safe. Therefore, you must make sure that any machine/apparatus has been fitted with independent monitoring and safety equipment. If the machine/apparatus should break down, if it is operated incorrectly, if the control unit breaks down or if the cables break or get disconnected, etc., the complete drive system must return – and be kept – in a safe operating mode.
Repairs	Be aware that you are not entitled to perform any repair on components supplied by maxon motor.
Danger to life	Touching live wires causes death or serious injuries!

- Consider any power cable as connected to live power, unless having proven the opposite!
- Make sure that neither end of cable is connected to live power!
- Make sure that power source cannot be engaged while work is in process!
- Obey lock-out/tag-out procedures!
- Make sure to securely lock any power engaging equipment against unintentional engagement and tag it with your name!

Max. supply voltage	The connected supply voltage must be between 10 VDC and 28 VDC. Permanently applied voltages above 30 VDC will destroy the unit.
Electrostatic sensitive components	The built-in electronics may be destroyed by externally applied electronic discharge during transport, installation, and during operation.

- Make sure to wear working cloth in compliance with ESD.
- Handle device with extra care.
- Limit the voltage between flange and live parts to 500 VDC.

Temperature	During operation, the temperature of housing, flange, or other components may exceed 60°C.

maxon motor

maxon motor ag Brünigstrasse 220 P.O. Box 263 CH-6072 Sachseln Phone +41 41 666 15 00 Fax +41 41 666 16 50 www.maxonmotor.com

Terms used

1-Q speed controller	The motor produces positive torque in the selected or programmed direction. The load is not actively decelerated when the speed set value is reduced or the direction changed (direction preselection version). Speed control recommences as soon as the load has reduced its speed by friction to the level specified by the set value speed.
Max. torque M_{max} [mNm]	The maximum torque the motor can produce for a short term. It is limited by the overload protection of the electronics.
Max. current I_{max} [A]	Supply current with which the peak torque is generated at nominal voltage. With an active speed controller, the supply current is not proportional to the torque, but also depends on the supply voltage. As a result, this value only applies at nominal voltage.
IP 00	No protection against access to dangerous parts. No protection against water.
IP 40	Protected against access to dangerous parts with a wire, tool or similar. ≥Ø1 mm and against foreign objects ≥Ø1 mm. No protection against water.
Direction CW/ CCW	As seen towards the mounting flange: • CW - shaft turns to the right (clockwise) • CCW - shaft turns to the left (counterclockwise)

1 Technical Data

Motor Data 15 Watt at 24 VDC				
IP 40 (with housing) IP 00 (without housing)		353400 353324	353401 353325	353399 / 370418 348801 / 370417
Nominal voltage	VDC	24	24	24
No load speed	rpm	3000	6000	6000
No load current	mA	43	86	86
Nominal speed	rpm	3000	6000	6000
Nominal torque	mNm	26.2	24	24
Nominal current	mA	590	950	950
Max. Torque	mNm	34.4	34	34
Max. current	mA	1200	1600	1600
Max. efficiency	%	54	64	64

Operating range n = f (M)
Nominal speed 3000 rpm
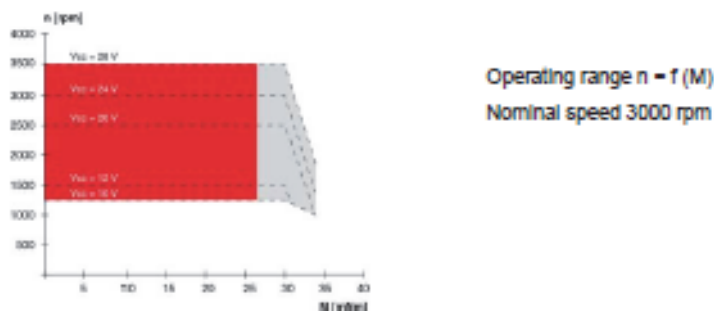
Figure 1 2-Wire Variant (353324) (353400)

144

maxon motor

maxon motor ag Brünigstrasse 220 P.O. Box 263 CH-6072 Sachseln Phone +41 41 666 15 00 Fax +41 41 666 16 50 www.maxonmotor.com

Figure 2   2-Wire Variant (353325) (353401)
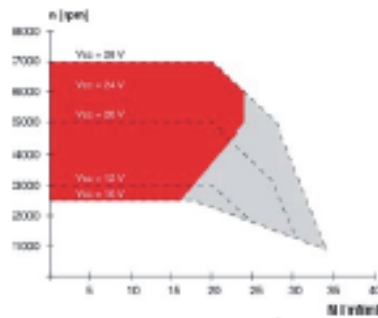
Operating range n = f (M)
Nominal speed 6000 rpm

Figure 3   5-Wire Variant (349801) (353399) (370417) (370418)
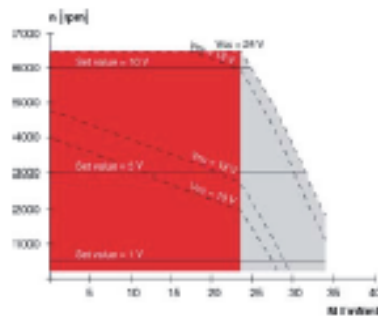
Operating range n = f (M)
Torque and speed depend on operating voltage

Controller Data				
Variant Nominal speed		2-wire 3000 rpm	2-wire 6000 rpm	5-wire 6000 rpm
Control variable		Speed	Speed	Speed
Supply voltage V_{CC}	V	10...28	10...28	10...28
Input set value speed	V	=VCC	=VCC	0.33...10.8
Scaling set value speed	rpm/V	125	250	600
Speed range	rpm	1250...3500	2500...7000	200...6480
Max. acceleration	rpm/s	3000	6000	6000
Direction of rotation		CW	CW	CW
Version Direction Preselection «CW/CCW»		–	–	CW/CCW

Thermal Data		
Version		16 Watt
Thermal resistance housing/ambient air	K/W⁻¹	7.6
Thermal resistance winding/housing	K/W⁻¹	5.9
Thermal time constant winding	s	10.3
Thermal time constant motor	s	72.6
Max. winding temperature	°C	+125
Max. temperature of electronics	°C	+105

maxon motor

maxon motor ag Brünigstrasse 220 P.O. Box 263 CH-6072 Sachseln Phone +41 41 666 15 00 Fax +41 41 666 16 50 www.maxonmotor.com

Mechanical Data (preloaded ball bearings)

Version			16 Watt
Rotor inertia		gcm^2	35
Axial play at axial load	<2 N >2 N	mm	0 0.14
Radial play			preloaded
Max. axial load	dynamic	N	6.8
Max. axial load	static supported *a	N	70 1000
Max. radial load *b		N	32
Motor weight		g	91

*a Static load with supported shaft
*b Admissible load 7.5 mm from flange

Electrical Connections

Wire	Description	Connection	Value
red	Supply voltage V_{CC}	Supply	10…28 VDC
black	GND	Supply	Ground
white (5-wire operation only)	Input set value speed	Input	0.33…10.8 VDC
green (wire operation only)	Monitor speed n	Output	6 counts per turn
Version Enable grey (5-wire operation only)	«Enable»	Input	2.4…28 VDC
Version Direction Preselection grey (5-wire operation only)	«CW/CCW»	Input	2.4…28 VDC
Cross section			AWG24 = 0.22 mm^2

Protective Functions

Inverse polarity protection	up to max. 30 VDC
Blockage protection	cut off with blocked motor after 2 s
Undervoltage	cut off at V_{CC} <8.5 V
Overvoltage protection	cut off at V_{CC} >29.5 V
Thermal monitoring of power stage	cut off at (typical) at T >100 °C
Overvoltage protection (transient)	150 mWs

Ambient Conditions

Temperature operation	-40…+40°C
Temperature operation with reduced power output	+40…+85°C
Temperature storage	-40…+85°C
Humidity (condensation not permitted)	20…80%

Voltage Supply

Ripple	<5%
Load-dependent output current (recommended)	≥1 A
Output current	min. 9.5 VDC max. 29 VDC

146

maxon motor

maxon motor ag Brünigstrasse 220 P.O. Box 263 CH-6072 Sachseln Phone +41 41 666 15 00 Fax +41 41 666 16 50 www.maxonmotor.com

Dimensional Drawings
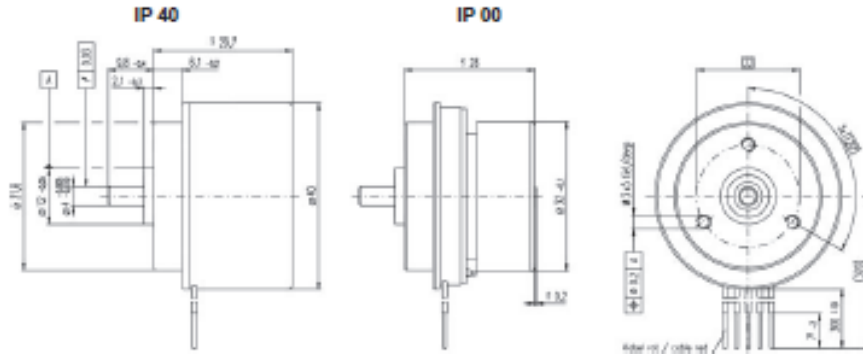
Figure 4   15 Watt Version – Dimensional Drawing [mm]

2   Installation

Electrostatic Sensitive Device (ESD)
- *Make sure to wear working cloth in compliance with ESD.*
- *Handle device with extra care.*

Possible irreversible Damage of Motor
- *Until completion of the installation, individual components can be permanently damaged by improper handling. Therefore, handle the components with particular care.*
- *Max. torque of flange screws is 1.1 Nm (grade 8.8 screws).*
- *Improved cooling through mounting a large metallic part.*
- *Cable outlet preferably downwards.*

EMC-compliant Installation

Cable length ≤300 mm:

- Usually, no shielding is required.
- Star wiring recommended if several EC 32 flat with integrated electronics are supplied by a common power supply.

Cable length >300 mm:

- The voltage drop in the connection cable must be minimized by choosing a sufficiently large wire cross section.
- In electromagnetically harsh environments, use of shielded cables connected to ground at both ends can improve immunity against interferences.
- Release cable shielding on one side if 50/60 Hz interference problems occur.
- The incidence surface for interferences can be reduced by shortening the unshielded original connection cable.
- Immunity against interferences and speed stability in case of fluctuating loads can be accomplished by routing the set speed value signal separately in a shielded cable that is put to ground on both sides. In addition to the set speed value signal, a second ground (GND) line must also be carried in this separate cable, but only connected on the motor side. The external set value speed signal must be potential-free.

147

3   Minimal Wiring

2-Wire Variant

Figure 5   2-Wire Variant with external Power Source

5-Wire Variant
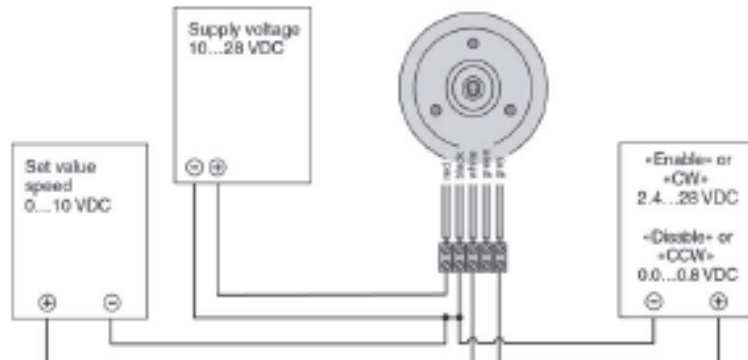
Figure 6   5-Wire Variant: Speed Set Value and Release «Enable» or Direction «CW/CCW» (depending on Version) with external Power Source
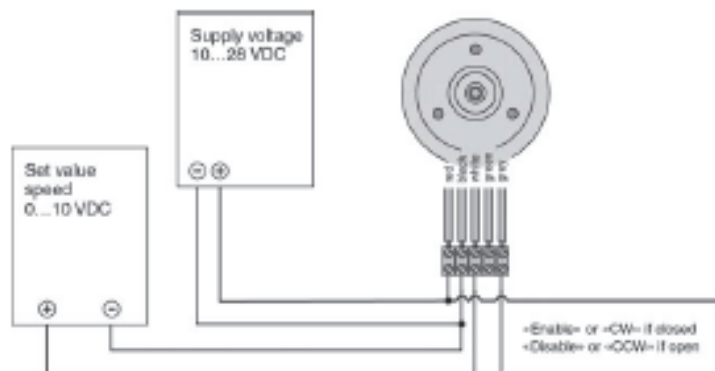
Figure 7   5-Wire Variant: Speed Set Value with external Power Source and Release «Enable» or Direction «CW/CCW» (depending on Version) with Potential-free contact

maxon motor

maxon motor ag Brünigstrasse 220 P.O. Box 263 CH-6072 Sachseln Phone +41 41 666 15 00 Fax +41 41 666 16 50 www.maxonmotor.com
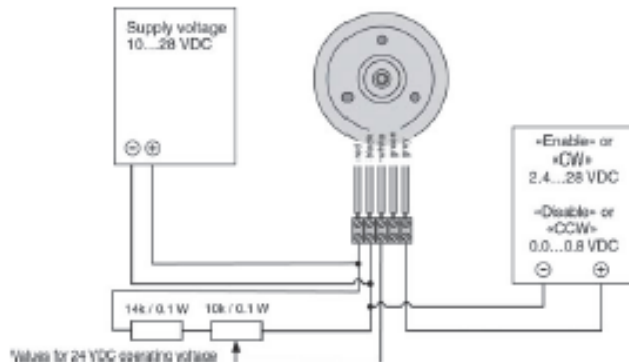
Figure 8 5-Wire Variant: Speed Set Value with external Potentiometer and Release «Enable» or Direction «CW/CCW» (depending on Version) with external Power Source
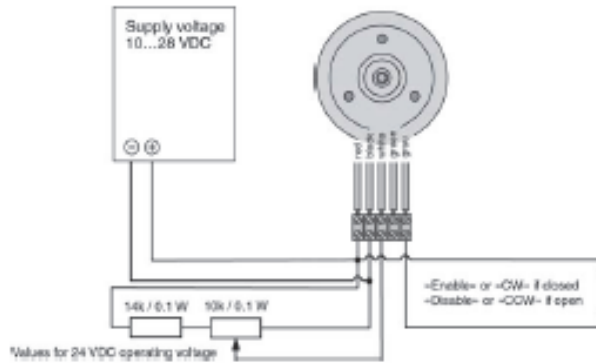
Figure 9 5-Wire Variant: Speed Set Value with external Potentiometer and Release «Enable» or Direction «CW/CCW» (depending on Version) with Potential-free Contact

149

maxon motor

maxon motor ag Brünigstrasse 220 P.O. Box 263 CH-6072 Sachseln Phone +41 41 666 15 00 Fax +41 41 666 16 50 www.maxonmotor.com

5-Wire Variant in Operating Mode "2-Wire"

The operating mode "2-Wire" can be simulated by shorting the connections of speed set value input and speed monitor output. Thereby, the speed proportional to the supply voltage (➔Figure 17).
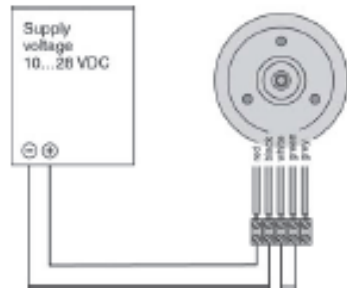
Figure 10   5-Wire in Operating Mode "2-Wire"

With the variant Direction Preselection «CW/CCW», the grey wire is used to define direction of rotation.
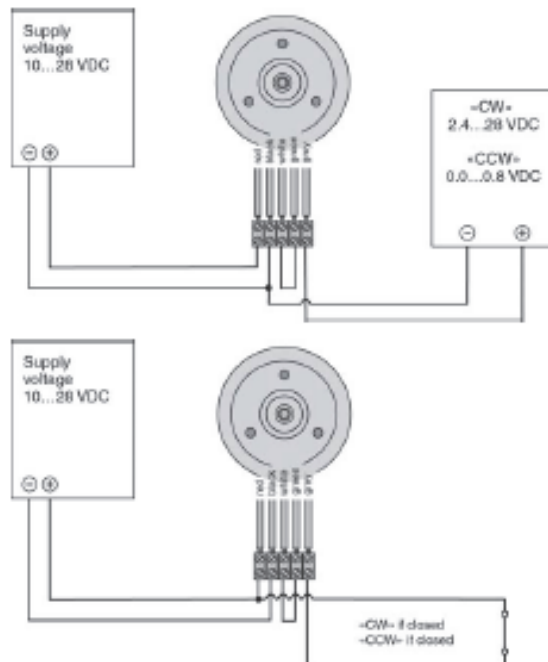
Figure 11   5-Wire Variant: Direction «CW/CCW» in Operating Mode "2-Wire"

maxon motor

maxon motor ag Brünigstrasse 220 P.O. Box 263 CH-6072 Sachseln Phone +41 41 666 15 00 Fax +41 41 666 16 50 www.maxonmotor.com

4 Functional Description of 2-Wire Variant

Speed proportional to supply voltage V_{CC}

- Motor speed is proportional to the supply voltage, independent of torque.
- Supply voltage can be varied within the permitted range.
- Speed at 24 V supply voltage is:
  - 3000 rpm (353324) (353400)
  - 6000 rpm (353325) (353401)
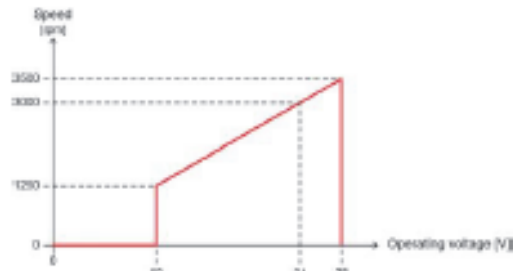
Figure 12   2-Wire Variant: Speed 3000 rpm as Function of the applied Supply Voltage
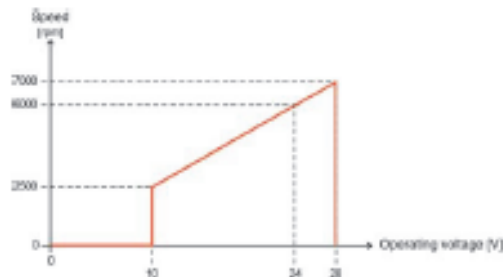
Figure 13   2-Wire Variant: Speed 6000 rpm as Function of the applied Supply Voltage

151

maxon motor

maxon motor ag Brünigstrasse 220 P.O. Box 263 CH-6072 Sachseln Phone +41 41 666 15 00 Fax +41 41 666 16 50 www.maxonmotor.com

5 Functional description of 5-Wire Variant

Set value speed input

Motor speed is set with an analog voltage at the input "Speed Set Value". The input is protected against overvoltage.

Pin assignment	Connection wire white
Input voltage range	0...+10.8 V (referenced to GND)
Input impedance	62 kΩ (in range of 0...+21.9 V) 47 kΩ (in range of +21.9...+30 V)
Continuous overvoltage protection	-30...+30 V
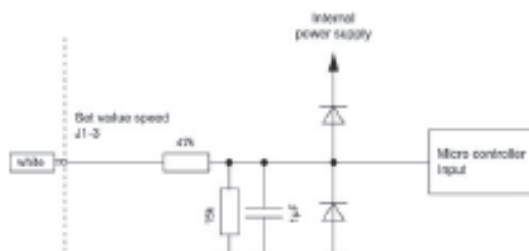
Figure 14   5-Wire Variant: Internal Circuitry of Input "Speed Set Value"

The speed set value is set with the voltage at the input "Speed Set Value". The set speed is controlled by the controller. Changes to speed set value are restricted by the maximum acceleration (→Controller Data on page 4).

To activate the power stage in the «Enable» version, the voltage at the input "Enable" must be higher than 2.4 V, while the speed set value must be above 0.17 V.

With the «CW/CCW» version, the power stage is activated when the speed set value is above 0.17 V.

| Set Value	Function	Remarks
0...0.17 V	«Disable»	Power stage disabled
0.17...0.33 V	Operation at minimal speed (200 rpm)	If «Enable» higher than 2.4 V (version «Enable»)
0.33...10.8 V	Linear speed setting between 200 and 6480 rpm $V_{ata} = \dfrac{n_{ata}}{600}$	In speed range 200...300 rpm, regulation accuracy of the speed controller is limited. The speed may considerably differ from the set value depending on load and supply voltage.

V_{Soll} Set value voltage

n_{Soll} Desired speed

maxon motor

maxon motor ag Brünigstrasse 220 P.O. Box 263 CH-6072 Sachseln Phone +41 41 666 15 00 Fax +41 41 666 16 50 www.maxonmotor.com

Figure 15   5-Wire Variant: Speed as Function of Set Value Voltage

Optionally, the controller can be set to 2-wire operation mode by linking (shorten) both connections speed monitor (green) and speed set value (white). Thereby, the connection must be established before applying the supply voltage.

Working Principle of Detection of "2-Wire" Operating Mode with 5-Wire Motor
After power on of the controller, the output "Speed Monitor" will be turned on after 270 ms, than turned off again after 40 ms. If the input "Speed Set Value" follows this regime via short circuit, the opera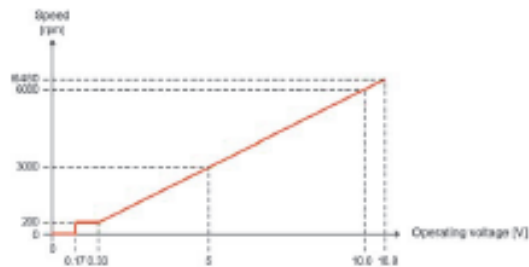ting mode "2-wire" will be activated. Thereby, for both measurements, the input "Speed Set Value" must be once above and once below 2.5 V. A fixed random or increasing speed set value upon power on is permitted.

In order not to interfere with detection of "2-wire" operating mode, the motor must neither be externally propelled during power on nor be in rundown.

Setting Speed Set Value by PWM Signal
The speed set value can be preset by fixed frequency and amplitude.

The desired set speed value change is obtained by variation of the duty cycle in range of 0...100%. Both, amplitude and duty cycle thereby have an effect on the resulting speed. The average of the applied PWM voltage corresponds to the analog input signal of the speed set value.

In order to prevent the controller to change to "2-wire" operating mode after power on, the speed set value voltage must not exceed 2.5 V 270 ms after power on and may not be below 2.5 V for another 40 ms. A fixed random or increasing speed set value upon power on is permitted.

Nominal value amplitude PWM set value	0...10.8 V
Max. value amplitude PWM set value	-30...+30 V
Frequency range PWM set value	500 Hz...20 kHz
Modulation PWM set value	0...100%
Continuous overvoltage protection	-30...+30 V

maxon motor

maxon motor ag Brünigstrasse 220 P.O. Box 263 CH-6072 Sachseln Phone +41 41 666 15 00 Fax +41 41 666 16 50 www.maxonmotor.com
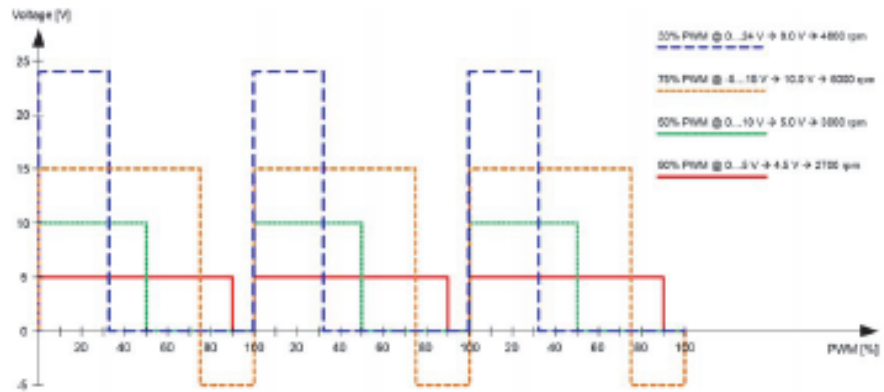
Figure 16   5-Wire Variant: Examples for possible PWM Level Control at Input "Speed Set Value"

Enabling with Version «Enable»

The power stage is activated with the digital input "Enable". It is protected against overvoltage.

Pin assignment	Connection wire grey
Input voltage range	0...+5.0 V (referenced to GND)
Input impedance	112 kΩ (in range of 0...+5.9 V) 12 kΩ (in range of +5.9...+30 V)
Continuous overvoltage protection	-30...+30 V
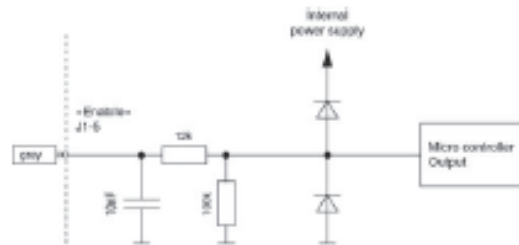
Figure 17   5-Wire Variant: Internal Circuitry of Input "Enable"

The power stage is activated by a voltage above 2.4 V at the input "Enable". The resulting speed is dependable on the voltage applied to the input "Speed Set Value".

The power stage is deactivated by a voltage below 0.8 V at the input "Enable". The motor runs out freely independent of the voltage applied to the input "Speed Set Value".

Input Voltage	Function	Remarks
0....0.8 V	«Disable»	Power stage disabled
2.4....5.0 V	«Enable»	Power stage enabled, if set value is above 0.17 V

154

maxon motor

maxon motor ag Brünigstrasse 220 P.O. Box 263 CH-6072 Sachseln Phone +41 41 666 15 00 Fax +41 41 666 16 50 www.maxonmotor.com

Enabling and Direction Preselection with Version «CW/CCW»

The power stage is activated if the voltage to the input "Speed Set Value" is above 0.17 V. Direction of rotation «CW/CCW» will be determined by digital input "Direction".

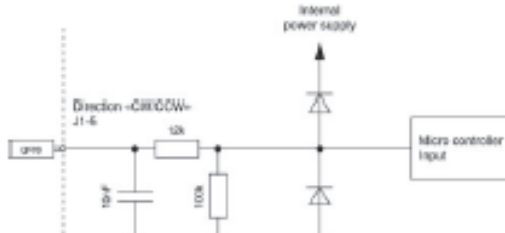| Pin assignment	Connection wire grey
Input voltage range	0...+5.0 V (referenced to GND)
Input impedance	112 kΩ (in range of 0...+5.9 V) 12 kΩ (in range of +5.9...+30 V)
Continuous overvoltage protection	-30...+30 V

Figure 18   5-Wire Variant: Internal Circuitry of Input "Direction"

The direction of rotation «CW» will be activated by a voltage above 2.4 V. The speed is dependent on the voltage at the input "Speed Set Value". If the direction of rotation is changed during operation, the motor runs down freely until reaching minimal speed, then accelerates in opposite direction of rotation. The power stage will be deactivated with a voltage below 0.17 V at the speed set value input. The motor runs down freely.

Input Voltage	Function	Remarks
0...0.8 V	Direction of rotation «CCW»	Motor turns in direction «CCW»
2.4...5.0 V	Direction of rotation «CW»	Motor turns in direction «CW»

Speed monitor «Monitor n»

The actual speed of the motor shaft can be monitored at the output "Speed Monitor". It is available as digital signal (High/Low) and delivers 6 pulses per mechanical turn.

The output "Speed Monitor" is also available in «Disable» state.

Pin assignment	Connection wire green
Voltage output range	0...+5.0 V (referenced to GND)
Output resistance	4.1 kΩ
Low level	max. 0.5 V (without load)
High level	min. 4.2 V (without load)
Duty cycle	50%
Continuous overvoltage protection	-30...+30 V
Frequency at speed monitor output	$f_{monitor} = \dfrac{n_{actual}}{10}$ $n_{actual} = 10 \cdot n$

$f_{Monitor}$ Frequency at speed monitor output [Hz]
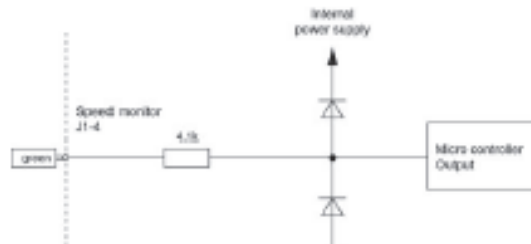
n_{Ist} Speed [rpm]

maxon motor

maxon motor ag Brünigstrasse 220 P.O. Box 263 CH-6072 Sachseln Phone +41 41 666 15 00 Fax +41 41 666 16 50 www.maxonmotor.com

Figure 19   5-Wire Variant: Internal Circuitry of Output "Speed Monitor"

6   Protective Functions

Inverse polarity protection	The supply voltage V_{CC} is protected against polarity reversal. Thereby, the negative input voltage must not exceed the maximum permitted supply voltage V_{CC}.
Undervoltage switch-off	The power stage is switched off when the supply voltage V_{CC} drops below approx. 8.5 V to prevent operation beyond the specified range.
	If the supply voltage exceeds the restart threshold of approx. 9 V, the EC 32 flat will be again ready for operation.
Overvoltage switch-off	The power stage is switched off when the supply voltage V_{CC} exceeds approx. 29.5 V to prevent operation beyond the specified range.
	If the supply voltage drops below the restart threshold of approx. 28.5 V, the EC 32 flat will be again ready for operation.
Overvoltage protection	The overvoltage protection comprises a bidirectional Transzorb diode (overvoltage protection diode) capable of receiving a maximum peak energy of 150 mWs. Continuous power loss is 1 W. Threshold voltage is a minimum of 31.1 V, independent of polarity.
Blockage protection	The power stage is switched off when the rotor is continuously blocked for 2 seconds.
	After 4 seconds, the EC 32 flat automatically executes a starting attempt.
Temperature monitoring	The power stage is switched off if the PCB temperature exceeds approx. 100°C. As soon as the PCB temperature has dropped below approx. 90°C, the EC 32 flat will be again ready for operation.
	The electronics' temperature protection can only safeguard the winding if the flange does not dissipate too much heat and an if the winding does not induce heat accumulation.
Current limiting	The winding current is electronically limited to approx. 1.6 A. Therefore, the maximum load torque is limited accordingly.
	If the motor shaft comes to a standstill due to activated current limiting, blockage protection engages after 2 seconds.

156

7   Troubleshooting

2-Wire Variant

- Supply voltage between 10.0 and 28.0 VDC?
- Supply voltage connected to red and black wires and switched on?
- Voltage at red motor connection positive compared to black connection?
- Power source not in current limiting?
- Motor not blocked mechanically?

5-Wire Variant

- Supply voltage between 10.0 and 28.0 V?
- Supply voltage connected to red and black wires and switched on?
- Voltage at red motor connection positive compared to black connection?
- Speed set value voltage between 0.33 and 10.0 V?
- Speed set value voltage connected to white and black wires and switched on?
- Voltage at white connection positive compared to black connection?
- Activation via voltage source (version «Enable» only)
  - Enable voltage between 2.4 and 28.0 VDC?
  - Enable voltage connected to grey and black wires and switched on?
  - Voltage at grey connection positive compared to black connection?
- Activation via potential-free contact (version «Enable» only)
  - Grey enable wire directly interconnected with red supply voltage connection?
  - Grey enable wire connected via switch with red supply voltage connection?
  - Switch or contact closed?
- Power source not in current limiting?
- Motor not blocked mechanically?
- Green wire need not necessarily be connected.

5-Wire Variant in Operating Mode "2-Wire"

- White and green wires directly interconnected (short-circuit)?
- Direct interconnection of white and green wire established prior connecting to supply voltage?
- No further connections to green and white wires?
- Supply voltage between 10.0 and 28.0 VDC?
- Supply voltage connected and switched on?
- Voltage at red motor connection positive compared to black connection?
- With version «Enable»: Grey wire need not necessarily be connected.
- With version «CW/CCW»: Grey wire may be used for direction of rotation (→5-Wire Variant in Operating Mode "2-Wire" on page 9).
- Power source not in current limiting?
- Motor not blocked mechanically?

Appendix B: LabVIEW Information

Figure 3.21, shows the block diagram from LabVIEW used for the pressure and flow rate data acquisition. In each DAQ assistant in Fig. 3.21, a conversion factor was used to convert the incoming signal to more meaningful units, such as pressure and flow rate. The top box in Fig 3.21 is for the pressure sensor, and the formula box contains the conversion factor (which is discussed later). The bottom box is for the flow meter where the conversion factor of 0.25233 is input directly into the DAQ assistant box.

Starting with the 5 psi pressure sensor, for 10V DC the output voltage should be 50 mV or 5 mV/V. The 15 psi range pressure sensor for 10V DC should be 100 mV, or 10 mV/V. Since 8.1 V is used for excitation, the manufacturer's calibration has to be converted according to this voltage. For the 5 psi range, the full range of sensor output is 40.5 mV, leading to 8.1 mV/psi. For the 15 psi range, 81 mV is the full range, leading to 5.4 mV/psi. This value needed to be converted next to a factor so that it could be input into LabVIEW, which is reading a voltage from the pressure sensor.

The flow meter's conversion factor was obtained experimentally using the average frequency output from the flow meter and volume of water, over a minute. The flow meter produces a certain number of pulses per gallon, which for this particular model of flow meter (FMG91-PVDF) was 15000 pulse/gallon.
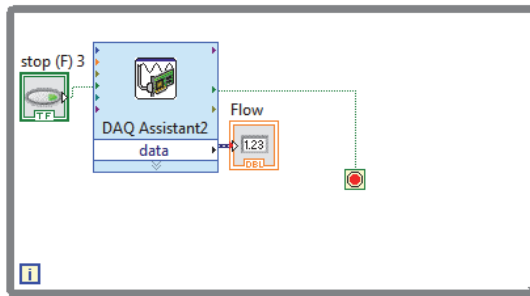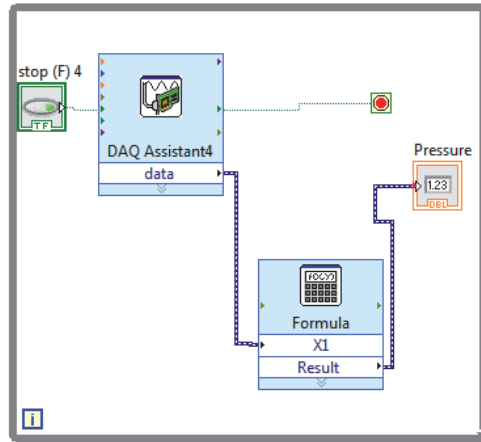
Figure B.1 Screen shot of the schematic of the data acquisition program in LabVIEW.